Dissertation

submitted to the

Combined Faculties for the Natural Sciences and Mathematics

of the Ruperto-Carola University of Heidelberg, Germany

for the degree of

Doctor of Natural Sciences

Put forward by

Alexander Helmboldt

Born in Mannheim, Germany

Oral examination: 19.07.2018

New insights into modified scalar sectors and exotic Higgs decays

Referees: Prof. Dr. Dr. h.c. Manfred Lindner

Prof. Dr. Tilman Plehn

New insights into modified scalar sectors and exotic Higgs decays

In the context of models with modified Higgs sectors, we examine different possible causes for a systematic absence of new physics from current searches at the Large Hadron Collider (LHC). First, having in mind the lack of clear signs for supersymmetry, we consider theories based on classical scale invariance as an alternative approach towards addressing the gauge hierarchy problem. Within the aforementioned framework, we present a systematic analysis of simple Standard Model (SM) extensions. As a result, we identify the minimal model, which allows for radiative electroweak symmetry breaking, is consistent with all current experimental constraints and does not reintroduce any fine-tuning issues. Next, given that very light scalar particles as predicted by several well-motivated beyond-the-SM theories have not yet been detected either, we propose a novel search strategy based on exotic Higgs decays into three of these light scalars. We show that said processes can be abundant enough to be observable at the LHC or future lepton colliders in exciting new signatures containing six SM fermions in the final state. In particular, we demonstrate the three-body channel's capabilities in probing scenarios which are inaccessible to existing searches exclusively relying on the related two-body Higgs decay. Our last study is motivated by the fact that new physics may manifest itself only through effects which are out of the LHC's reach due to the large amounts of hadronic background. As an example, we consider quark-flavor-violating Higgs decays involving bottom quarks and evaluate the expected sensitivity of direct searches at the proposed International Linear Collider (ILC). In doing so, we identify hadronic SM Higgs decays with mistagged jets as the dominant background processes and find that a dedicated analysis is anticipated to explore branching ratios down to the per-mill level.

Neue Erkenntnisse über modifizierte Higgs-Sektoren und exotische Higgs Zerfälle

Im Rahmen von Modellen mit modifizierten Higgs-Sektoren untersuchen wir verschiedene mögliche Ursachen für eine systematische Abwesenheit neuer Physik von entsprechenden Suchen am Large Hadron Collider (LHC). Angesichts des Fehlens klarer Hinweise auf Supersymmetrie betrachten wir als Erstes klassisch skaleninvariante Theorien, die einen alternativen Zugang zur Lösung des Hierarchieproblems darstellen. Innerhalb solcher Theorien führen wir eine systematische Studie einfacher Standardmodell (SM) Erweiterungen durch. Somit können wir das minimale Modell identifizieren, welches radiative elektroschwache Symmetriebrechung erlaubt und vereinbar mit allen experimentellen Schranken ist, ohne dabei ein Feinabstimmungsproblem wiedereinzuführen. Auch leichte skalare Teilchen, deren Existenz von etlichen gut motivierten Modellen jenseits des SM vorhergesagt wird, konnten bisher nicht gefunden werden. Daher schlagen wir als Nächstes eine neue Suchstrategie vor, die auf exotischen Higgszerfällen in drei dieser leichten Skalare basiert. Wir finden, dass besagte Prozesse häufig genug vorkommen können, um am LHC oder zukünftigen Leptonbeschleunigern in neuen, spektakulären Signaturen mit sechs SM Fermionen im Endzustand beobachtet zu werden. Insbesondere zeigen wir, dass der Drei-Körper-Zerfall Szenarien testen kann, die für bestehende Suchen, welche ausschließlich auf dem verwandten Zwei-Körper-Zerfall beruhen, unzugänglich sind. Unsere letzte Studie ist dadurch motiviert, dass neue Physik sich möglicherweise nur durch solche Signaturen manifestiert, welche wegen des vielen hadronischen Untergrundes am LHC nicht nachweisbar sind. Als Beispiel betrachten wir Quark-Flavor-verletzende Higgszerfälle mit Bottom-Quarks und bestimmen die erwartete Sensitivität direkter Suchen am geplanten International Linear Collider (ILC). Dabei erkennen wir hadronische SM Higgszerfälle mit falsch identifizierten Jets als die dominanten Untergrundprozesse und finden, dass eine geeignete Analyse es erlauben wird, Verzweigungsverhältnisse im Promillebereich zu prüfen.

Contents

Chapter 1

Introduction and motivation

July 4^{th} 2012 will go down in history as one of the most memorable days for particle physicists during the last decades. The seminal discovery of the Higgs boson at the Large Hadron Collider (LHC) [1, 2], which was announced on that Wednesday, marked the long-awaited experimental observation of the last missing piece of the Standard Model (SM) of particle physics, and thus the culmination of years of extensive effort to track down a particle which was already predicted in the 1960s, and which is of immense importance for high-energy physics. Whereas, for instance, a third generation of quarks and leptons seems expendable from a purely formal point of view, the existence of the Higgs field is absolutely crucial for writing down a consistent quantum field theory describing the fundamental interactions of Nature, barring gravity [3–5]. Although the minimal SM has thus been completed from a theoretical perspective, it still leaves many fundamental questions of modern physics unanswered.

For example, while the Standard Model as it stands accurately captures phenomena related to the electromagnetic, weak and strong forces, a consistent quantum theory of gravity could not be incorporated so far. It is furthermore still unclear if and how dark matter and dark energy, which after all make up more than 95 % of the universe's energy density [6, 7], may be accounted for within the framework of particle physics. But also the origins of phenomena whose ties to elementary particles are more obvious remain unresolved. Thus, for instance, the actual mechanisms behind massive neutrinos or the baryon asymmetry of the universe are yet unknown. Driven by this large variety of open problems, the field of beyond-the-SM (BSM) model building has long pursued, and still pursues, a plethora of different and ever new directions with the aim of including one or several of the aforementioned phenomena in a consistent theory of particle physics. Interestingly, many of the existing approaches involve postulating further scalar bosons, or otherwise modifying the Higgs sector of the minimal SM

(see e.g. [8] for a recent comprehensive review).[a] The question of whether or not the particle found by the ATLAS and CMS experiments is indeed precisely that predicted by the Standard Model is therefore one of the most pressing questions of contemporary high-energy physics.

One additional reason to believe that the SM scalar sector is incomplete and requires modification stems from the very nature of said sector itself. Specifically, the SM Higgs being an elementary spinless boson implies the emergence of the infamous gauge hierarchy problem [9–14] as soon as the Standard Model is embedded in a more fundamental quantum field theory involving additional heavy particles. Although as a question about naturalness the hierarchy problem poses more of an aesthetic issue rather than a theoretical inconsistency, the quest for its solution has crucially shaped model building and the search for new physics over the last decades. Remarkably, conventional approaches to resolve or at least alleviate the hierarchy problem, like theories of low-scale supersymmetry [15–19] or composite Higgs models [20–23], typically suggest the existence of new particles at around the TeV scale, whose interactions with known matter are expected to be reasonably strong. Correspondingly, those particles were and still are anticipated to be in reach of appropriate experimental searches at the LHC.

However, as of now, neither the eagerly awaited superpartners predicted by supersymmetry were found at the LHC, nor is there any direct observational evidence pointing towards the realization of any other model solving the hierarchy problem in Nature. Also going beyond considerations based on naturalness as an incentive to search for BSM phenomena at the TeV scale does not change the situation. In fact, definitive signals of *any* kind of new physics are absent from the LHC to date. This, of course, includes the well-motivated models predicting a modified scalar sector, which were previously mentioned to play a crucial role in addressing most of today's BSM issues. In particular, several years of dedicated studies have shown no significant deviations of the found Higgs boson's properties from the corresponding predictions of the minimal SM [24].

Admittedly, the LHC is still far from the end of its lifespan and many interesting BSM phenomena may well emerge from its future runs, in particular from those during its high-luminosity phase, where substantially more data will be accumulated than there is at the moment [25, 26]. Also the proposed high-energy upgrade of the LHC to more than twice of the currently available center-of-mass energies certainly would have the potential to uncover new physics [27]. Nevertheless, it is worth to take one step back and think about possible causes for the lack of positive results so far. Except for the obvious one, namely that we simply have to wait for the LHC to de-

[a] When speaking of modified Higgs or scalar sectors in the following, we refer to models which involve additional elementary scalar particles beyond the already found Higgs boson, or predict altered properties of the latter with respect to the Standard Model expectations.

liver larger statistics and higher center-of-mass energies, there exist several further potential reasons for a *systematic* absence of any new physics signal from the current searches at the LHC, which can be broadly divided into three classes. At the risk of oversimplifying, we summarize the contents of said categories as:

1. We may be looking for the **wrong models**.
2. We may be looking in the **wrong search channels**.
3. We may be looking with the **wrong experiment**.

In the present work, we will discuss each of these three options in more detail in the context of concrete examples involving modified scalar sectors, which, as we have argued before, constitute an integral part of particularly well-motivated extensions of the minimal Standard Model. Before we do so, let us, however, first have a slightly closer look at the entries in the above list, thereby also introducing the main topics of this thesis.[b]

Item 1 indicates the possibility that the generally used theories which were devised to solve the aforementioned BSM issues are simply not the ones realized in Nature. The awareness of this problem naturally lead to an enhanced interest in alternative approaches during the last years. Thus, for instance, many new models and ideas addressing the hierarchy problem were developed [28–31], which conceptually go beyond supersymmetry or compositeness. One such relatively novel framework is based on classically conformal theories supplemented by radiative electroweak symmetry breaking [32–38]. Here, a large separation between the electroweak and the Planck scale is naturally explained by tying the former to an approximate global symmetry, namely scale invariance. Although many concrete realizations of classically conformal models were devised and thoroughly investigated during the last years, a systematic analysis to reveal the minimal consistency requirements of such a model remained absent. Nevertheless, the merits of such an analysis are obvious, since it would not only enable us to identify the minimal conformal model, but also allow us to learn how to systematically accommodate additional aspects of BSM physics in a classically scale-invariant framework. We will therefore provide a comprehensive study of a considerably broad class of conformal theories in Chapter 3. As is well known, a consistent implementation of radiative electroweak symmetry breaking generally requires the presence of extra massive scalar particles. Hence, our study will necessarily involve a discussion about extended scalar sectors. Notably, said discussion is complicated by the fact that successfully avoiding the reintroduction of fine-tuning in classically scale-invariant

[b] In this introduction, we will primarily restrict ourselves to establishing said main topics and to integrating them in the present line of reasoning. A more thorough motivation of the individual subjects is relegated to the respective chapters.

theories crucially relies on the absence of any physical threshold scale between the TeV regime and the Planck energy [34, 35]. In particular, this necessitates a stable renormalization group (RG) evolution of the candidate model's couplings, which is peculiarly difficult to realize in a theory with an enlarged scalar sector. Our analysis will therefore also help to understand how the required RG behavior can be achieved nonetheless.

The second entry from our above list signifies that some of the currently used strategies to search for new particles at the LHC are limited in the sense that they systematically miss certain regions of a given model's parameter space. In some cases those same regions may, however, become accessible in supplementary analyses based on different signatures which have not been thought of before. As an example for such a scenario we will study theories whose particle spectra contain additional light elementary scalar bosons with masses of order 10 GeV and below in Chapter 4. At the moment, direct searches for the aforementioned new light states at the LHC primarily rely on the existence of particular cascade processes, where a single SM-like Higgs boson first decays into *two* low-mass scalars, which then in turn decay into pairs of SM fermions or gauge bosons, see [39, 40]. In contrast, the related process where the initial Higgs decay is into *three* instead of two light scalars is presently neither considered by the experiments at the LHC nor by any phenomenological study in the literature. As a first step towards filling this gap, we thoroughly investigate basic aspects of said three-body Higgs decay mode both in a model-independent framework and in a specific extension of the minimal SM, namely that by one real gauge singlet scalar field. Apart from computing expected Higgs decay rates and raw event yields of interesting final states, one of our main results will be that direct collider searches for the three-body channel would indeed be able to probe portions of parameter space, which are otherwise inaccessible, thereby providing information complementary to that obtained in conventional approaches.

Finally, item 3 from our enumeration of possible reasons for the systematic absence of BSM signals at the LHC is based on the observation that new physics events may indeed be produced at the currently available energies, but only induce such signatures which are fundamentally out of reach for detection at a hadron collider. Scenarios affected are most notably those where rare BSM processes lead to purely hadronic final states, which are notoriously plagued by large amounts of QCD background at the LHC. In the context of modified scalar sectors, one interesting class of processes which falls into the aforementioned category is that of quark-flavor-violating Higgs decays, i.e. decays of the SM-like Higgs boson into a pair of quarks of *unequal* flavor. Notably, the associated branching fractions are generally anticipated to be small due to existing indirect constraints on the corresponding non-standard Higgs couplings coming from low-energy precision measurements [41]. Whereas the LHC's capabilities to probe quark-flavor-violating Higgs decays are thus clearly limited, potential future Higgs factories like

the proposed International Linear Collider (ILC) [42–47] would provide a complementary approach to high-energy particle physics, and could therefore help to overcome the LHC's inherent restrictions. Specifically, as an electron-positron collider, the ILC would offer a much cleaner experimental environment, which would allow to measure the properties of the found SM-like Higgs boson with high precision. Thus motivated, Chapter 5 presents the first thorough study of the prospects for discovering or constraining the quark-flavor-violating Higgs decay into a bottom and a strange quark at the ILC.

Outline

In line with the above motivation, the thesis is organized as follows. First, we will briefly review the basics of the Standard Model of particle physics in Chapter 2. In doing so we will predominantly concentrate on those aspects which will be needed for a proper understanding of the rest of the thesis. Particular focus will be placed on the scalar sector of the minimal SM and its role in the spontaneous breaking of electroweak symmetry (Sections 2.1 and 2.2), as well as on the already mentioned gauge hierarchy problem as it appears in generic SM embeddings (Section 2.3). Chapter 3 is then mainly devoted to an in-depth systematic study of a broad class of classically conformal extensions of the SM with the aim to identify the minimal model which is consistent with theory and experiment. Said study in Section 3.3 is preceded by a short review on how tree-level scale invariance is argued to remedy the hierarchy problem in Section 3.1. In Chapter 4, we then discuss decays of the SM-like Higgs boson into three light extra scalars both from a model-independent perspective (Section 4.1) and in the context of the real scalar singlet extension of the SM (Section 4.2). Prospects for new physics searches at current and near-future colliders based on the three-body channel are studied in Section 4.3. Following this, Chapter 5 is dedicated to the study of quark-flavor-violating Higgs decays, specifically to that into a bottom and a strange quark. To set the stage, we begin by briefly introducing the planned International Linear Collider (ILC) and its Higgs physics program in Section 5.1, followed by a short discussion on the basics of effective field theory in the context of flavor-violating Higgs couplings (Section 5.2). Afterwards, we present a detailed analysis of the ILC's expected performance in probing the aforementioned Higgs decay (Section 5.3). We finally conclude in Chapter 6. Note that each of the principal chapters of this thesis (3, 4 and 5) is preceded by an introduction where its respective subject is thoroughly motivated and put into context of contemporary particle physics. At the end of those chapters, we furthermore present summaries of the main results and their physical impact.

Disclaimer

Parts of the present thesis are based on results which arose from collaborative work with others and which were already published in peer-reviewed journals.

- The systematic study of conformal extensions of the Standard Model presented in Section 3.3, as well as the corresponding results summarized in Section 3.4 were first published in Reference [48] in collaboration with Pascal Humbert, Manfred Lindner and Juri Smirnov.
- The analysis of Higgs boson decays into three light scalars in Chapter 4 is based on work done in collaboration with Manfred Lindner which was published in Reference [49]. The model-independent discussion presented in Section 4.1 was, however, enlarged by new results as compared to the aforementioned reference and in its entirety represents the author's original work.
- The study of quark-flavor-violating Higgs decays in Chapter 5 elaborates on Reference [50] which originates from collaborative work with Daniele Barducci.

Chapter 2

The Standard Model and beyond

The Standard Model (SM) of particle physics is a theory describing the fundamental constituents of matter and the forces through which they mutually interact. It is extremely successful in doing so, accurately explaining a broad range of different phenomena spanning from atomic physics at energies of about 100 eV all the way up to LHC physics at the TeV scale and possibly even beyond.

One of the prime examples to be mentioned here is the free electron g-factor which was empirically determined with a relative uncertainty of $2.8 \cdot 10^{-13}$ [51]. Still, this truly remarkable level of precision is achievable by state-of-the-art SM calculations [52] with the absolute difference between experiment and theory being of order 10^{-12}. But also high-energy particle physics has long entered the era of precision measurements with experiments at LEP (Large Electron-Positron Collider) and SLC (SLAC Linear Collider) reaching the per-mill or even ppm-level. However, no significant deviations from SM predictions were found [53].

Importantly, the achievements of the SM are not limited to reproducing a vast amount of experimental results. Rather, many of the elementary particles known today were originally predicted on the basis of the SM years – or sometimes even decades – before they were first discovered. Of course, the Higgs boson immediately comes to mind, which was part of the SM right from its beginnings in the late 1960s [4, 5], before it was finally observed in 2012 [1, 2]. The list of successful SM predictions also includes the charm quark which was introduced to explain the empirically found absence of so-called flavor-changing neutral currents [54] only to be discovered four years later [55, 56]. Likewise, the observed violation of CP symmetry implied the existence of a third family of quarks [57] and eventually lead to their detection [58–60]. Lastly, we should mention the weak gauge bosons, W and Z, which are essential for formulating a consistent unified theory of

electromagnetism and weak interactions [3–5]. They were both discovered in 1983 [61–64], i.e. more than ten years after their introduction.

In the following chapter, we will revisit the foundations of the Standard Model starting with a brief summary of its formal basics (Section 2.1). Since the present thesis is mainly about Higgs physics, we will pay particular attention to the Higgs mechanism and its role in electroweak symmetry breaking (Section 2.2). The gauge hierarchy problem, which plagues generic extensions of the SM and which has therefore crucially shaped model building in the last decades, will then be the subject of Section 2.3.

Throughout this chapter, we will concentrate on aspects which are vital for the development and understanding of this work's principal results thus setting the stage for the rest of the thesis. Further details on the aspects covered here or on the Standard Model in general can be found in the numerous textbooks on quantum field theory and/or particle physics, like [65] and [66].

2.1 The Standard Model in a nutshell

The Standard Model in its textbook form is a combined description of the electroweak interactions [3–5] and the strong force as captured by quantum chromodynamics (QCD). As this work is mainly concerned with Higgs physics, we will almost exclusively review the electroweak sector of the SM here. Formally, the Standard Model is a local quantum field theory (QFT) based on the gauge group

$$G_{\mathrm{SM}} = \mathrm{SU}(3)_c \times \mathrm{SU}(2)_L \times \mathrm{U}(1)_Y \ , \tag{2.1}$$

where the first factor is the local symmetry group of QCD, while the other two factors constitute the electroweak gauge group. For reasons of theoretical consistency, each *local* symmetry group comes with its own set of *massless* spin-1 particles, the gauge bosons (see e.g. [65]). For the SM, those are the gluons of QCD, denoted as G^a_μ in the following, as well as the electroweak gauge fields W^a_μ and B_μ associated with $\mathrm{SU}(2)_L$ and $\mathrm{U}(1)_Y$, respectively. Here, μ is a spacetime index, while a is the index of the respective group's adjoint representation. In contrast to the above statement, we know empirically that the electroweak sector only contains one massless spin-1 particle, namely the photon, whereas the W and Z bosons are massive.

For the purpose of reconciling theory and experiment, the Higgs mechanism [67–71] is invoked in the SM to spontaneously break the electroweak symmetry group down to the one of electromagnetism, i.e.

$$\mathrm{SU}(2)_L \times \mathrm{U}(1)_Y \longrightarrow \mathrm{U}(1)_{\mathrm{em}} \ , \tag{2.2}$$

thereby giving mass to the weak gauge bosons W and Z, while the photon remains massless as required. More details on the Higgs mechanism and

	symbol	$\mathrm{SU}(3)_c$	$\mathrm{SU}(2)_L$	$\mathrm{U}(1)_Y$
Quarks	$Q_L^i = \begin{pmatrix} u_L^i \\ d_L^i \end{pmatrix}$	**3**	**2**	$1/6$
	u_R^i	**3**	**1**	$2/3$
	d_R^i	**3**	**1**	$-1/3$
Leptons	$L^i = \begin{pmatrix} \nu_L^i \\ e_L^i \end{pmatrix}$	**1**	**2**	$-1/2$
	e_R^i	**1**	**1**	-1
Higgs	$\Phi = \begin{pmatrix} \phi^+ \\ \phi^0 \end{pmatrix}$	**1**	**2**	$1/2$

Table 2.1: Standard Model particle content. All fermion fields exist in three generations, i.e. $i \in \{1, 2, 3\}$. Throughout this work, we use conventions for the hypercharge Y such that $Q = T^3 + Y$, where Q is a particle's electric charge after EWSB and T^3 is the third component of its weak isospin (Gell-Mann Nishijima formula [72, 73]).

electroweak symmetry breaking (EWSB) will be discussed in the next section. For now, it suffices to say that the aforementioned procedure is realized within the SM by introducing one complex scalar field $\Phi = (\phi^+, \phi^0)^\intercal$, the Higgs field, which transforms under G_{SM} as

$$\Phi \sim \left(\mathbf{1}, \mathbf{2}, \tfrac{1}{2}\right) \ . \tag{2.3}$$

Upon EWSB the Higgs field acquires a non-zero vacuum expectation value v and can be re-written in unitary gauge as

$$\Phi = \frac{1}{\sqrt{2}} \begin{pmatrix} 0 \\ v + H \end{pmatrix} \ , \tag{2.4}$$

where H is an electrically neutral scalar which is present in the theory's particle spectrum after symmetry breaking and is referred to as the Higgs boson.

Let us continue with reviewing the Standard Model's fermion content. First, all matter fields are divided into two classes of particles, namely quarks, which interact via QCD, and leptons, which do not feel the strong force. Second, since the SM is a *chiral* gauge theory, it is to be formulated using Weyl spinors. From a physics point of view, this implies that the left-handed and right-handed components of a given particle species couple to the gauge forces in different ways. Notably, explicit fermion (Dirac) mass terms are thus forbidden by gauge symmetry. In Table 2.1, we list all SM fermion fields as well as the complex Higgs doublet from equation (2.3) supplemented by their respective quantum numbers.

We are now in the position to formulate the Standard Model's Lagrangian. The latter consists of precisely those renormalizable and Lorentz-invariant terms that respect the local symmetry group of equation (2.1) and that can be written down using only the fields from Table 2.1. It reads

$$\mathcal{L}_{\text{SM}} = \mathcal{L}_{\text{gauge}} + \mathcal{L}_{\text{fermion}} + \mathcal{L}_{\text{scalar}} + \mathcal{L}_{\text{Yukawa}} \,, \tag{2.5}$$

where the individual parts are given by

$$\mathcal{L}_{\text{gauge}} = -\tfrac{1}{4} G^a_{\mu\nu} G^{a\mu\nu} - \tfrac{1}{4} W^a_{\mu\nu} W^{a\mu\nu} - \tfrac{1}{4} B_{\mu\nu} B^{\mu\nu} + \frac{\theta g_3^2}{32\pi^2} G^a_{\mu\nu} \widetilde{G}^{a\mu\nu} \,, \tag{2.6a}$$

$$\mathcal{L}_{\text{fermion}} = \mathrm{i} \bar{L}^i \not{D} L^i + \mathrm{i} \bar{e}^i_R \not{D} e^i_R + \mathrm{i} \overline{Q}^i_L \not{D} Q^i_L + \mathrm{i} \bar{u}^i_R \not{D} u^i_R + \mathrm{i} \bar{d}^i_R \not{D} d^i_R \,, \tag{2.6b}$$

$$\mathcal{L}_{\text{scalar}} = (D_\mu \Phi)^\dagger (D^\mu \Phi) - V(\Phi) \,, \tag{2.6c}$$

$$\mathcal{L}_{\text{Yukawa}} = -y_e^{ij} \bar{L}^i \Phi e^j_R - y_d^{ij} \overline{Q}^i_L \Phi d^j_R - y_u^{ij} \overline{Q}^i_L \tilde{\Phi} u^j_R - \text{h.c.} \,. \tag{2.6d}$$

A few comments on the notation and on the physics captured by the different contributions in equations (2.6) are in order.

The gauge part $\mathcal{L}_{\text{gauge}}$ contains, first and foremost, the kinetic terms of the SM gauge bosons as well as their self-interactions provided the underlying gauge symmetry is non-Abelian. The corresponding operators are all of the same structure, namely $F^a_{\mu\nu} F^{a\mu\nu}$. The field strength tensor $F^a_{\mu\nu}$ associated with gauge fields A^a_μ can be conveniently defined via an appropriate gauge-covariant derivative D_μ

$$F_{\mu\nu} \equiv F^a_{\mu\nu} T^a := -\frac{\mathrm{i}}{g} [D_\mu, D_\nu] \quad \text{with} \quad D_\mu = \partial_\mu + \mathrm{i} g A^a_\mu T^a \,.$$

Here, the coupling g quantifies the gauge interaction's strength, while T^a are the corresponding gauge group's generators. Unlike the other operators in equation (2.6a), the last term, containing the dual gluon field strength tensor $\widetilde{G}^{a\mu\nu} = \frac{1}{2} \epsilon^{\mu\nu\rho\sigma} G^a_{\rho\sigma}$, violates CP invariance. The smallness of its coefficient θ lies at the heart of the so-called strong CP problem (see [74] for a review).

The fermion gauge-kinetic part $\mathcal{L}_{\text{fermion}}$ describes the dynamics of massless fermion fields as well as their interaction with the gauge bosons according to their quantum numbers (see Table 2.1). In writing down equation (2.6b), we employed the Feynman slash notation, specifically $\not{D} := \gamma^\mu D_\mu$, where γ^μ is the four-tuple of Dirac matrices, while D_μ again represents a gauge-covariant derivative. Of course, the exact form of the latter depends on the fermion it acts on. For instance, in case of the left-handed quark doublet Q_L, which is charged under all three factors of G_{SM}, it reads

$$D_\mu = \partial_\mu \mathbb{1} + \mathrm{i} g_3 G^a_\mu T^a + \mathrm{i} g_2 W^a_\mu \tau^a + \mathrm{i} g_1 Y B_\mu \mathbb{1} \,, \tag{2.7}$$

where T^a and τ^a are the generators in the fundamental representations of SU(3) and SU(2), respectively, while $Y = \frac{1}{6}$ for Q_L. For a color (weak

isospin) singlet the second (third) term is not present. The hypercharge has to be adjusted as well.

The scalar sector Lagrangian from equation (2.6c) itself consists of two parts. On the one hand, the scalar potential $V(\Phi)$ captures the Higgs field's self-interactions. Importantly, its particular structure triggers the spontaneous breakdown of electroweak symmetry within the minimal SM. In this context, the potential will be discussed in more detail in Section 2.2. On the other hand, the Lagrangian $\mathcal{L}_{\text{scalar}}$ contains the gauge-kinetic term for the Higgs boson, in which the covariant derivative D_μ is an appropriately modified version of that given in equation (2.7). Analogous to the fermionic case, the scalar gauge-kinetic term describes the coupling of Φ to the SM gauge bosons. As we will explicitly see in the next section, it is precisely these interactions that render the weak vector bosons massive during EWSB.

Lastly, let us discuss the Yukawa sector $\mathcal{L}_{\text{Yukawa}}$, in which the Higgs boson couples left- to right-handed fermion fields. To appreciate the physical significance of the Yukawa-type operators, recall from before that in a chiral gauge theory as the SM, *explicit* fermion mass terms are forbidden.[a] They may, however, be *spontaneously* generated, which is exactly what happens in equation (2.6d) once the Higgs acquires a finite vev during EWSB. For instance, the down-type quark Yukawa operator gives

$$-\mathcal{L}_{\text{Yukawa}} \supseteq y_d^{ij}\overline{Q}_L^i \Phi d_R^j + \text{h.c.} = M_d^{ij}\bar{d}_L^i d_R^j \left(1 + \frac{H}{v}\right) + \text{h.c.}\,, \tag{2.8}$$

where we have employed equation (2.4) and defined the down-type quark mass matrix as $M_d = y_d v/\sqrt{2}$, which is a complex 3×3 matrix in flavor space.

Since the Yukawa interaction in equation (2.8) does not derive from any gauge principle (as do, for instance, the gauge-kinetic terms in $\mathcal{L}_{\text{fermion}}$), there is no reason why the matrices y_d and M_d should be diagonal (see e.g. [65]). Consequently, the electroweak interaction eigenstates d in equation (2.8) will in general not coincide with the mass eigenstates d'. In order to find the latter, we need to diagonalize the matrix M_d. This can be achieved by means of a bi-unitary transformation,[b] specifically $V_d^\dagger M_d U_d = \text{diag}(m_d, m_s, m_b)$ with $U_d, V_d \in \text{U}(3)$ and non-negative current quark masses m_q. Defining the mass eigenstates d' accordingly,

$$d_L'^i = (V_d^\dagger)^{ij} d_L^j \quad \text{and} \quad d_R'^i = (U_d^\dagger)^{ij} d_R^j\,, \tag{2.9}$$

[a] This statement only holds for Dirac mass terms. In contrast, Majorana masses are allowed, but require fermions that are not charged under any gauge symmetry. Such fermion representations are absent in the minimal SM, though.

[b] Mathematically speaking, we perform a singular value decomposition of M_d.

one can finally re-write equation (2.8) as

$$-\mathcal{L}_{\text{Yukawa}} \supseteq \sum_{i=d,s,b} m_i \bar{d}'^i_L d'^i_R \left(1 + \frac{H}{v}\right) + \text{h.c.} \,. \tag{2.10}$$

The Yukawa Lagrangian in the aforementioned form does not only describe a Dirac-type mass for the down-type quarks, but also their interaction with the physical Higgs boson H after EWSB. Clearly, the exact same logic as applied to the down-type quark Yukawa operator in the discussion above, holds for the other terms in $\mathcal{L}_{\text{Yukawa}}$ as well. Importantly, equation (2.10) therefore demonstrates that there are no tree-level flavor-changing neutral currents (FCNC) in the Higgs sector of the minimal SM. In other words, barring quantum effects, the physical Higgs H exclusively couples to pairs of *same*-flavor fermions. In Chapter 5, we will use this result to argue that detecting quark flavor violating Higgs decays, like $H \to \bar{b}s$, at near-future collider experiments would be an unambiguous sign of beyond-the-SM physics.

The basis change in equation (2.9) also impacts other parts of the SM, specifically $\mathcal{L}_{\text{fermion}}$. After EWSB, the weak interactions involving W bosons can be brought into the form $\mathcal{L}_{\text{fermion}} \supseteq -g_2 J^\mu_+ W^+_\mu + \text{h.c.}$ The quark part of the so-called weak charged current J^μ_+ is then

$$J^\mu_+ = \frac{1}{\sqrt{2}} \bar{u}^i_L \gamma^\mu d^i_L = \frac{1}{\sqrt{2}} \bar{u}'^j_L \gamma^\mu \left(V_u^\dagger V_d\right)^{jk} d'^k_L \,. \tag{2.11}$$

By convention, one now defines the Cabibbo-Kobayashi-Maskawa (CKM) matrix as $V_{\text{CKM}} := V_u^\dagger V_d$ [57, 75]. As V_u and V_d, it is a complex 3×3 unitary matrix, which can be shown to be parameterized by three Euler angles and one CP-violating phase δ_{CP} [57]. In general, V_{CKM} will be non-diagonal, such that equation (2.11) implies the mixing of distinct quark generations in charged-current processes. Note that the absence of a right-handed neutrino field implies the neutrinos' exact masslessness in the SM. The latter, in turn, prevents the above argument from being applicable to the lepton sector. Charged currents are therefore lepton-flavor conserving in the minimal SM.

Let us finally have a look at the situation in the neutral gauge sector. Here, fermion couplings to the Z and the photon are diagonal in weak isospin space. For instance, the part of the weak neutral current J^μ_Z involving left-handed quarks reads

$$\begin{aligned} J^\mu_Z &\supseteq c^{(u)}_L \bar{u}^i_L \gamma^\mu u^i_L + c^{(d)}_L \bar{d}^i_L \gamma^\mu d^i_L \\ &= c^{(u)}_L \bar{u}'^j_L \gamma^\mu \left(V_u^\dagger V_u\right)^{jk} u'^k_L + c^{(d)}_L \bar{d}'^j_L \gamma^\mu \left(V_d^\dagger V_d\right)^{jk} d'^k_L \,, \end{aligned}$$

where $c^{(i)}_L$ are suitable weak charges and the current enters the Lagrangian as $\mathcal{L}_{\text{fermion}} \supseteq -\sqrt{g_1^2 + g_2^2} J^\mu_Z Z_\mu$. The other terms in J^μ_Z and in the electromagnetic current are of a similar form. From the unitarity of the transformation

SM sector	Parameter	Symbol
Electroweak	$\mathrm{SU}(2)_L$ gauge coupling	g_2
	$\mathrm{U}(1)_Y$ gauge coupling	g_1
	Electroweak scale	v
	Higgs self-coupling	λ
QCD	$\mathrm{SU}(3)_c$ gauge coupling	g_3
	QCD vacuum angle	θ
Fermion	fermion masses ($\times 9$)	m_f
	CKM parameters	α, β, γ, δ_{CP}

Table 2.2: Free parameters of the Standard Model and the corresponding notation used in the present thesis. In case of quarks, m_f refers to current quark masses.

matrices V_i and U_i, we can thus infer that there are no tree-level FCNCs in the gauge sector, either.

This concludes our brief discussion of the Standard Model Lagrangian from equation (2.5). Considering the complex physics and the plethora of different experimental observations that are captured by $\mathcal{L}_{\mathrm{SM}}$, it is remarkable that the theory needs only 19 input parameters to be fully specified. Those are summarized in Table 2.2.

2.2 Electroweak symmetry breaking

As has been alluded to in the last section, the Higgs mechanism is crucial for the success of the Standard Model in describing Nature. To appreciate its relevance, let us start with the following fact: For basic reasons of consistency, fundamental spin-1 fields in a Lorentz-invariant theory must necessarily be associated to a local gauge symmetry.[c] The empirically validated existence of particles with spin 1 thus directly implies the need for gauge theories to describe them. Accordingly, the SM is a theory based on the local symmetry group G_{SM} given in equation (2.1). To be slightly more precise, the non-Abelian nature of G_{SM} makes the SM an example of a so-called Yang-Mills (YM) theory [77].

A further important concept in quantum field theories is that of renormalizability, which is inherently linked to the feature of a theory being predictive and consistent at all energy scales. These are, of course, desirable properties for a fundamental theory of Nature. For a long time, it was far from obvious that Yang-Mills theories as the SM exhibit the feature of renormalizability. It was eventually proven for YM theories with *massless* gauge bosons by 't Hooft [78]. Unfortunately, renormalizability is lost as soon as

[c] A very nice pedagogical review on the necessity of gauge theories is given e.g. in [76].

we extend massless YM theory by introducing an explicit mass term for the vector bosons (thereby explicitly breaking gauge invariance). Naively, this seems to imply that in a renormalizable QFT all degrees of freedom with spin 1 must be massless, in stark contrast to what we observe in Nature. The way out of this apparent contradiction lies in the realization that YM theories are, in fact, renormalizable provided the masses of the vector bosons are generated spontaneously by the Higgs mechanism [79].

The Higgs mechanism itself was originally introduced in the context of Abelian gauge theories [67–70]. To the non-Abelian case, it was first applied in [71]. In the following, we will discuss the mechanism's realization within the SM and its relation to electroweak symmetry breaking (EWSB) [4, 5]. In the course of the previous section, we have already introduced the SM Higgs field Φ and its potential $V(\Phi)$ in equations (2.3) and (2.6c), respectively. The latter is the key to understanding how EWSB occurs. Its form in the SM is

$$V(\Phi) = \mu^2 \Phi^\dagger \Phi + \lambda (\Phi^\dagger \Phi)^2 \,, \tag{2.12}$$

where the first term renders the Higgs field massive, while the second one describes its quartic self-interactions. In order for the theory to possess a ground state (also referred to as vacuum in the following), its total energy content must be positive definite. In particular, this requires the potential to be bounded from below, which, in turn, implies $\lambda > 0$. The aforementioned (classical) ground state value of the Higgs field $\Phi_0 \equiv \langle \Phi \rangle$ can then be found by minimizing the potential, yielding

$$|\Phi_0| \equiv \frac{v}{\sqrt{2}} = \sqrt{\frac{-\mu^2}{2\lambda}} \quad \text{for} \quad \mu^2 < 0 \tag{2.13}$$

or $|\Phi_0| = 0$ in the case of $\mu^2 \geqslant 0$. In the following, we will exclusively be interested in the tachyonic case of negative μ^2. Importantly, equation (2.13) only fixes the magnitude of the vacuum expectation value (vev), while its direction is not determined. The freedom of global SU(2) rotations, however, allows us to conveniently write the Higgs vev as

$$\Phi_0 \equiv \langle \Phi \rangle = \frac{1}{\sqrt{2}} \begin{pmatrix} 0 \\ v \end{pmatrix} \,. \tag{2.14}$$

Furthermore and without loss of generality, we have chosen the vev to be real in accordance with the fact that spontaneous CP violation is not possible in the minimal SM: A non-zero phase α, as in $v\mathrm{e}^{\mathrm{i}\alpha}$, can always be absorbed in an irrelevant global phase and thus will not have any physical impact (see e.g. [80]).

Since the Higgs field Φ transforms non-trivially under $\mathrm{SU}(2)_L \times \mathrm{U}(1)_Y$, a non-zero ground state configuration $\langle \Phi \rangle \neq 0$ as in equation (2.14) indicates

that the theory's vacuum is no longer invariant under the electroweak symmetry, which is therefore said to have been spontaneously broken (EWSB). From a physical point of view, this implies that the $\mathrm{SU}(2)_L \times \mathrm{U}(1)_Y$ symmetry will no longer be manifest in the theory's particle spectrum. Crucially, our choice of the Higgs field's hypercharge, $Y = \frac{1}{2}$, still renders the vacuum $\langle\Phi\rangle$ invariant under a U(1) subgroup with associated charge $Q := T^3 + Y$, where T^3 is the third component of weak isospin. In line with experimental observations, this unbroken subgroup of the full electroweak group is to be identified with the gauge group of electromagnetism. In summary, we thus obtain the symmetry breaking pattern, already quoted in equation (2.2) and repeated here

$$\mathrm{SU}(2)_L \times \mathrm{U}(1)_Y \longrightarrow \mathrm{U}(1)_{\mathrm{em}} \ .$$

From a more technical point of view, performing perturbative calculations in QFT requires an expansion around the theory's true vacuum, which is now given by equation (2.14). Correspondingly, we have to re-write the SM Lagrangian using an appropriately shifted Higgs field, namely

$$\Phi = \langle\Phi\rangle + \begin{pmatrix} \mathrm{i}G^+ \\ \frac{1}{\sqrt{2}}(H - \mathrm{i}G^0) \end{pmatrix} \ , \tag{2.15}$$

where the complex field G^+ and the real scalars H and G^0 have zero vacuum expectation value in accordance with equation (2.14). Plugging equation (2.15) into the scalar potential $V(\Phi)$ and using the tree-level vacuum condition (2.13), reveals that the fields G^i are massless, while the physical Higgs boson H acquires a finite mass

$$m_H = \sqrt{2\lambda}\, v = 125.09\,\mathrm{GeV} \ . \tag{2.16}$$

Here, we quoted the measured value from the combined ATLAS and CMS analysis of the LHC run-1 data [81].

As we have already mentioned several times, the Higgs mechanism generates finite masses for formerly massless gauge bosons, specifically for those associated with broken symmetry generators. To see how this works, let us insert the shifted field from equation (2.15) into the scalar gauge-kinetic term of equation (2.6c). In a first step, we concentrate on terms bilinear in the gauge fields and not containing a scalar. We obtain

$$(D_\mu\Phi)^\dagger(D^\mu\Phi) \supseteq \frac{g_2^2 v^2}{4} W_\mu^+ W^{\mu-} + \frac{1}{2}\frac{(g_1^2 + g_2^2)v^2}{4} Z_\mu Z^\mu \ , \tag{2.17}$$

where we defined $W_\mu^\pm = (W_\mu^1 \mp \mathrm{i}W_\mu^2)/\sqrt{2}$ and $Z_\mu = \cos\theta_{\mathrm{W}} W_\mu^3 - \sin\theta_{\mathrm{W}} B_\mu$. The neutral gauge fields W_μ^3 and B_μ have mixed to give two mass eigenstates, one of which is the massive Z boson. The other eigenstate, $A_\mu = \sin\theta_{\mathrm{W}} W_\mu^3 + \cos\theta_{\mathrm{W}} B_\mu$, remains massless and is identified with the photon of

quantum electrodynamics (QED). The mixing in the neutral gauge sector can conveniently be described by one real mixing angle, the Weinberg angle θ_{W}, which satisfies $\sin\theta_{\mathrm{W}} = g_1/\sqrt{g_1^2+g_2^2}$. Equation (2.17) explicitly demonstrates that the non-zero Higgs vev induces a finite mass for the W and Z bosons as required by experiment. Specifically, one finds the tree-level relations

$$m_W = \tfrac{1}{2} g_2 v \;, \quad m_Z = \tfrac{1}{2}\sqrt{g_1^2+g_2^2}\, v \;. \tag{2.18}$$

As a brief digression, we remark that these identities are interesting for two reasons. On the one hand, they allow to express the vacuum expectation value v via the particularly well measured Fermi coupling constant G_{F} [82]. The latter can be related to SM quantities in an effective field theory approach yielding (see e.g. [65])

$$\frac{G_{\mathrm{F}}}{\sqrt{2}} = \frac{g_2^2}{8 m_W^2} \quad \overset{(2.18)}{\Longrightarrow} \quad v = \left(\sqrt{2} G_{\mathrm{F}}\right)^{-1/2} = 246.22\,\mathrm{GeV} \;, \tag{2.19}$$

where we used the current PDG value for the Fermi constant in the second step [83]. On the other hand, equation (2.18) illustrates a special feature of EWSB in the SM, namely

$$\rho := \frac{m_W^2}{m_Z^2 \cos^2\theta_{\mathrm{W}}} = 1 \;, \tag{2.20}$$

which was experimentally established at a 5 ‰ level of accuracy [53].[d] All alternative theories of EWSB should therefore somehow implement the above property. Accordingly, we will use the constraint $\rho = 1$ as one of the major guidelines to identify potentially viable models with enlarged scalar sectors in Chapter 3.

To gain slightly more insight into how the Higgs mechanism works, let us consider another class of operators emerging from the scalar gauge-kinetic term upon insertion of equation (2.15), specifically

$$(D_\mu \Phi)^\dagger (D^\mu \Phi) \supseteq m_W \left(W_\mu^+ \partial^\mu G^- + W_\mu^- \partial^\mu G^+\right) + m_Z Z_\mu \partial^\mu G^0$$

Based on these couplings, it can be shown that the *massless* scalar fields G^i behave exactly as would the longitudinal modes of *massive* vector bosons. To be more specific, one finds that e.g. the field G^0 has the correct properties to be re-interpreted as the third degree of freedom of the now massive Z boson. An analogous association between the charged scalars $G^\pm$ and the W bosons exists. As a consequence, the massless scalar modes G^0 and $G^\pm$ do no longer appear in the physical particle spectrum of the SM, which,

[d] The observed deviation from the classical relation $\rho = 1$ is fully consistent with expected effects due to quantum corrections.

however, now contains massive vector bosons with three degrees of freedom each. The Higgs boson is thus the only fundamental scalar mode remaining in the physical spectrum after EWSB. Accordingly, finding an additional fundamental spin-0 particle would be a direct proof of BSM physics, which – among other things – motivates our study in Chapter 4.

We finish our analysis of the scalar gauge-kinetic term after EWSB by considering the trilinear interaction of the massive weak gauge bosons with the Higgs particle H

$$(D_\mu \Phi)^\dagger (D^\mu \Phi) \supseteq \frac{m_W^2}{v} H W_\mu^+ W^{\mu -} + \frac{1}{2} \frac{m_Z^2}{v} H Z_\mu Z^\mu \,. \tag{2.21}$$

These couplings are necessary for mediating the dominant production processes of a single Higgs boson at lepton colliders and are therefore crucial for the understanding of Chapter 5.

This concludes our discussion of electroweak symmetry breaking as it is implemented in the minimal Standard Model.

2.3 The gauge hierarchy problem in generic extensions of the minimal Standard Model

As we have argued in Chapter 1, the minimal SM as previously introduced does not account for all observed physical phenomena and thus cannot be valid at all energy scales. Even if new physics aspects such as particle dark matter, small neutrino masses or baryogenesis could all be accommodated without introducing a new large mass scale, one would still generally expect the SM to be replaced by a theory of quantum gravity at energies of order of the Planck scale $M_{\text{Pl}} \simeq 1.22 \cdot 10^{19}\,\text{GeV}$. Interestingly, even if gravity turned out to be an emergent phenomenon without the need for an embedding at around M_{Pl}, the SM would nevertheless break down eventually due to the Landau pole in the hypercharge gauge coupling, which can be calculated to develop at roughly $10^{41}\,\text{GeV}$. All this suggests the existence of a finite energy scale Λ at which the minimal SM is embedded into a more complete theory of high-energy physics, and which may well be much larger than the electroweak scale, $\Lambda \gg v$. Crucially, the embedding scale Λ will be associated with a *physical* mass or threshold scale M as soon as the UV completion is specified and is therefore not to be confused with, for instance, a technical cutoff introduced to regulate spurious divergences in quantum field theory. In particular, terms containing Λ (or equivalently M) will still be present in expressions for physical observables after the theory has been fully renormalized.

With that said, the gauge or electroweak hierarchy problem [9–14] refers to the two-fold shortcoming of generic embeddings of the SM at a high scale Λ, which can typically neither *explain* the large difference $v \ll \Lambda$, nor

stabilize it under quantum corrections. To see why, let us first introduce the notion of Dirac naturalness [84, 85]. Employing the standard language of QFT as well as natural units [65], the latter states that the natural size of the coefficient g_O of a local operator O with scaling dimension Δ_O in a four-dimensional theory with fundamental mass scale Λ is

$$g_O = c_O \cdot \Lambda^{4-\Delta_O} \ , \tag{2.22}$$

where c_O is a dimensionless numerical constant of order unity. In Chapter 2, we have learned that the scale of electroweak symmetry breaking in the minimal SM is set by the Higgs mass parameter μ^2, which, in turn, is the coefficient of the dimension-two operator $\Phi^\dagger\Phi$, cf. equations (2.12) and (2.13). According to equation (2.22) the natural size of the electroweak scale – or equivalently that of the Higgs mass m_H – is therefore of order Λ in stark contrast to the assumed $v \ll \Lambda$, thus illustrating the first part of the gauge hierarchy problem.

To also understand the second and more severe part of the hierarchy problem, recall that in perturbative QFT a renormalized physical observable can be written as a sum of a bare quantity and appropriate quantum corrections. Accordingly, the renormalized Higgs mass m_H is

$$m_H^2 = m_{H,0}^2 + \delta m_H^2 \tag{2.23}$$

where $m_{H,0}^2$ denotes the bare mass parameter while δm_H^2 arises from loop effects. Importantly, even if we accept that the bare coupling $m_{H,0}^2$ attains a value much smaller than its natural size in the Dirac sense of equation (2.22), $m_{H,0} \ll \Lambda$, this assumption is not meaningful since it is usually not stable under radiative corrections. To be more precise, it is straightforward to show that δm_H^2 and therefore also the renormalized Higgs mass is quadratically sensitive to any large physical mass scale with which the Higgs field interacts, even if said coupling is only indirect, e.g. via gravity. Specifically, if the SM is embedded into a more complete theory at a finite scale Λ, which is also employed to regulate loop momenta, δm_H^2 is given by (see e.g. [65])

$$\delta m_H^2 = f(g_i) \cdot \Lambda^2 \ , \tag{2.24}$$

with f being some suitable function of the theory's couplings g_i, which is generally not too small. Hence, equations (2.23) and (2.24) imply that the observed Higgs mass should be of order of the high-energy embedding scale Λ, even in cases where the bare mass is much smaller. Explaining the difference $m_H \ll \Lambda$ then requires to assume that the bare mass is set in a way as to precisely cancel the radiative contribution of equation (2.24). The corresponding delicate fine-tuning constitutes the gauge hierarchy problem's second part.

A few comments on the above discussion are in order. First, we stress again that (the second part of) the hierarchy problem is a statement about

the Higgs mass parameter's strong sensitivity to UV physics, rather than about the used regularization scheme. To illustrate, let us assume for now that the UV completion of the minimal SM involves a heavy particle of mass $M \gg m_H$, which somehow couples to the Higgs field. Instead of cutoff regularization as before, we now want to employ dimensional regularization together with modified minimal subtraction ($\overline{\text{MS}}$). Since this is a mass-independent scheme, we have to explicitly match the full high-energy theory onto the low-energy effective one in which the heavy particle has already been integrated out. Said matching is performed at the physical threshold scale $\bar{\mu} = M$, where $\bar{\mu}$ is the arbitrary mass scale introduced in the $\overline{\text{MS}}$ scheme, and can easily be shown to produce the following correction to the Higgs mass in the low-energy effective theory

$$\delta m_H^2 = \tilde{f}(g_i) \cdot M^2 \ . \tag{2.25}$$

Analogous to equation (2.24), the radiative contribution to the Higgs mass is again found to be quadratically sensitive to the high-energy physics scale.

As a second remark, let us mention that fermion and gauge bosons masses do not suffer from a similar problem. If, for instance, we had an extra light fermion f of mass $m_f \ll M$ in the above situation, the corresponding threshold correction δm_f^2 would be proportional to m_f^2 rather than to M^2. This property can be shown to originate from the fact that the f-sector becomes chirally invariant in the limit $m_f \to 0$. Couplings like m_f, whose vanishing enhances a theory's symmetry, are referred to as technically natural [14]. Although they may still be unnaturally small in the Dirac sense of equation (2.22), that smallness is now radiatively stable and thus does not imply any fine-tuning of bare parameters. Similarly, gauge boson masses are protected by gauge symmetry. The problematic strong sensitivity on UV physics found in the case of the Higgs in equations (2.24) and (2.25) can consequently be traced back to the fact that the Higgs boson is a (fundamental) scalar field and the absence of an appropriate protective symmetry.

Finally, it is worth noting that the electroweak hierarchy problem does not afflict the minimal SM, because the latter is a renormalizable QFT with only one explicit physical scale, namely the electroweak vev (cf. Table 2.2). Any cutoff scale which may be introduced for regularization in expressions such as equation (2.24) must therefore be unphysical and can hence be renormalized away [32].

Chapter 3

Minimal conformal extensions of the Higgs sector

The gauge hierarchy problem [9–14] as discussed in Chapter 2 is arguably one of the most pressing issues of beyond-the-Standard Model (BSM) physics. Although as a naturalness problem it is more of an aesthetic issue rather than a theoretical inconsistency, the quest for its solution has crucially shaped model building and the search for new physics over the last decades. Correspondingly, there exists a large variety of proposed theoretical frameworks which offer remedies to overcome or at least alleviate the hierarchy problem. The most prominent one of these is certainly provided by low-scale supersymmetry (SUSY) [15–19]. However, even though the relevant SUSY scenarios typically suggest the existence of BSM phenomena in the TeV range, no appropriate new particles were found at the LHC to date, see e.g. [86]. As a consequence, the simplest and most appealing SUSY models are severely constrained by now and thereby become increasingly unnatural themselves [87–89].

Obviously, the aforementioned absence of experimental evidence for supersymmetry lead to an enhanced interest in alternative approaches towards solving the hierarchy problem. Well-established frameworks include extra-dimensional theories [90–92] as well as technicolor [11–13, 93–95], composite Higgs [20–23] and little Higgs models [96–99]. Importantly, and analogous to the case of SUSY, all of the above examples introduce extra symmetries in order to prevent the electroweak scale from becoming unstable against radiative corrections. More recently, many new ideas such as cosmological relaxation [28], twin Higgs models [29], Nnaturalness [30] and clockwork theories [31] were developed and are being thoroughly investigated at the moment.

Finally, also theories based on classically scale-invariant[a] Lagrangians attracted some attention in the last years and will be the main subject of the present chapter. Similar to some of the above examples, the electroweak scale is again tied to an approximate global symmetry – namely scale invariance – and is thereby protected against quadratic divergences [32]. More details on how this works exactly are provided in Section 3.1. Crucially, a common feature of conformal extensions of the Standard Model (SM) is that spontaneous electroweak symmetry breaking necessarily has to be a consequence of the model's *quantum dynamics*, since by definition there exists no explicit mass scale in the classical theory. Early works which advocated the aforementioned protection mechanism based on scale invariance include [33–38]. These basic studies have subsequently inspired the exploration of numerous further conformal models, which then additionally addressed various other open questions of BSM physics, like the particle nature of dark matter, the smallness of neutrino masses or baryogenesis [103–118].

Nevertheless, there does not exist any systematic study of the minimal requirements to be fulfilled by a scale-invariant model of particle physics in order to allow for consistent dynamical electroweak symmetry breaking, while also satisfying basic experimental constraints. With the following study we try to fill this gap at least for a reasonably broad class of classically scale-invariant models defined by the following set of working assumptions:

1. Spontaneous breakdown of scale invariance is supposed to be triggered by *perturbative* effects in a Coleman-Weinberg-like scenario [119].
2. Spontaneous breakdown of scale invariance is furthermore assumed to occur at energies around the electroweak scale.
3. All models are to be built around the gauge symmetry group of the minimal Standard Model (SM) given in equation (2.1).

A few remarks on the above items are in order. First, it is well known that the scale-invariant version of the minimal SM does not facilitate radiative symmetry breaking à la Coleman-Weinberg, since large top quark fluctuations destabilize the effective potential so that the resulting theory is rendered inconsistent. Therefore, assumption 1 implies that a viable conformal model in our sense has to extend the minimal SM's field content by extra bosonic degrees of freedom, which must be sufficiently heavy so as to stabilize the effective potential. Since we restrict ourselves to the SM gauge group according to assumption 3, successful radiative symmetry breaking requires the existence of additional massive *scalar* particles. In

[a] Since scale and conformal invariance were proven to be equivalent at the classical level in any four-dimensional unitary and renormalizable field theory [100–102], we will use the terms "scale-invariant" and "conformal" interchangeably in the following, always referring to the classical symmetry. An exception to this is Section 3.1 where carefully distinguishing tree- and quantum-level symmetries is more important.

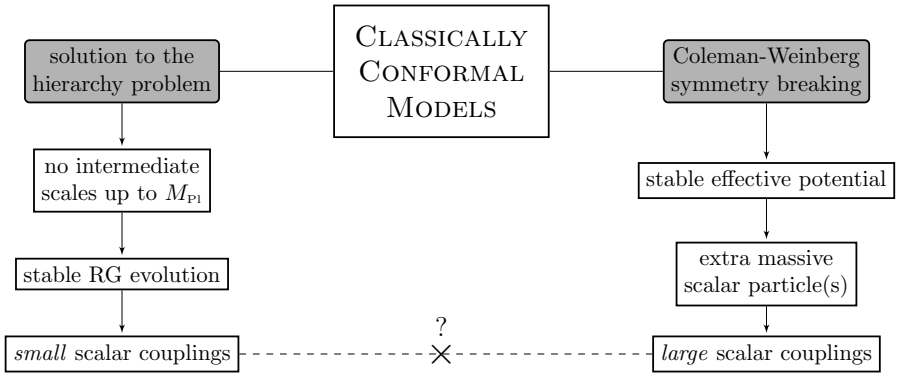

Figure 3.1: Schematic illustration of the opposing tendencies being at work in the class of classically conformal models under consideration in the present chapter.

other words, viable candidate models inevitably possess an enlarged scalar sector. The exact minimization of the associated effective potential and thus the determination of the theory's ground state is therefore typically a computationally expensive task. However, Gildener and S. Weinberg developed a simple approximate approach for solving that problem [120], which we will use throughout the present chapter, and which will be discussed in more detail in Section 3.2.

Next, assumption 2 is introduced for the purpose of avoiding unnecessarily tiny scalar portal couplings, which would be needed if the scales of spontaneous conformal and electroweak symmetry breaking were to be widely separated. Although fully consistent and technically natural [14] scale-invariant models with a substantial hierarchy between the aforementioned scales can be written down (cf. e.g. [121]), this is not the approach we want to pursue here, partly because said models still fail to explain the origin of the portal couplings' smallness. An important consequence of assumption 2 now is the need for at least one sizable scalar coupling in order to guarantee the presence of a sufficiently heavy scalar particle to *stabilize* the theory's effective potential. Such large couplings will, on the other hand, typically *destabilize* the model's renormalization group (RG) running and thus eventually lead to the appearance of Landau poles. As we will argue in the next section, the absence of such infinities signaling the breakdown of perturbation theory below the Planck scale is a necessary condition for the success of classically scale-invariant models in solving the hierarchy problem. The situation just described is schematically summarized in Figure 3.1.

Thus, investigating how the aforementioned opposing tendencies due to substantial scalar couplings may balance within a conformal set-up is one of the prime goals of the present chapter. Doing this in a systematical way starting with the simplest extensions of the SM will ultimately allow us to identify the minimal consistent scale-invariant model which can re-

produce phenomenologically viable electroweak symmetry breaking. In this context, minimality means that the number of particle representations is as small as possible. The chapter is now organized as follows. General aspects of conformal model building and more details on how classically scale-invariant theories can solve the hierarchy problem are presented in Section 3.1. The Gildener-Weinberg formalism is subsequently introduced in Section 3.2. Thus prepared, Section 3.3 contains our systematic study of conformal extensions of the SM, adopting the assumptions outlined on page 22, and culminating in the identification of the minimal consistent theory in Section 3.3.3.B. We finally conclude in Section 3.4.

3.1 Basics of scale-invariant model building

In order to appreciate the fundamental principles of conformal model building, which will be applied in the course of our systematic study in Section 3.3, it is helpful to initially understand how classically scale-invariant theories are supposed to solve the gauge hierarchy problem. To this end, let us first recall that during our discussion of the hierarchy problem in generic extensions of the minimal SM in Chapter 2, one of the major conclusions was the following: Unlike a low-mass fundamental Higgs boson, light fermions or gauge bosons are not plagued by severe fine-tuning issues, since the corresponding mass parameters are protected by chiral and gauge symmetry, respectively, and are thus technically natural [14]. One may now naively think that scale invariance[b] can act in the same way to prevent the SM Higgs mass parameter μ^2 from obtaining large radiative corrections. And indeed, since μ^2 is the only explicit dimensionful parameter in the SM, setting it to zero renders the theory's Lagrangian scale invariant and thereby enhances its symmetry. There is, however, a crucial difference with respect to chiral and gauge symmetries, which makes the present situation more complicated. Specifically, scale invariance is in general explicitly broken by radiative effects via the conformal anomaly [123–130] and is thus only a symmetry of the classical action rather than of the full quantum action. Conversely, it is relatively straightforward to construct theories without chiral or gauge anomalies.

To see why *classical* scale invariance is still considered to be a useful guiding principle in addressing the hierarchy problem, it is instructive to study the anomalous conformal Ward identity. The latter encodes *how* scale symmetry is violated in a general renormalizable quantum field theory, and

[b] Also known as dilatation symmetry. For a formal definition of scale transformations in field theory and a discussion of related notions, see e.g. [65, 122] and references therein.

schematically reads [101, 131]

$$T^{\mu}{}_{\mu}(x) = \sum_j \beta_j \cdot O_j(x) + \mathcal{M}(x) \ . \tag{3.1}$$

Here, $T^{\mu\nu}$ is the theory's improved symmetric energy-momentum tensor [101], while the index j runs over all possible local operators O_j which are consistent with the theory's symmetries. The corresponding beta functions are denoted as β_j. Furthermore, restricting to models defined on a flat spacetime, $\mathcal{M}$ can be shown to be the sum of precisely those terms of the Lagrangian which involve dimensionful coefficients and thus explicitly break dilatation symmetry already at *tree-level* [101]. Importantly, in a classically conformal theory where all dimensionful Lagrangian parameters are absent [132], said contributions to the trace vanish identically, i.e. $\mathcal{M}(x) \equiv 0$. In the scenario just described, we are hence left with the first term of equation (3.1). Since the beta functions appearing there encode the couplings' dependence on the renormalization scale implied by quantum effects, a non-zero beta function obviously violates dilatation symmetry. In other words, we can conclude that the first term captures the *anomalous* breaking of scale invariance. As the scale dependence induced by the RG running of the theory's dimensionless couplings is only logarithmic, equation (3.1) crucially demonstrates that in a classically scale-invariant model, radiative corrections can at most reintroduce a *logarithmic* sensitivity of IR parameters, like the observed Higgs mass, to UV physics. The existence of radiatively stable and exponentially separated scales can thus, in principle, be explained. Interestingly, the above logic continues to hold once scale invariance is in addition spontaneously broken, because it is nevertheless still non-linearly realized in theses cases, so that the Ward identity of equation (3.1) remains unchanged.

Note that all of the previous considerations are not too helpful when applied to the minimal SM only, except for explicitly demonstrating that the latter does not suffer from the electroweak hierarchy problem [32] (cf. also Chapter 2). However, if the SM is embedded in some more fundamental theory at a scale Λ, classical conformal invariance may offer a means of stabilizing the Higgs mass against said embedding scale and thus avoid otherwise present fine-tuning issues. Still, due to the particular character of scale symmetry the details are rather subtle. In particular, the following two aspects must be kept in mind:

1. Since Nature inherently includes quantum effects, a classical symmetry is not meaningful as such. Accordingly, tree-level scale invariance has to arise from and must be explained by some more fundamental theory.
2. Also the question of how the classical conformal SM (or its extensions) may be embedded in the aforementioned underlying frameworks without reintroducing the gauge hierarchy problem is non-trivial.

The first issue in the above list would, for instance, be solved if anomalously broken dilatation symmetry was restored at the quantum level in the UV within the framework of a conformal quantum field theory (CFT) replacing the SM at energies above Λ. There is, however, an immediate problem with such an approach. Specifically, since the considered conformal UV completion is supposed to be based on standard concepts of QFT, the Wilsonian view of renormalization [133–135] is expected to be applicable. Here, one regards the SM as a low-energy effective theory which is obtained from the complete theory by appropriately integrating out large-momentum modes. Accordingly, the Higgs mass parameter is then anticipated to obtain radiative corrections of the order of the physical transition scale between the two aforementioned descriptions Λ (cf. equation (2.24) and e.g. [65] for further details). Unfortunately, this reintroduces the gauge hierarchy problem unless Λ is in the TeV range. Obviously, any embedding of the classically conformal SM in a UV completion based on standard concepts of QFT is plagued by the same problem. Even though classically scale-invariant models of electroweak symmetry breaking supplemented by a suitable low-energy CFT are thus conceivable, there exists no successful implementation so far, and we will not follow this option here.

Learning from the previous discussion, we will assume in the following that the theory completing the SM at energies above Λ involves concepts *beyond* traditional quantum field theory, so that the Wilsonian line of arguments is not guaranteed to hold and the hierarchy problem may remain absent even for large Λ. Clearly, an approach which relies on the existence of non-QFT physics may seem to be of limited use at first, since the bulk of BSM scenarios are well describable using QFT. On the other hand, it is far from obvious whether or not a quantum theory of *gravity* may be formulated within the bounds of conventional quantum field theory. Accordingly, Meissner and Nicolai [34–36] argue that scale-invariance of the classical particle physics action may arise from embedding the SM or suitable extensions of it at the Planck scale in a finite theory of quantum gravity, which is assumed not to rely on standard field theory concepts.[c] The reappearance of fine-tuning issues would thus be avoided and anomalously broken classical scale symmetry would explain the exponential lowering of the Higgs mass with respect to the embedding scale $\Lambda := M_{\mathrm{Pl}}$ as argued before. In particular, the anomalous contributions to the conformal Ward identity (3.1) are in this context interpreted as being induced by gravity effects [36].

For the rest of the present thesis, we will assume that a scenario of the aforementioned type is realized. Requiring a consistent implementation of low-energy particle physics as part of the thus-defined framework then has several consequences for model building within classically conformal extensions of the SM, which we will briefly discuss in the following. First, as

[c] For a heuristic justification of why this assumption is well-motivated, see [35].

already mentioned during the introduction to this chapter, scale invariance of the tree-level action implies that the electroweak scale must be generated dynamically. The corresponding mechanism, through which quantum effects induce the emergence of a dimensionful quantity from a classical theory without mass scale, is known as dimensional transmutation and comes in two different variants. On the one hand, and completely analogous to the situation in QCD with massless quarks [136, 137], an explicit scale may arise from non-perturbative effects in a strongly interacting theory. On the other hand, a mass scale can equally well be induced by weakly coupled physics as was first demonstrated by Coleman and E. Weinberg [119]. Even though both versions have successfully been used to write down consistent classically scale-invariant theories in the past, we will restrict to scenarios of the latter type in this thesis (cf. our assumption 1 on page 22).

A second consequence for conformal model building follows from the previously worked out fact, that embedding a classically scale-invariant model in a more fundamental theory based on concepts of QFT will reintroduce fine-tuning issues unless the embedding scale Λ is in the TeV range. Hence, consistently avoiding the gauge hierarchy problem within the presently considered framework implies the absence of any intermediate physical thresholds between the electroweak and the Planck scale [35]. In particular, this forbids the presence of any Landau poles in the renormalization group flow of the model's couplings across the aforementioned energy range [34]. The existence of vacuum instabilities would render our approach inconsistent in a similar way. During our systematic study in the next section, we will therefore only consider those models as viable in which an RG extrapolation all the way up to the Planck scale can successfully be performed in the above sense. The previous discussion also highlights one of the primary goals of conformal model building, which is to accommodate as many BSM phenomena as possible without introducing any new independent physical thresholds between the electroweak and the Planck scale.

3.2 The Gildener-Weinberg formalism

The Gildener-Weinberg (GW) formalism as introduced in [120] is an approach to determine the (approximate) minimum of the one-loop effective potential in a theory with an arbitrary number of massless scalar fields. As such, it is excellently suited to investigate the spontaneous symmetry breaking properties of classically scale-invariant models. In this context, it notably presents an economic alternative to the time-consuming numerical minimization of a multivariate function using brute-force algorithms. Having in mind that our systematic study of minimal conformal extensions of the SM in Section 3.3 will make extensive use of the GW approach, we will review the latter's formal basics in the present section. Following the original

work by Gildener and Weinberg [120], our starting point is the most general tree-level scalar potential V that is invariant under scale transformations. It can be conveniently written as

$$V(\mathbf{\Phi}) = \tfrac{1}{24}\, f_{ijk\ell}\, \phi_i\, \phi_j\, \phi_k\, \phi_\ell \ , \tag{3.2}$$

where $\mathbf{\Phi}$ denotes the vector containing all (real) scalar degrees of freedom ϕ_i. Moreover, $f = f(\Lambda)$ is an appropriate set of coupling constants, which will in general be rendered scale dependent by quantum effects and thus become functions of the renormalization scale Λ.

In the following, we will be interested in the situation where the theory's high-energy phase exhibits a symmetric vacuum, such that all symmetries of the underlying Lagrangian are respected. For large enough Λ, the potential V is therefore supposed to possess a global minimum at the origin of scalar field space. Furthermore, we will assume that loop corrections to the classical potential at this high scale are sufficiently small and do not shift the minimum of V away from zero.

However, let us now imagine that at some scale Λ_{GW}, the Gildener-Weinberg scale, the couplings $f(\Lambda_{\mathrm{GW}})$ are such that the tree-level potential develops a flat direction, along which it is identically zero. This flat direction will be a ray through the origin of scalar field space and can therefore be conveniently parameterized as

$$\mathbf{\Phi}_{\mathrm{flat}} = \boldsymbol{n}\varphi \tag{3.3}$$

with a fixed unit vector $\boldsymbol{n}$ and a real parameter φ specifying the position along the ray. Whereas the *classical* potential thus exhibits a continuous set of degenerate minima $\mathbf{\Phi}_{\mathrm{flat}}$, *quantum effects* will induce a non-zero curvature along the flat direction thereby singling out a particular point $\langle \mathbf{\Phi}_{\mathrm{flat}} \rangle$ as the extremum along $\mathbf{\Phi}_{\mathrm{flat}}$. Provided the loop-induced curvature is positive around the aforementioned extremum, this point will be the true global vacuum of the quantum theory. If $\langle \mathbf{\Phi}_{\mathrm{flat}} \rangle$ and thus $\langle \varphi \rangle$ is non-vanishing, spontaneous symmetry breaking (SSB) occurs. Equation (3.3) then tells us that exactly those scalar fields ϕ_i acquire finite vacuum expectation values (vev), for which the corresponding components n_i of the vector $\boldsymbol{n}$ are non-zero. The numerical values of the entries in $\boldsymbol{n}$ also determine the relative magnitudes of the different vevs. In other words, each possible flat direction comes with its own symmetry breaking pattern, while $\langle \varphi \rangle$ sets the overall scale for effects related to SSB.

Before we turn to the precise formulation of the above idea within a one-loop calculation, let us briefly mention the following. The requirement on the tree-level potential from (3.2) to develop a flat direction can be encoded in an implicit equation for the couplings $f(\Lambda_{\mathrm{GW}})$, the so-called Gildener-

Weinberg condition, which can schematically be written as[d]

$$R(f)\Big|_{\Lambda=\Lambda_{\mathrm{GW}}} = 0\ . \tag{3.4}$$

Using the above constraint, one formerly free coupling can be eliminated. In contrast, we have introduced a dimensionful parameter, namely the scale Λ_{GW}. As previously mentioned, this phenomenon, where the inclusion of quantum effects leads to the appearance of a mass scale in an originally scale-invariant theory, goes by the name of dimensional transmutation and is best known from QCD. However, unlike in QCD, the scale is generated in a perturbative way in the present Coleman-Weinberg-like scenario.

As it becomes clear from our discussion up to this point, a major advantage of the Gildener-Weinberg formalism is that not the full one-loop effective potential must be known. Rather, quantum corrections are only considered along the flat direction thus making the problem of finding the true vacuum effectively one dimensional. Specifically, the one-loop effective potential along Φ_{flat} can be brought into the form [120]

$$V_{\mathrm{eff}}^{(1)}(\boldsymbol{n}\varphi) = A\varphi^4 + B\varphi^4 \log\left(\frac{\varphi^2}{\Lambda_{\mathrm{GW}}^2}\right)\ , \tag{3.5}$$

with Λ_{GW} being the renormalization point. In equation (3.5), the loop functions A and B are found to be

$$A = \frac{1}{64\pi^2\langle\varphi\rangle^4}\sum_i (-1)^{2s_i} d_i \cdot m_i^4\left(\boldsymbol{n}\langle\varphi\rangle\right)\left(\log\frac{m_i^2(\boldsymbol{n}\langle\varphi\rangle)}{\langle\varphi\rangle^2} - c_i\right)\ , \tag{3.6a}$$

$$B = \frac{1}{64\pi^2\langle\varphi\rangle^4}\sum_i (-1)^{2s_i} d_i \cdot m_i^4\left(\boldsymbol{n}\langle\varphi\rangle\right)\ . \tag{3.6b}$$

The sums in the above expressions run over the set of all particles in the theory at hand. Particle i is supposed to have field-dependent tree-level mass $m_i(\boldsymbol{\Phi})$, spin s_i and d_i real degrees of freedom. Moreover, the constants c_i are renormalization scheme dependent. In the $\overline{\mathrm{MS}}$ scheme employed here, one finds $c_i = \frac{5}{6}$ for gauge bosons and $c_i = \frac{3}{2}$ in the case of fermions or scalars.

Computing the extremum $\langle\varphi\rangle$ of the potential from equation (3.5) is straightforward and yields

$$\langle\varphi\rangle = \Lambda_{\mathrm{GW}} \cdot \exp\left(-\frac{1}{4} - \frac{A}{2B}\right)\ . \tag{3.7}$$

Note that the above expression demonstrates that the extremal value $\langle\varphi\rangle$ and Λ_{GW} will be of the same order of magnitude if the same is true for A

[d] More details on how to obtain the Gildener-Weinberg condition for a fixed model and a given symmetry breaking pattern can be found in the next section, as well as in the original paper [120] or in other works using the Gildener-Weinberg approach like [106].

and B. Importantly, the extremum $\langle\varphi\rangle$ is a minimum if and only if the loop function B is positive. The classically massless scalar excitation along the flat direction $\mathbf{\Phi}_{\text{flat}}$ then acquires a positive mass squared, namely

$$m_{\text{PGB}}^2 = \left.\frac{\mathrm{d}^2 V_{\text{eff}}^{(1)}(\boldsymbol{n}\varphi)}{\mathrm{d}\varphi^2}\right|_{\varphi=\langle\varphi\rangle} = 8B\langle\varphi\rangle^2 \,. \tag{3.8}$$

It is to be identified with the pseudo-Goldstone boson (PGB) of spontaneously broken scale invariance, sometimes referred to as scalon [120]. The appearance of a light scalar boson is also one of the key features of classically scale-invariant models from a phenomenological point of view.

3.3 Finding the minimal conformal model

As outlined in the introduction to this chapter, we will now systematically study conformal extensions of the minimal SM, adopting the assumptions previously listed on page 22. In doing so, we will search for the model with the smallest number of field representations which facilitates consistent radiative breaking of scale invariance while also correctly reproducing well-established aspects of electroweak phenomenology. In particular we will require the Higgs mass and the electroweak scale to attain their measured values, which were already quoted in Chapter 2, equations (2.16) and (2.19):

$$m_H \stackrel{!}{=} 125\,\text{GeV} \quad \text{and} \quad v \stackrel{!}{=} 246\,\text{GeV} \,. \tag{3.9}$$

The RG evolution of all models is analyzed using the appropriate full one-loop beta functions, which we compile in Appendix B.

3.3.1 SM + one scalar representation

As we have argued before, the consistent implementation of radiative symmetry breaking in a phenomenologically viable model of particle physics based on the SM gauge group, requires introducing additional scalar degrees of freedom. Correspondingly, already the simplest extension of the minimal SM by one real scalar gauge singlet might be successful. Slightly generalizing this idea, we will in a first step study models in which the SM field content is supplemented by one in general complex, colorless scalar $\text{SU}(2)_L$ multiplet χ of dimension N and hypercharge Y,

$$\chi \sim (\mathbf{1}, \boldsymbol{N}, Y) \,.$$

Consequently, our discussion of Coleman-Weinberg symmetry breaking in the present segment will rely on the following potential, which respects the

SM gauge symmetries, as well as scale invariance

$$\begin{aligned} V = {} & \lambda_1(\Phi^\dagger\Phi)^2 + \lambda_2(\chi^\dagger\chi)^2 + \lambda_3(\chi^\dagger T^a\chi)^2 \\ & + \kappa_1(\Phi^\dagger\Phi)(\chi^\dagger\chi) + \kappa_2(\Phi^\dagger\tau^a\Phi)(\chi^\dagger T^a\chi) \,. \end{aligned} \tag{3.10}$$

A few remarks on the above potential and the employed notation are in order. First, the quantum numbers of the field $\Phi = (\phi^+, \phi^0)^\intercal$ are assumed to be those of the usual complex Higgs doublet of the minimal SM, which we introduced in equation (2.3). In line with the transformation properties of Φ and χ, the matrices τ^a and T^a then denote the infinitesimal generators of SU(2) in the fundamental representations and in the N-dimensional irreducible representation (irrep), respectively.

Second, let us mention that the most general gauge- and scale-invariant potential involving the fields Φ and χ should, in principle, contain further dimension-four operators, specifically, ones of the form $(\chi^\dagger T^{a_1}\dots T^{a_n}\chi)^2$, as well as the associated portal terms to the Φ-sector. However, a dedicated study in [138] demonstrated that the most stable RG running is obtained in the case where all of the corresponding couplings vanish in the IR, i.e. at the Gildener-Weinberg scale in the present context. Still, we will take into account the simplest representatives of the aforementioned class of operators, namely those proportional to λ_3 and κ_2.[e]

Furthermore, particular representations $(\boldsymbol{N}, Y)$ of the electroweak group may allow additional gauge-invariant dimension-four operators to be present. However, the results from [138] apply to the thus introduced couplings as well, so that we will also ignore the aforementioned special terms, unless otherwise stated.

A Real multiplet with vanishing vacuum expectation value

Motivated by minimality, let us start by investigating the situation, in which χ is a *real* $\mathrm{SU}(2)_L$ multiplet. In order to formally distinguish real from complex multiplets, we first need to recall that all irreducible representations of SU(2) are either real or pseudo-real. Hence, for each irrep, there exists a unitary matrix $\mathcal{C}$ in the associated representation of the SU(2) algebra such that

$$\mathcal{C}^{-1}T^a\mathcal{C} = -(T^a)^\intercal \tag{3.11}$$

holds for all $a \in \{1, 2, 3\}$. If the field χ now transforms in the N-dimensional irrep of SU(2), equation (3.11) implies that the same is true for the conjugate

[e] Importantly, some of the mentioned contributions may turn out to be redundant in the sense that they are expressible in terms of operators containing less generator matrices. For an SU(2) doublet, for instance, one can derive $(\Phi^\dagger\tau^a\Phi)^2 = (\Phi^\dagger\Phi)^2/4$ and $(\Phi^\dagger\tau^a\tau^b\Phi)^2 = (\Phi^\dagger\Phi)^2/16$ by using the Fierz identity for the τ^a.

multiplet $\tilde{\chi} := \mathcal{C}\chi^*$. The following definition of a real SU(2) multiplet is therefore natural and will be adopted throughout this chapter:

$$\chi \text{ real} \quad :\Leftrightarrow \quad \tilde{\chi} \overset{!}{=} \chi \,. \tag{3.12}$$

The above definition has some interesting consequences, relevant to the present discussion. For one, real multiplets can be seen to contain only half as many degrees of freedom as a complex multiplet of equal dimension, for which $\tilde{\chi} \neq \chi$. Furthermore, it is straightforward to show that a real multiplet cannot carry any finite U(1) charge and therefore necessarily has zero hypercharge. Lastly, using equations (3.11) and (3.12), the expression $\chi^\dagger T^a \chi$ can be demonstrated to vanish identically for any real SU(2) multiplet χ, regardless of the irrep it transforms in. The general potential introduced in equation (3.10) thus reduces to

$$V = \lambda_1(\Phi^\dagger\Phi)^2 + \lambda_2(\chi^\dagger\chi)^2 + \kappa_1(\Phi^\dagger\Phi)(\chi^\dagger\chi) \,, \tag{3.13}$$

provided χ is a real multiplet.

At the Gildener-Weinberg scale Λ_{GW}, the above potential is assumed to develop a flat direction such that quantum effects lead to a non-trivial vacuum configuration which spontaneously breaks not only scale invariance, but also electroweak symmetry. Notably, the potential exhibits an accidental global $\mathrm{O}(4) \times \mathrm{O}(N)$ symmetry, which will become important later since it implies the appearance of massless Goldstone modes once χ obtains a finite vacuum expectation value (vev). For now, we will, however, assume that the additional scalar fields satisfy

$$\langle \chi_i \rangle = 0 \quad \forall i \in \{1, \ldots, N\} \,.$$

The electroweak vev is then necessarily identical to that of the Higgs doublet, $v \equiv v_\phi$ and each of the extra scalar's components obtains the same mass m_χ upon EWSB. Specifically, an explicit calculation based on equation (3.13) and using $\phi^0 = (v + H)/\sqrt{2}$ reveals

$$m_\chi^2 = \kappa_1 v^2 \,. \tag{3.14}$$

Similarly, the physical Higgs boson's tree-level mass is found to be $m_H^2 = 3\lambda_1 v^2$, while all remaining SM particles acquire masses in exactly the same way as they do in the minimal SM. Importantly, equation (3.14) requires the portal coupling κ_1 to be non-negative at Λ_{GW}, as all physical masses must be real.

The vacuum configuration described before is realized, provided the flat direction develops along the ϕ^0-axis in scalar field space. This, in turn, corresponds to the Gildener-Weinberg condition $\lambda_1(\Lambda_{\text{GW}}) = 0$. As expected, the leading-order mass of the physical Higgs mode H thus vanishes so that H is to be identified with the pseudo-Goldstone boson (PGB) of spontaneously

broken scale invariance. Since scale symmetry is anomalously broken via quantum effects, the Higgs will, however, acquire a finite mass at the one-loop level as per equation (3.8). In the present case, one finds

$$m_H^2 = 4\left(B_{\mathrm{SM}} + \frac{N\kappa_1^2}{16\pi^2}\right)v^2 \,, \tag{3.15}$$

where B_{SM} is defined in Appendix A, equation (A.1) and can be calculated to be negative. Solving equation (3.15) for the portal coupling allows us to compute the unique value for $\kappa_1(\Lambda_{\mathrm{GW}}) > 0$ that is consistent with the phenomenological constraints of equation (3.9), namely

$$\kappa_1(\Lambda_{\mathrm{GW}}) = \frac{2\pi}{v}\sqrt{m_H^2 - 4B_{\mathrm{SM}}v^2}\cdot N^{-1/2} \quad \text{with} \quad B_{\mathrm{SM}} < 0 \,. \tag{3.16}$$

Let us remark that, strictly speaking, m_H in the above equation is not the Higgs pole mass measured at the LHC, but rather its renormalized mass evaluated at Λ_{GW}. However, the error we make by inserting $m_H = 125\,\mathrm{GeV}$ is expected to be small, since the RG running of the mass is only logarithmic and we always assume Λ_{GW} to be reasonably close to the electroweak scale. That being said, equation (3.16) demonstrates that adding a larger scalar multiplet to the SM entails a smaller initial value for κ_1 at Λ_{GW}. As we will explicitly argue later (cf. e.g. Figure 3.2b), a sufficiently small portal coupling is essential in order to avoid low-scale Landau poles. Hence, one might naively expect the RG evolution towards the UV to become stable for large enough N. However, at the same time, a large multiplet dimension N also amplifies the RG flows of several model parameters, most importantly those of the scalar sector couplings, as well as that of the $\mathrm{SU}(2)_L$ gauge coupling (see Appendix B.1). The number of extra scalar degrees of freedom N therefore enters the problem in a non-trivial way so that dedicated numerical analyses of the models' RG evolutions are needed.

In doing so, we adopt several additional simplifications. On the one hand, we ignore the term proportional to B_{SM} in equation (3.16), i.e. we fix

$$\kappa_1(\Lambda_{\mathrm{GW}}) := 2\pi\frac{m_H}{v}\cdot N^{-1/2} \,. \tag{3.17}$$

Since B_{SM} is always negative, we thereby underestimate the initial value of κ_1, thus making the RG running more stable. Potential Landau poles are therefore expected to be shifted towards larger energy scales. On the other hand, note that while choosing the portal coupling according to equation (3.17) guarantees that the ratio m_H/v attains its physical value, the correct overall scale of v (or m_H) must be adjusted by appropriately setting the Gildener-Weinberg scale. How this can be consistently done within a full treatment of the problem is the subject of Appendix A. Here, we instead fix $\Lambda_{\mathrm{GW}} = 500\,\mathrm{GeV}$, keeping in mind that our approach towards radiative

symmetry breaking forbids Λ_{GW} to deviate too much from the electroweak scale. Even though the aforementioned special choice will, in general, not reproduce the true Higgs mass, it is anticipated to only marginally impact the actual position of potential Landau poles, whose determination is the prime objective of the current study. Varying the renormalization point Λ_{GW} in the range $[100\,\mathrm{GeV}, 1\,\mathrm{TeV}]$ explicitly confirmed that expectation.

Having set λ_1, κ_1 and Λ_{GW} as described above, only the initial value for the extra multiplet's quartic self interaction, λ_2, remains to be fixed. Since there are no phenomenological constraints on $\lambda_2(\Lambda_{\mathrm{GW}})$, we will just vary it in the perturbative regime and eventually choose the value that allows for the farthest extrapolation towards the UV. The corresponding scale of maximal extrapolation will be referred to as Λ_{UV}.

Results and discussion. Based on the procedure just outlined and for a given multiplet dimension N, we performed the model's RG evolution towards the UV, starting at the Gildener-Weinberg scale Λ_{GW}. In doing so, we checked the perturbativity of all couplings after each RG step, thereby eventually determining the quantity Λ_{UV} introduced above. The outcome is shown in Figure 3.2a. Notably, due to our approximation made in equation (3.17), the quoted values for Λ_{UV} are to be seen as an upper bound for the scale of maximal extrapolation. Since Landau poles were found to always appear significantly below the Planck scale, this is, however, sufficient to rule out the present model's UV completeness.

From a qualitative point of view, the results of Figure 3.2a can be easily interpreted with the help of the model's beta functions presented in Appendix B.1. Concentrating on the scalar subsystem in a first step (blue circles), we can learn from the RG equations in (B.2) that all contributions to the scalar flow are always greater than zero, provided the portal coupling is positive, $\kappa_1 > 0$. Hence, no cancellations are possible and the scalar couplings are driven towards ever higher values until one of them hits a Landau pole. Of course, this positive feedback mechanism is more effective for larger initial values. While $\lambda_1(\Lambda_{\mathrm{GW}})$ is fixed via the GW condition and $\lambda_2(\Lambda_{\mathrm{GW}})$ can be chosen arbitrarily small, the initial value of κ_1 decreases for larger multiplets according to equation (3.17). Correspondingly, we observe that Λ_{UV} slowly increases with the multiplet dimension N. However, Λ_{UV} saturates at around $10^6\,\mathrm{GeV}$, since large N also amplify the scalar RG flow.

Additionally taking into account contributions due to the top quark (red squares) leads to the same qualitative dependence of Λ_{UV} on the multiplet dimension, but with an overall degraded performance.

In contrast, including the gauge instead of the top sector (green triangles) induces a significantly different behavior. On the one hand, equations (B.3) reveal that the scalar flow obtains negative and thus stabilizing contributions proportional to the scalar couplings themselves and the SU(2) gauge

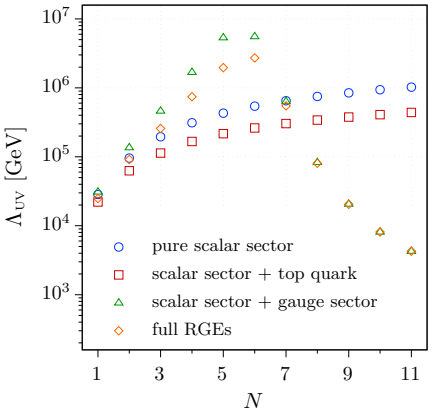

(a) Maximum possible scale of RG extrapolation Λ_{UV}. The color code indicates which set of one-loop beta functions and which contributions to them are taken into account.

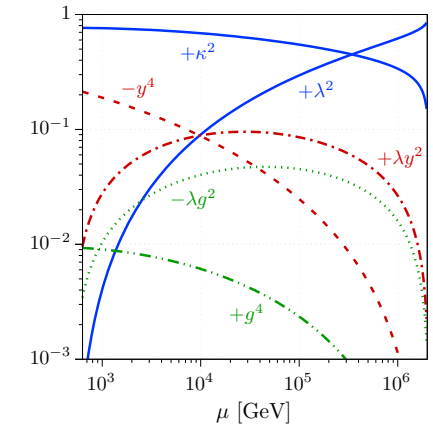

(b) Scale dependence of the *relative* contributions to the beta function of λ_1 for $N = 5$. Scalar, Yukawa and gauge sector contributions are displayed in blue, red and green, respectively. The dashed red and dotted green curves show absolute values of the negative terms involving y^2 and λg^2, respectively.

Figure 3.2: Results for extensions of the classically scale-invariant SM by one real $\mathrm{SU}(2)_L$ multiplet of dimension N with zero vev.

coupling, specifically g_2^2. Said terms typically grow as N^2 and will outweigh the also existing positive contributions involving g_2^4, if the gauge coupling remains sufficiently small. We hence see a substantial rise in Λ_{UV} as long as $N \leqslant 6$, where g_2 is asymptotically free. Nevertheless, the stabilizing terms due to gauge interactions can only delay but not prevent the appearance of Landau poles in one of the scalar couplings.

On the other hand, the presence of an extra SU(2) multiplet entails additional positive contributions to the flow of g_2, in which the multiplet dimension enters to the third power, see equation (B.5). As a consequence, the SU(2) gauge coupling stops being asymptotically free for $N \geqslant 7$ and will thus ultimately develop a Landau pole. In particular, g_2 now also increases with energy scale, so that the aforementioned positive contributions to the scalar flow proportional to g_2^4 become relevant. The latter enter the beta functions of λ_1, λ_2 and κ_1 with coefficients that scale as 1, N^4 and N^2, respectively. Correspondingly, λ_2 is found to be the parameter which hits a Landau pole first and thus limits the model's extensibility towards the UV

for $N > 6$.

Adding effects due to the top quark cannot improve the performance just described, since y_t neither directly enters the flow of λ_2 nor that of g_2. Thus, using the full one-loop RGEs (orange diamonds) results in nearly the same values for Λ_{UV} as before when $N > 6$. For $N \leqslant 6$, the maximum reachable UV scale even decreases. In summary, Figure 3.2a demonstrates that we cannot extrapolate the present set-up all the way up to the Planck scale.

In order to further illuminate the above observations, we analyze the interplay between the contributions of the different particle sectors to the model's RG flow. As an example, we use the beta function of the Higgs self-coupling λ_1 for $N = 5$, the relative contributions to which are displayed in Figure 3.2b as functions of renormalization scale μ. Several features are particularly crucial to note. First, we see that in the gauge sector the stabilizing contribution proportional to $-\lambda g^2$ soon overpowers the positive $+g^4$ term. However, both contributions are constantly outweighed by the destabilizing $+\lambda y^2$ term, which dominates the Yukawa sector for sufficiently large energy scales. Second, and more importantly, Figure 3.2b demonstrates that the portal coupling κ_1 has the biggest impact on the flow of λ_1, with the associated relative contribution being roughly one order of magnitude larger than those due to non-scalar interactions. The appearance of a Landau pole in the running of λ_1 is thus triggered by said $+\kappa_1^2$ term and could only be avoided, if κ_1 was kept sufficiently small. However, consistency with electroweak phenomenology as enforced by equation (3.16) prevents small values for κ_1 in the present case. On a related note, it is also important to remark that complete cancellations between the Yukawa and gauge sectors, on the one hand, and the scalar sector, on the other hand, are not achievable. Stabilization of the scalar RGE subsystem in the presence of substantial scalar couplings therefore has to originate from negative terms within the scalar sector, which are, however, absent as long as $\kappa_1 > 0$ is necessary.

B Real multiplet with finite vacuum expectation value

Slightly expanding our set-up of the previous section, we will now allow the real scalar field χ to develop a non-zero vacuum expectation value v_χ. Just as the Higgs doublet's vev v_ϕ before, also v_χ is assumed to be induced by the radiative breaking of scale invariance at Λ_{GW}. Importantly, since the electromagnetic symmetry is observed to be intact at low energies, only an electrically neutral component of χ, say χ_{i_0}, can acquire a finite vev in a phenomenologically consistent way,

$$\chi_{i_0} = v_\chi + \sigma \,, \tag{3.18}$$

with σ being an appropriate radial excitation. Recalling that real SU(2) multiplets cannot carry hypercharge, and employing the Gell-Mann Nishijima formula from Chapter 2, we find that the index i_0 needs to be chosen

such that the third component of weak isospin vanishes for χ_{i_0}, specifically $i_0 = (N+1)/2$. Notably, the thus determined i_0 is only an integer for odd N, which immediately excludes even-dimensional multiplets from our current discussion.

In the spirit of the Gildener-Weinberg formalism and using the notation introduced in Section 3.2, we parameterize the vevs v_ϕ and v_χ as

$$\begin{aligned} \frac{v_\phi}{\sqrt{2}} = \langle \phi^0 \rangle &= n_1 \langle \varphi \rangle \equiv \sin\beta \cdot \langle \varphi \rangle \,, \\ v_\chi = \langle \chi_{i_0} \rangle &= n_2 \langle \varphi \rangle \equiv \cos\beta \cdot \langle \varphi \rangle \,, \end{aligned} \tag{3.19}$$

taking into account that they both derive from the same dynamically generated scale $\langle \varphi \rangle$. Without loss of generality, we choose the angle β to range within $(0, \pi/2)$. Employing the tadpole equations of the tree-level potential in equation (3.13), i.e.

$$\left.\frac{\partial V}{\partial v_\phi}\right|_{\text{vac.}} = 0 \quad \text{and} \quad \left.\frac{\partial V}{\partial v_\chi}\right|_{\text{vac.}} = 0 \,,$$

as well as requiring both n_1 and n_2 from equation (3.19) to be non-zero, we can now derive the Gildener-Weinberg condition associated with the desired vev configuration, namely

$$4\lambda_1\lambda_2 - \kappa_1^2 = 0 \,, \quad n_1^2 = \frac{\kappa_1}{\kappa_1 - 2\lambda_1} \,. \tag{3.20}$$

The (largest) energy at which the former relation is fulfilled then defines the scale of spontaneous symmetry breaking Λ_{GW}. Notably, the second identity in equation (3.20) implies that the portal coupling must be negative, $\kappa_1 < 0$, since n_1 necessarily ranges between zero and one, while λ_1 has to be positive due to stability reasons. Combining equations (3.19) and (3.20) also allows us to express the angle β in terms of quantities at defined at Λ_{GW}. Specifically, we find

$$\tan\beta = \frac{v_\phi}{\sqrt{2} v_\chi} = \sqrt{-\frac{\kappa_1}{2\lambda_1}} \,. \tag{3.21}$$

A qualitatively new feature, which emerges once $v_\chi > 0$, is that of scalar mixing. Parameterizing the electrically neutral component of the Higgs doublet as $\phi^0 = (v_\phi + \phi)/\sqrt{2}$, we observe that the CP-even scalar degrees of freedom ϕ and σ have the same quantum numbers and will therefore, in general, mix. Specifically, the corresponding mass terms can be written as

$$V_{\text{mass}} \supseteq \tfrac{1}{2} \begin{pmatrix} \phi & \sigma \end{pmatrix} \begin{pmatrix} 3\lambda_1 v_\phi^2 + \kappa_1 v_\chi^2 & 2\kappa_1 v_\phi v_\chi \\ 2\kappa_1 v_\phi v_\chi & 12\lambda_2 v_\chi^2 + \kappa_1 v_\phi^2 \end{pmatrix} \begin{pmatrix} \phi \\ \sigma \end{pmatrix} \,. \tag{3.22}$$

The above scalar mass matrix (henceforth denoted as M^2) is symmetric and real and may therefore be diagonalized by an orthogonal matrix U, which is

parameterized by one real mixing angle α. For later convenience, we choose α to range between $-\pi/4$ and $\pi/4$ without loss of generality. Clearly, one of the two resulting mass eigenstates will have to be identified with the 125 GeV Higgs boson H. Since the latter is empirically observed to behave very similarly to what is expected from the minimal SM [24], H is to be predominantly composed of ϕ (see also [109, 110]). Our aforementioned choice for the range of α thus implies the following assignment

$$\begin{pmatrix} H \\ S \end{pmatrix} = U \begin{pmatrix} \phi \\ \sigma \end{pmatrix} = \begin{pmatrix} \cos\alpha \cdot \phi - \sin\alpha \cdot \sigma \\ \cos\alpha \cdot \sigma + \sin\alpha \cdot \phi \end{pmatrix} , \tag{3.23}$$

where S is an additional physical scalar mode in the theory's particle spectrum. The mass squared matrix M^2 introduced in equation (3.22) possesses two eigenvalues corresponding to the eigenstates' tree-level masses. They are given by

$$m_{\pm}^2 = \frac{1}{2}\left[\operatorname{Tr} M^2 \pm \sqrt{(\operatorname{Tr} M^2)^2 - 4 \cdot \det M^2}\right] .$$

Employing equations (3.20) to (3.22), we can evaluate the above expression and obtain the eigenvalues in terms of parameters at Λ_{GW}, namely

$$m_+^2 = 2(\lambda_1 - \kappa_1)v_\phi^2 > 0 \quad \text{and} \quad m_-^2 = 0 , \tag{3.24}$$

where we additionally used $\lambda_1 > 0$ and $\kappa_1 < 0$. Crucially, equation (3.24) explicitly confirms the presence of a CP-even scalar particle whose tree-level mass vanishes, and which must therefore be identified with the PGB of anomalously broken scale invariance. Note, that it is not a priori clear which of the eigenstates H and S acquires which mass upon symmetry breaking. This rather depends on the sign of the mixing angle α as we will discuss shortly.

Before, let us however investigate the relation between the scalar mixing angle and the other model parameters introduced so far. Requiring the matrix $UM^2U^\intercal$ to be diagonal, as well as employing equation (3.21) to eliminate the vevs in favor of the angle β, yields the identity

$$\tan 2\alpha = \frac{4\sqrt{2}\kappa_1 \tan\beta}{(12\lambda_2 - \kappa_1) - 2(3\lambda_1 - \kappa_1)\tan^2\beta} .$$

Additionally exploiting the extra constraint set on the model's parameter space by the Gildener-Weinberg condition of equation (3.20), allows to further simplify the above expression to eventually give

$$\tan 2\alpha = \frac{2\sqrt{2}\tan\beta}{1 - 2\tan^2\beta} . \tag{3.25}$$

Notably, the angle β quantifying the vev ratio and the mixing angle of CP-even scalars α are thus uniquely related in the conformal models under

scalar mixing angle	PGB	relation between α and β	scale hierarchy
$\alpha > 0$	$\neq H$	$\tan\alpha = \sqrt{2}\tan\beta$	$v_\phi < v_\chi$
$\alpha < 0$	$= H$	$\tan\alpha = -(\sqrt{2}\tan\beta)^{-1}$	$v_\phi > v_\chi$

Table 3.1: Phenomenological differences between models with positive and negative scalar mixing angle $\alpha \in \{-\pi/4, \pi/4\}$. The origin of the statements in the second column is explained in the main text after equation (3.25). The relations in the third and fourth columns are based on equations (3.25) and (3.21).

consideration, whereas they can be varied independently in a general theory. Specifically, equation (3.25) possesses two solutions, which are valid for different signs of α and can be found in Table 3.1. Furthermore, a closer look at said solutions reveals that the sign of α also determines whether the ratio v_ϕ/v_χ is larger or smaller than one. The corresponding relation is listed in Table 3.1 as well.

Now that we have an explicit expression for the scalar mixing angle, it is straightforward to show, that performing the diagonalization of the mass squared matrix M^2 for *positive* α gives $UM^2U^\intercal = \mathrm{diag}(m_+^2, m_-^2)$. In accordance with equation (3.23), we then need to identify the scalar mode S with the classically massless PGB, while the leading-order Higgs mass is equal to m_+. Similarly, the Higgs boson H corresponds to the PGB for *negative* α (cf. Table 3.1). In the following, we will investigate the two cases $\alpha > 0$ and $\alpha < 0$ in turn, starting with the former.

On the one hand, a positive mixing angle entails a sizable vev v_χ according to Table 3.1, specifically $v_\chi > v_\phi$. But a non-negligible vev contributing to the electroweak scale will generally induce a significant deviation of the leading-order ρ-parameter from its SM value of one, which we have derived in Chapter 2, equation (2.20). Since $\rho \approx 1$ has been experimentally verified with high precision [53], this feature typically rules out models with a large vev v_χ. There exist, however, certain representations of the electroweak group, i.e. particular combinations of N and Y, for which the tree-level identity $\rho = 1$ is reproduced regardless of the size of v_χ (see e.g. [139]). Requiring the extra multiplet to be real, i.e. $Y = 0$, only leaves one of the aforementioned exceptions, namely the singlet with $N = 1$. Accordingly, we restrict the present discussion of positive α to the real singlet case.

As we have argued before, a positive mixing angle also requires the extra scalar mode S to be identified with the PGB, whereas the physical Higgs boson H obtains the leading-order mass $m_+ = m_H$. Computing the one-loop effective potential's curvature along the leading-order flat direction then amounts to adding the positive contribution of the 125 GeV Higgs scalar to that of SM fermions and gauge bosons. The latter is dominated by the fermionic top quark loop and therefore strongly negative. Correspondingly, an explicit calculation reveals that the overall curvature is negative as well,

so that the theory exhibits a maximum instead of a minimum at the dynamically selected local extremum $\langle\varphi\rangle$.[f] The singlet case with $\alpha > 0$ can thus also be discarded as inconsistent.

Negative mixing angles, on the other hand, imply the scale hierarchy $v_\chi < v_\phi$. Hence, arbitrarily small vevs v_χ are possible and constraints coming from the tree-level ρ-parameter can, in principle, be circumvented. Accordingly, our study of the $\alpha < 0$ scenario will not be restricted to the singlet case as before, but will also include larger (odd) multiplets. As a consequence, it is crucial to observe that the presence of a finite vev in the χ-sector spontaneously breaks part of the global symmetry of the potential in equation (3.13), specifically $\mathrm{O}(N) \to \mathrm{O}(N-1)$. In line with Goldstone's theorem, the model's particle spectrum will therefore contain $N-1$ exactly massless scalar modes, whose existence can explicitly be demonstrated by using the GW condition from equation (3.20). Instead of addressing potential phenomenological issues of additional massless and electrically charged scalars, we will here focus on their implications on radiative electroweak symmetry breaking and the model's RG evolution.

To that end, we recall from Table 3.1 that negative mixing angles require the 125 GeV Higgs boson to be identified with the PGB. The only further massive scalar particle in the physical spectrum is the CP-even mode S, which acquires an a priori unknown tree-level mass m_+, parameterized as in equation (3.24). The Higgs boson's one-loop mass can then be calculated via equation (3.8), namely

$$m_H^2 = 8\left(B_{\mathrm{SM}} + \frac{m_+^4}{64\pi^2\langle\varphi\rangle^4}\right)\langle\varphi\rangle^2 < \frac{n_1^2}{\pi^2}(\lambda_1-\kappa_1)^2 v_\phi^2 \,,$$

where we employed equations (3.19) and (3.24), as well as $B_{\mathrm{SM}} < 0$ in the second step. Next, we observe that the electroweak scale v can generally be written as $v^2 = v_\phi^2 + c^2 v_\chi^2$ in the present class of theories, where c is a model-dependent and real constant. Using $v_\phi \leqslant v$ accordingly, and isolating the empirically known quantities m_H and v, we find the inequality

$$n_1^2(\lambda_1-\kappa_1)^2 > \pi^2\frac{m_H^2}{v^2} =: r^2 \,.$$

Here, n_1 is given by equation (3.20) and the parameters on the left-hand side are to be evaluated at Λ_{GW}. Solving the above relation for one of the unknown Lagrangian parameters, say $\lambda_1(\Lambda_{\mathrm{GW}})$, yields

$$\lambda_1(\kappa_1) > \frac{(r^2-\kappa_1^2) \pm \sqrt{r^2(r^2-\kappa_1^2)}}{-\kappa_1} \,. \tag{3.26}$$

For any given portal coupling $\kappa_1(\Lambda_{\mathrm{GW}})$, replacing the inequality (3.26) by an equality amounts to underestimating the initial value of λ_1, thus rendering

[f] Further details can be found in Section 3.2, especially in equations (3.6b) and (3.8).

the RG running more stable. Since we are presently only interested in an upper bound on the scale of potential Landau poles, we will adopt the above simplification during our analysis.

As a last point before discussing actual results, let us investigate the allowed range for the parameter $\kappa_1(\Lambda_{\mathrm{GW}})$. Of course, $\lambda_1(\Lambda_{\mathrm{GW}})$ has to be real and positive which singles out the solution with the plus sign in equation (3.26) and confines the portal coupling to $|\kappa_1| \leqslant r$. As mentioned before, a negative mixing angle implies $v_\phi > v_\chi$ according to Table 3.1, which, in turn, requires $|\kappa_1| \geqslant \lambda_1$ as per equation (3.21). Using the inequality (3.26), the latter condition can be recast into $|\kappa_1| > \sqrt{3}r/2$. Numerically evaluating the aforementioned constraints on κ_1 yields

$$1.38 \leqslant |\kappa_1| \leqslant 1.60 \,. \tag{3.27}$$

In summary, our analysis of the models' RG equations will be based on the initial conditions which are fixed by the following procedure: Similar to before, we first simplify the calculation by choosing $\Lambda_{\mathrm{GW}} = 500\,\mathrm{GeV}$. We then vary $\kappa_1(\Lambda_{\mathrm{GW}})$ in the viable region presented in equation (3.27). For given portal coupling, $\lambda_1(\Lambda_{\mathrm{GW}})$ is set according to equation (3.26) with the inequality replaced by an equality, while $\lambda_2(\Lambda_{\mathrm{GW}})$ is determined by the Gildener-Weinberg condition of equation (3.20).

Results and discussion. Also for the present set-up, we are interested in the maximum possible scale of RG extrapolation Λ_{UV}, i.e. the largest energy scale which can be reached before at least one running coupling becomes non-perturbative. The values for Λ_{UV} shown in Figure 3.3 were determined as previously described on page 34 with obvious adjustments to the present context. Most importantly, Figure 3.3 demonstrates that also allowing for a finite vev $v_\chi < v_\phi$ does not produce a theory whose RG flow remains perturbative all the way up to the Planck scale. Rather, barring the singlet case, all models discussed here hit a Landau pole at even smaller scales than their counterparts with vanishing vev in the χ-sector.

Interestingly, the results of Figures 3.2 and 3.3 not only differ quantitatively, but also qualitatively: While the UV scale as a function of multiplet dimension exhibited a (well-understood) peak for zero v_χ, Λ_{UV} monotonously decreases with N in the present study. To understand this difference, recall that in the absence of a vev in the χ-sector, the number of massive scalar particles rises linearly with N, so that large-dimensional multiplets allow for small initial values of the portal coupling. In contrast, owing to the spontaneously broken accidental $\mathrm{O}(N)$ symmetry of the potential, there is always only one massive scalar degree of freedom next to the physical Higgs boson, if χ acquires a finite vev. Hence, RG running invariably starts on the same hypersurface in parameter space, which is fixed by requiring the ratio m_H/v to attain its physical value, see equation (3.26). At the same time, the RG

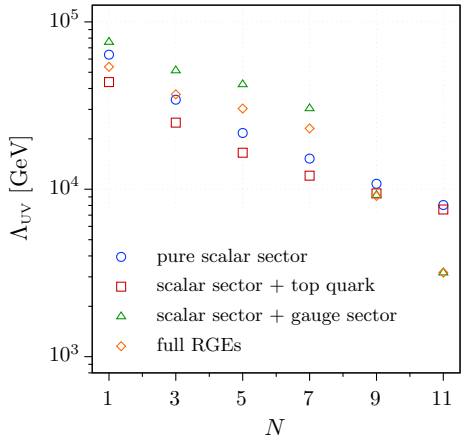

Figure 3.3: Maximum possible scale of RG extrapolation $\Lambda_{\rm UV}$ in extensions of the scale-invariant SM by one real $\mathrm{SU}(2)_L$ multiplet of dimension N with finite vev $v_\chi < v_\phi$. The color code indicates which set of one-loop beta functions and which contributions to them are taken into account. Note that we only study odd-dimensional representations in line with our discussion below equation (3.18).

flow increases with N, which now cannot be compensated by smaller initial values. Correspondingly, models with larger multiplets develop Landau poles at lower scales.

Whereas the overall behavior of the UV scale as a function of multiplet dimension N thus strongly depends on whether or not χ acquires a vev, the observed impact of including different contributions to the theory's RG flow for fixed N does not. Specifically, the relative magnitudes of $\Lambda_{\rm UV}$ calculated using distinct sets of RGEs is very similar to those of Figure 3.2, where $v_\chi = 0$ was assumed. This behavior is expected, as the beta functions do not rely on the precise value of v_χ so that our discussion from the previous section still applies.

C Complex multiplet with vanishing vacuum expectation value

Let us continue to study extensions of the minimal SM, where the Higgs sector is supplemented by only one colorless scalar $\mathrm{SU}(2)_L$ multiplet χ. However, in contrast to the previous sections, let us now remove the restriction of considering exclusively real multiplets and investigate how the situation changes once χ is allowed to be complex in the sense discussed below equation (3.12). Such a complex multiplet will generally carry a non-zero hypercharge Y. Notably, the theory of a complex SU(2) multiplet with vanishing hypercharge can be recast into that of two real multiplets of equal dimensions, which will be covered in Section 3.3.3. Here, we will therefore assume a non-zero hypercharge without loss of generality.

In line with the scalar particle content presently under consideration, our

analyses will be based on the full potential of equation (3.10). Furthermore, recall from our discussion below equation (3.10) that there exist additional operators which are only gauge-invariant for particular representations of the electroweak group. One of those is given by

$$\Delta V_1 = \kappa_3 \Big[(\Phi^\intercal \varepsilon \tau^a \Phi)(\chi^\intercal \mathcal{C} T^a \chi) + \text{h.c.} \Big] \,, \tag{3.28}$$

where $\mathcal{C}$ is the matrix introduced in equation (3.11), while ε is the two-dimensional representation of said matrix. The above term can easily be shown to be symmetric for the choice $Y = -Y_\phi = \frac{1}{2}$. Importantly, this statement holds regardless of the multiplet dimension N. However, the matrices $\mathcal{C}T^a$ are anti-symmetric in all odd-dimensional SU(2) representations[g] so that the operator in equation (3.28) vanishes identically for odd N. Since ΔV_1 is still present in a whole class of models, we decided to take it into account during our analysis.

Similar to the real case, let us assume in a first step that the extra multiplet's vacuum expectation value vanishes, i.e. $v_\chi = 0$, whereas the Higgs doublet is supposed to acquire a finite vev, specifically $\phi^0 = (v + H)/\sqrt{2}$. As before, the physical Higgs boson H is then to be identified with the PGB of broken scale invariance, with the associated Gildener-Weinberg condition being $\lambda_1(\Lambda_{\text{GW}}) = 0$.

An important difference to the scenario where χ is a real multiplet lies in the fact that the potential of equation (3.10) supplemented by ΔV_1 no longer enjoys a global O($2N$) symmetry in the χ-sector.[h] The latter is explicitly broken by the terms proportional to κ_2, κ_3 and λ_3. Correspondingly, not all components of χ obtain the same mass during EWSB as in the real case. Rather, the O($2N$)-violating portal operators induce a mass splitting between the individual complex fields χ_k. Ignoring contributions due to ΔV_1 for now, an explicit calculation yields

$$m_k^2 = \tfrac{1}{8}\big[4\kappa_1 - (N - 2k + 1)\kappa_2\big] v^2 \,, \tag{3.29}$$

where $k \in \{1, \dots, N\}$ and the couplings are to be understood as evaluated at Λ_{GW}. Importantly, requiring all of the above masses to be real implies a non-negative value of $\kappa_1(\Lambda_{\text{GW}})$. Additionally asking for at least one finite mass in the χ-sector, constrains κ_1 to be positive at the Gildener-Weinberg scale. Both statements remain valid upon inclusion of ΔV_1. However, the presence of the corresponding operator leads to a much more complex χ mass spectrum than that of equation (3.29). In particular, a mass splitting

[g] This is true in the so-called spherical basis of the SU(2) Lie algebra (see e.g. [140]). Said basis is, however, unique in the sense that the component fields of the multiplet χ then have well-defined weak isospin T_3 and thus a definite electric charge.

[h] Note that the global symmetry in the χ-sector of the constrained potential in equation (3.13) is enhanced from O(N) to O($2N$) when going from a real to a complex multiplet due to the doubling of degrees of freedom.

proportional to κ_3 is introduced between the CP-even and the CP-odd modes of the electrically neutral component. Still, all mass eigenvalues can be calculated analytically. According to equation (3.8), the Higgs boson's one-loop mass is then given by $m_H^2 = 8(B_{\text{SM}} + B_{\text{add}})\langle\varphi\rangle^2$, where $B_{\text{SM}} < 0$ and

$$B_{\text{add}} := \frac{2}{64\pi^2\langle\varphi\rangle^4} \sum_{k=1}^{N} m_k^4 = \frac{4N\kappa_1^2 + D\kappa_2^2 + (N^2 + 12N - 24)\kappa_3^2}{128\pi^2} \,.$$

Here, the overall factor of two accounts for the fact that each component field is complex and thus encodes two real degrees of freedom. Moreover, D denotes the Dynkin index of the N-dimensional SU(2) irrep, which is given by $D = N(N^2-1)/12$. Following our approach from the previous sections, we use $B_{\text{SM}} < 0$ and isolate the phenomenologically known quantities m_H and v to obtain

$$\sqrt{4N\kappa_1^2 + D\kappa_2^2 + (N^2 + 12N - 24)\kappa_3^2} > 4\sqrt{2}\pi\frac{m_H}{v} \,.$$

Replacing the above inequality by an equality will again lead to a more stable RG running, since it implies an underestimation of the portal couplings at Λ_{GW}. Given the multiplet dimension N as well as the initial values of the O(N)-violating portal couplings, $\kappa_2(\Lambda_{\text{GW}})$ and $\kappa_3(\Lambda_{\text{GW}})$, the resulting equation can then be uniquely solved for κ_1, specifically

$$\kappa_1(\Lambda_{\text{GW}}) := \frac{1}{2}\sqrt{32\pi^2\frac{m_H^2}{v^2} - D\kappa_2^2 - (N^2 + 12N - 24)\kappa_3^2}\cdot N^{-1/2} \,. \tag{3.30}$$

Note, however, that only real solutions with $\kappa_1(\Lambda_{\text{GW}}) > 0$ are viable in accordance with our discussion below equation (3.29).

Apart from λ_1 and κ_1 whose initial values are set by the Gildener-Weinberg condition and equation (3.30), respectively, all other parameters at Λ_{GW} are varied in the perturbative regime. Additionally fixing $\Lambda_{\text{GW}} = 500\,\text{GeV}$ as before, completes the initial conditions for the model's RG evolution towards the UV.

Results and discussion. In Figure 3.4, we show the maximum possible scale of RG extrapolation Λ_{UV} for theories extending the SM by one additional complex multiplet of dimension N and hypercharge Y, which does not acquire a finite vev. The results were computed using the full RGEs given in Appendix B.2. Most importantly, none of the models can be extrapolated beyond $10^7\,\text{GeV}$. Specifically, the figure demonstrates that the appearance of Landau poles gets delayed the most for quintuplet and sextet models with small hypercharges. In that regard, the present findings are similar to those obtained for the case of real multiplets with vanishing vev, where Λ_{UV} was observed to possess a maximum for $N = 6$ (see Figure 3.2a). The strong decrease in Λ_{UV} for large hypercharges is consistent with the fact that the flow

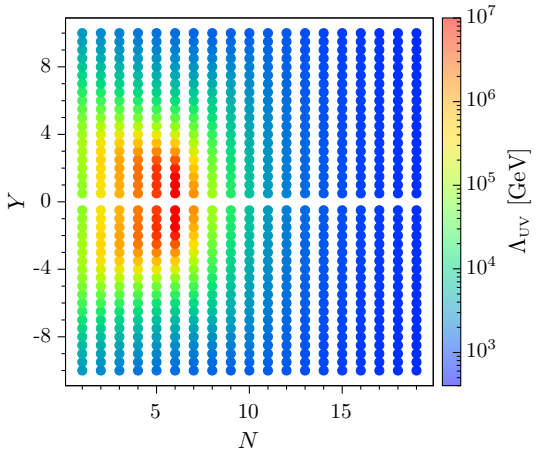

Figure 3.4: Maximum possible scale of RG extrapolation $\Lambda_{\rm UV}$ in extensions of the scale-invariant SM by one complex $\mathrm{SU}(2)_L$ multiplet of dimension N and hypercharge Y with zero vev.

of the U(1) gauge coupling g_1 and that of the scalar subsystem are amplified by terms growing as Y^2 or even Y^4. This particularly affects the portal coupling κ_1 whose starting value cannot be arbitrarily small due to equation (3.30), and whose beta function includes a contribution proportional to $Y^4 g_1^4$.

As already mentioned, the hypercharge enters only with even powers into the model's beta functions, which are therefore invariant under the replacement $Y \to -Y$. Correspondingly, Figure 3.4 exhibits a reflection symmetry with respect to the line of vanishing hypercharge. Notably, the presence of the additional $\mathrm{O}(N)$-violating operator proportional to κ_3 for $Y = -\frac{1}{2}$ explicitly breaks the aforementioned exchange symmetry of the RGE system. However, the optimal initial value of κ_3, producing the largest $\Lambda_{\rm UV}$ for a given N, is found to be near zero in all investigated cases. Since κ_3 is renormalized multiplicatively, it then stays small during the entire RG evolution, which explains the fact that the hypercharge conjugation symmetry is still manifest in Figure 3.4. On a related note, our study also reveals that the most stable RG running is achieved for initial values of λ_3 and κ_2 close to zero. Thus, our analysis is consistent with the discussion after equation (3.10), as well as with the previously mentioned results of [138].

Lastly, let us briefly mention a particularly interesting model that is contained within the present class of theories, namely the Inert Doublet Model (IDM) [141–143]. Here, the SM Higgs sector is supplemented by a second doublet $\chi \sim (\mathbf{1}, \mathbf{2}, \frac{1}{2})$, which transforms non-trivially under an exact $\mathbb{Z}_2$ symmetry and therefore does not acquire a finite vev. Notably, particle content and symmetries of the IDM allow for an additional operator in the

scalar potential of equation (3.10), namely

$$\Delta V_2 = \kappa_4 \Big[(\Phi^\dagger \chi)^2 + \text{h.c.} \Big] \,. \tag{3.31}$$

The IDM has received considerable attention during the last decade, since it is a simple and tractable extension of the SM, which was found to provide a viable dark matter candidate. Its conformal version was first studied in [103], however without addressing potential issues due to Landau poles in the model's RG running. Taking into account the complete set of RGEs including contributions from the term of equation (3.31), we found that the conformal IDM remains perturbative only up to scales of around $\Lambda_{\text{UV}} \simeq 10^5\,\text{GeV}$ and therefore does not offer a consistent realization of radiative EWSB.

D Complex multiplet with finite vacuum expectation value

Having already extensively studied extensions of the minimal SM by one extra *real* scalar multiplet with non-zero vev (cf. Section 3.3.1.B), the generalization to a *complex* scalar field χ is now straightforward. Assuming the absence of spontaneous CP violation for simplicity, we parameterize the electrically neutral component of χ as

$$\chi_{i_0} = \tfrac{1}{\sqrt{2}}(v_\chi + \sigma + \mathrm{i}\pi^0) \,, \tag{3.32}$$

where σ is an appropriate radial excitation, while π^0 is a neutral CP-odd field. Utilizing the Gell-Mann Nishijima formula introduced in Chapter 2, the index i_0 can be determined as $i_0 = (N+1)/2 + Y$, with N and Y being the extra multiplet's dimension and hypercharge, respectively. Obviously, only those representations which allow for an integer i_0 are viable. For the sake of convenience, let us furthermore introduce the following set of auxiliary quantities:

$$\begin{aligned} v'_\phi &:= v_\phi \,, \quad v'_\chi := v_\chi \,, \quad \lambda'_1 := \lambda_1 \,, \\ \lambda'_2 &:= \tfrac{1}{4}\left[\lambda_2 + (1-\delta_{N,1})Y^2\lambda_3\right] \,, \\ \kappa'_1 &:= \tfrac{1}{2}\left[\kappa_1 + \tfrac{1}{2}(1-\delta_{N,1})Y\kappa_2\right] \,, \quad \text{and} \\ \tan\beta' &:= \tfrac{1}{\sqrt{2}}\tan\beta \,. \end{aligned} \tag{3.33}$$

Restricting to the physics of the CP-even scalar sector, a dedicated calculation then reveals that the results obtained for a complex χ based on the potential of equation (3.10) are formally equivalent to those of the real case when written in the primed quantities. For instance, the Gildener-Weinberg condition corresponding to finite vevs for both Φ and χ now reads $4\lambda'_1\lambda'_2 - \kappa'^2_1 = 0$.[i] In the same way, equations (3.21) to (3.25) as well as the

[i] As an additional condition one finds $\kappa_3(\Lambda_{\text{GW}}) = 0$. Since κ_3 is multiplicatively renormalized, it necessarily vanishes at all scales, see Appendix B.

contents of Table 3.1 are reproduced using the auxiliary parameters of equation (3.33). In particular, we thus recover the mixing phenomenology of the real case, which was previously summarized in Table 3.1, and which was crucially influenced by the sign of the mixing angle $\alpha \in (-\pi/4, \pi/4)$.

A positive mixing angle, on the one hand, hence again requires $v_\chi > v_\phi$ and thereby a substantial vacuum expectation value in the χ-sector. Such a vev will generally contribute to the model's tree-level ρ-parameter introduced in equation (2.20) of Chapter 2, and will therefore spoil the well-established empirical finding $\rho \approx 1$ [53]. However, as mentioned before, the leading-order ρ-parameter will be identically one irrespective of the size of v_χ, if χ transforms under certain representations of the electroweak group (see e.g. [139]). Restricting to $N \leqslant 20$, there exist three such representations, namely the singlet with zero hypercharge, the doublet with $Y = \frac{1}{2}$ and the septet with $Y = 2$, which we will discuss in turn.

First, it is easy to prove that the theory of one *complex* hyperchargeless singlet is equivalent to that of two *real* singlets (see e.g. [140]), which will be covered in detail in Section 3.3.3.

The second case, $(\boldsymbol{N}, Y) = (\mathbf{2}, \frac{1}{2})$, corresponds to the well-studied two-Higgs-doublet model, which is comprehensively reviewed e.g. in [144]. Here, the extra scalar χ has the exact same quantum numbers as the SM Higgs (cf. equation (2.3)), which leads to a particularly rich phenomenology. However, without any additional assumptions, the model's particle content allows for Yukawa terms coupling all SM fermions to the second scalar field. Since both doublets are assumed to obtain a finite vev, this situation is incompatible with the Glashow-Weinberg criterion [145] and thus may lead to unacceptably large tree-level flavor-changing neutral currents (FCNC). Avoiding said FCNCs requires to either introduce additional new physics in the form of new particles, or to restrict the theory's Lagrangian by imposing extra symmetries, which then typically also act on the fermion sector. Both of the above options are, however, in conflict with our notion of minimality, so that the conformal two-Higgs-doublet model will not be discussed any further.

Finally, in the extension of the scale-invariant SM by a complex septet with $Y = 2$, the large multiplet dimension and hypercharge of the additional scalar field strongly enhance the RG flow of the $\mathrm{U}(1)_Y$ gauge coupling, cf. equation (B.6) in Appendix B. As a consequence, the latter develops a Landau pole already below the Planck scale, which rules out the septet model as well. Since all possible representations with $N > 20$ which also leave the ρ-parameter invariant are plagued by an even larger RG flow of the hypercharge gauge coupling, this already exhausts all options for $\alpha > 0$.

A negative scalar mixing angle α, on the other hand, implies $v_\phi > v_\chi$. Assuming that v_χ is sufficiently small, the leading-order SM relation $\rho = 1$ can then be approximately reproduced regardless of the representation under which χ transforms. Nevertheless, we do not expect to find a model

without low-scale Landau poles within the present class of conformal SM extensions either. To see why, let us first recall from Table 3.1 that a negative α requires the physical Higgs boson H to be identified with the PGB of broken scale invariance, whose mass is only generated through quantum effects as shown in Section 3.2. In particular, implementing the necessary relation $m_{\text{PGB}} = 125\,\text{GeV}$ then demands the presence of relatively heavy scalar degrees of freedom whose contributions to m_{PGB} are large enough so as to outweigh those originating from top quark fluctuations. Also the aforementioned loop suppression has to be overcome.

Now, let us furthermore recall that the potential in the real case exhibited a global $\text{O}(N)$ symmetry (cf. equation (3.13)), which was spontaneously broken down to $\text{O}(N-1)$ during electroweak symmetry breaking. Correspondingly, only the radial excitation σ acquired a finite mass, whereas all other degrees of freedom in χ remained massless according to Goldstone's theorem. Consequently, the above requirement of large scalar fluctuations contributing to the Higgs mass could only be realized at the price of a sizable scalar portal coupling (cf. equation (3.27)), which, in turn, severely destabilized the RG flow.

As opposed to that, the $\text{O}(2N)$ symmetry of the χ-sector in the complex case[j] is no longer exact, but is rather explicitly violated by the λ_3- and κ_2-terms in the potential of equation (3.10). Accordingly, not only will the electrically neutral, CP-even mode of a complex χ become massive upon EWSB, but so will the CP-odd field as well as the formerly massless charged components χ_i with $i \neq i_0$. One may thus naively think that the required Higgs mass can now be generated without the need for large scalar couplings. Importantly though, Goldstone's theorem also implies that the masses of the CP-odd excitation and of the electrically charged modes of χ must necessarily be proportional to the coefficients of the $\text{O}(2N)$-breaking operators, namely λ_3 and κ_2. Our previous analysis of the complex case with *vanishing* v_χ, revealed, however, that said couplings are to be chosen close to zero, in order to facilitate a reasonably stable RG evolution. Taking into account that the theory's RG evolution is independent of whether or not χ obtains a non-zero vev, we expect the above result to also pertain to the present scenario. Thus, the $\text{O}(2N)$ symmetry of the potential is approximately restored and the line of reasoning from the real case can be applied, which suggests that a low-scale Landau pole will appear well below the Planck scale.

Apart from the symmetry-based argument just discussed, we can also use the findings from our previous analyses to argue that the present class of models is unlikely to provide a viable candidate for a consistent conformal theory. Specifically, comparing the outcome obtained for the real (Figure 3.2a) and complex (Figure 3.4) cases with vanishing vev, we realize that

[j] Confer footnote h on page 43.

they are very similar both from a qualitative and from a quantitative point of view. Analogously, we do not expect a drastic change when going from a real multiplet χ with $v_\chi \neq 0$ and negative mixing angle to its complex counterpart. A dedicated analysis of the latter is therefore anticipated to yield similar results to those displayed in Figure 3.3, simply generalized to the N-Y plane.

3.3.2 SM + one scalar and one fermionic representation

After having exhausted all possibilities of models where the SM Higgs sector is supplemented by only one scalar multiplet, let us briefly discuss the option of extending these theories by an additional *fermionic* representation. However, one immediately realizes that also the resulting class of models cannot remedy the issues described in the previous section. Rather, extra massive fermions coupling to the scalar sector will induce a two-fold destabilization of the resulting model's RG evolution.

On the one hand, said fermionic particles will give negative contributions to the effective potential's curvature along its leading-order flat direction as per equation (3.6b). Requiring a stable vacuum therefore typically necessitates heavier scalar degrees of freedom and thus larger scalar couplings at Λ_{GW} than in the same model without additional fermions.

On the other hand, a fermion which interacts with some scalar field with Yukawa coupling strength y, will amplify the RG flow of said scalar's self-coupling λ via a positive contribution which grows as $+\lambda y^2$. Admittedly, the beta function of λ will then also contain an additional negative term proportional to $-y^4$, but in the regime of large scalar couplings the $+\lambda y^2$ term will always be the dominant one. The situation may be even worse for the RG flow of the associated scalar portal couplings where the stabilizing $-y^4$ contribution is only present if both of the involved scalars interact with the extra fermion.

In summary, we conclude that if a given conformal model produces Landau poles well below the Planck scale, then augmenting said model by additional fermions cannot change this outcome. In particular, the simple and hence popular theory studied in [34], in which the classically scale-invariant SM is extended by a real scalar singlet and right-handed sterile neutrinos cannot be perturbatively extrapolated all the way up to the Planck scale.[k]

3.3.3 SM + two scalar representations

Completely analogous to our discussion of Section 3.3.1, we will now investigate theories where the minimal Standard Model's Higgs sector is supplemented by two scalar SU(2) multiplets denoted as χ and ξ. The scale- and

[k] The authors of [34] arrive at a different conclusion since they neglect the aforementioned destabilizing contributions to the scalar RG flow which grow as $+\lambda y^2$.

gauge-invariant leading-order potential on which our analyses in the present section will rely reads

$$\begin{aligned} V = {} & \lambda_\phi (\Phi^\dagger \Phi)^2 + \lambda_\chi (\chi^\dagger \chi)^2 + \lambda_\xi (\xi^\dagger \xi)^2 \\ & + \kappa_{\phi\chi} (\Phi^\dagger \Phi)(\chi^\dagger \chi) + \kappa_{\phi\chi} (\Phi^\dagger \Phi)(\xi^\dagger \xi) + \kappa_{\chi\xi} (\chi^\dagger \chi)(\xi^\dagger \xi) \ , \end{aligned} \tag{3.34}$$

where $\Phi = (\phi^+, \phi^0)^\intercal$ is again the complex SM Higgs doublet introduced in equation (2.3). Note that in writing down the above potential, we restrict ourselves to those terms which are present irrespective of the involved multiplets' quantum numbers. As we have argued several times before and as we have explicitly seen during our previous studies, the inclusion of additional operators for individual models is not expected to qualitatively change our results, since the associated couplings must be small in order to allow for a stable RG evolution [138].

A Two real multiplets with vanishing vacuum expectation value

In a first step, we assume both of the extra scalars to be real in the sense of equation (3.12). Furthermore, their vacuum expectation values are supposed to vanish. The resulting study is then a simple generalization of that presented in Section 3.3.1.A. In particular, electroweak symmetry breaking proceeds via $\phi^0 = (v + H)/\sqrt{2}$ and the physical Higgs mode H is to be identified with the PGB of anomalously broken scale invariance. The associated Gildener-Weinberg condition is again $\lambda_\phi(\Lambda_{\text{GW}}) = 0$, which signifies a flat direction of the tree-level potential along the ϕ^0-axis at Λ_{GW}. Upon EWSB all components of a given real multiplet then obtain the same leading-order mass, namely

$$m_\chi^2 = \kappa_{\phi\chi} v^2 \quad \text{or} \quad m_\xi^2 = \kappa_{\phi\xi} v^2 \ . \tag{3.35}$$

In contrast, the Higgs boson remains classically massless, but acquires a finite mass via quantum effects at the one-loop level. Its exact form is given by equation (3.8). Evaluating the latter using the results of equation (3.35) yields

$$m_H^2 = 4 \left(B_{\text{SM}} + \frac{N_\chi \kappa_{\phi\chi}^2 + N_\xi \kappa_{\phi\xi}^2}{16\pi^2} \right) v^2 \ . \tag{3.36}$$

Once more exploiting that B_{SM} is negative, we recast the above identity into

$$\sqrt{N_\chi \kappa_{\phi\chi}^2 + N_\xi \kappa_{\phi\xi}^2} > 2\pi \frac{m_H}{v} \ ,$$

where the portal couplings are to be understood as evaluated at Λ_{GW}. As before, we are only interested in assessing an upper bound on the scale of potential Landau poles. Correspondingly, we can simplify the previous

relation by replacing the inequality with an equality. Thereby, the portal couplings' initial values are underestimated so that the RG evolution is expected to become more stable and potential Landau poles are shifted towards larger energy scales. In the approximation just described the value of e.g. $\kappa_{\phi\xi}$ at Λ_{GW} can be calculated in terms of the multiplet dimensions and the other parameter involved, $\kappa_{\phi\chi}(\Lambda_{\mathrm{GW}})$, namely

$$\kappa_{\phi\xi}(\Lambda_{\mathrm{GW}}) := \sqrt{4\pi^2 \frac{m_H^2}{v^2} - N_\chi \kappa_{\phi\chi}^2} \cdot N_\xi^{-1/2} \,. \tag{3.37}$$

Notably, requiring all physical masses to be real, confines both portal couplings $\kappa_{\phi\chi}$ and $\kappa_{\phi\xi}$ to be non-negative at Λ_{GW} according to equation (3.35).

Apart from λ_ϕ and $\kappa_{\phi\xi}$ whose initial values are set by the Gildener-Weinberg condition and equation (3.37), respectively, all other parameters at Λ_{GW} are varied in the perturbative range. In doing so, we bear in mind that λ_χ, λ_ξ and $\kappa_{\phi\chi}$ must be non-negative due to vacuum stability and equation (3.35), respectively. In contrast, there is no a priori constraint on the sign of $\kappa_{\chi\xi}$. Lastly, fixing $\Lambda_{\mathrm{GW}} = 500\,\mathrm{GeV}$ as before, completes the initial conditions for the model's RG evolution towards the UV.

Results and discussion. Our findings for the maximum possible scale of RG extrapolation Λ_{UV} in the present category of models are displayed in Figure 3.5. In complete analogy to our analyses in Section 3.3.1, the four panels of Figure 3.5 show the UV scale as a function of the multiplet dimensions N_χ and N_ξ, calculated using distinct sets of RGEs from Appendix B.1. Notably, all plots exhibit a reflection symmetry with respect to the diagonal in the N_χ-N_ξ plane, which originates from the fact that the models' RG flows are fully invariant under the exchange $N_\chi \leftrightarrow N_\xi$.

From a qualitative point of view, the current results can be seen as a simple generalization of those obtained for one extra real and vev-less scalar, so that they are expected to show similar characteristics (cf. Figure 3.2a). For instance, by comparing the left panels of Figures 3.5a and 3.5b with the respective ones on the right-hand side, we observe that including fermionic contributions due to the top quark consistently shifts Landau poles towards lower energies. Similarly, taking into account gauge contributions is again found to induce a rapid decrease of Λ_{UV} once the SU(2) gauge coupling g_2 stops being asymptotically free.

A quantitative evaluation of the results now reveals that the farthest extrapolation is achieved in the SM extension by two real quintets, which remains perturbative up to around $10^8\,\mathrm{GeV}$. Although the aforementioned maximum possible UV scale is still far away from the Planck scale, it is one order of magnitude larger than its counterpart in the case of only one extra real scalar. This observation can be understood as follows: The introduction of a third scalar representation induces several structurally new terms in

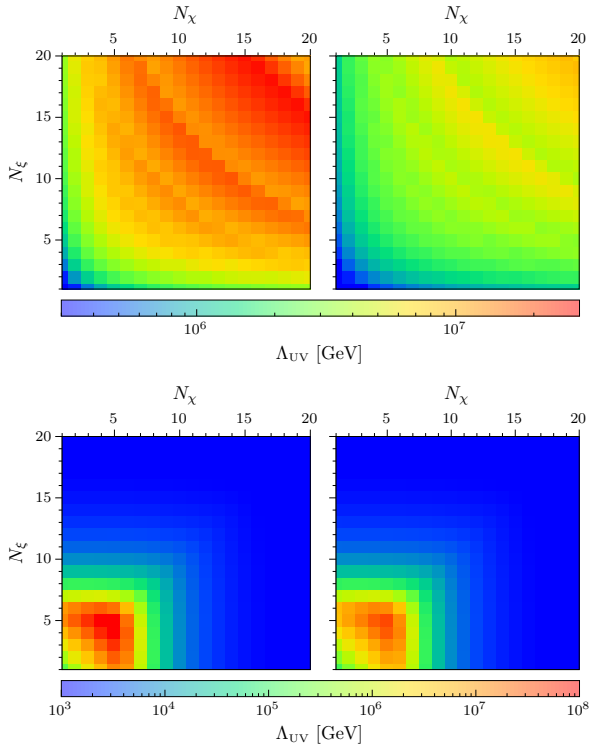

(a) Results were obtained taking into account scalar contributions only (*left*) or scalar and top-quark contributions (*right*), respectively.

(b) Results were obtained taking into account scalar and SM gauge boson contributions (*left*) or using the full one-loop RGEs (*right*), respectively.

Figure 3.5: Maximum possible scale of RG extrapolation Λ_{UV} in extensions of the scale-invariant SM by two real $\mathrm{SU}(2)_L$ multiplets of dimensions N_χ and N_ξ with zero vev. The individual plots differ in the contributions to the model's RGEs that were included.

the models' RG flows. Most importantly, the Higgs portal couplings obtain additional contributions, namely

$$\beta^{(1)}_{\kappa_{\phi\chi}} \supseteq +4N_\xi \kappa_{\phi\xi}\kappa_{\chi\xi} \quad \text{and} \quad \beta^{(1)}_{\kappa_{\phi\xi}} \supseteq +4N_\chi \kappa_{\phi\chi}\kappa_{\chi\xi} \,. \tag{3.38}$$

Recall that, while $\kappa_{\phi\chi}$ and $\kappa_{\phi\xi}$ must be positive at the GW scale, the sign of $\kappa_{\chi\xi}$ is a priori unconstrained. Choosing $\kappa_{\chi\xi}(\Lambda_{\mathrm{GW}})$ to be less than zero then introduces negative terms in the beta functions of all portal couplings, which may (partially) compensate for the other positive contributions from the scalar sector. Thus, the terms of equation (3.38) may to some extent prevent too large flows of the scalar couplings, which were found to be the main source of instabilities in models with only one extra scalar (cf. Figure 3.2b and the associated discussion). Accordingly, Landau poles are shifted towards higher energies. Completely in line with the above reasoning, the most stable RG running was found for negative and often sizable initial values of $\kappa_{\chi\xi}$.

Although cancellations are now possible within the scalar subsystem, the initial portal couplings required by the consistency condition of equation (3.36) are still too large to fully avoid the appearance of Landau poles.

B The minimal conformal model

All of our previous attempts of finding a phenomenologically consistent model of radiative electroweak symmetry breaking, which can be perturbatively extrapolated all the way up to the Planck scale, failed. The main obstacles in most of the investigated theories was found to be an unstable subsystem of scalar RGEs, in which positive feedback unavoidably leads to the appearance of low-scale Landau poles. Interestingly, our analysis of the last section demonstrated that in models with three scalar representations, the presence of phenomenologically less constrained portal couplings may stabilize the scalar subsystem to some extent. However, consistently reproducing the measured Higgs mass required too large initial values for some of the scalar couplings, so that the aforementioned stabilizing effects were insufficient to prevent Landau poles from developing.

Learning from this, we will now study theories which still extend the SM Higgs sector by two real scalar multiplets, but in which one of the extra scalars dynamically acquires a finite vacuum expectation value. In fact, it turns out that we can restrict ourselves to the simplest case, where both of the additional scalars are gauge singlets, since already this model allows for an perturbative extrapolation all the way up to the Planck scale. The most general gauge- and scale-invariant leading order potential then reads

$$\begin{aligned} V = {} & \lambda_\phi(\Phi^\dagger\Phi)^2 + \lambda_S S^4 + \lambda_R R^4 \\ & + \kappa_{\phi S}(\Phi^\dagger\Phi)S^2 + \kappa_{\phi R}(\Phi^\dagger\Phi)R^2 + \kappa_{SR}S^2R^2 \\ & + \kappa_4 SR(\Phi^\dagger\Phi)^2 + \kappa_5 S^3 R + \kappa_6 S R^3 \,. \end{aligned} \tag{3.39}$$

with the complex SM Higgs doublet Φ and the real scalar singlets S and R. For the purpose of reducing the number of free parameters, we introduce a global $\mathbb{Z}_2$ parity under which one of the singlets, say R, is odd,

$$R \xrightarrow{\mathbb{Z}_2} -R \,, \tag{3.40}$$

whereas all other fields are supposed to be left invariant. Assuming that said $\mathbb{Z}_2$ symmetry remains unbroken has two immediate consequences. On the one hand, all terms in the third line of equation (3.39) transform non-trivially under the operation of equation (3.40) and are thus forbidden. On the other hand, an exact $\mathbb{Z}_2$ parity prevents R from acquiring a finite vev. The pattern of electroweak symmetry breaking to be considered here is

$$\phi^0 = \frac{v_\phi + \phi}{\sqrt{2}} \quad \text{and} \quad S = v_S + \sigma \,. \tag{3.41}$$

Since S is a gauge singlet, the electroweak scale v is then only set by the Higgs vev, i.e. $v \equiv v_\phi$. Note that, interestingly, the resulting model is formally equivalent to the extension of the classically scale-invariant SM by

one complex singlet with zero hypercharge which acquires a finite, but CP-conserving vev. The aforementioned model was discussed in different contexts in the literature, see e.g. [107, 109–111].

As opposed to S, the second extra scalar R is does not develop a non-zero vev and therefore does not mix with the other CP-even scalar degrees of freedom ϕ and σ. Rather, an explicit calculation based on equations (3.39) and (3.41) implies that R obtains the following tree-level mass

$$m_R^2 = \kappa_{\phi R} v_\phi^2 + 2\kappa_{SR} v_S^2 \,. \tag{3.42}$$

In contrast, the scalar modes ϕ and σ do mix. The resulting phenomenology turns out to be identical to that described in Section 3.3.1.B, where there was only one extra real scalar added to the SM. Correspondingly, upon renaming the relevant parameters,

$$\begin{aligned} \lambda_1 &\to \lambda_\phi \,, \quad & \lambda_2 &\to \lambda_S \,, \\ \kappa_1 &\to \kappa_{\phi S} \,, \quad & v_\chi &\to v_S \,, \end{aligned} \tag{3.43}$$

all identities derived there – see equations (3.19) to (3.25) – also apply to the ϕ-σ-sector of the present model. In particular, the sign of the ϕ-σ mixing angle α again crucially influences the theory's properties at the electroweak scale (cf. Table 3.1).

In the following, we restrict ourselves to the case of positive α. According to our listing in Table 3.1, the physical Higgs boson H is then not identified with the PGB of anomalously broken scale invariance, but rather obtains its mass already at tree-level. Before we continue, let us briefly recall, why we ruled out this scenario's counterpart in Section 3.3.1.B, where the second extra scalar R was absent. In the corresponding discussion on pages 39–40, we argued that the Higgs alone was not heavy enough to overcome the large negative top quark contribution to the curvature of the effective potential. The latter therefore developed a maximum instead of a minimum, which is clearly unacceptable. In contrast, the presence of the additional scalar particle R in the current theory's physical spectrum invalidates the above line of reasoning, since now also R gives a positive contribution to the effective potential's curvature. Hence, if R is sufficiently heavy, the theory can, indeed, dynamically acquire a stable non-trivial vacuum.

That being said, let us now study what parameters of the potential in equation (3.39) are constrained by basic electroweak phenomenology. First, stability of the tree-level potential requires [146]

$$\begin{gathered} \lambda_\phi \geqslant 0 \,, \quad \lambda_S \geqslant 0 \,, \quad \lambda_R \geqslant 0 \,, \\ \bar{\sigma}_{\phi S} := \kappa_{\phi S} + 2\sqrt{\lambda_\phi \lambda_S} \;\geqslant 0 \,, \\ \bar{\sigma}_{\phi R} := \kappa_{\phi R} + 2\sqrt{\lambda_\phi \lambda_R} \geqslant 0 \,, \\ \bar{\sigma}_{SR} := \kappa_{SR} + 2\sqrt{\lambda_S \lambda_R} \geqslant 0 \,, \\ \kappa_{\phi S}\sqrt{\lambda_R} + \kappa_{\phi R}\sqrt{\lambda_S} + \kappa_{SR}\sqrt{\lambda_\phi} + 2\sqrt{\lambda_\phi \lambda_S \lambda_R} + \sqrt{\bar{\sigma}_{\phi S}\bar{\sigma}_{\phi R}\bar{\sigma}_{SR}} \geqslant 0 \,. \end{gathered}$$

Second, the adopted symmetry breaking pattern of equation (3.41) implies a negative portal coupling $\kappa_{\phi S}$ (cf. equation (3.20) and the associated discussion). On a related note, within the framework of the Gildener-Weinberg formalism the assumed vev configuration is equivalent to the previously derived condition of equation (3.20). As before, the latter can be used to eliminate one dimensionless coupling in favor of the scale of radiative symmetry breaking Λ_{GW}, specifically

$$\lambda_S = \frac{\kappa_{\phi S}^2}{4\lambda_\phi} \quad \text{at } \Lambda_{\text{GW}} \,. \tag{3.44}$$

Second, as already mentioned above, the leading-order mass of the physical Higgs boson H is parameterized as m_+ from equation (3.24),

$$m_H^2 = 2(\lambda_\phi - \kappa_{\phi S})v^2 \quad \Leftrightarrow \quad \lambda_\phi = \kappa_{\phi S} + \frac{m_H^2}{2v^2} \quad \text{at } \Lambda_{\text{GW}} \,. \tag{3.45}$$

For a given portal coupling, the second identity allows us to calculate the corresponding value of λ_ϕ which is consistent with the physical point of the ratio m_H/v. Furthermore, equation (3.45) together with equation (3.21) and the information from Table 3.1 can be used to obtain a one-to-one relation between $\kappa_{\phi S}$ and the scalar mixing angle $\alpha > 0$, namely

$$\sin\alpha = \sqrt{2|\kappa_{\phi S}|}\frac{v}{m_H} \,. \tag{3.46}$$

Finally, note that while imposing equation (3.45) guarantees the ratio m_H/v to attain its physical value, the overall scale of v (or m_H) must still be set consistently. It is now straightforward to show that fixing v and, for instance, the PGB mass m_{PGB}, one can determine the unique value of the Gildener-Weinberg scale Λ_{GW}, as well as that of the heavy scalar mass m_R, for which the theory correctly reproduces the electroweak scale. Since the corresponding calculation is quite technical, it has been relegated to Appendix A.

Summarizing, the model's relevant phenomenology at Λ_{GW} is fully specified once the scalar mixing angle $\alpha \in (0, \pi/4)$ and the PGB mass are fixed. Uniquely solving the model's complete one-loop RGEs for the purpose of searching for potential Landau poles additionally requires to choose initial values for λ_R and for one of the two remaining portal couplings $\kappa_{\phi R}$ or κ_{SR} (the other one then being fixed by equation (3.42)).

Results and discussion. The main findings of our analysis of the minimal conformal model are presented in Figure 3.6. However, before we explicitly evaluate the information displayed there, it makes sense to first review the meanings of the plot's individual components. As mentioned before, fixing the scalar mixing angle α together with the PGB mass m_{PGB}

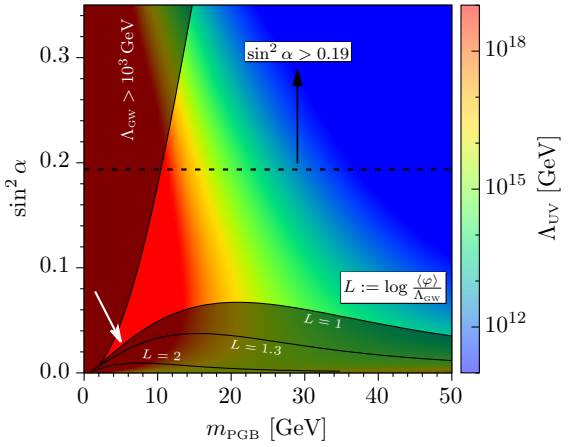

Figure 3.6: Maximum possible scale of RG extrapolation $\Lambda_{\rm UV}$ in the minimal conformal model. The white arrow indicates the benchmark point of equation (3.47). For details on the included constraints, see the main text on the next page.

completely specifies the model's relevant phenomenology at the Gildener-Weinberg scale. In particular, the couplings of the Φ-S-sector λ_S, λ_ϕ and $\kappa_{\phi S}$ are then given by equations (3.44), (3.45) and (3.46), respectively. Similarly, the heavy scalar's mass m_R can be fixed by self-consistently solving equations (A.5) and (A.6) as described in the Appendix. As a consequence, it is most convenient to investigate the subspace of the model's full parameter space that is spanned by $m_{\rm PGB}$ and $\sin^2\alpha$, which is exactly what we do in Figure 3.6.

Next, the color code represents the maximum possible scale of RG extrapolation $\Lambda_{\rm UV}$, which is computed as follows: For a given pair $(m_{\rm PGB}, \alpha)$, we vary the remaining free couplings, λ_R and κ_{SR}, within the perturbative regime. For each individual point of said parameter scan, we then use the complete set of one-loop beta functions to calculate all couplings' RG running towards the UV, thereby determining the model's UV cutoff corresponding to the currently considered parameter point. The aforementioned UV cutoff is defined as the energy scale up to which the model's RG evolution is free of any Landau poles or tree-level vacuum instabilities. Additionally, we check whether the leading-order scalar potential develops any further flat directions at some scale Λ' above $\Lambda_{\rm GW}$. If so, the effective potential would have developed a non-trivial vacuum at Λ', so that dynamical symmetry breaking would have already occurred then. Since this would invalidate our initial assumption that $\Lambda_{\rm GW}$ is the scale of radiative EWSB, we also stop the RG running once a flat direction is found and set the UV cutoff accordingly. The largest UV cutoff found in the way just described is then identified with $\Lambda_{\rm UV}$ for the given values of $m_{\rm PGB}$ and α. Note that it is not meaningful in the current approach to extrapolate the model's parameters beyond the Planck scale. Hence, we stop our calculation there at the latest so that $\Lambda_{\rm UV} \leqslant M_{\rm Pl}$

always holds.

Lastly, Figure 3.6 shows some relevant constraints on the model's parameter space. On the one hand, the dark shaded areas are disfavored for different reasons of theoretical consistency: First, in line with our working assumption that radiative symmetry breaking occurs at around the electroweak scale, we discard points for which the Gildener-Weinberg scale is too large, specifically $\Lambda_{\mathrm{GW}} > 1\,\mathrm{TeV}$ (cf. assumption 2 on page 22). Second, parts of the parameter space where there is a substantial hierarchy between the renormalization scale Λ_{GW} and the condensate $\langle\varphi\rangle$ are possibly problematic. To see why, note that the effective potential's perturbative expansion is only reliable as long as the appropriate expansion parameter $\lambda/(2\pi)\cdot\log(\langle\varphi\rangle/\Lambda_{\mathrm{GW}})$ is sufficiently small, where λ is some generic and properly normalized scalar coupling [147] (cf. also the corresponding discussion in [120]). Consequently, more care must be taken in order to determine whether perturbation theory is still applicable, once the above logarithm is larger than unity.

On the other hand, we also include a generic experimental bound on the mixing angle between the physical Higgs boson and the PGB of a classically scale-invariant model, which was derived in [109, 110]. Here, the authors used the fact that too large a mixing would modify the signal strengths of Higgs events beyond what is compatible with measurements at the LHC. The found limit of $\sin^2\alpha < 0.19$ is independent of the PGB mass and is shown as horizontal dashed line in Figure 3.6.

The most important feature of the plot in Figure 3.6 is now the existence of a parameter region (red area), where a fully consistent extrapolation of the model all the way up to the Planck scale is possible. Interestingly, imposing UV completeness in the above sense only allows for PGB masses of up to around 15 GeV and requires the mixing angle to be relatively small.

Now that we have learned that the current set-up provides parameter points, for which Landau poles below the Planck scale are absent, it is instructive to investigate how the RG running is actually stabilized in those cases. Thereby, one will be able to specifically construct non-minimal conformal models, which may then accommodate further aspects of BSM physics as, for instance, neutrino masses or dark matter, and will thus yield a more complete picture of particle physics. With this in mind, we will follow our approach from Section 3.3.1 and study the different contributions to the flow of the Higgs self-coupling as functions of the RG scale. The corresponding results are shown in Figure 3.7a and were calculated based on the benchmark point indicated by the white arrow in Figure 3.6, namely

$$m_{\mathrm{PGB}} = 5\,\mathrm{GeV}\,, \quad \sin\alpha = 0.16\,, \tag{3.47}$$

supplemented by the choices $\lambda_R = 0.015$ and $\kappa_{SR} = 0.021$, which, indeed, allow for an extrapolation of the model up to the Planck scale. Further details on the above example point are listed in Figure 3.7b.

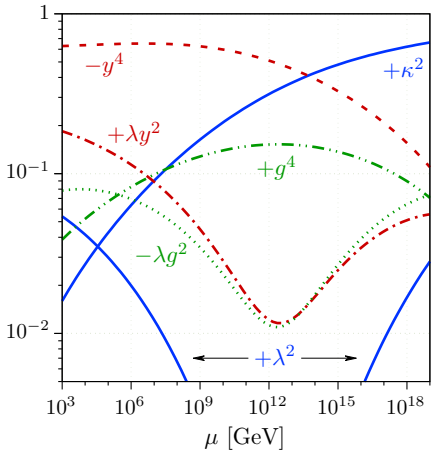

(a)

quantity	value at Λ_{GW}
m_{PGB}	5 GeV
$\sin\alpha$	$1.6 \cdot 10^{-1}$
λ_R	$1.5 \cdot 10^{-2}$
κ_{SR}	$2.1 \cdot 10^{-2}$
m_R	327 GeV
Λ_{GW}	585 GeV
$\langle\varphi\rangle$	1506 GeV

(b)

Figure 3.7: Scale dependence of the *relative* contributions to the beta function of λ_ϕ in the minimal conformal model (panel (a)) for the benchmark point of equation (3.47), on which additional information is provided in panel (b). For further details, see also the caption of Figure 3.2b.

The key difference between the current scenario and the running displayed in Figure 3.2b is that the scalar portal contribution is no longer the largest one over the whole energy range. Instead, the stabilizing $-y^4$ term due to the top-quark loop dominates for energies up to $10^{14}\,\text{GeV}$, so that the Higgs self-coupling first decreases. It does so, however, without ever becoming negative. At large enough scales, the Yukawa contribution is then finally exceeded by the positive portal terms. The latter will therefore ultimately trigger the appearance of a Landau pole in the running of λ_ϕ, but, as our analysis demonstrates, only at energies beyond the Planck scale.

The theory's improved extensibility towards the UV can be mainly ascribed to two features of its portal couplings and their RG running. Interestingly, both of the aforementioned features originate from the presence of more than two independent scalar multiplets in the model's Higgs sector. First and foremost, imposing a positive curvature of the effective potential along its leading-order flat direction no longer necessitates one single scalar coupling to be particularly large at the Gildener-Weinberg scale. To be more precise, Figure 3.6 together with equation (3.46) reveals that the parameter $\kappa_{\phi S}$ at Λ_{GW} is preferably of order 10^{-2} or smaller in the minimal conformal model. Also the other portal couplings, $\kappa_{\phi R}$ and κ_{SR}, can attain initial values of moderate size without rendering the model's electroweak phenomenology inconsistent. In contrast, at least one of the portal couplings in previously investigated theories with only one extra scalar was typically required to be of order unity, see e.g. equations (3.16) and (3.27). Similarly, sizable portal couplings $\kappa_{\phi\chi}$ or $\kappa_{\phi\xi}$ were implied in the case of

two additional vev-less scalars, since the relatively heavy physical Higgs boson had to be identified with the PGB, see equation (3.36). In the present model, the latter constraint is removed so that lower PGB masses and hence smaller scalar couplings are possible.

The second reason for the more stable RG evolution of the scalar subsystem in the minimal conformal model originates in the potentially stabilizing terms already mentioned in equation (3.38) (cf. also the associated discussion on page 52). As all scalar couplings can now be of the same order of magnitude, different contributions to the portal couplings' beta functions may effectively cancel each other. Said cancellations will then help to keep the RG flow in the scalar subsystem small and under control.

C Non-minimal conformal models

After having gained insight into how a stable RG evolution could be realized within the minimal conformal model (MCM), we will now briefly discuss some possibilities to extend the latter in order to eventually build more complete theories of particle physics.

As a first example of a consistent and non-minimal conformal model, we consider the theory which is obtained by exchanging the second singlet R of the MCM for a real, vev-less scalar $\mathrm{SU}(2)_L$ triplet Σ (henceforth referred to as CSMTS). The corresponding scale- and gauge-invariant scalar potential can then be written as

$$\begin{aligned} V = {} & \lambda_\phi (\Phi^\dagger \Phi)^2 + \lambda_S S^4 + \lambda_\Sigma (\operatorname{Tr} \Sigma^2)^2 \\ & + \kappa_{\phi S} (\Phi^\dagger \Phi) S^2 + \kappa_{\phi \Sigma} (\Phi^\dagger \Phi) \operatorname{Tr} \Sigma^2 + \kappa_{S\Sigma} S^2 \operatorname{Tr} \Sigma^2 \,, \end{aligned}$$

where we imposed a global O(3) symmetry in the triplet sector as a generalization of the minimal conformal model's $\mathbb{Z}_2$ parity introduced in equation (3.40). Repeating our complete analysis from before, we are able to determine the model's UV extensibility which is shown in Figure 3.8. Interestingly, the present triplet model allows for larger PGB masses of up to roughly 35 GeV, while still providing a stable renormalization group running all the way up to the Planck scale. This extended range of possible PGB masses can be explained as follows: As compared to the MCM, the particle spectrum of the CSMTS after radiative symmetry breaking contains two additional heavy bosonic degrees of freedom, $\Sigma^\pm$. According to equations (3.8) and (3.6b), a given value for m_{PGB} can then be realized for smaller initial values of the scalar couplings. Potential Landau poles will therefore appear at larger scales than in the MCM.

Remarkably, models like the MCM or the CSMTS are of peculiar interest since they provide an electrically neutral and stable particle, which might provide the cold dark matter of the universe. Correspondingly, studies of the minimal conformal model's dark matter phenomenology indicate that

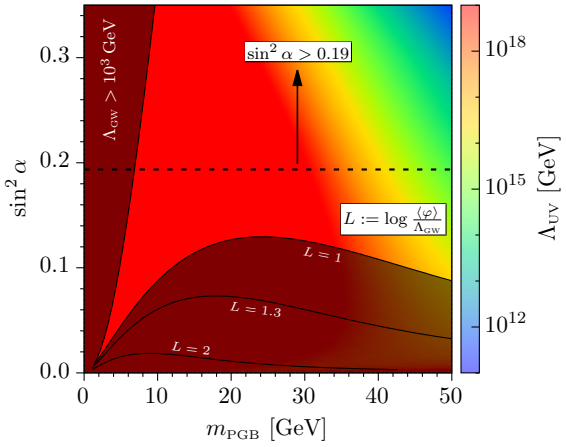

Figure 3.8: Maximum possible scale of RG extrapolation $\Lambda_{\rm UV}$ in the CSMTS. For details on the included constraints, see the main text on page 57.

there exist regions of parameter space where the scalar mode R correctly reproduces the observed dark matter relic abundance if thermally produced [107, 109–111]. A similar analysis does not yet exist for the CSMTS. Note that the dark matter candidates' stability in the aforementioned examples had to be enforced by introducing an ad hoc global symmetry. In contrast, the required stability is guaranteed by an accidental symmetry once the potential dark matter particle originates from a real $\mathrm{SU}(2)_L$ septet [148, 149]. The latter theory is therefore a particularly well motivated extension of the SM. In line with our previous analyses, we expect it to support a fully consistent conformal realization, as well.

As a second class of non-minimal conformal theories, extensions of the MCM that allow for the inclusion of finite neutrino masses certainly are also worth exploring (see [113] for an overview). For instance, supplementing the MCM by fermionic gauge singlets to be identified with right-handed neutrino fields immediately introduces two additional terms in the model's gauge- and scale-invariant Lagrangian, through which the right-handed neutrinos interact with some of the remaining particles: a Majorana-type Yukawa coupling to the scalar singlet S, as well as a Dirac-type Yukawa operator involving the SM lepton and Higgs doublets. Once radiative symmetry breaking occurs, the aforementioned Yukawa terms induce a neutrino mass matrix, which realizes a type-I seesaw mechanism [150–153], provided the associated Yukawa coupling parameters are chosen appropriately [113]. In particular, the smallness of active neutrino masses implies reasonably heavy right-handed neutrinos within the type-I seesaw scenario. Due to their fermionic nature the right-handed neutrinos give substantial negative contributions to the effective potential's curvature as per equation (3.6b). Requiring the effective potential to be bounded from below therefore typically necessitates larger

scalar masses as compared to the MCM, which may, in turn, destabilize the scalar RG subsystem. Alternatively, additional bosonic degrees of freedom may be introduced in order to outweigh the negative contributions due to the right-handed neutrinos without having to resort to larger scalar masses. Also more elaborate mechanisms of neutrino mass generation may be realized in a classically scale-invariant setup. Good examples are given by the conformal inverse see-saw, which was investigated in [115, 116], and radiative neutrino mass models as studied in [117, 118]. Crucially, determining whether any of the aforementioned models allows for a consistent perturbative extrapolation all the way up to the Planck scale has exploited or will exploit methods and results presented in this chapter.

3.4 Summary and conclusion

In the present chapter, we systematically studied simple classically conformal extensions of the minimal Standard Model (SM), thereby following our original analysis in [48]. In doing so, we assumed that the spontaneous breaking of scale invariance is triggered by perturbative effects in a Coleman-Weinberg-like scenario at energies around the electroweak scale. Since, furthermore, all of the investigated models were based on the SM gauge group, radiative symmetry breaking consistent with electroweak phenomenology was seen to require the introduction of additional heavy scalar degrees of freedom, which, in turn, necessitated the presence of sizable scalar couplings. A further vital consistency condition was argued to be the absence of any intermediate physical scales between that of spontaneous conformal symmetry breaking and some high-energy scale, at which new concepts beyond those of quantum field theory (QFT) may lead to boundary conditions appropriate for a classically scale-invariant model at lower energies. Only thus can conformal models protect the Higgs mass from becoming quadratically sensitive to UV physics and thereby solve the longstanding electroweak hierarchy problem as first suggested in [32]. A prime candidate for the aforementioned high-energy scale is the Planck scale M_{Pl}, where effects due to quantum gravity are expected to become relevant. As a consequence, all investigated models were required to exhibit a stable renormalization group (RG) running all the way up to M_{Pl}, which, however, typically needs small scalar couplings.

The main result of the present chapter is the identification of the minimal conformal model for which the opposing tendencies just described can be successfully reconciled. Specifically, said minimal theory was shown to extend the SM by two real scalar gauge singlets, precisely one of which acquires a finite vacuum expectation value (vev) of the same order of magnitude as the electroweak scale. The aforementioned scalar field then mixes with the neutral CP-even component of the SM Higgs doublet to form the

physical 125 GeV Higgs boson as well as a light scalar particle with a mass of preferably $\mathcal{O}(10\,\text{GeV})$ or less. The latter was identified with the pseudo-Goldstone boson associated with broken scale invariance. The extra vev-less scalar, on the other hand, was found to be necessarily heavier than 300 GeV in accordance with our expectations. In a detailed analysis of the model's one-loop effective potential and its RG equations, it was then proven that the presence of three independent scalar field representations together with the second finite vev was essential for controlling the scalar couplings' size at the scale of spontaneous conformal symmetry breaking and thereby for a stable RG evolution.

As a byproduct, our systematic study of conformal models explicitly ruled out popular scale-invariant extensions of the SM like the original model by Meissner and Nicolai in which the SM is supplemented by one scalar singlet field and right-handed neutrinos [34], or the classically conformal version of the Inert Doublet Model [103].

Obviously, the minimal model does not address all of the issues of beyond-the-SM physics such as small neutrino masses. Therefore, we finally had a glimpse at non-minimal consistent conformal theories of electroweak symmetry breaking, where we briefly discussed possible directions for further well-motivated SM extensions. This already illustrates that our result constitutes an important step towards systematically constructing non-minimal conformal models, which may then accommodate further aspects of new physics and will thus yield a more complete picture of particle physics in a classically scale-invariant framework. Likewise, our study can be seen as a prototype for similar systematic analyses of different classes of conformal models, in which one or more of our initial assumptions is altered or abandoned.

Chapter 4

Three-body Higgs boson decays into extra light scalars

In the last chapter, we have encountered an explicit example of why the scalar sector of the minimal Standard Model (SM) may need to be extended. Specifically, addressing the long-standing gauge hierarchy problem via the phenomenologically consistent implementation of Coleman-Weinberg symmetry breaking at around the electroweak scale required the presence of extra bosonic degrees of freedom. Further reasons to study theories with an enlarged scalar sector were already given in Chapter 1 in the context of various beyond-the-Standard Model (BSM) scenarios (see also [8] for a recent comprehensive review).

Regardless of the actual underlying motivation, there are several aspects common to all such models. Most importantly, each additional fundamental scalar field S inevitably interacts with the SM Higgs doublet Φ. To see why this is true, note that the dimension-two operator $S^\dagger S$ is a singlet under any linearly realized internal symmetry that S may transform under. Irrespective of the quantum numbers of S, the theory's most general, renormalizable Lagrangian $\mathcal{L}$ will therefore inevitably contain a term of the form

$$\mathcal{L} \supseteq -\lambda_p \big(\Phi^\dagger \Phi\big)\big(S^\dagger S\big) \,, \tag{4.1}$$

with a dimensionless coupling λ_p. Equation (4.1) is usually referred to as (scalar) Higgs portal and has a number of important phenomenological consequences. Here, we will mostly be interested in exotic processes involving the 125 GeV Higgs boson, which are induced by the above portal term or similar operators. In particular, equation (4.1) implies that, once the Higgs doublet acquires a finite vacuum expectation value (vev), its physical excitation H can decay into a pair of extra scalars,

$$H \to SS \,, \tag{4.2}$$

provided the final-state particles are sufficiently light.

Indeed, as we have seen in Chapter 3, extra *light* scalar degrees of freedom may arise naturally as pseudo-Goldstone bosons of some spontaneously broken, approximate global symmetry.[a] But also without underlying symmetry, the presence of low-mass scalar particles may be well motivated. Famously, the physical spectrum of the next-to-minimal supersymmetric SM can contain a light pseudoscalar consistent with all existing experimental constraints, cf. [154, 155] for recent reviews. Similar situations may be realized in the two-Higgs-doublet model and its variants (for an overview, see e.g. [144]).

Assuming for now the existence of a low-mass scalar S, the exotic Higgs decay in equation (4.2) in principle offers a promising possibility to search for these light particles at collider experiments.[b] Depending on the actual properties of S, the aforementioned decay will lead to different signatures. For one, if the light scalar does not interact with any detector component and at the same time possesses a sufficiently long lifetime, such that it does not decay itself within the detector, the process $H \to SS$ will not be directly observable. Still, it would contribute to the invisible Higgs width. Such BSM contributions to the Higgs boson's total width are, for instance, *indirectly* constrained by precise measurements of Higgs signal strengths as performed by both ATLAS and CMS [24]. Based on the 7 and 8 TeV proton-proton data sets, the collaborations were able to obtain a 95 % CL upper bound of 0.34 on the total branching ratio of BSM Higgs decays [24]. Furthermore, *direct* searches for invisible Higgs decays exist [156, 157] and may also help to constrain models with light extra scalars. The current 95 % CL upper limits on the invisible Higgs branching fraction provided by ATLAS and CMS are 0.25 [156] and 0.24 [157], respectively. Both the aforementioned direct and indirect bounds are, of course, expected to significantly improve during the LHC's high-luminosity phase and, in particular, at potential future electron-positron colliders, see e.g. [158]. Note, furthermore, that the above limits also constrain scenarios, where the light scalar S decays promptly, but only into particles that do not leave traces in any of the detector components.

Next, let us discuss the case in which a low-mass scalar S is unstable and decays into SM states within a typical detector radius. The basic process in equation (4.2) will then lead to interesting non-standard Higgs decay signatures, potentially observable at current and future colliders, namely

$$H \to SS \to 4\,\mathrm{SM}\,, \tag{4.3}$$

where the Higgs is seen to decay into two pairs of SM particles, both of which

[a] Recall from Chapter 3 that there the relevant symmetry was anomalously broken scale invariance. Correspondingly, the scalon only became massive via radiative corrections and could thus be significantly lighter than the 125 GeV Higgs boson.

[b] Apart from high-energy collider experiments, there are multiple other ways to directly or indirectly search for low-mass scalars. We will touch on some of them in the course of Sections 4.1.1 and 4.2.1. A full review, however, is beyond the scope of the present study.

have the same invariant mass. Depending on the actual model and the light scalar's decay modes, there may be a plethora of possible final states to be considered here. Correspondingly, the ATLAS and CMS collaborations put great effort into searching processes of the general form given in equation (4.3). Comprehensive reviews on existing LHC analyses of two-body scalar Higgs decays are e.g. provided in [39, 40].

In contrast, prior to our study in [49], the related decay of the Higgs boson into *three* scalars,

$$H \to SSS \,, \tag{4.4}$$

has never been discussed in the literature, despite the fact that it is predicted by a large variety of models which extend the minimal SM by extra scalar fields. In particular, all BSM theories in which new CP-even scalar degrees of freedom mix into the physical 125 GeV Higgs boson inevitably entail the process of equation (4.4) as long as it is kinematically accessible.

The present chapter will therefore be devoted to investigating the phenomenology of three-body scalar Higgs decays. As one of our main results, we will demonstrate that said exotic processes may occur abundantly enough to be observed at current and near-future collider experiments via certain six-particle signatures which all exhibit very special and characteristic kinematic features. Interestingly, it turns out that a signal in the three-body channel may even be found in scenarios where Higgs decays into only two light scalars are suppressed and hence undetectable. Correspondingly, the three-body mode can be seen as a complementary approach towards searching for light scalar sectors at colliders. While the aforementioned findings are obtained within a particular model, we also derive several model-independent statements about the physical requirements which have to be fulfilled in order for the three-body decay to be relevant.

The chapter is thereby structured as follows. In Section 4.1, we start by discussing the formal basics of Higgs decays into light scalars. In doing so, we do not resort to a specific model realization, but rather consider a generic two-scalar potential. Based on this set-up we then review both experimental and theoretical constraints on the generic scalar couplings, which are subsequently used to determine prerequisites for three-body Higgs decays to become reasonably abundant. These model-independent results are then complemented by in-detail studies of multibody scalar Higgs decays within a specific model, namely the SM extension by one real scalar gauge singlet (henceforth simply referred to as the "singlet-extended SM"). The latter is introduced in Section 4.2, while its collider phenomenology is discussed in Section 4.3. In particular, we identify the most promising signatures which may lead to the detection of three-body scalar Higgs decays. We conclude in Section 4.4.

4.1 Higgs boson decays into scalars – a model-independent analysis

Let us start by discussing some *model-independent* aspects of scalar-to-scalar decays in theories describing particle physics at low energies. For that purpose, we consider a generic model whose particle spectrum after electroweak symmetry breaking is assumed to contain two electrically neutral and colorless physical scalar mass eigenstates, which will be denoted as H and h. Without loss of generality, we adopt $m_H \geqslant m_h$. The corresponding most general leading-order potential at the renormalizable level will then be of the following form

$$\begin{aligned} V(H,h) = {} & \tfrac{m_H^2}{2} H^2 + \tfrac{m_h^2}{2} h^2 + \lambda_{4H} H^4 + \lambda_{4h} h^4 \\ & + \kappa_{3H} H^3 + \kappa_{3h} h^3 + \kappa_{H2h} H h^2 + \kappa_{2Hh} H^2 h \\ & + \lambda_{2H2h} H^2 h^2 + \lambda_{3Hh} H^3 h + \lambda_{H3h} H h^3 \,. \end{aligned} \tag{4.5}$$

The scalars' mutual and self-interactions are parameterized by the dimensionless couplings λ_i, as well as by the dimensionful parameters κ_i and m_i. Since the present chapter is devoted to studying exotic decays of the 125 GeV Higgs boson into scalars, we will always identify the heavier state H with the SM-like Higgs found at the LHC. Accordingly, the low-mass scalar h is attributed to some beyond-the-Standard Model (BSM) sector. As a side note, we remark that some terms in the most general potential of equation (4.5) may be forbidden by possible extra symmetries of the underlying theory or its particle content.

From now on, we will always assume the scalar mass eigenvalues to satisfy $m_H \geqslant 3m_h$, so that both the Higgs decay into two and into three low-mass states h are kinematically accessible. On the one hand, the leading-order two-body decay rate is then calculated to be

$$\Gamma_2 \equiv \Gamma(H \to 2h) = \frac{\kappa_{H2h}^2}{8\pi m_H} \cdot \ell_2(x) \,, \tag{4.6}$$

with the mass ratio $x := m_h/m_H$ and the kinematic threshold function $\ell_2(x) = \sqrt{1-4x^2}$. On the other hand, the interactions covered by the potential in equation (4.5) equally imply the presence of three-body Higgs decays already at tree-level. The corresponding relevant Feynman diagrams are displayed in Figure 4.1. The process $H \to 3h$ is thus mediated by the contact interaction operator proportional to λ_{H3h} (Figure 4.1a), as well as by the virtual exchange of a light scalar (Figure 4.1b). Notice that contributions similar to that in Figure 4.1b, but with an intermediate Higgs H are suppressed by the small ratio m_h^2/m_H^2 and will therefore be neglected

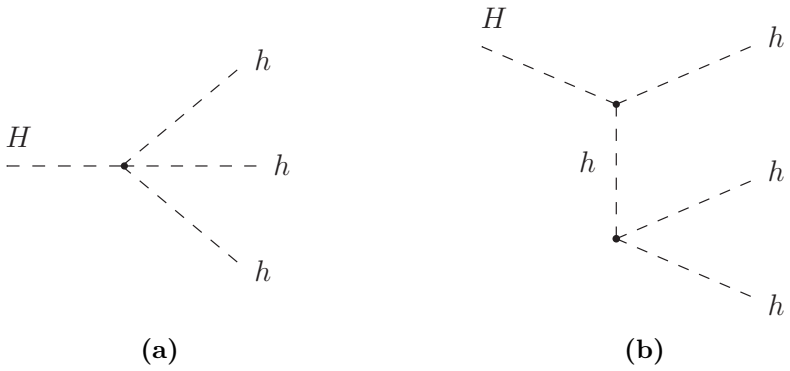

Figure 4.1: Leading-order Feynman graphs giving relevant contributions to the decay $H \to 3h$: (a) contact interaction and (b) virtual h-exchange. There exist two extra inequivalent final-state permutations for (b), which are not shown.

throughout this work. An explicit leading-order computation then yields

$$\Gamma_3 \equiv \Gamma(H \to 3h) = \frac{9 m_H}{64\pi^3} \Bigg[\frac{\lambda_{H3h}^2}{12} \ell_3^{(0)}(x) + \lambda_{H3h} \frac{\kappa_{H2h}\kappa_{3h}}{m_H^2} \ell_3^{(1)}(x) + \frac{\kappa_{H2h}^2 \kappa_{3h}^2}{m_H^4} \left(\ell_3^{(2)}(x) + 2\ell_3^{(1,1)}(x) \right) \Bigg] , \tag{4.7}$$

where the full expressions of the various three-body threshold functions ℓ_3 can be found in Appendix C. To further our understanding of the formula for Γ_3 in equation (4.7), let us have a brief look at the individual terms involved. On the one hand, the first and third terms originate from the squared contact and h-exchange interaction diagrams, respectively. On the other hand, the second term is due to the interference between the aforementioned contributions. Similarly, the fourth term arises from the interference among h-exchange graphs of different final-state permutations.

One of the present study's major goals is to assess the three-body mode's importance relative to its two-body counterpart. A convenient measure to do so is given by the ratio of the associated partial widths, specifically

$$r := \frac{\Gamma_3}{\Gamma_2} \equiv \frac{\mathcal{B}(H \to 3h)}{\mathcal{B}(H \to 2h)} \, . \tag{4.8}$$

Of course, we will be particularly interested in identifying scenarios where r is of order unity or even larger. Nevertheless, one naively anticipates r to be much smaller than one. Therefore, the usual approach towards multi-Higgs models is to neglect existing three-body channels entirely, even if they are kinematically allowed. As a justification of this simplification various rationales come to mind. For one, energy conservation requires the three-body final state to have a smaller phase space than its two-body counterpart. However, the associated phase space suppression decreases as the mass ratio

m_h/m_H becomes tiny. Correspondingly, we will mostly focus on the situation where $m_h \ll m_H$. Furthermore, processes involving the exchange of a virtual particle are usually suppressed with respect to pure contact interactions by an extra coupling and the mass of the internally propagating state. The h-mediated contribution to the three-body rate (cf. Figure 4.1b) may hence seem to be negligible. Still, if the low-mass state h is sufficiently light and κ_{3h} is not too small also these topologies can, in principle, contribute significantly.

Apart from the three-body channel's *relative* importance quantified by r, also the *absolute* relevance of Higgs decays into scalar final states is of interest. The latter can be measured by the associated inclusive branching fraction, specifically[c]

$$\mathcal{B}_{\text{scalar}} := \mathcal{B}(H \to 2h) + \mathcal{B}(H \to 3h) \,. \tag{4.9}$$

The size of $\mathcal{B}_{\text{scalar}}$ is obviously crucial for assessing the prospects for detecting *any* scalar Higgs decays at collider experiments. Let us finally remark that given r and $\mathcal{B}_{\text{scalar}}$ the individual branching ratios are readily computed as

$$\mathcal{B}(H \to 2h) = \frac{\mathcal{B}_{\text{scalar}}}{1+r} \quad \text{and} \quad \mathcal{B}(H \to 3h) = \frac{r \cdot \mathcal{B}_{\text{scalar}}}{1+r} \,. \tag{4.10}$$

Before we further investigate the range of possible values for r (and $\mathcal{B}_{\text{scalar}}$), let us first discuss existing experimental and theoretical constraints on models based on the generic scalar potential of equation (4.5).

4.1.1 Model-independent constraints

In this section, we will study constraints that can be set on the general scalar sector described by the potential of equation (4.5). Specifically, we aim at finding all such constraints which are derived solely on the basis of the aforementioned potential and are thus as model independent as possible. Notice that the generic potential (4.5) does not provide any information on the light scalar's couplings to other particles beside the 125 GeV Higgs boson. In particular, the decay properties of h remain unspecified. In the following, we will discuss experimental and theoretical constraints in turn.

A Experimental constraints

Empirical constraints on models with light scalar degrees of freedom usually originate from high-precision measurements of suitable low- and medium energy processes, especially meson decays. Important experiments in this context include but are not limited to beam-dump facilities and fixed-target

[c] In our definition of $\mathcal{B}_{\text{scalar}}$ we ignore contributions from Higgs decays into n scalars with $n \geqslant 4$. We will comment on why this is expected to be a reasonable approximation later in Section 4.1.2 on page 75.

experiments, such as those of the NA48 family. In addition, direct searches at B factories, like BaBar or Belle, or at high-energy electron-positron colliders, such as LEP, may be relevant. Further details on this subject can, for instance, be found in the corresponding passages of [159, 160]. However, constraints based on the aforementioned experiments typically depend on the low-mass scalar's production and decay modes and thus necessarily on its couplings to SM fermions or gauge bosons. They are therefore not of interest to the present discussion. Note that also results from direct LHC searches for invisible or other exotic Higgs decays involving light scalars are not applicable here, since they have to make assumptions on the possible decay channels of h as well.

Here, we will therefore focus on a different kind of measurements performed at the LHC, namely those of Higgs signal strengths. In a combined analysis based on Run 1 data, the ATLAS and CMS collaborations found the SM predictions to be well reproduced, thus setting an *indirect*, but nearly model-independent upper limit on the total branching fraction of non-standard Higgs decays, specifically [24]

$$\mathcal{B}(H \to \text{BSM}) \leqslant \mathcal{B}_{\text{BSM}}^{\text{max}} = 0.34 \quad \text{at } 95\,\% \text{ CL} \,. \tag{4.11}$$

The above result was obtained assuming that the investigated 125 GeV Higgs boson H is a single CP-even state with an SM-like tensor coupling structure, as well as SM-like production and decay kinematics. Furthermore, the validity of the narrow-width approximation was assumed. Lastly, the Higgs coupling modifiers in the κ-framework [161] were supposed to remain unchanged when going from 7 to 8 TeV and to satisfy $|\kappa_W|, |\kappa_Z| \leqslant 1$, as well as $\kappa_W \cdot \kappa_Z > 0$.

The indirect limit on $\mathcal{B}(H \to \text{BSM})$ in equation (4.11) can be translated into an 95 % CL upper bound on the non-standard Higgs width,

$$\Gamma(H \to \text{BSM}) \leqslant \Gamma_H^{\text{SM}} \frac{\mathcal{B}_{\text{BSM}}^{\text{max}}}{1 - \mathcal{B}_{\text{BSM}}^{\text{max}}} \simeq 2.1\,\text{MeV} \,, \tag{4.12}$$

where we assumed that the Higgs partial width for decays into SM final states is similar to that predicted by the minimal SM, namely $\Gamma_H^{\text{SM}} = 4.1\,\text{MeV}$ [162]. In a general model of new physics, the Higgs can have further BSM decay channels in addition to those involving light scalars. For the following study, we will, however, restrict ourselves to scenarios in which all contributions due to decays into non-scalar final states are negligible, i.e.

$$\mathcal{B}(H \to \text{BSM}) = \mathcal{B}_{\text{scalar}} = \frac{\Gamma_2 + \Gamma_3}{\Gamma_H^{\text{SM}} + \Gamma_2 + \Gamma_3} \,, \tag{4.13}$$

where we used the definition of $\mathcal{B}_{\text{scalar}}$ from equation (4.9) in the second step. Combining equations (4.11) and (4.13) then obviously yields $\mathcal{B}_{\text{scalar}} \leqslant 0.34$.

The latter result also enables us to constrain the allowed ranges for some of the couplings in the generic potential of equation (4.5). On the one hand, neglecting the three-body decay mode $H \to 3h$ for the moment, equations (4.11) and (4.13) permit us to derive

$$\frac{|\kappa_{H2h}|}{m_H} \lesssim \sqrt{8\pi \frac{\Gamma_H^{\mathrm{SM}}}{m_H} \frac{\mathcal{B}_{\mathrm{BSM}}^{\mathrm{max}}}{1-\mathcal{B}_{\mathrm{BSM}}^{\mathrm{max}}}} \simeq 0.02 \,, \tag{4.14}$$

where we employed Γ_2 in the form of equation (4.6) with $m_h \ll m_H$, in which case the threshold function $\ell_2(x)$ is close to unity. Similarly, one arrives at a bound on λ_{H3h} if one temporarily ignores the two-body channel $H \to 2h$, specifically

$$|\lambda_{H3h}| \lesssim \sqrt{\frac{256\pi^3}{3} \frac{\Gamma_H^{\mathrm{SM}}}{m_H} \frac{\mathcal{B}_{\mathrm{BSM}}^{\mathrm{max}}}{1-\mathcal{B}_{\mathrm{BSM}}^{\mathrm{max}}}} \simeq 0.2 \,. \tag{4.15}$$

Here, we used that theoretical consistency requires $|\kappa_{3h}| \lesssim \mathcal{O}(m_h)$ as we will explicitly demonstrate in the next paragraph. Hence, $|\kappa_{3h}|$ is necessarily much smaller than m_H, so that we can approximately neglect the corresponding terms in the formula for Γ_3 in equation (4.7). Additionally employing that $\ell_3^{(0)}(x)$ approaches unity for $m_h \ll m_H$ finally gives the limit in equation (4.15).

B Theoretical constraints

Complementary to the empirical bounds derived in the previous paragraph, we are now interested in how purely theoretical considerations may help in narrowing down the viable parameter space for our generic two-scalar model based on equation (4.5).

We will start by reviewing limits originating from tree-level perturbative unitarity (see e.g. [163] and our account in Appendix D for details). The underlying idea is based on the observation that probability has to be conserved in any well-behaved quantum field theory. This, in turn, necessitates the unitarity of the theory's S-matrix which then inevitably constrains said theory's scattering amplitudes. To put it differently, unitarity bounds implement the intuitive requirement that the probability for a given process to occur can never be larger than one. From a more technical point of view, perturbative unitarity is most conveniently imposed on the partial-wave amplitudes a_j associated with a given process, which are thereby forbidden to become arbitrarily large. For instance, the corresponding bound in the case of *elastic* scattering of two *identical* particles of mass m is

$$|\mathrm{Re}\, \tilde{a}_j(s)| \leqslant 1 \qquad \forall j \geqslant 0 \,, \tag{4.16}$$

which has to be satisfied for all kinematically allowed center-of-mass energies $\sqrt{s}$. Notably, equation (4.16) does not contain the exact coefficients a_j of the considered partial-wave expansion, but a modified version defined by

$$\tilde{a}_j := \xi(s) a_j(s) \quad \text{with} \quad \xi(s) = \sqrt{1 - \frac{4m^2}{s}} \, .$$

The above form crucially involves the energy-dependent function $\xi(s)$ and thus guarantees to properly take into account kinematic effects near the threshold $s_{\text{th}} = 4m^2$. Accordingly, one recovers $\tilde{a}_j \to a_j$ far above the aforementioned threshold.

For the purpose of applying the ideas just outlined to our general model, we calculated the matrix elements of two-to-two scalar scattering processes solely based on the generic potential of equation (4.5). Thereby, the severest constraints on the scalar couplings were found to arise from the s-wave amplitude (i.e. $j = 0$) associated to elastic scattering of light scalars, $hh \to hh$. For computational details, we again refer to Appendix D. Interestingly, imposing the unitarity bound of equation (4.16) over the whole range of accessible energies allows to constrain multiple parameters at the same time.

First, at asymptotically large energies, $s \to \infty$, the only finite contribution to $a_0(hh \to hh)$ originates from momentum-independent contact interactions. Consequently, perturbative tree-level unitarity induces an upper bound on λ_{4h} as per equation (4.16), which is found to be

$$\lambda_{4h} \leqslant \frac{2\pi}{3} \simeq 2.1 \, . \tag{4.17}$$

The next constraint derives from the observation that $hh \to hh$ scattering is dominated by s-channel Higgs exchange at energies around the Higgs pole. Accordingly, the function $|\text{Re}\, \tilde{a}_0|$ is anticipated to exhibit a local maximum close to $s \simeq m_H^2$. A dedicated calculation of the partial-wave amplitude and requiring the unitarity bound of equation (4.16) to be satisfied across the Higgs resonance result in

$$\frac{|\kappa_{H2h}|}{m_H} \leqslant \sqrt{8\pi \frac{\Gamma_H}{m_H}} \simeq 0.03 \, . \tag{4.18}$$

In numerically evaluating the right-hand side above, we employed the measured Higgs mass [81], as well as the SM prediction for the Higgs boson's total decay width [162]. Obviously, new physics effects like the presently considered Higgs decays into light scalars will generally lead to an enlarged Γ_H (cf. equation (4.12)). Using the maximally allowed value for Γ_H consistent with current Higgs signal strength measurements, one obtains a relaxed upper limit of $\kappa_{H2h}/m_H \lesssim 0.04$. In any case, the constraints on the trilinear portal coupling arising from perturbative unitarity turn out to be less stringent than that from experiment presented in equation (4.14).

Lastly, contributions from t- and u- channel h-exchange were found to typically dominate the s-wave amplitude of $hh \to hh$ scattering near the kinematic threshold at $s_{\text{th}} = 4m_h^2$. In particular, the function $|\text{Re}\,\tilde{a}_0|$ as given in Appendix D possesses a further local maximum at small energies, whose exact position depends on the light scalar's self-couplings κ_{3h} and λ_{4h}, as well as on its decay width. Asking the unitarity bound of equation (4.16) to hold at said maximum then enables us to put an upper limit on κ_{3h}. Assuming $\Gamma_h \ll m_h$, as is usually the case for low-mass scalars, and vanishing λ_{4h}, we find

$$\frac{|\kappa_{3h}|}{m_h} \lesssim 1.64 \,. \tag{4.19}$$

Finite values of λ_{4h} will lead to cancellations in $|\text{Re}\,\tilde{a}_0|$ between contributions from contact and h-exchange diagrams. Accordingly, the limit of equation (4.19) is slightly relaxed for $\lambda_{4h} > 0$. Adopting, for instance, $\lambda_{4h} = \frac{1}{2}$ implies $|\kappa_{3h}|/m_h \lesssim 1.73$. Notably, the quoted bounds on κ_{3h} are intuitive in the sense that they confirm the naive expectations based on dimensional analysis: the dimensionful trilinear scalar self-coupling cannot significantly exceed the associated particle's mass (cf. also [164]).

A second category of theoretical consistency checks arises from requiring the validity of the perturbative expansion of physical observables in a given quantum field theory. For instance, let us consider a generic quartic scalar self-interaction operator with dimensionless coefficient λ. If the operator is normalized such that the associated Feynman rule is $-\mathrm{i}\lambda$, then the relevant expansion parameter of the perturbative series can be shown to be $\lambda/(4\pi)$. Correspondingly, a necessary condition for the perturbative approach to be applicable in the case just described is $|\lambda| < 4\pi$, which is the form of the perturbativity bound that is widely used in the literature. Taking into account the different normalizations of the operators in the potential of equation (4.5) and rescaling the above perturbativity limit accordingly, we obtain

$$\lambda_{H3h} < \frac{2\pi}{3} \simeq 2.1 \,, \quad \lambda_{4h} < \frac{\pi}{6} \simeq 0.52 \quad \text{and} \quad \lambda_{2H2h} < \pi \simeq 3.1 \,, \tag{4.20}$$

as well as similar constraints on the remaining quartic couplings, which are, however, not relevant to us here. Notably, the perturbativity bound on λ_{4h} is significantly better than the limit arising from unitarity in equation (4.17).

4.1.2 Model-independent results

After our discussion of generic constraints on models with extra light scalars in the previous paragraphs, we are now in the position to derive some model-independent[d] statements on scalar Higgs decays in general, and on the three-

[d] When deriving the constraint based on Higgs signal strength measurements, a number of mild assumptions on the underlying model were made, which are outlined between

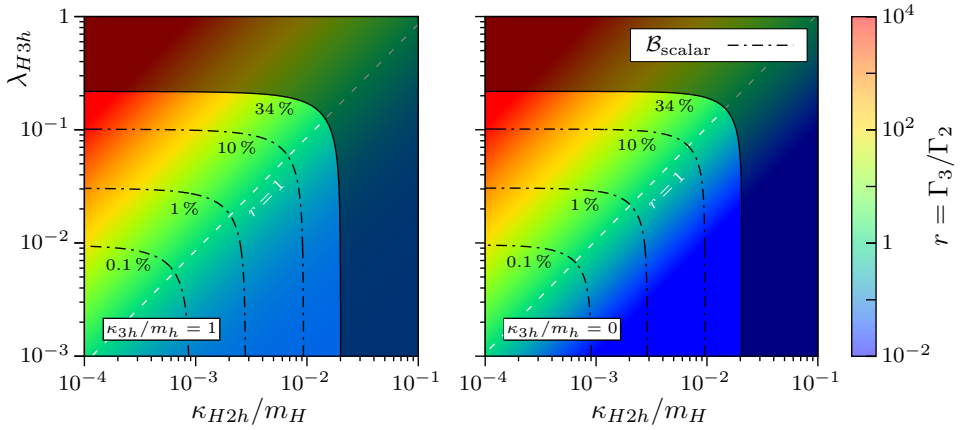

Figure 4.2: Ratio $r = \Gamma_3/\Gamma_2$ as a function of κ_{H2h} and λ_{H3h} for $m_h = 5\,\text{GeV}$ and different values of κ_{3h}/m_h. The $r = 1$ contour is drawn as white dashed line. Additionally, contours of constant scalar Higgs branching fraction $\mathcal{B}_{\text{scalar}}$ are shown as black dash-dotted lines. The dark shaded regions are excluded by Higgs signal strength measurements as per equation (4.11).

body mode's relevance in particular. Said statements build on the results summarized in Figures 4.2 and 4.3. Here, the color code represents the ratio $r = \Gamma_3/\Gamma_2$, which is plotted as a function of different couplings that parameterize the rates of scalar Higgs decays. Additionally, we draw contour lines of constant branching ratio $\mathcal{B}_{\text{scalar}}$ as defined in equations (4.9) and (4.13). Note that all plots are based on the full formulas for the partial widths Γ_2 and Γ_3 in equations (4.6) and (4.7), respectively. In the following, contributions to the three-body rate due to contact and h-mediated interactions will be schematically denoted as Γ_3^c and Γ_3^h, respectively.

Figure 4.2 now shows the ratio r and the branching fraction $\mathcal{B}_{\text{scalar}}$ in the κ_{H2h}-λ_{H3h} plane with all other model parameters held constant. Specifically, we fixed the light scalar's mass to 5 GeV. The left and right panels were then obtained for two different values of κ_{3h}/m_h. In both plots, the shaded regions are excluded by current Higgs signal strength measurements and the approximate bounds of equations (4.14) and (4.15) are well reproduced.

Most importantly, Figure 4.2 demonstrates that a substantial part of the available parameter space entails values for r greater than unity. Interestingly, both r and $\mathcal{B}_{\text{scalar}}$ can be large at the same time so that the three-body channel may indeed be relevant to the model's phenomenology. Furthermore, the light scalar's sizable trilinear self-interactions, adopted to produce the results of the left panel, are found to lead to a slightly enhanced rate Γ_3 and thus to values for r which are somewhat larger than those in the right panel. The aforementioned effect is particularly pronounced in the

equations (4.11) and (4.13). Besides, we assumed $\Gamma_h \ll m_h$ in order to deduce the unitarity bound on κ_{3h}.

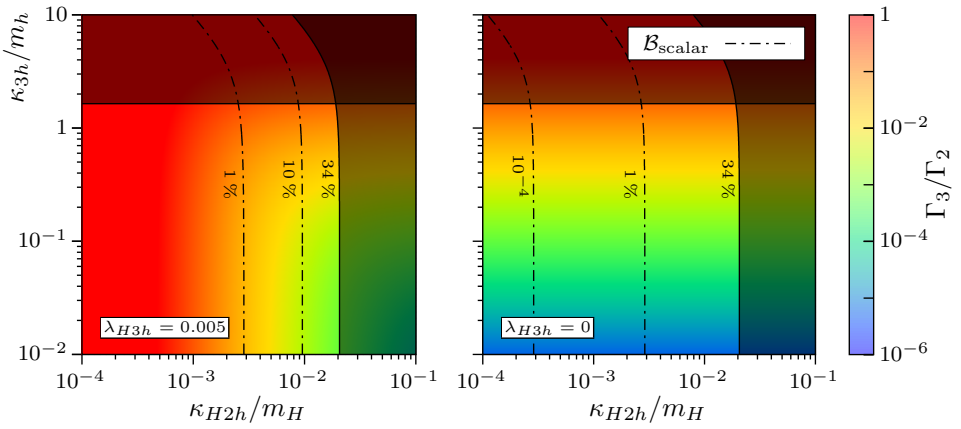

Figure 4.3: Ratio $r = \Gamma_3/\Gamma_2$ as a function of κ_{H2h} and κ_{3h} for $m_h = 5\,\text{GeV}$ and different values of λ_{H3h}. Contours of constant scalar Higgs branching fraction $\mathcal{B}_{\text{scalar}}$ are shown as black dash-dotted lines. The dark shaded regions on the right sides of each plot are excluded by Higgs signal strength measurements as per equation (4.11). Similarly, the shaded regions of large κ_{3h}/m_h are ruled out by tree-level perturbative unitarity according to equation (4.19). Note the different color scale as compared to Figure 4.2.

phenomenologically less interesting region where $r < 1$. In contrast, both plots are virtually identical in the $r > 1$ regime, which is a first indication of the fact that it is most of all the size of the contact interactions λ_{H3h} that determines whether the three-body channel can be dominant or not.

The above statement is further substantiated by the findings displayed in Figure 4.3. In a similar manner to before, the corresponding plots show the quantities of interest r and $\mathcal{B}_{\text{scalar}}$ in the κ_{H2h}-κ_{3h} plane. Again, all other parameters were fixed and $m_h = 5\,\text{GeV}$ was chosen. The two panels now differ in the size of the contact contribution to the three-body rate Γ_3^c: Whereas the latter is finite in the left plot, it vanishes in the right one. For both scenarios, we include constraints on the parameter space due to Higgs signal strength measurements and perturbative unitarity.

The comparison between the two panels in Figure 4.3 allows for several important conclusions. First, the nearly vertical contour lines imply that the overall rate of scalar Higgs decays for a given value of λ_{H3h} is mainly fixed by κ_{H2h}. In contrast, the impact of the light scalar's trilinear self-coupling on $\mathcal{B}_{\text{scalar}}$ is only of minor importance. Rather, the right plot reveals that κ_{3h} sets the relative size of the h-mediated contribution Γ_3^h with respect to the two-body rate Γ_2, as is expected based on equations (4.6) and (4.7). Correspondingly, in cases where the contact contribution Γ_3^c is negligible, the ratio r is found to grow as κ_{3h}^2 while not depending on any other couplings. The unitarity bound on κ_{3h} presented in equation (4.19) will therefore inherently limit the range of possible r values, if contact interactions are absent. Specifically, r is observed to never exceed $\mathcal{O}(10^{-1})$

in this scenario. The situation changes, however, once λ_{H3h} becomes non-zero. Since the corresponding contact contribution Γ_3^c stays finite as κ_{H2h} and thus Γ_2 tend to zero, we find relatively large ratios r in the left panel's left half. Larger values for λ_{H3h} will finally extend the regime of sizable r towards larger κ_{H2h} and hence larger $\mathcal{B}_{\text{scalar}}$.

We conclude, that the existence of a region in parameter space with $r \gtrsim 1$ inevitably requires the presence of finite contact interactions contributing to $H \to 3h$ and thus a non-zero value of λ_{H3h}. In contrast, a limit on the trilinear self coupling κ_{3h} from perturbative tree-level unitarity prevents r from increasing beyond $\mathcal{O}(10^{-1})$ for vanishing λ_{H3h}.

In order to appreciate the necessity of this last observation, let us temporarily assume that κ_{3h} was allowed to exceed the aforementioned unitarity bound. As a consequence, ratios r of order unity could be realized even in the absence of contact interactions. In a similar manner, the rates of Higgs decays into more than three light scalars might become large as well, ultimately leading to the clearly unphysical scenario where $\Gamma_2 \simeq \Gamma_3 \simeq \Gamma_4 \simeq \ldots$. In reality, boosting r from $\mathcal{O}(10^{-1})$ to $\mathcal{O}(1)$ or above must therefore necessarily rely on additional tree-level contact interactions as we have argued before. Crucially, such contact interactions contributing to the scalar n-body Higgs decays $H \to nh$ are absent at the renormalizable level for $n \geqslant 4$. Still, within the effective field theory framework, the operators Hh^n may be induced due to integrating out some heavy new degree of freedom. However, said operators are irrelevant for $n \geqslant 4$ in the sense of the renormalization group, so that their coefficients will be unavoidably suppressed by the heavy particle's mass. The associated contributions and hence Higgs decays into four or more light scalars in general are therefore expected to be negligible. In that sense, the three-body channel is indeed unique.

4.2 Scalar singlet-extension of the Standard Model

The discussion on multibody scalar Higgs decays presented in the last section was largely independent of the underlying theory's details. However, we also stressed the importance of the light scalar's properties when it comes to actually searching for this type of exotic Higgs decay signatures at collider experiments. Therefore, we will now study a specific particle physics model, in which a scalar potential of the form given in equation (4.5) is realized at low energies. Specifically, we consider the simple extension of the Standard Model (SM) by one real scalar gauge singlet S (see e.g. [165–169]). Its most general renormalizable tree-level potential before electroweak symme-

try breaking (EWSB) reads

$$\begin{aligned} V(\Phi, S) = \mu^2 \Phi^\dagger \Phi + \lambda (\Phi^\dagger \Phi)^2 \\ + \frac{\delta_1}{2} (\Phi^\dagger \Phi) S + \frac{\delta_2}{2} (\Phi^\dagger \Phi) S^2 \\ + \kappa_1 S + \frac{\kappa_2}{2} S^2 + \frac{\kappa_3}{3} S^3 + \frac{\kappa_4}{4} S^4 \,, \end{aligned} \tag{4.21}$$

where Φ denotes the usual complex Higgs doublet of the minimal SM as defined in equation (2.3). Its self-interactions are captured by the first line of equation (4.21), which is equivalent to the SM Higgs potential introduced in equation (2.12). The second line then contains the possible operators connecting the doublet and singlet sectors, including the generic dimension-four scalar portal already mentioned in equation (4.1). The scalar field S being a real gauge singlet not charged under any extra symmetry, implies the presence of an additional portal term which is trilinear in the fields and has a dimensionful coefficient δ_1. Lastly, the third line of equation (4.21) describes the self-interactions of S. Here, too, operators with an odd number of singlet fields appear due to the trivial symmetry properties of S.

As in the minimal SM, the Higgs doublet Φ acquires a finite vev v upon EWSB. Working in unitary gauge, we can write in analogy to equation (2.4)

$$\Phi = \tfrac{1}{\sqrt{2}} \begin{pmatrix} 0 \\ v + \phi \end{pmatrix} \quad \text{with} \quad v = 246\,\text{GeV} \,. \tag{4.22}$$

A priori, also the singlet field can possess a non-zero vev v_s. The leading-order vacuum field configuration can then be determined by solving the model's tadpole equations, which follow from the minimization conditions of the tree-level potential in equation (4.21) and can be computed to be

$$\mu^2 = -\lambda v^2 - \tfrac{1}{2} v_s (\delta_1 + \delta_2 v_s) \,, \tag{4.23a}$$

$$\kappa_1 = -\tfrac{1}{4} \delta_1 v^2 - v_s \left(\kappa_2 + \kappa_3 v_s + \kappa_4 v_s^2 + \tfrac{1}{2} \delta_2 v^2 \right) \,. \tag{4.23b}$$

The second equation demonstrates that the presence of the term linear in S and proportional to κ_1 allows us to set $v_s = 0$ without loss of generality. In this case, the tadpole equations (4.23) are solved by $\mu^2 = -\lambda v^2$ and $\kappa_1 = -\delta_1 v^2/4$.

For the phenomenology of the singlet-extended SM, the following observation is especially crucial. The CP-even scalar fields ϕ and S share the same set of quantum numbers. In particular, both are colorless and electrically neutral. Therefore, the trilinear portal term proportional to δ_1 will in general induce mixing of the aforementioned gauge eigenstates ϕ and S into two mass eigenstates, which will be denoted as H and h. The translation between those two sets of eigenstates is described by a two-dimensional rotation in field space, i.e.

$$\phi = \cos\theta \cdot H - \sin\theta \cdot h \quad \text{and} \quad S = \cos\theta \cdot h + \sin\theta \cdot H \,, \tag{4.24}$$

where the size of the real mixing angle θ quantifies the misalignment of the two eigenbases and thus the strength of the mixing. In line with the physical scenario we have in mind, we will identify the eigenstate H with the SM-like Higgs boson discovered at the LHC, while h will be assumed to be a much lighter scalar particle, i.e. $m_h \ll m_H = 125.09\,\text{GeV}$ [81]. Under these premises, existing experimental results constrain the mixing angle to be relatively small, as we will see explicitly in Section 4.2.1.A. Importantly, note that only the gauge eigenstate ϕ couples to the SM fermions and gauge bosons, namely in the way reviewed in Chapter 2 (see in particular equations (2.10) and (2.21)). Still, the presence of mixing as given in equation (4.24) implies that both physical scalars H and h interact with the remaining SM particles. In particular, the low-mass state h will have the *same* couplings as a SM Higgs, but suppressed by a factor of $\sin\theta$. Likewise, the heavy state's interaction strengths will be slightly degraded as compared to those of the Higgs boson in the minimal Standard Model, namely by $\cos\theta$.

A more formal description of mixing in the sector of CP-even scalars starts with the realization that the corresponding mass squared matrix is non-diagonal. Specifically, the model's potential after EWSB and in unitary gauge can be brought into the form

$$V = \tfrac{1}{2}\begin{pmatrix}\phi & S\end{pmatrix}\begin{pmatrix}2\lambda v^2 & \frac{1}{2}\delta_1 v \\ \frac{1}{2}\delta_1 v & \kappa_2 + \frac{1}{2}\delta_2 v^2\end{pmatrix}\begin{pmatrix}\phi \\ S\end{pmatrix} + \text{higher-order interactions}$$

As already indicated, the above mass squared matrix can be diagonalized analytically by means of the rotation in equation (4.24). Thereby, it is possible to calculate the physical particle masses as well as the mixing angle in terms of Lagrangian parameters. The thus obtained relations can also be inverted, resulting in

$$\begin{aligned}\lambda &= \frac{m_H^2\cos^2\theta + m_h^2\sin^2\theta}{2v^2}\,, \\ \kappa_2 &= -\frac{\delta_2 v^2}{2} + m_h^2\cos^2\theta + m_H^2\sin^2\theta\,, \\ \delta_1 &= \frac{m_H^2 - m_h^2}{v}\sin 2\theta\,.\end{aligned} \tag{4.25}$$

Equations (4.25) conveniently allow to eliminate the less intuitive Lagrangian couplings λ, κ_2 and δ_1 in favor of the two physical masses and the scalar mixing angle. The model's scalar sector is now fully characterized by three dimensionless parameters ($\sin\theta$, δ_2, κ_4) and two dimensionful quantities (m_h and κ_3). The electroweak scale v and the Higgs mass m_H will be regarded as fixed and are therefore set to their measured values.

For the purpose of making contact with our model-independent formulation of multibody scalar Higgs decays in the previous section, we first need to express the model's potential in terms of the scalar mass eigenstates H

and h. To that end, we plug in equations (4.22) to (4.25) into said potential (4.21). The resulting form will then be that of the generic potential in equation (4.5) so that we can simply read off the relevant couplings. For the purposes of this work, the most interesting parameters are

$$\begin{aligned}
\lambda_{H3h} &= \tfrac{1}{2}\sin(2\theta)\Big[\big(\kappa_4 - \tfrac{1}{2}\delta_2\big)\cos^2\theta \\
&\quad + \tfrac{1}{2}\left(\delta_2 - \hat{m}_H^2\cos^2\theta - \hat{m}_h^2\sin^2\theta\right)\sin^2\theta\Big] \,, \\
\lambda_{4h} &= \tfrac{1}{4}\big(\kappa_4\cos^4\theta + \delta_2\cos^2\theta\sin^2\theta \\
&\quad + \tfrac{1}{2}\hat{m}_H^2\cos^2\theta\sin^4\theta + \tfrac{1}{2}\hat{m}_h^2\sin^6\theta\big) \,, \\
\lambda_{2H2h} &= \tfrac{1}{16}\delta_2\Big[1 + 3\cos(4\theta)\Big] \\
&\quad + \tfrac{3}{16}\sin^2(2\theta)\left(2\kappa_4 + \hat{m}_H^2\cos^2\theta + \hat{m}_h^2\sin^2\theta\right) \,, \\
\kappa_{H2h} &= \tfrac{1}{2}v\cos\theta\Big[\delta_2 + \hat{\kappa}_3\sin(2\theta) + \big(\hat{m}_H^2 + 2\hat{m}_h^2 - 3\delta_2\big)\sin^2\theta\Big] \,, \\
\kappa_{3h} &= \tfrac{1}{3}\kappa_3\cos^3\theta - \tfrac{1}{2}v\sin\theta\left(\delta_2\cos^2\theta + \hat{m}_h^2\sin^2\theta\right) \,,
\end{aligned} \tag{4.26}$$

where we introduced the dimensionless trilinear self-coupling $\hat{\kappa}_3 := \kappa_3/v$, as well as the dimensionless mass parameters $\hat{m} := m/v$. As already alluded to above, experiments require the mixing angle θ to be small. For the sake of clarity and to identify the dominant terms, it is instructive to expand the exact expressions in equation (4.26) to first order in θ. One obtains

$$\begin{aligned}
&\lambda_{H3h} \simeq (\kappa_4 - \tfrac{1}{2}\delta_2)\theta \,, \qquad && \lambda_{4h} \simeq \tfrac{\kappa_4}{4} \,, && \lambda_{2H2h} \simeq \tfrac{\delta_2}{4} \,, \\
&\kappa_{H2h} \simeq \tfrac{1}{2}\delta_2 v + \kappa_3\theta \,, && \kappa_{3h} \simeq \tfrac{1}{3}\kappa_3 - \tfrac{1}{2}\delta_2 v\theta \,.
\end{aligned} \tag{4.27}$$

Note, however, that we will use the exact relations of equation (4.26) in all of our calculations throughout this chapter.

Nevertheless, the approximate identities of equation (4.27) are helpful since they make some important features of the model particularly manifest. For instance, the parameter λ_{H3h} is seen to be proportional to the mixing angle and thus vanishes in the decoupling limit $\theta \to 0$, where the light Higgs does not interact with any of the SM fermions or gauge bosons. According to our model-independent discussion of Section 4.1.2, the three-body decay channel is therefore hardly relevant in this limit. In the case of non-zero mixing, λ_{H3h} is governed by the quartic singlet self-coupling κ_4 and by the dimensionless portal δ_2. As opposed to λ_{H3h}, all of the remaining couplings that we considered above stay finite in the decoupling limit. In particular, the low-mass scalar's trilinear self-coupling κ_{3h} is then given by κ_3, which thus controls the size of the h-mediated contribution to the three-body rate relative the partial width of the two-body mode. In conclusion, relatively strong self-interactions in the singlet sector are found to be a a necessary condition for the three-body channel to be relevant. Correspondingly, the non-observation of three-body decays may be exploited to derive limits on said self-interactions.

4.2.1 Constraints on the parameter space

Now that we study a particular model of BSM physics and know how the light scalar h couples to all SM fermions and gauge bosons, we are in the position to expand our review of model-independent constraints presented in Section 4.1.1. Accordingly, we will now address both experimental and theoretical constraints specific to the real singlet extension of the SM. In doing so, we focus on those model parameters which were previously identified to govern multibody scalar Higgs decays, cf. our discussion after equation (4.27).

A Experimental constraints

As we have already outlined in the introduction to the present chapter, as well as in Section 4.1.1.A, there exist various experiments to directly or indirectly search for low-mass scalars. In the following, we will briefly review those measurements which have the strongest impact on the parameter space of the singlet-extended SM. For a more complete account on the subject, we refer the reader to [159].

Notably, the applicability of a given constraint crucially depends on the mass of the light scalar h. We will therefore discuss different regions of m_h in turn. First, let us assume the light scalar's mass to lie below $(m_K - m_\pi) \approx 360\,\text{MeV}$. In this regime, precise measurements of kaon decays turn out to confine the mixing angle θ to tiny values of order 10^{-3} or smaller [159]. Consequently, the singlet sector virtually decouples, which was previously demonstrated to significantly reduce the relevance of the three-body Higgs decay mode $H \to 3h$. We will therefore ignore the mass region below 360 MeV in the following, even though we will briefly study the decoupling limit $\theta \to 0$ for larger masses of h in Section 4.3.1.

For light scalar masses greater than 360 MeV the constraints on the mixing angle relax to some extent, since the on-shell kaon decay $K \to \pi + h$ is no longer kinematically accessible. Below the B-meson mass threshold at $m_B \approx 5\,\text{GeV}$ the most stringent bounds on θ then originate from measurements of B-meson decays [159]. Specifically, the presence of a light scalar interacting with the SM fermions and gauge bosons contributes to the inclusive decay channel $B \to X_s \ell^+ \ell^-$ via additional penguin diagrams. As a consequence, the associated branching ratios must fulfill the relevant experimental limit, namely [83]

$$\mathcal{B}(B \to X_s + h) \cdot \mathcal{B}(h \to \mu^+ \mu^-) < \mathcal{B}(B \to X_s \ell^+ \ell^-) = \left(3.66^{+0.76}_{-0.77}\right) \cdot 10^{-6} \,.$$

The branching fraction of the initial B decay can be computed using effective field theory [170], which then leads to

$$\sin^2\theta \cdot \mathcal{B}(h \to \mu^+ \mu^-) \lesssim 0.51 \cdot 10^{-6} \,. \tag{4.28}$$

In complete analogy, the exclusive decay mode $B \to K\mu^+\mu^-$ can be used to derive a constraint similar to that in equation (4.28), see [159]. In order to obtain an actual bound on the mixing angle θ, both cases require knowledge about the branching ratio of the light scalar decay into a pair of muons. However, calculating said branching fraction involves properly taking into account non-perturbative QCD effects as will be discussed in more detail in Section 4.2.2. Here, we restrict ourselves to stating that $\mathcal{B}(h \to \mu^+\mu^-)$ is found to vary between roughly 1 % and about 10 % in the considered mass range, so that the mixing angle cannot exceed 10^{-2} as per equation (4.28).

For low-mass scalars heavier than the B-meson threshold, the initial on-shell decay $B \to X_s + h$ is kinematically forbidden as well. Relevant bounds on the mixing angle now arise from Υ decays [171] and from LEP searches for the Bjorken process $e^+e^- \to Z^*h$ [172–174], with the severest constraints coming from the latter. Specifically, the L3 analysis of [173] implies

$$\sin\theta \lesssim 0.1 \quad \text{at } 95\,\% \text{ CL} \tag{4.29}$$

for light scalar masses below 10 GeV, while the corresponding ALEPH bound based on [172] is somewhat weaker [159]. Notably, both of the aforementioned studies make assumptions on the possible decay channels of h, which are, however, fulfilled by the light scalar in the singlet-extended SM. Hence, we do not have to resort to the OPAL analysis of [174], which is decay-mode independent indeed, but also produces the least stringent limits.

In the case of even heavier scalars, $m_h \gtrsim \mathcal{O}(10\,\text{GeV})$, a substantial phase space suppression begins to reduce the rate of the three-body Higgs decay. In conclusion, within the singlet-extended SM, the light scalar mass range

$$360\,\text{MeV} \lesssim m_h \lesssim \mathcal{O}(10\,\text{GeV}) \tag{4.30}$$

is anticipated to produce the most promising phenomenology with respect to scalar three-body Higgs decays at current or future collider experiments.

Note that all of the constraints presented up to now derive from the fact that interactions of h with SM fermions and gauge bosons are not allowed to be arbitrarily strong. Thus, said constraints could only limit the scalar mixing angle θ, which parameterizes these interaction strengths. Additional restrictions on the model's parameter space follow from the model-independent bounds based on Higgs signal strength measurements, which we discussed in Section 4.1.1.A. In the following analyses, we will therefore always require the associated constraint from equation (4.11) to be satisfied.

B Theoretical constraints

The model-independent constraints from imposing unitarity and perturbativity, which we already discussed in Section 4.1.1.B, can be straightforwardly applied to the singlet-extended SM, thus limiting its fundamental

parameters. To that end, we require the scalar couplings in the form of equation (4.26) to satisfy all of the consistency conditions given in equations (4.17) to (4.20). Note that it is these exact bounds that we will impose in all explicit calculations in the rest of the present chapter.

Nevertheless, in order to get a feeling for how the above constraints actually restrict the model's parameter space, let us have a closer look at their implications in the decoupling limit $\theta \to 0$. On the one hand, perturbative tree-level unitarity then necessitates

$$\kappa_4 \lesssim 8.4 \,, \quad |\delta_2| \lesssim 0.029 \quad \text{and} \quad \frac{|\kappa_3|}{m_h} \lesssim 4.9 \tag{4.31}$$

as per equations (4.17), (4.18) and (4.19), respectively. On the other hand, applying the perturbativity limits from equation (4.20) for $\theta \to 0$ yields

$$\kappa_4 < \frac{2\pi}{3} \simeq 2.1 \quad \text{and} \quad |\delta_2| < 4\pi \simeq 13 \,. \tag{4.32}$$

In addition, we require the leading order potential in equation (4.21) to be bounded from below, thus producing a stable vacuum. A straightforward calculation (cf. e.g. [175]) yields the following criteria for absolute stability:

$$\lambda \geqslant 0 \,, \quad \kappa_4 \geqslant 0 \quad \text{and} \quad \delta_2 \geqslant -2\sqrt{\lambda\kappa_4} \,, \tag{4.33}$$

where λ is given by equation (4.25) and is automatically positive in the chosen parameterization. Obviously, the aforementioned stability bounds must hold for all values of the scalar mixing angle θ.

4.2.2 Decay properties of the light scalar

As we have learned before, the light scalar h in the singlet-extended SM couples to Standard Model fermions and gauge bosons like the physical Higgs particle of the minimal SM, but with coupling strengths that are suppressed by a common factor of $\sin\theta$ (see equation (4.24) and the ensuing discussion). The branching fractions for decays of h are therefore independent of the mixing angle and correspond precisely to those of a SM Higgs of the same mass. In determining the decay properties of h, we can thus resort to the existing literature on this subject. As is to be expected, said decay properties strongly depend on the light scalar's mass m_h and we will study different mass regions in turn.

Let us start with the mass range between 360 MeV and roughly 1 GeV. Here, the light scalar will predominantly decay into muon and pion pairs, as well as kaon pairs, provided its mass is larger than the associated threshold at $2m_K \approx 988\,\text{MeV}$, see e.g. [176]. Whereas the leading-order partial width of the decay into muons is readily computed,

$$\Gamma(h \to \mu^+\mu^-) = \sin^2\theta \frac{m_\mu^2 m_h}{8\pi v^2} \left(1 - \frac{4m_\mu^2}{m_h^2}\right)^{3/2} \,, \tag{4.34}$$

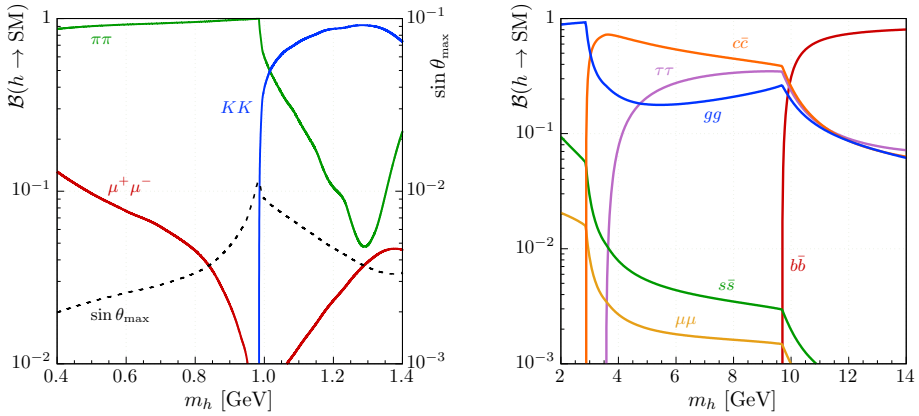

(a) Low-mass regime **(b)** High-mass regime

Figure 4.4: Branching fractions of the light scalar in the singlet-extended SM. The results were obtained based on [176] (panel (a)) and [177] (panel (b)), respectively. For the low-mass regime, we also plot the maximally allowed mixing angle according to equation (4.28).

the calculation of both $\Gamma(h \to \pi\pi)$ and $\Gamma(h \to KK)$ is more intricate and thus requires advanced techniques. The reason for this is twofold: First, a simple perturbative treatment of the aforementioned hadronic processes is not meaningful, as m_h is assumed to be of the order of the QCD scale. Consequently, non-perturbative effects need to be accounted for and suitable approaches, like e.g. chiral perturbation theory (χPT), must be used. In this spirit, the partial width of the decay into pions was computed in [178–180] applying leading-order χPT. It reads

$$\Gamma(h \to \pi\pi) = \sin^2\theta \frac{m_h^3}{216\pi v^2}\left(1 + \frac{11}{2}\frac{m_\pi^2}{m_h^2}\right)^2 \sqrt{1 - \frac{4m_\pi^2}{m_h^2}}\,. \tag{4.35}$$

A second complication in calculating the hadronic branching fractions of h arises from the fact that final-state meson-meson interactions were found to be non-negligible and to substantially alter results like that in equation (4.35) [181]. A fully consistent treatment of the problem was given in [176], where the authors used next-to-leading order χPT supplemented by dispersion theory so as to consistently take into account the aforementioned final-state interactions. Based on these results, we have computed the branching ratios of the light scalar h in the low-mass regime between 360 MeV and roughly 1 GeV. Together with the maximally allowed scalar mixing angle consistent with the experimental bound of equation (4.28), said branching fractions are shown in Figure 4.4a. Note that the large enhancement in the rate of the pion channel just below the kaon mass threshold $2m_K$ originates from the existence of the scalar isosinglet resonance $f_0(980)$, which induces a resonant amplification of final-state interactions.

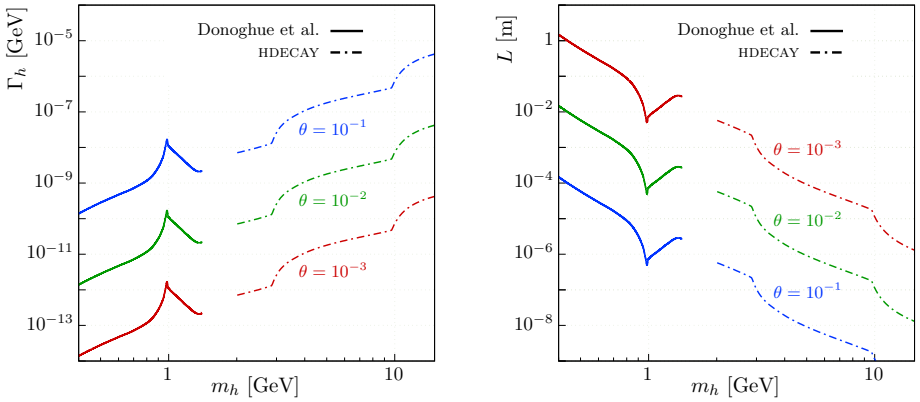

(a) Total decay width **(b)** Decay length

Figure 4.5: Mass-dependent decay properties of the light scalar in the singlet-extended SM for various mixing angles θ. The shown results were obtained based on [176] ($m_h \leqslant 1.4\,\text{GeV}$) and [177] ($m_h \geqslant 2\,\text{GeV}$), respectively. The decay length in (b) was calculated as per equation (4.36) assuming $E_h \simeq m_H/3$.

For light scalars heavier than roughly 1 GeV, non-perturbative effects from QCD start to become irrelevant, so that the partial decay widths of h can be calculated in conventional perturbation theory. Notably, larger values for m_h also open up a variety of new final states. We have calculated the branching ratios for the most important decay modes of h using `HDECAY` [177] and display our results in Figure 4.4b.

Having determined the rates of all of the light scalar's relevant decay channels, its total width Γ_h is, of course, straightforward to compute. As shown in Figure 4.5a, Γ_h turns out to be relatively small. Especially in the low-mass regime below 1 GeV, where the mixing angle is required to be small by consistency with experiment and only a few final states are kinematically accessible, the total decay width is found to be tiny. It is therefore useful to also determine the light scalar's typical decay length L. Assuming that all scalars originating from an initial Higgs decay are produced with characteristic lab-frame energies of order of the Higgs mass, $E_h \simeq \mathcal{O}(m_H) \gg m_h$, their decay length is approximately given by

$$L = \frac{E_h}{m_h \Gamma_h} + \mathcal{O}\left(\frac{m_h^2}{E_h^2}\right) . \tag{4.36}$$

Setting $E_h \simeq m_H/3$ for the sake of concreteness, the mass dependence of L is presented in Figure 4.5b. As an example, our findings imply for the decay length of a 500 MeV scalar

$$L \simeq \left(\frac{10^{-3}}{\sin\theta}\right)^2 \cdot 0.55\,\text{m} . \tag{4.37}$$

For typical values of the scalar mixing angle in the low-mass regime, $\sin\theta = \mathcal{O}(10^{-3})$, decays of h are thus expected to occur on macroscopic length scales. Consequently, the associated decay vertices must be anticipated to be clearly displaced from the primary interaction vertex and searches have to be performed accordingly. As an aside, let us mention that in the case of even smaller mixing angles, light scalar decays will happen largely outside of a typical detector radius so that scalar Higgs decays may remain invisible. However, future large surface detectors like the recently proposed MATHUSLA are designed to observe decays of neutral long-lived particles and could hence provide a remedy [182].

Figure 4.5b furthermore signifies that displaced vertices are not necessarily produced for larger masses of h. To be more specific, the decay length for a 5 GeV scalar with energy $E_h \simeq m_H/3$ is exemplarily calculated as

$$L \simeq \left(\frac{0.1}{\sin\theta}\right)^2 \cdot 9.1\,\text{nm}\,. \tag{4.38}$$

4.3 Scalar Higgs decays at colliders

In the following section we will study the detection prospects at current or near-future collider experiments for three-body Higgs decays into light scalars as predicted by the singlet-extended SM. As already argued in Section 4.2, the model's collider phenomenology will crucially depend on the light scalar's mass, which, on the one hand, fixes the maximally allowed amount of mixing between the model's CP-even scalar degrees of freedom, and, on the other hand, determines the light scalar's major decay modes. We will therefore distinguish low-, intermediate- and high-mass regimes and discuss their physics in turn in Sections 4.3.1, 4.3.2 and 4.3.3. In doing so, we will identify regions of parameter space where the three-body decay channel can have rates comparable to or larger than those of its two-body counterpart. We will then calculate the cross-sections of processes which best lend themselves as potential discovery channels of a light scalar sector via Higgs decays.

4.3.1 Low-mass regime

Let us start by investigating the case of light scalars with masses between the kaon decay threshold at $(m_K - m_\pi) \approx 360\,\text{MeV}$ and the kaon pair production threshold at $2m_K \approx 988\,\text{MeV}$. In order to identify phenomenologically interesting regions of parameter space, we calculate the ratio of partial Higgs decay widths $r = \Gamma_3/\Gamma_2$ introduced in equation (4.8) as a function of the quartic portal coupling δ_2 and the light scalar's trilinear self-interaction strength κ_3. Our results for a 900 MeV scalar boson are shown in Figure 4.6. Obviously, the presented plots are very similar to those in Figure 4.3 and

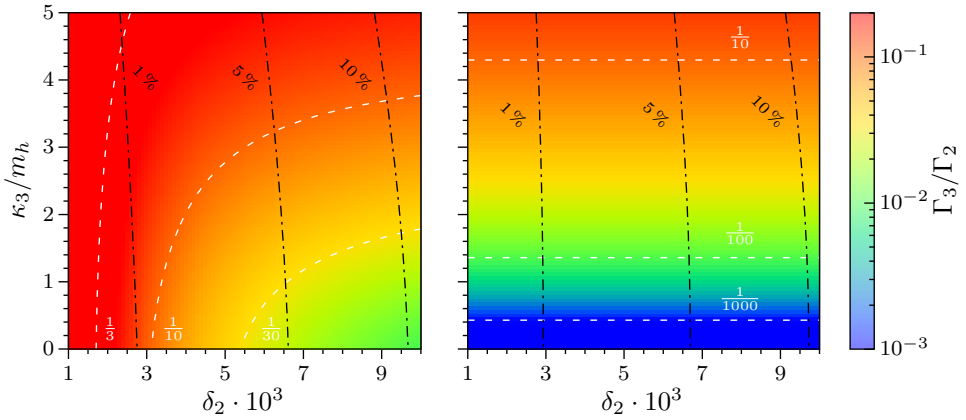

Figure 4.6: Ratio $r = \Gamma_3/\Gamma_2$ in the singlet-extended SM as a function of δ_2 and κ_3 for $m_h = 900\,\text{MeV}$. We show contours of constant r as white dashed lines. Additionally, contours of constant scalar Higgs branching fraction $\mathcal{B}_{\text{scalar}}$ are drawn as black dash-dotted lines. All points displayed here satisfy the constraints discussed in Section 4.2.1, in particular that on κ_3/m_h from equation (4.31). We compare the cases of finite and vanishing contact coupling λ_{H3h}, which are realized by setting $\theta = 4.8 \cdot 10^{-3}$ and $\kappa_4 = 2.0$ (*left panel*) or $\theta \to 0$ and $\kappa_4 = 0.1$ (*right panel*), respectively.

the associated discussion from Section 4.1.2 can be directly applied to the present situation. Most importantly, Figure 4.6 explicitly confirms our previous conclusion that ratios r of order one or larger require the presence of non-negligible contact interactions contributing to the three-body decay width via the Feynman diagram in Figure 4.1a. Accordingly, r is found to not exceed $\mathcal{O}(10^{-1})$ if λ_{H3h} vanishes. In view of the importance of contact interactions for the three-body mode's relevance, it is instructive to estimate the maximum possible value of the associated coupling λ_{H3h} for a light scalar in the low-mass regime of the singlet-extended SM. Employing the approximate formula for λ_{H3h} from equation (4.27), we obtain

$$\lambda_{H3h} \simeq (\kappa_4 - \tfrac{1}{2}\delta_2)\theta \lesssim 1.5 \cdot 10^{-3} \cdot \mathcal{B}(h \to \mu^+\mu^-)^{-1/2} \,, \tag{4.39}$$

where we adopted $\delta_2 = 0$ and applied the relevant constraints on θ and κ_4 from equations (4.28) and (4.32), respectively.

Next, let us study the model's Higgs decay phenomenology in more detail for a set of appropriately chosen benchmark points, namely

$$m_h = 500\,\text{MeV} \,, \quad \kappa_3 = 2.45\,\text{GeV} \,, \quad \kappa_4 = 1.0 \,, \quad \theta = 2.4 \cdot 10^{-3} \,, \tag{4.40a}$$

$$m_h = 500\,\text{MeV} \,, \quad \kappa_3 = 0.50\,\text{GeV} \,, \quad \kappa_4 = 0.1 \,, \quad \theta = 0.0 \,. \tag{4.40b}$$

From a physics point of view, the former parameter point describes a scenario where the singlet sector exhibits sizable self-interactions and is relatively strongly coupled to the SM sector, with the mixing angle saturating

Point	δ_2	Γ_2 [GeV]	Γ_3 [GeV]	Γ_4 [GeV]
(4.40a)	10^{-3}	$5.3 \cdot 10^{-6}$	$1.1 \cdot 10^{-6}$	$2.0 \cdot 10^{-7}$
	10^{-2}	$4.9 \cdot 10^{-4}$	$6.4 \cdot 10^{-5}$	$8.8 \cdot 10^{-6}$
(4.40b)	10^{-3}	$4.8 \cdot 10^{-6}$	$2.6 \cdot 10^{-8}$	$2.8 \cdot 10^{-10}$
	10^{-2}	$4.8 \cdot 10^{-4}$	$2.6 \cdot 10^{-6}$	$2.8 \cdot 10^{-8}$

Table 4.1: Leading-order partial widths of Higgs decays into multiple light scalars in the low-mass regime of the singlet-extended SM. Model parameters were set according to the benchmark points from equation (4.40). The rates Γ_2 and Γ_3 were calculated based on equations (4.6) and (4.7), respectively, while `CalcHEP` [183] was used for four-body decays.

the relevant experimental bound of equation (4.28). In contrast, the latter benchmark point is characterized by small self-couplings κ_3 and κ_4, as well as by the absence of mixing in the CP-even sector.[e]

As a first step, it is useful to compute the partial widths of Higgs decays into two, three and four light scalars for the above benchmark scenarios. We list our findings in Table 4.1. Crucially, all investigated points satisfy $\Gamma_4 \ll \Gamma_3$, as is expected based on our model-independent discussion in Section 4.1.2. Accordingly, we will ignore four-body decays in the following.

Building on the results of Table 4.1, we are now in the position to calculate typical cross-sections of processes which may help to directly observe three-body scalar Higgs decays at current and near-future collider experiments. For that purpose, first recall that in the presently considered mass range, the light scalar will mainly decay into pairs of pions and muons, if the mixing angle θ is finite. In this case, the presence of the process $H \to 3h$ therefore implies the existence of very interesting signatures, where a single Higgs boson decays into six SM particles. Most spectacularly, a six-muon final state is predicted, specifically

$$H \to 3h \to 6\mu \,. \tag{4.41}$$

Apart from their uncommon particle contents, all of the possible six-body final states exhibit very peculiar kinematics. For one, final-state particles will occur in pairs of the same invariant mass m_h. Besides, the assumed mass hierarchy $m_h \ll m_H$ leads to highly boosted light scalars, whose decay products will then typically be collimated. In the currently discussed low-mass regime, the unavoidably small mixing angle and the accompanying sizable decay length of the light scalars additionally suggest that the muon and pion pairs are produced at clearly displaced secondary vertices

[e] Strictly speaking, the light scalar h is stable in the decoupling limit $\theta \to 0$. Hence, the event numbers that will be presented in Tables 4.2 and 4.3 for the benchmark point of equation (4.40b) are to be seen as lower bounds for the case of tiny mixing angles.

(cf. equation (4.37)). In conclusion, processes like the one in equation (4.41) are anticipated to offer very clean signatures with virtually no irreducible SM background.

A more quantitative study now starts with the realization that $\Gamma \ll m$ holds for both CP-even scalars. Consequently, we can employ the narrow-width approximation to compute the collider cross sections of interest:

$$\begin{aligned}\sigma_{(2n\mu)(2m\pi)} &:= \sigma_{\text{prod}} \cdot \mathcal{B}(H \to (n+m)h) \\ &\quad \cdot \mathcal{B}^n(h \to \mu^+\mu^-) \cdot \mathcal{B}^m(h \to \pi\pi) \cdot \binom{n+m}{m} \,,\end{aligned} \tag{4.42}$$

where the last factor is a binomial coefficient to properly account for combinatorics, while σ_{prod} denotes an appropriate single-Higgs production cross section and therefore depends on the collider experiment under consideration. Regardless of the Higgs production channel at hand, σ_{prod} in the singlet-extended SM is given by

$$\sigma_{\text{prod}} = \cos^2\theta \cdot \sigma_{\text{prod}}^{\text{SM}} \,,$$

with $\sigma_{\text{prod}}^{\text{SM}}$ being the corresponding cross section in the minimal SM. Also the Higgs boson's total width is modified in the singlet-extended SM, namely

$$\Gamma_H \approx \cos^2\theta \cdot \Gamma_H^{\text{SM}} + \Gamma_2 + \Gamma_3 \,,$$

where $\Gamma_H^{\text{SM}} = 4.1\,\text{MeV}$ [162] and we ignored Higgs decays into four or more light scalars. We use the above form of Γ_H together with the partial widths from Table 4.1 in order to calculate the Higgs branching ratios needed as input for equation (4.42). Similarly, employing the results from Figure 4.4, the branching fractions of a 500 MeV Higgs-like scalar are found to be $\mathcal{B}(h \to \mu^+\mu^-) = 9.1\,\%$ and $\mathcal{B}(h \to \pi\pi) = 90.9\,\%$.

Specifying a collider experiment and thereby the relevant Higgs production channel as well as the anticipated amount of data to be collected, we can now use equation (4.42) to numerically calculate expected raw event numbers of the most interesting processes involving multibody scalar Higgs decays. At the LHC, for instance, single-Higgs production at 14 TeV is dominated by gluon fusion, whose cross-section in the minimal SM is approximately $\sigma_{\text{prod}}^{\text{SM}} \approx 55\,\text{pb}$ [162]. Anticipating an integrated luminosity of $300\,\text{fb}^{-1}$ for the 14 TeV run, we list the corresponding event numbers in Table 4.2. Notably, the upcoming high-luminosity phase of the LHC (HL-LHC) is planned to deliver a total integrated luminosity of $3000\,\text{fb}^{-1}$ [25, 26] and will thus provide ten times larger statistics. Most importantly, Table 4.2 now reveals that the six-muon final state may be in reach of the LHC or its high-luminosity stage, provided that the portal coupling δ_2 is sufficiently large and contact interactions contribute substantially to the three-body Higgs decay. This is, for instance, the case for the parameter point of equation (4.40a) supplemented by the choice $\delta_2 = 10^{-2}$, for which we expect

Collider	Point	δ_2	$N_{4\mu}$	$N_{6\mu}$	$N_{4\mu2\pi}$	$N_{2\mu4\pi}$
LHC	(4.40a)	10^{-3}	177	3	99	990
		10^{-2}	14 400	171	5100	51 000
	(4.40b)	10^{-3}	162	0	2	23
		10^{-2}	14 400	7	210	2100

Table 4.2: Expected raw event numbers of selected final states in $\sqrt{s} = 14\,\text{TeV}$ pp collisions at the LHC with $300\,\text{fb}^{-1}$ of integrated luminosity. Single-Higgs production via gluon fusion is assumed.

$\mathcal{O}(100)$ events in the full 14 TeV run, or $\mathcal{O}(1000)$ events after the luminosity upgrade. In contrast, six-muon final states are unlikely to be observed at the LHC, if the quasi-decoupling scenario ($\theta \to 0$) of the second benchmark point is realized in Nature. That being said, extending our study to also include final states involving pions may allow to even probe the aforementioned quasi-decoupling case of equation (4.40b), provided δ_2 is not too small. Specifically, and regardless of the considered parameter point, the $4\mu2\pi$ and $2\mu4\pi$ channels are observed to be 30 and 300 times more abundant than the six-muon mode. At the same time, signatures containing pions are not as experimentally clean as the one consisting exclusively of muons.

The above discussion already signifies that finding the optimal search channel for Higgs decays into three light scalars will ultimately require dedicated analyses based on event and detector simulations. Only thus can one reliably compute kinematic spectra for the final-state particles, which are, in turn, crucial for determining trigger acceptances, as well as track reconstruction and particle identification efficiencies.[f] Furthermore, each potential search channel comes with its own set of relevant SM background modes, which need to be taken into account. For instance, the six muon final-state will receive non-negligible contributions from associated $t\bar{t}W$, $t\bar{t}Z$ and $t\bar{t}b\bar{b}$ production followed by (semi)leptonic decays of the produced particles. The corresponding cross-sections are, however, relatively small [186, 187]. Even more importantly, there exist several cuts which are expected to very efficiently reject the aforementioned background processes. For one, due to the signal signature's very special kinematics, asking the invariant masses of the three reconstructed muon pairs to be compatible with each other will already substantially reduce signal contamination. Moreover, events containing muons that originate from b-quark decays can be vetoed by defining suitable dimuon isolation criteria (see e.g. [188]). The above considerations

[f] In particular, collimated pairs of muons or pions that are produced at displaced vertices were seen to pose challenges to the detector's trigger and reconstruction capabilities [184, 185].

Collider	Point	δ_2	$N_{4\mu}$	$N_{6\mu}$	$N_{4\pi}$	$N_{6\pi}$
ILC	(4.40a)	10^{-3}	2	0	160	31
		10^{-2}	130	2	13 000	1550
	(4.40b)	10^{-3}	1	0	145	1
		10^{-2}	130	0	13 000	65

Table 4.3: Expected raw event numbers of selected final states in $\sqrt{s} = 250\,\text{GeV}$ e^+e^- collisions at the ILC with $500\,\text{fb}^{-1}$ of integrated luminosity. Single-Higgs production via Higgsstrahlung is assumed.

again stress the particularities of the six-muon final state, which make it a prime candidate as a search channel for extra light scalars. Still, a more thorough analysis is indispensable, but beyond the scope of this thesis.

After this short digression on more experimental aspects, let us now return to our previous discussion of interesting six-body signatures at colliders. There we explicitly saw that the large branching ratio of the light Higgs decay into pions leads to relatively sizable event yields in the corresponding final states $4\mu 2\pi$ or $2\mu 4\pi$. Although the six-pion channel would consequently provide an even higher event rate, we did not consider it before, since it is highly non-trivial to search for at the LHC, due to several reasons which include but are not limited to the overwhelming amount of QCD background. Notably, the latter issue is absent in the clean experimental environment of an electron-positron collider. However, the inclusive Higgs production cross-section is then significantly reduced with respect to hadron machines. The relatively abundant six-pion final state may therefore indeed be the most promising signature to look for Higgs decays into three low-mass scalars at future lepton colliders like the proposed 250 GeV International Linear Collider (ILC) [42–47]. Here, a single Higgs is predominantly produced in association with an on-shell Z (Higgsstrahlung). The corresponding cross-section in the minimal SM is roughly $\sigma^{\text{SM}}_{\text{prod}} \approx 300\,\text{fb}$ [43].[g] Anticipating the targeted integrated luminosity of the full initial 250 GeV run ($500\,\text{fb}^{-1}$ [189]), Table 4.3 compiles the expected raw event numbers of selected decay channels for the previously defined benchmark points from equation (4.40). Clearly, the six-muon mode is too rare to be observed at the ILC, even when taking into account the proposed luminosity upgrade to $2000\,\text{fb}^{-1}$ of accumulated data [189]. Conversely, the six-pion channel is found to yield $\mathcal{O}(1000)$ events in the more optimistic scenario of equation (4.40a), provided the portal coupling δ_2 is of order 10^{-2}. For similar values of δ_2, $\mathcal{O}(100)$ six-pion events from three-body Higgs decays are expected in

[g] For the sake of simplicity, we will assume throughout the present chapter that the ILC collects *all* of its data with polarized beams in the configuration $\mathcal{P}(e^-, e^+) = (-0.8, +0.3)$. A more detailed analysis clearly would have to take into account realistic polarization sharing scenarios as discussed in [189] and Chapter 5 of this thesis.

the conservative scenario of equation (4.40b), so that an observation may be in reach of the ILC even in this case.

Lastly, let us remark that six-body final states in the low-mass regime of the singlet-extended SM are always less abundant than their four-particle counterparts, so that a discovery of the light scalar in Higgs cascade decays will most likely occur via one of the latter. However, in the event of an actual signal in one of the four-body channels, searches for the corresponding six-particle signatures may help to distinguish the singlet-extended SM from different BSM scenarios, as well as give information about self-interactions in the singlet sector.

4.3.2 Intermediate-mass regime

Let us now briefly discuss the case of light scalars with slightly larger masses, namely between the kaon pair production threshold at $2m_K \approx 988\,\text{MeV}$ and the B-meson decay threshold at $m_B \approx 5\,\text{GeV}$. Note, however, that direct searches for scalar three-body Higgs decays at the LHC offer only limited prospects of success in the aforementioned mass region of the singlet-extended SM: On the one hand, the light scalar's couplings to SM fermions and gauge bosons remain severely constrained by precision measurements of B-meson decays. Accordingly, the mixing angle θ is still not allowed to exceed $\mathcal{O}(10^{-2})$ and the contact interaction strength λ_{H3h}, which was previously identified to be crucial for generating sizable values of Γ_3, cannot become too large. On the other hand, an increasing m_h implies a larger number of accessible final states for light scalar decays. As a consequence, the branching ratio of the cleanest decay mode, namely $h \to \mu^+\mu^-$, decreases to $\mathcal{O}(1\,\%)$ or below (cf. Figure 4.4). The most abundant final-state signatures thus unavoidably involve either mesons or jets and therefore suffer from large QCD backgrounds at a hadron collider like the LHC.

In contrast, the ILC will provide a much cleaner environment, so that the aforementioned hadronic final states may well be in reach of dedicated searches. In order to roughly assess the prospects for an observation of Higgs decays into three light scalars at the ILC, we investigate the following benchmark point

$$m_h = 1.2\,\text{GeV}\,, \quad \delta_2 = 0.01\,, \quad \kappa_3 = 5.88\,\text{GeV}\,, \quad \kappa_4 = 2.0\,, \quad \theta = 4.8 \cdot 10^{-3}\,, \tag{4.43}$$

where we assume relatively strong interactions in the spirit of the previously discussed rather optimistic scenario of equation (4.40a). Our results are compiled in Table 4.4 and demonstrate that six-meson final states can indeed occur in reasonably large numbers. However, as before in the low-mass regime, a more detailed analysis of the detector performance and the relevant SM background processes will be necessary to arrive at robust statements about the sensitivity of the ILC to the considered channels.

$\mathcal{B}$ [%]	$H \to 2h$	$H \to 3h$	$h \to \mu^+\mu^-$	$h \to \pi\pi$	$h \to \bar{K}K$
	12.3	1.77	2.3	10.5	87.2
ILC	N_{4K}	N_{6K}	$N_{6\pi}$	$N_{2\mu 4K}$	$N_{2\pi 4K}$
	14 071	1760	3	139	636

Table 4.4: Higgs boson and light scalar branching ratios for the intermediate-mass benchmark point (4.43), as well as the corresponding expected raw event numbers of selected final states in $\sqrt{s} = 250\,\text{GeV}$ e^+e^- collisions at the ILC with $500\,\text{fb}^{-1}$ of integrated luminosity. Single-Higgs production via Higgsstrahlung is assumed.

4.3.3 High-mass regime

Let us finally investigate the case of light scalars which are heavier than the B-meson decay threshold at $m_B \approx 5\,\text{GeV}$ while still satisfying $m_h \ll m_H$. Most importantly, the thus defined mass range was previously demonstrated to allow for relatively large mixing angles of up to $\theta = \mathcal{O}(0.1)$, cf. equation (4.29). This entails two major consequences for the phenomenology of scalar Higgs decays in the singlet-extended SM.

On the one hand, the three-body channel can now receive substantial contributions from the contact interaction diagram of Figure 4.1a. Specifically, applying the aforementioned constraint on θ as well as the perturbativity bound on κ_4 from equation (4.32), we can estimate the maximum possible value of the associated coupling λ_{H3h} to be

$$\lambda_{H3h} \simeq (\kappa_4 - \tfrac{1}{2}\delta_2)\theta \lesssim 0.2\,, \tag{4.44}$$

where we used the approximate formula for λ_{H3h} of equation (4.27), and assumed δ_2 to be negligibly small. In the presently discussed scenario, λ_{H3h} may thus attain values which are at least one order of magnitude larger than in the low- and intermediate-mass regimes, cf. equation (4.39). In particular, the model-independent bound from equation (4.15) may even be saturated.

On the other hand, larger mixing angles may lead to anomalously small decay rates for the two-body process $H \to 2h$. To see why, it is instructive to have a closer look at the small-θ expansion of the corresponding generic coupling κ_{H2h} in equation (4.27). Here, the first-order term can become of similar size as the leading-order contribution, provided θ is sufficiently large. Specifically, an explicit calculation reveals that a cancellation up to second order in θ will occur in κ_{H2h}, if the following relation is fulfilled

$$\kappa_{H2h} \overset{!}{=} \mathcal{O}(\theta^2) \quad \Leftrightarrow \quad \frac{\kappa_3}{m_h} \simeq -0.12 \cdot \left(\frac{0.1}{\theta}\right)\left(\frac{10\,\text{GeV}}{m_h}\right)\left(\frac{\delta_2}{10^{-3}}\right)\,. \tag{4.45}$$

Notably, for mixing angles much smaller than $\mathcal{O}(0.1)$, the above condition and the unitarity bound on κ_3 in equation (4.31) can only be simultaneously satisfied for negligibly small δ_2. Cancellations in κ_{H2h} are therefore

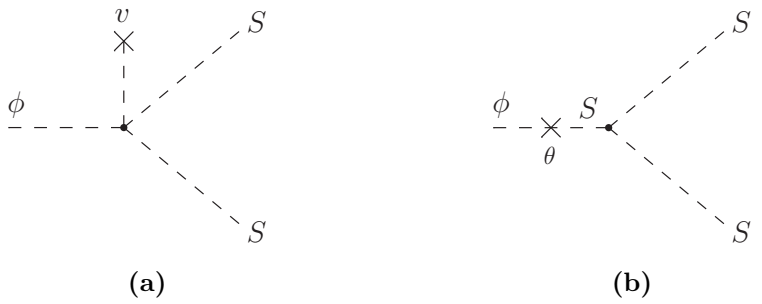

Figure 4.7: Illustration of the cancellations in the effective coupling κ_{H2h} using Feynman diagrams involving the scalar gauge eigenstates ϕ and S. The displayed graphs are those contributing to the process $H \to 2h$ at first order in θ. Correspondingly, we obtained the identity $\kappa_{H2h} = \frac{1}{2}\delta_2 v + \kappa_3 \theta + \mathcal{O}(\theta^2)$ in equation (4.27).

phenomenologically irrelevant in the low- and intermediate-mass regimes, where θ cannot exceed $\mathcal{O}(10^{-2})$ and tiny δ_2 were seen to render the rates of all scalar Higgs decays unobservably small. Let us furthermore remark that the aforementioned cancellations can also be understood as those between the leading Feynman diagrams contributing to the effective coupling κ_{H2h} (cf. Figure 4.7).

As a first step towards assessing the phenomenological relevance of three-body scalar Higgs decays in the high-mass regime, we again analyze the behavior of the ratio $r = \Gamma_3/\Gamma_2$ in the δ_2-κ_3 plane. Our results for a 5 GeV and a 10 GeV light scalar are shown in Figure 4.8, where we additionally assumed sizable quartic self-interactions in the singlet sector as well as a relatively large mixing of the CP-even scalar degrees of freedom, namely

$$\kappa_4 = 1.0 \quad \text{and} \quad \sin\theta = 0.08 \,. \tag{4.46}$$

Interestingly, the plots demonstrate that in a substantial part of the viable parameter space, the model predicts three-body decays to be more abundant than their two-body counterparts, i.e. $r > 1$. In particular, the above-described cancellation in κ_{H2h} leads to greatly enhanced values of r roughly along the line defined by equation (4.45).

Building on the previous results and for the purpose of getting a first hint on the detection prospects for multi-scalar Higgs decay events at colliders, we multiply the found Higgs branching fractions by appropriate single-Higgs production cross-sections. The outcome is presented in Figure 4.9 as a function of δ_2. A few comments on the resulting plots are in order. First, note that we again study the benchmark point introduced in equation (4.46) supplemented by the choice $\kappa_3 = 0$. In doing so, we juxtapose the findings for a 5 GeV with those for a 10 GeV light scalar, but do not observe any interesting differences, so that we will discuss the two cases entirely in parallel. Second, we compare the expected performances of the 14 TeV LHC and the

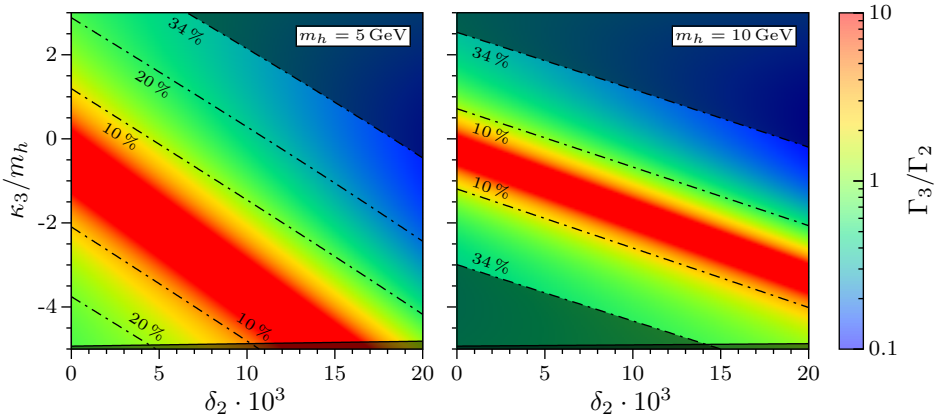

Figure 4.8: Ratio $r = \Gamma_3/\Gamma_2$ in the singlet-extended SM as a function of δ_2 and κ_3 for $\sin\theta = 0.08$ and $\kappa_4 = 1.0$. The light scalar's mass was set to 5 GeV (*left*) and 10 GeV (*right*), respectively. Contours of constant scalar Higgs branching fraction $\mathcal{B}_{\mathrm{scalar}}$ are drawn as black dash-dotted lines. The large shaded areas are excluded by Higgs signal strength measurements as per equation (4.11). Similarly, the thin dark bands on the bottom of each plot are ruled out by tree-level perturbative unitarity according to equation (4.19).

250 GeV ILC. As before, the ILC results are based on single-Higgs production via Higgsstrahlung, whereas those for the LHC now assume the Higgs to be produced in association with an on-shell W-boson, which is furthermore supposed to decay leptonically. Although the corresponding cross-section of only $\sigma^{\mathrm{SM}}_{\mathrm{prod}} \approx 0.17\,\mathrm{pb}$ [162] is significantly smaller than those of the gluon fusion (ggH) or vector boson fusion (VBF) channels, the presence of the extra lepton is essential in cases where the Higgs cascade decay produces jets only. Namely, said lepton can then be employed for providing the trigger and for rejecting background events. If, however, at least one of the light scalars decays into a pair of tau leptons, there is a reasonably high chance of an electron or a muon from tau decays being present in the final state, which could then be used for the above purposes. Correspondingly, in these cases it is meaningful to also consider VBF or ggH as possible Higgs production channels which would enhance the numbers presented here by roughly one or two orders of magnitude, respectively.

Crucially, Figure 4.9 now reveals two interesting aspects about scalar Higgs decays in the high-mass regime of the singlet-extended SM. On the one hand, the three-body channel possesses a considerably large cross section, which is found to stay roughly constant over the entire investigated δ_2 range. On the other hand, the two-body mode's rate can become negligibly small, namely in the vicinity of the point of cancellation approximately defined by equation (4.45). Consequently, there exist regions in the model's parameter space, where direct searches for the light scalar h exploiting six-particle final states may be successful, while looking for conventional four-body channels

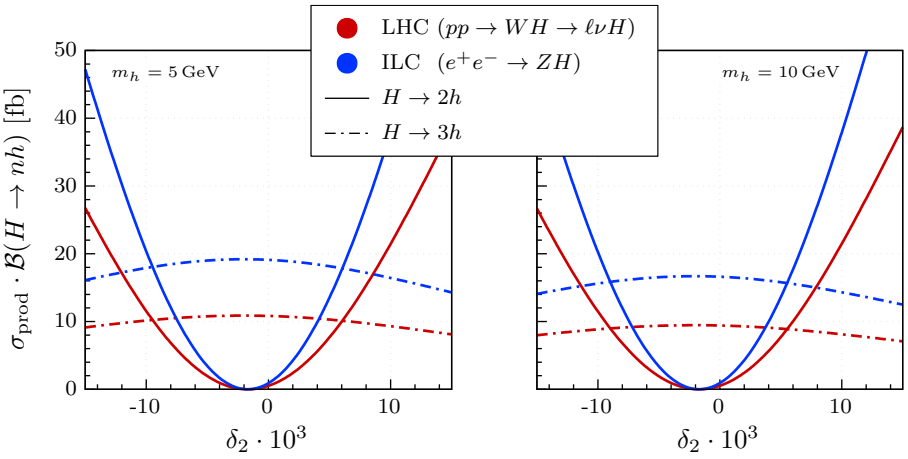

Figure 4.9: Higgs production cross section times branching fraction for its decays into two or three scalars in the singlet-extended SM as functions of δ_2. The light scalar's mass was set to 5 GeV (*left*) and 10 GeV (*right*), respectively, while the remaining model parameters were fixed at $\sin\theta = 0.08$, $\kappa_3 = 0$ and $\kappa_4 = 1.0$. The expectations for the 14 TeV LHC (red) are compared to those for the 250 GeV ILC.

will inevitably produce null results. Notably, Figure 4.8 suggests that results similar to those in Figure 4.9 are to be expected for other values of κ_3 as well, but with curves that are appropriately shifted in δ_2.

Finally, a more thorough study of scalar Higgs decay phenomenology clearly requires knowledge about the exclusive cross sections for given four- or six-body final states. Said cross sections can easily be obtained by multiplying our previous results from Figure 4.9 by suitable branching ratios of light scalar decays and by potential combinatorial multiplicities, cf. equation (4.42). From Figure 4.4 we know that a Higgs-like scalar in the considered mass range mainly decays into tau leptons or jets. The associated branching fractions are

$$\mathcal{B}(h \to \tau^+\tau^-) = 20.7\,\%\,, \quad \mathcal{B}(h \to jj) = 79.1\,\% \quad \text{for } m_h = 5\,\text{GeV and}$$
$$\mathcal{B}(h \to \tau^+\tau^-) = 23.5\,\%\,, \quad \mathcal{B}(h \to jj) = 76.3\,\% \quad \text{for } m_h = 10\,\text{GeV}\,,$$

where j denotes any jet regardless of its flavor. While for a 5 GeV light scalar c-quark and gluon jets are most relevant, a 10 GeV scalar can additionally decay into a pair of b-quarks. Obviously, cascade decays of the 125 GeV Higgs boson thus may entail an enormous variety of conceivable four- or six-body final states, which will all differ in terms of cleanliness and abundance. Restricting to the case where the initial Higgs decay is into *two* light particles, comprehensive overviews of the possible search channels' sensitivities were given both for the LHC [39] and for future electron-positron machines [190]. In our study, we also include *three*-body scalar Higgs decays and list the expected raw event numbers of selected final states in Table 4.5. Our findings confirm that there exist scenarios where the four-body modes

Collider	m_h	$\delta_2 \cdot 10^3$	$N_{4\tau}$	$N_{6\tau}$	$N_{4\tau 2j}$	$N_{2\tau 4j}$
LHC	5 GeV	−2	71	9262	106 500	408 000
		5	31 610	8763	100 700	386 000
	10 GeV	−2	83	11 940	116 100	376 500
		5	41 250	11 300	109 900	356 400

(a) Expectations for the 14 TeV LHC with 300 fb^{-1} of accumulated data assuming single-Higgs production via gluon fusion.

Collider	m_h	$\delta_2 \cdot 10^3$	$N_{4\tau}$	$N_{6\tau}$	$N_{4\tau 2j}$	$N_{2\tau 4j}$
ILC	5 GeV	−2	1	84	968	3709
		5	287	80	916	3509
	10 GeV	−2	1	109	1056	3423
		5	375	103	999	3240

(b) Expectations for the 250 GeV ILC with 500 fb^{-1} of accumulated data assuming single-Higgs production via Higgsstrahlung.

Table 4.5: Expected raw event numbers of selected final states for a 5 GeV and a 10 GeV light scalar. The remaining model parameters were fixed at $\sin\theta = 0.08$, $\kappa_3 = 0$ and $\kappa_4 = 1.0$.

are strongly suppressed, while their six-body counterparts are reasonably abundant and may thus be in reach of dedicated searches. As before, deriving robust statements about the considered channels' actual sensitivities requires event and detector simulations, as well as a thorough discussion of possible SM background processes.

4.4 Summary and conclusion

Following our original study in [49], this chapter presented a detailed account on decays of the 125 GeV Higgs boson H into multiple light scalar particles h both from a model-independent point of view and in the context of a specific theory of new physics, namely the real singlet extension of the Standard Model (SM). While the existing literature on exotic Higgs decays either ignores the three-body channel $H \to 3h$ completely or discards it as being irrelevant, we included it in our discussion and systematically identified scenarios in which it can become important for beyond-the-SM (BSM) phenomenology.

In our model-independent analysis, we first argued that the three-body decay process is mediated by two classes of Feynman diagrams (see Figure 4.1). Specifically, apart from renormalizable contact interactions due to the dimension-four operator Hh^3, it is induced by the exchange of virtual light

scalars. Importantly, contributions of the latter type to the relevant decay rate $\Gamma_3 := \Gamma(H \to 3h)$ were demonstrated to be fundamentally limited by requiring perturbative unitarity in two-to-two scalar scattering processes. In the absence of contact interactions, the two-body decay $H \to 2h$ was correspondingly found to dominate, with rates exceeding those of the three-body channel always by at least one order of magnitude. By implication, sizable yet theoretically consistent contact interactions were proven to be absolutely crucial for elevating Γ_3 beyond its two-body counterpart Γ_2. Interestingly, a comparable enhancement mechanism is missing for Higgs decays into more than three light scalars. Rather, the lack of *renormalizable* contact interactions and the still valid restrictions on the scalar couplings imposed by perturbative unitarity suggest that those processes are always significantly less abundant than the two- and three-body modes. *Non-renormalizable* contact operators of mass dimension $n + 1$ may, of course, also contribute to Higgs decays into n light scalars for $n > 3$, but are necessarily suppressed by some heavy mass scale.

In the second part of the present chapter, we applied our previously obtained results to the singlet-extended SM. Here, the particles' quantum numbers imply the existence of mass mixing between the SM Higgs doublet's CP-even degree of freedom and the new scalar gauge singlet after electroweak symmetry breaking. Contributions to the three-body Higgs decay hence come from both contact interactions and h-exchange. As a first important result, we showed that the size of the former is proportional to the scalar mixing angle θ, while that of the latter stays finite even in the decoupling limit $\theta \to 0$. A relatively large quartic self-coupling in the singlet sector was established as a second prerequisite for sizable contact interactions and thereby for substantial values of Γ_3. We then argued that collider phenomenology of multibody scalar Higgs decays strongly depends on the mass of the light scalar since the latter determines its main decay channels and also the allowed mixing with the physical 125 GeV Higgs boson.

In the low- and intermediate-mass regimes defined by $360\,\text{MeV} \lesssim m_h \lesssim 5\,\text{GeV}$, the light scalar predominantly decays into pairs of muons, pions or kaons, and the mixing angle is tightly limited by high-precision measurements of meson decays, which necessitates the contact contribution to Γ_3 to be relatively small. Accordingly, three-body decay rates were found to be consistently exceeded by their two-body counterparts. Therefore, a potential discovery of the light scalar sector through Higgs decays would likely proceed via the two-body process in this mass region. However, we demonstrated that the three-body mode may still be sufficiently abundant to be observable in various six-particle final states. Specifically, regarding direct searches at the 14 TeV LHC or its high-luminosity upgrade, the most interesting signature was argued to involve six muons. Similarly, the Higgs cascade decay into six pions was calculated to occur frequently enough to be potentially in reach of the proposed 250 GeV ILC.

In the high-mass regime characterized by light scalars above the B meson threshold at roughly 5 GeV, experimental constraints on the mixing angle relax. The light scalar now mainly decays into pairs of tau leptons or jets. In accordance with expectations, substantial mixing in the scalar sector was shown to entail large rates of the three-body decay mode, provided quartic self-interactions of the scalar singlet field were not too small. As a consequence, several six-particle final states were demonstrated to be reasonably abundant, so that they offer good prospects for direct searches at the 14 TeV LHC or the 250 GeV ILC. Interestingly, a sizable mixing angle of order 0.1 was also found to allow for scenarios where the two-body scalar Higgs decay channel has an anomalously small rate and is therefore undetectable. In these cases, the three-body mode might be the only remaining way to directly observe extra light scalars in Higgs decays.

Regardless of the light scalar's mass, there are a few other aspects which were argued to render three-body scalar Higgs decays particularly suited for studying the scalar sector of the singlet-extended SM. First, the aforementioned six-body signatures were seen to exhibit very peculiar kinematics in that the final-state particles will occur in three pairs of the same invariant mass m_h. This special property can be exploited to effectively reduce signal contamination due to SM processes in an actual analysis, which lead us to expect that, for instance, the six-muon final state is virtually free of any SM background. But also searches for other six-particle signatures would, of course, profit from said specific kinematic configuration. Second, the three-body channel was shown to be the only realizable approach towards probing self-interactions in the singlet sector at current or near-future collider experiments.

Let us stress that Higgs decays into three light scalars as well as the associated merits just described are by no means exclusive to the singlet-extended SM. Rather, it is a common feature of a large variety of models including theories where some light scalar degree of freedom mixes into the physical Higgs boson. Importantly, the properties of the underlying model will determine the details of its scalar decay phenomenology, such as the possible range of the ratio Γ_3/Γ_2, the light scalar's dominant decay channels etc. Correspondingly, information drawn from dedicated searches for three-body scalar Higgs decays may also be used to discriminate different BSM scenarios, which would otherwise be indistinguishable. A more systematic phenomenological investigation of contemplable models is, however, needed for that purpose.

Although the results presented in this chapter already seem very promising, deriving robust statements about whether or not three-body scalar Higgs decays may be observable in near-future collider runs will require dedicated analyses based on event and detector simulations. Only thus can one reliably compute kinematic spectra for the final-state particles, which are, in turn, crucial for determining trigger acceptances, as well as track re-

construction and particle identification efficiencies. Along the same lines, a thorough discussion of potential SM background processes will be essential.

In conclusion, the previously ignored Higgs decay into three light scalars was demonstrated to offer exciting possibilities to search for new physics, thereby complementing existing approaches which focus exclusively on the related two-body decay. Specifically, it provides an experimentally straightforward option to probe a variety of BSM theories with extended scalar sectors, as well as to distinguish between different models of said kind.

Chapter 5

Quark-flavor-violating Higgs boson decays at the ILC

In the previous chapter, we have discussed an example of how the search for exotic Higgs boson decays may help to directly test new physics at present and near-future collider experiments. Assuming the existence of additional light scalar degrees of freedom, it was argued that new final states for Higgs decays become accessible and that their (non-)observation can be employed to constrain beyond-the-Standard Model physics scenarios.

In the present chapter, we will take a similar, yet still somewhat complementary approach towards finding new physics via non-standard Higgs couplings. To be more precise, we will investigate cases where the Higgs boson decays into well-known particles, but in a way which is not to be expected in the minimal Standard Model (SM). Observing processes of this kind would still be a direct proof of physics beyond the SM (BSM), even though no new particle species are directly detected in this way. Specifically, such unexpected Higgs interactions would be interpreted as residual effects of extra heavy particles associated to new physics. This is the usual effective field theory (EFT) approach to BSM theories.

Concretely, we will study Higgs decays into pairs of *different*-flavor quarks in this chapter. In order to understand why processes of this kind are indeed worth investigating, recall our discussion of the SM Yukawa sector from Chapter 2. As we have explicitly shown there, flavor-changing neutral currents (FCNC) do not exist in the SM at tree-level. In particular, this implies that the Higgs boson only couples to pairs of *same*-flavor fermions at the classical level (cf. equation (2.10)). Nevertheless, the inclusion of quantum effects does induce flavor-violating Higgs interactions also in the SM. In the absence of new physics the corresponding processes are, however, not only loop- but also GIM suppressed [54]. Consequently, the associated rates predicted by the SM are tiny. For instance, the Higgs decay into a bottom and an anti-strange quark, $H \to b\bar{s}$, can be calculated to have a branching ratio

of order 10^{-7} [191], which makes it undetectable at the LHC and all near-future collider experiments. Obviously, any direct observation of a Higgs interaction that is non-diagonal in flavor space would therefore be an unambiguous sign of physics beyond the SM. Indeed, there exists quite a number of well-motivated SM extensions which predict sizable flavor-violating Higgs couplings. Examples include but are not limited to supersymmetric models [191–194], two-Higgs-doublet models [144, 195–197], models with a composite Higgs [198] and models of extra dimensions [199, 200].

Correspondingly, the ATLAS and CMS collaborations put great effort into searching non-diagonal Higgs-fermion interactions. In doing so, they mostly concentrate on flavor-violating Higgs decays into pairs of charged leptons. In particular, a dedicated CMS analysis of the 8 TeV dataset from 2012 showed a slight excess in the channel $H \to \mu\tau$ [201]. However, an ATLAS search for the same process and also based on 8 TeV data observed no statistically significant deviation from the SM expectations [202]. Furthermore, a recent CMS study using a data sample collected in proton-proton collisions at a center-of-mass energy of 13 TeV could not confirm the aforementioned indication for a non-zero branching fraction $\mathcal{B}(H \to \mu\tau)$ [203]. Searches for the other leptonic channels, $H \to e\tau$ and $H \to e\mu$, did not find any evidence of a signal, either [203–205].

In contrast to the leptonic case, quark-flavor-violating (QFV) Higgs interactions receive considerably less attention at the moment. This is mainly for two reasons. First, indirect constraints on QFV Higgs couplings coming from low-energy flavor measurements are usually much stronger than comparable bounds in the lepton sector. Accordingly, one generally expects QFV Higgs decays to occur at a lower rate [41].[a] Second, when it comes to the detection of rare processes with final states involving only quarks, the capabilities of the LHC are inherently limited due to the large amount of QCD background. Both restrictions are circumvented to some degree in the case of flavor-violating Higgs couplings to the top quark. Here, low-energy constraints are the least stringent ones in the quark sector [41] and the observed mass spectrum allows for searches in exotic top decays $t \to Hq$, with q being either a charm or an up quark [206, 207]. In contrast, both of the aforementioned limitations – tiny branching ratios and enormous QCD background – apply to QFV Higgs decays involving bottom quarks. Hence, processes like $H \to bj$, with j representing a light quark, are extremely challenging for the LHC, even taking into account its high-luminosity phase, where $\mathcal{O}(3000\,\text{fb}^{-1})$ of data will be collected.

The physical relevance of *direct* searches for QFV Higgs decays as an approach complementary to *indirect* low-energy measurements is still beyond any doubt. If, for instance, deviations from the SM predictions are observed in some experiment, only direct measurements are able to pin down their

[a] We will quantitatively discuss the corresponding relation in Section 5.2.

exact origin and to give us a handle on determining the values of the new couplings involved. Furthermore, conclusions drawn from indirect searches may be invalidated due to cancellations in relevant processes as they appear in certain models of new physics (see e.g. [191] or [197]). It is therefore essential to assess whether proposed future colliders will provide capabilities for directly searching those QFV processes for which the LHC's sensitivity is insufficient. In particular, e^+e^- colliders are interesting in this context, since they offer a much cleaner environment compared to hadron accelerators like the LHC. Of the several e^+e^- projects that are currently proposed, the International Linear Collider (ILC) is certainly the most mature one.

In line with the above discussion, the following chapter will focus on QFV Higgs decays into a bottom and a light quark and analyze the prospects for detecting or constraining these processes with the ILC. As our main result, we will demonstrate that the achievable performance is comparable to or surpasses that of currently available indirect measurements. The chapter is thereby organized as follows. Since it is crucial for understanding the rest of our study, we will begin with a basic introduction to the ILC and its planned Higgs physics program in Section 5.1. Afterwards, in Section 5.2, we briefly outline the theoretical background of effective QFV Higgs interactions and summarize existing indirect limits on the corresponding couplings. Section 5.3 then offers a detailed description of our numerical analysis and contains the main results of the present chapter. We summarize our findings in Section 5.4.

5.1 The ILC and Higgs physics

In the introduction we argued that quark-flavor-violating Higgs decays involving bottom quarks are unlikely to be in reach of the LHC considering the already existing rather stringent indirect constraints and the large amount of QCD background at a hadron collider. In contrast, electron-positron machines with their clean experimental environments may offer the ideal conditions to *directly* measure the aforementioned exotic Higgs processes. Indeed, there exist proposals for several high-luminosity e^+e^- colliders – both linear and circular – which we summarize in Table 5.1.

From all proposals, the ILC arguably has the best chance of being realized in the near future, which is why we concentrate on it in the following. According to its technical design report (TDR), the ILC baseline machine is planned to operate at center-of-mass energies of up to 500 GeV,[b] with

[b] As a measure of cost reduction and to further the realization of the ILC, an alternative to the baseline 500 GeV machine was put forward in late 2017 [47]. This option advocates to build a 250 GeV collider first, which might eventually be extended to higher energies. The physics case for such a 250 GeV stage is summarized in [214, 215]. Note that the staging report [47] was published after our work [50] had been completed. Correspondingly, the analyses presented in this chapter will take the 500 GeV machine as a basis.

Name	collider	$\sqrt{s}$ [GeV]	beam polarization	R&D status
ILC	linear	90–1000	$\lvert\mathcal{P}(e^-)\rvert = 0.8$ $\lvert\mathcal{P}(e^+)\rvert = 0.3$	TDR [42–47]
CLIC	linear	350–3000	$\lvert\mathcal{P}(e^-)\rvert = 0.8$ $\lvert\mathcal{P}(e^+)\rvert = 0.0$	CDR [208–211]
CEPC	circular	90–250	–	preliminary CDR [212, 213]
FCC-*ee*	circular	90–350	–	CDR expected by the end of 2018

Table 5.1: Overview of proposals for future electron-positron colliders. Included are the International Linear Collider (ILC), the Compact Linear Collider (CLIC), the Circular Electron Positron Collider (CEPC) and the Future Circular Collider's e^+e^- mode (FCC-*ee*).

the accelerating technology being entirely based on superconducting radio frequency cavities. A possible upgrade to a 1 TeV machine is also discussed. For the ILC's time of operation different running scenarios are considered, the most prominent of which is dubbed H-20 and involves physics runs at 250 GeV, 350 GeV and 500 GeV [189]. One crucial advantage of a linear collider such as the ILC over a circular machine is the possibility to realize polarized particle beams. Correspondingly, the baseline design of the ILC includes both polarized electron and positron beams, specifically $\mathcal{P}(e^-) = \pm 0.8$ and $\mathcal{P}(e^+) = \pm 0.3$, where the plus (minus) sign means running mainly with right- (left-)handed particles. From a physics point of view, beam polarization comes with several benefits. On the one hand, the cross sections of some interesting processes are enhanced. The prime example in this context is, of course, Higgs production (cf. Figure 5.1). At the same time, the use of polarized beams will suppress certain background channels. For instance, due to the W boson's chiral couplings, the rate of W pair production is greatly reduced in the $(+0.8, -0.3)$ configuration. On the other hand, there are some observables which are only made accessible by the use of beam polarization. Note furthermore that since all of the four possible polarization combinations come with their own advantages and drawbacks, it was proposed to distribute the full integrated luminosity among the different configurations [189].

Apart from the accelerator, the TDR also provides the baseline designs for two detectors, which are proposed to be placed in a so-called push-pull configuration at the single interaction point: the International Large Detector (ILD) and the Silicon Detector (SiD) [46]. A detailed description of these detectors and all of their individual components would be beyond the scope of this section. Rather, we will only briefly mention one particular

feature provided by both detectors, which will turn out to be crucial in the search for QFV Higgs decays, namely high-purity and high-efficiency jet-flavor tagging. In particular, very precise vertex detectors will facilitate to distinguish displaced charm from bottom vertices and thus enable the identification of charm jets (c-tagging, see e.g. [46, 216] for details). We finally remark that both the ILD and the SiD allow to record all events on tape, i.e. no on-line triggers are required unlike for the detectors at the LHC.

After this short summary of the ILC's baseline design, let us now review its physics case. Extensive discussions on the complete physics program at linear electron-positron colliders in general [217], at the ILC baseline machine [218] and at its 250 GeV stage [214, 215] can be found in the given references. One of the ILC's major physics goals is the precise determination of the Higgs boson's properties.[c] For instance, measurements of the Higgs's mass and its width can be performed with unprecedented precision and in a model-independent way by exploiting the so-called recoil mass technique, which allows to tag a Higgs boson without having to detect any of its decay products. Of course, also the Higgs boson's interactions are planned to be investigated in detail. For one, measurements of its couplings to most of the known SM fermions and gauge bosons with a precision of $\mathcal{O}(1\,\%)$ (or even better) will become possible. Furthermore, a model-independent determination of the Higgs trilinear self-coupling [220] will give information about the exact form of the Higgs potential and may therefore provide further insight into the nature of electroweak symmetry breaking. Lastly, interactions of the Higgs not predicted by the SM are of interest as well. In particular, invisible or other exotic Higgs decays will be searched for. It is this last category, to which belong the QFV Higgs decays discussed in the present chapter.

For the sake of learning how to identify these and other Higgs processes at the ILC, it is important to fully understand the ways in which the Higgs boson is produced at an e^+e^- machine. Correspondingly, we show the most relevant processes for single Higgs production at the ILC alongside with their cross-sections in Figure 5.1. The plot demonstrates that the inclusive production cross section reaches its maximum close to $\sqrt{s} = 250\,\text{GeV}$, which explains why running at this center-of-mass energy is crucial for the ILC to achieve its aforementioned goals. The by far dominant contribution at 250 GeV originates from the so-called Higgsstrahlung process, $e^+e^- \to ZH$, where the Higgs is produced in association with a Z boson (Figure 5.1b). Depending on the Z decay mode, this offers several different event signatures whose advantages and drawbacks will be discussed in the following.

First, Z decays into pairs of same-flavor quarks are the most frequent ones with a branching fraction of $\mathcal{B}(Z \to q\bar{q}) \simeq 70\,\%$ [83] (*hadronic channel*). At the same time, they produce the least clean final state, in particular in

[c] A comprehensive review on Higgs physics at the ILC is given in [219].

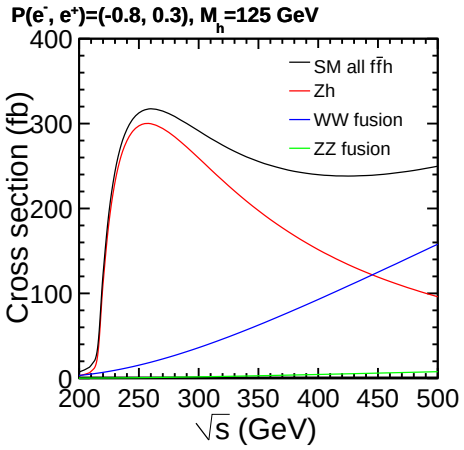

(a)

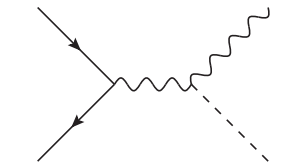

(b) Higgsstrahlung

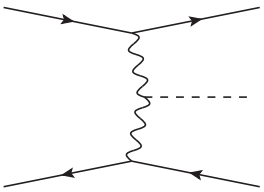

(c) Vector boson fusion

Figure 5.1: Single-Higgs boson production cross-sections at the ILC as functions of center-of-mass energy $\sqrt{s}$. The most relevant production channels are Higgsstrahlung or Z-associated Higgs production, $e^+e^- \to ZH$ (*red*), W boson fusion, $e^+e^- \to \nu_e\bar{\nu}_e H$ (*blue*) and Z boson fusion, $e^+e^- \to e^+e^- H$ (*green*). Importantly, all major production modes rely on the Higgs coupling to the massive electroweak gauge bosons, see equation (2.21). The plot assumes a Higgs mass of $m_H = 125\,\text{GeV}$ and a beam polarization of $\mathcal{P}(e^-, e^+) = (-0.8, +0.3)$. Figure (a) taken from [43].

cases where the Higgs boson decays hadronically as well. The resulting four- or six-jet signatures then suffer from both a large SM background and from combinatorial ambiguities which arise in associating the jets to the Z and Higgs decays [221]. We will evaluate the hadronic search channel's performance in the context of QFV Higgs decays in Section 5.3.2.

Next, let us consider Z decays into electron or muon pairs (*charged lepton channel*). Being electrically charged and detector-stable, these particles can be reconstructed and identified with high efficiency. The aforementioned recoil mass technique then allows to reliably tag a produced Higgs regardless of its decay products and only using observables related to lepton kinematics. Hence, the charged lepton channel plays a crucial role in precisely determining Higgs couplings and properties in a model-independent fashion. However, it is statistically limited due to the small branching ratio $\mathcal{B}(Z \to \ell^+\ell^-) := \mathcal{B}(Z \to e^+e^-) + \mathcal{B}(Z \to \mu^+\mu^-) \simeq 6.7\,\%$ [83]. It may therefore not be the optimal choice if the sought-after Higgs decay itself only occurs at a small rate. The sensitivity of a search for the QFV process $H \to bj$ in the charged lepton channel is investigated in Section 5.3.3.B.

Lastly, invisible Z decays into neutrino pairs with a branching fraction of $\mathcal{B}(Z \to \nu\bar{\nu}) \simeq 20\,\%$ [83] are of interest (*neutrino channel*). Apart from the Higgs decay products, the signature then only contains missing energy. Clearly, the corresponding final states are not as clean as those with a pair

of charged leptons. At the same time, they do not suffer from the high jet multiplicity as does the hadronic channel. Accordingly, the neutrino search mode is usually a reasonable compromise between cleanliness and event rate. Its performance in the context of QFV Higgs decays will be studied in Section 5.3.3.C.

As already mentioned earlier, production channels other than Higgs-strahlung are negligible at a center-of-mass energy of 250 GeV. In contrast, Figure 5.1 demonstrates that during an ILC run at $\sqrt{s} = 500\,\text{GeV}$ most Higgs bosons are produced through W-fusion, the cross section of which is then roughly 160 fb. The resulting final-state signature, containing the Higgs decay products along with missing energy, is obviously very similar to that of the neutrino mode of Z-associated Higgs production discussed above. The latter contributes with a cross section of about 20 fb at a 500 GeV run. The sensitivity of a search for the QFV process $H \to bj$ in this combined neutrino channel is evaluated in Section 5.3.3.C.

5.2 Theoretical framework and indirect constraints

As we have seen in the introduction to this chapter, there exist many theories of beyond-the-SM (BSM) physics, which predict flavor violation in the Higgs sector. In order to be able to apply our results to a broad range of BSM scenarios, our analysis should be as model independent as possible. A first step towards realizing this goal is the following observation: Many of the aforementioned models have in common that they introduce new physics associated to extra heavy particles. However, for understanding the phenomenology of those models at around the electroweak scale, the dynamics of such heavy degrees of freedom or, to be more general, the precise knowledge of the models' high-energy details should not be relevant. The theoretical foundation for this heuristic argument is a theorem due to Appelquist and Carazzone [222] which describes how heavy particles decouple at energies far below their mass. The corresponding technical implementation goes by the name of effective field theory (EFT) and offers a way to parameterize new physics effects at low energies in a model-independent way.[d] This parameterization employs non-renormalizable operators invariant under the SM gauge group and composed of SM fields only.

Assuming that just the known SM particles are dynamical degrees of freedom below the electroweak scale, while all additional fields are sufficiently heavy to be integrated out, we can use the EFT language and parameterize the interactions of the Higgs with two down-type quarks accordingly. The lowest-order operator is then given by the SM Yukawa term in equation (2.8). The first operators which potentially lead to non-standard contributions to down-type Yukawa couplings are of mass dimension 6. In the

[d] For an introduction to EFT, see e.g. [223].

so-called Warsaw basis they read [224]

$$\mathcal{Q}_d^{ij} = (\overline{Q}_L^i \Phi d_R^j)(\Phi^\dagger \Phi) \,, \tag{5.1a}$$

$$\mathcal{Q}_{Hq}^{ij} = (\overline{Q}_L^i \gamma^\mu Q_L^j)(\Phi^\dagger \mathrm{i}\overleftrightarrow{D}_\mu \Phi) \,, \tag{5.1b}$$

$$\mathcal{Q}_{Hq}'^{ij} = (\overline{Q}_L^i \sigma^k \gamma^\mu Q_L^j)(\Phi^\dagger \mathrm{i}\overleftrightarrow{D}_\mu^k \Phi) \quad \text{and} \tag{5.1c}$$

$$\mathcal{Q}_{Hd}^{ij} = (\bar{d}_R^i \gamma^\mu d_R^j)(\Phi^\dagger \mathrm{i}\overleftrightarrow{D}_\mu \Phi) \,. \tag{5.1d}$$

Here, we have used the notation for the SM fields introduced in Chapter 2 (see Table 2.1). Moreover, we have defined $\Phi^\dagger \mathrm{i}\overleftrightarrow{D}_\mu \Phi = \Phi^\dagger \mathrm{i} D_\mu \Phi + (\mathrm{i} D_\mu \Phi)^\dagger \Phi$ and $\Phi^\dagger \mathrm{i}\overleftrightarrow{D}_\mu^k \Phi = \Phi^\dagger \sigma^k \mathrm{i} D_\mu \Phi + (\mathrm{i} D_\mu \Phi)^\dagger \sigma^k \Phi$ with the Pauli matrices σ^k. Even though the terms in equations (5.1b) to (5.1d) are of the correct form, it can be shown that they do not produce Higgs couplings to a quark pair upon EWSB [41]. Adding the remaining operator $\mathcal{Q}_d$ to the Lagrangian of equation (2.8), we must again find the quark mass eigenstates once the Higgs has acquired a finite vev. However, unlike in the steps that lead to equation (2.10), the presence of $\mathcal{Q}_d$ implies that the mass and Yukawa matrices are in general misaligned and can therefore not be diagonalized simultaneously. The effective down-type quark Yukawa sector after EWSB in the fermion *mass* basis is [41]

$$-\mathcal{L}_{\text{Yukawa}} \supseteq m_i \bar{d}_L^i d_R^i + \frac{y_{ij}}{\sqrt{2}} H \bar{d}_L^i d_R^j + \text{h.c.} \,, \tag{5.2}$$

where i, j are generation indices and $d^i = (d, s, b)^\intercal$ is the vector of down-type quark fields in flavor space.[e] The corresponding physical current quark masses are denoted as m_i (cf. Table 2.2), while y_{ij} is a, in general, complex-valued and non-diagonal matrix in flavor space. Comparing the above Lagrangian with that of equation (2.10), we notice that the minimal SM is reproduced in the case of $y_{ij} = \sqrt{2} m_i / v \delta_{ij}$. Here, we are interested in scenarios where the existence of new physics induces flavor-violating Higgs couplings, i.e. $y_{ij} \neq 0$ for at least one pair $i \neq j$. The corresponding non-standard interaction vertices as well as the associated Feynman rules are shown in Figure 5.2. From a physics point of view, the presence of the non-diagonal Yukawa terms has several potentially observable consequences.

First, additional decay channels for the Higgs boson become accessible. An explicit leading-order calculation based on the effective Lagrangian in equation (5.2) gives for the squared amplitude of the process $H \to d^i \bar{d}^j$

$$\overline{|\mathcal{M}_{i\bar{j}}^2|} = \frac{N_c m_H^2}{2} \Big[\left(|y_{ij}|^2 + |y_{ji}|^2 \right) \left(1 - \hat{m}_i^2 \hat{m}_j^2 \right) - 4 \hat{m}_i \hat{m}_j \, \mathrm{Re}(y_{ij} y_{ji}) \Big] \,, \tag{5.3}$$

[e] The fields d^i in equation (5.2) are quark mass eigenstates. Compared to our notation introduced in equation (2.9) we have, however, removed the primes for the sake of readability. Furthermore, we use a different normalization for the Yukawa matrix y_{ij} than the authors of [41, 50] in order to be consistent with our convention in Chapter 2.

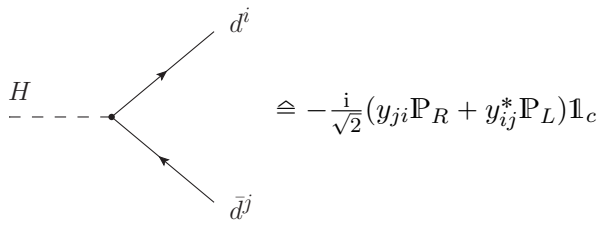

Figure 5.2: Quark-flavor-violating Higgs coupling to down-type quarks ($i \neq j$) and the corresponding Feynman rule as obtained from the general Lagrangian in equation (5.2). Here, the chiral projectors $\mathbb{P}$ are given by $\mathbb{P}_{L,R} = (\mathbb{1} \mp \gamma_5)/2$ and $\mathbb{1}_c$ is the unit operator in color space.

where $\hat{m} := m/m_H$ with the Higgs mass $m_H = 125.09\,\mathrm{GeV}$ [81], and $N_c = 3$ is the number of colors in QCD. The corresponding decay rate can then be calculated as

$$\Gamma(H \to d^i \bar{d}^j) = \frac{\lambda^{1/2}(1, \hat{m}_i^2, \hat{m}_j^2)}{16\pi m_H} \cdot \overline{|\mathcal{M}_{i\bar{j}}^2|}\,, \tag{5.4}$$

with $\lambda(a,b,c) = (a-b-c)^2 - 4bc$ being the Källén triangle function. Note that in a typical collider search for Higgs decays one will not be able to distinguish between a given final-state quark and its anti-particle. We are therefore equally interested in the conjugate process $H \to \bar{d}^i d^j$, whose decay width will, however, be the same as the one presented in equation (5.4), since the Yukawa sector of equation (5.2) conserves CP symmetry. Incoherently summing the decay amplitudes of both processes then simply yields

$$\overline{|\mathcal{M}_{ij}^2|} := \overline{|\mathcal{M}_{i\bar{j}}^2|} + \overline{|\mathcal{M}_{\bar{i}j}^2|} = 2 \cdot \overline{|\mathcal{M}_{i\bar{j}}^2|}\,,$$

which implies an analogous identity for the partial widths

$$\Gamma(H \to d^i d^j) := \Gamma(H \to d^i \bar{d}^j) + \Gamma(H \to \bar{d}^i d^j) = 2 \cdot \Gamma(H \to d^i \bar{d}^j)\,. \tag{5.5}$$

Combining equations (5.3) to (5.5) and employing $m_i, m_j \ll m_H$, i.e. the limit of a massless final state $\hat{m} \to 0$, ultimately gives

$$\Gamma(H \to d^i d^j) = \frac{N_c m_H}{16\pi}\left(|y_{ij}|^2 + |y_{ji}|^2\right)\,. \tag{5.6}$$

Apart from providing additional decay channels for the Higgs boson, the flavor-violating couplings in equation (5.2) lead to a second class of potentially observable effects. Specifically, they introduce tree-level FCNCs which will give contributions to neutral meson oscillations and mixing [41]. Precision measurements of the aforementioned phenomena thus impose stringent limits on the non-diagonal entries of y_{ij}, which we summarize in Table 5.2. This summary demonstrates that the couplings in the B_s^0 sector are the ones

Observable	Coupling	Constraint
B_d^0 oscillations	$\lvert y_{db}\rvert^2$, $\lvert y_{bd}\rvert^2$	$< 4.6 \cdot 10^{-8}$
	$\lvert y_{db} y_{bd}\rvert$	$< 6.6 \cdot 10^{-9}$
B_s^0 oscillations	$\lvert y_{sb}\rvert^2$, $\lvert y_{bs}\rvert^2$	$< 3.6 \cdot 10^{-6}$
	$\lvert y_{sb} y_{bs}\rvert$	$< 5.0 \cdot 10^{-7}$
K^0 oscillations	$\mathrm{Re}\, y_{ds}^2$, $\mathrm{Re}\, y_{sd}^2$	$[-1.2 \ldots 1.1] \cdot 10^{-9}$
	$\mathrm{Im}\, y_{ds}^2$, $\mathrm{Im}\, y_{sd}^2$	$[-5.8 \ldots 3.2] \cdot 10^{-12}$
	$\mathrm{Re}\, y_{ds}^* y_{sd}$	$[-1.1 \ldots 1.1] \cdot 10^{-10}$
	$\mathrm{Im}\, y_{ds}^* y_{sd}$	$[-2.8 \ldots 5.6] \cdot 10^{-13}$

Table 5.2: Current 95 % confidence level (CL) limits on the quark-flavor-violating effective Higgs couplings introduced in equation (5.2) as obtained from meson oscillation experiments. The reported constraints are taken from [41] and have been appropriately adjusted to the coupling normalization used here.

with the loosest constraints and therefore the prime candidates to induce exotic Higgs decays, namely $H \to bs$, with non-negligible rates. To be more concrete, we can employ equation (5.6) to translate the limits from Table 5.2 into bounds on the corresponding branching ratio. Two examples are

$$\mathcal{B}(H \to bs) < \begin{cases} 1.8 \cdot 10^{-3} & \text{for } y_{bs} = y_{sb} \,, \\ 6.6 \cdot 10^{-3} & \text{for } y_{bs} \neq 0 \text{ and } y_{sb} = 0 \text{ or vice versa} \,. \end{cases} \tag{5.7}$$

Here, we assumed that the combined partial width of non-standard Higgs decays is sufficiently small such that the Higgs total width is still well approximated by its SM value, i.e. $\Gamma_H \simeq \Gamma_H^{\mathrm{SM}} = 4.1\,\mathrm{MeV}$ [162].

When quoting upper limits like those in equation (5.7) one should always keep in mind that low-energy flavor measurements can only provide *indirect* constraints on the effective couplings involved. As we have mentioned before, such bounds may become invalid if there exist multiple new physics contributions to the relevant neutral meson oscillations, which mutually cancel to some degree. However, such cancellations typically necessitate a certain amount of parameter tuning, if the different sources of FCNC are independent of each other. For instance, the authors of [197] recently demonstrated that, within the framework of a two-Higgs-doublet model, an appropriate tuning of the neutral scalar masses leads to branching fractions for $H \to bs$ of 10 % and more, while all indirect constraints are satisfied. Similarly large values can be obtained in the Minimal Supersymmetric Standard Model, provided one accepts some fine tuning in the mixing between second and third generation squarks [191].

A further reason which might invalidate the bounds in equation (5.7) is the following. The leading order relation between the effective couplings y_{ij} on the one hand and the observable partial width $\Gamma(H \to d^i d^j)$ on the other

hand may be altered by sizable quantum corrections, especially those from QCD (cf. [225] for the SM counterpart). In particular, the characteristic energy scales of the two phenomena – meson oscillations and Higgs decays – differ by two orders of magnitude, so that the running of the y_{ij} may play a role. To our best knowledge, the aforementioned effects have not yet been investigated in the literature. Their further discussion also goes beyond the scope of this thesis.

Considering the above caveats concerning equation (5.6), we will take the branching ratio $\mathcal{B}(H \to bs)$ as the free parameter for our analyses, instead of the effective Yukawa couplings y_{bs} and y_{sb}. Notice, however, that there is no experimental way to distinguish a jet coming from a strange quark from one originating from a down quark. Hence, the actual observable for which our analyses will provide a handle is $\mathcal{B}(H \to bj) := \mathcal{B}(H \to bs) + \mathcal{B}(H \to bd)$.

5.3 Analysis and results

In the following section, we will present the main results of this chapter and analyze the prospects for discovering or constraining the quark-flavor-violating Higgs decay $H \to bj$ at the ILC. In line with our discussion of the different Higgs production modes at a e^+e^- collider in Section 5.1, we will split our analysis according to the sought-after signal signature, with the hadronic and leptonic search channels being studied in Section 5.3.2 and Section 5.3.3, respectively. We start, however, with a summary of several aspects that are common to all of our analyses.

5.3.1 General aspects of the analyses

Let us first summarize the tools we employed for the purpose of performing our detector-level analyses. We started by implementing the effective Yukawa interactions of equation (5.2) in the `UFO` format [226] with the help of the `FeynRules` package [227]. Based on the produced model file, we then generated parton-level events for the signal processes using `Whizard 2.5.0` [228] supplemented by the `O'Mega` matrix element generator [229]. Background events were created in the same way, but based on a `UFO` implementation of the minimal SM. Note that `O'Mega` provides tree-level scattering amplitudes only. Correspondingly, all cross sections were, in general, calculated at leading order. One exception is given by background processes where an on-shell Higgs decays to a pair of same-flavor quarks. Here, we used the higher-order-corrected SM Higgs branching fractions from [162], since their tree-level counterparts are far off due to neglecting substantial QCD corrections [225]. In the same spirit, we also included the sizable effective coupling of the SM Higgs to a pair of gluons. For illustrative purposes and later reference, we collect all tree-level Feynman diagram topologies relevant to our analyses in Figure 5.3. In order to reproduce the situation at

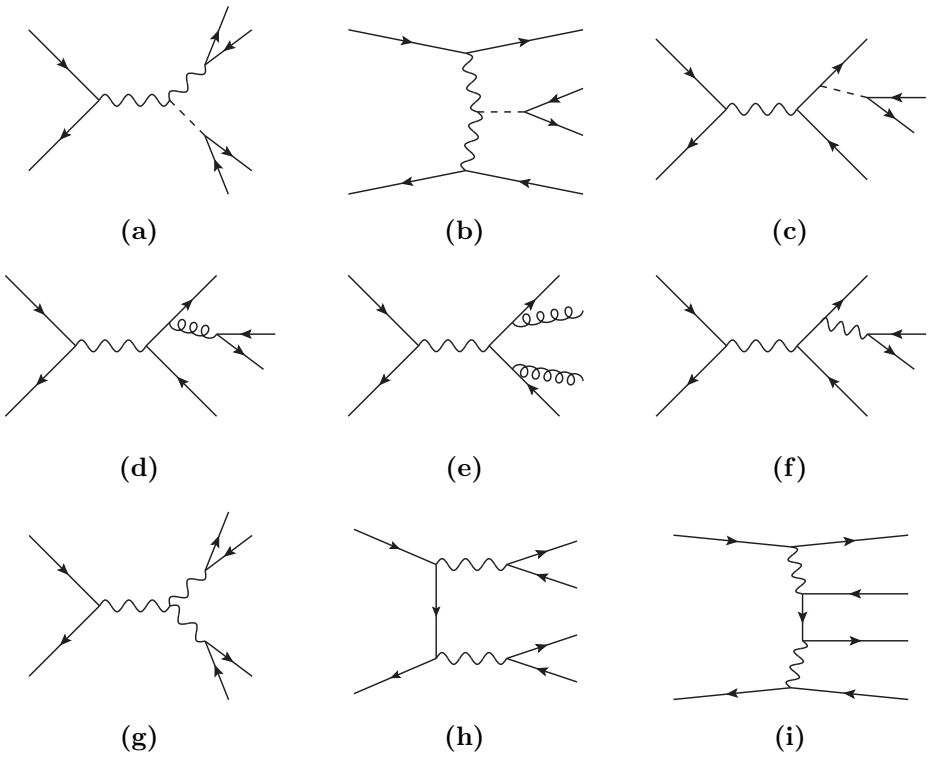

Figure 5.3: Tree-level Feynman diagrams for signal and background processes relevant to our analyses of the QFV Higgs decay $H \to bj$. Incoming fermions lines always represent an electron-positron pair. The fermion pair originating from the Higgs in diagrams (a) to (c) and from the gluon in diagram (d) can be replaced by a gluon pair to produce further relevant diagrams. Lastly, both gluons in diagram (e) can also be on the same outgoing quark leg.

the ILC as realistic as possible, we furthermore took into account beam polarization and non-trivial beam energy spectra due to initial state radiation and beamstrahlung.[f] Parton showering and hadronization was carried out using `PYTHIA8` [231], while a fast detector simulation was performed with `Delphes 3` [232]. Details about the specifications of the proposed ILC detectors were provided by the dedicated `DSiD` detector card [233], which is based on the information given in the TDR [46]. Jets were reconstructed with `FastJet` [234] via the `anti-kT` algorithm [235] with a cone radius parameter of $R = 0.4$. Detector-level events were finally analyzed employing `MadAnalysis5` [236].

Distinguishing the sought-after signal involving the Higgs decay $H \to bj$ from SM background processes like $H \to b\bar{b}$ makes reliable flavor identification of final-state quarks particularly important. Realistic values for the

[f] While `Whizard` itself provides functionalities to include effects from beam polarization and initial state radiation, beamstrahlung is accounted for by the `CIRCE` package [230].

tagging efficiencies at the ILC experiments are

$$\mathcal{P}(b\text{-tag}\,|\,b) = 0.80\,, \quad \mathcal{P}(c\text{-tag}\,|\,c) = 0.70\,. \tag{5.8a}$$

According to the expected performance of the `LCFIPlus` software [216], which is used by both ILC detector concept groups for jet flavor tagging [46], the corresponding misidentification rates are then given by

$$\begin{aligned} \mathcal{P}(b\text{-tag}\,|\,c) &= 0.08\,, \quad \mathcal{P}(b\text{-tag}\,|\,j) = 0.01\,, \\ \mathcal{P}(c\text{-tag}\,|\,b) &= 0.17\,, \quad \mathcal{P}(c\text{-tag}\,|\,j) = 0.10\,. \end{aligned} \tag{5.8b}$$

As we have already mentioned in the introduction to this chapter, flavor tagging at the ILC will still not allow to differentiate between s and d jets. The QFV Higgs decays to bs and bd final states therefore effectively induce the same signature such that our analysis will only be sensitive to the combined quantity $\mathcal{B}(H \to bj) := \mathcal{B}(H \to bs) + \mathcal{B}(H \to bd)$ rather than to the branching ratios of the two modes separately.

A further aspect that is relevant to all of our analyses is that of beam polarization, a feature unique to linear colliders and one of their major advantages over circular machines. The ILC is planned to provide both polarized electron and positron beams with expected specifications $\mathcal{P}(e^-) = \pm 80\,\%$ and $\mathcal{P}(e^+) = \pm 30\,\%$, thus offering four distinct polarization configurations. Since different physics searches imply different optimal polarization settings, the data will not be collected using only one combination, but rather according to well-motivated sharing scenarios. In order to gain a deeper insight into the performance of the individual search channels for QFV Higgs decays and their dependence on the chosen polarization setting, our results will be presented in two ways. On the one hand, we will compare the sensitivity of the four possible combinations thus determining the optimal polarization setting for each channel. On the other hand, we will analyze two realistic polarization sharing scenarios of an actual run as proposed in [189], namely

$$\begin{aligned} &\textbf{Scenario 1:} \quad \mathcal{P}_{-+,+-,++,--} = \big(67.5\,\%, 22.5\,\%, 5\,\%, 5\,\%\big)\,, \\ &\textbf{Scenario 2:} \quad \mathcal{P}_{-+,+-,++,--} = \big(40\,\%, 40\,\%, 10\,\%, 10\,\%\big)\,, \end{aligned} \tag{5.9}$$

with the first and second sign denoting the polarization of the electron and positron beams, respectively. For the recently advanced 250 GeV stage [47], a polarization sharing of $(45\,\%, 45\,\%, 5\,\%, 5\,\%)$ was suggested in [214], which is, however, very similar to our second benchmark scenario from above.

As for the amount of accumulated data itself, we decide to use the specifications of the previously mentioned H-20 running scenario [189, 214]. Accordingly, we assume an available integrated luminosity of $2\,\text{ab}^{-1}$ ($4\,\text{ab}^{-1}$) at a center-of-mass energy of 250 GeV (500 GeV). Besides, initial phases at both energies are anticipated to collect $500\,\text{fb}^{-1}$ of data each.

Finally, the statistical evaluation of our simulation results will be based on a simple cut-and-count analysis. As a measure for the statistical significance of a given signal, we will employ the standard score z. Expecting a large number of background events allows us to use its normal approximation, specifically

$$z = \frac{S}{\sqrt{S + B + \epsilon_{\text{syst}}^2 B^2}} \,, \tag{5.10}$$

where the number of signal and background events are denoted as S and B, respectively. Furthermore, we introduced the parameter ϵ_{syst} which encodes the systematic uncertainty on the background determination, i.e. $\epsilon_{\text{syst}} = \Delta B/B$. Based on equation (5.10), we can also define the 95 % CL upper limit on the number of signal events: For given B and ϵ_{syst}, it corresponds to the value $S_{95\%}$ for which the right-hand side yields $z = \Phi^{-1}(0.95) \approx 1.64$ with Φ^{-1} being the probit function. Additional details on the statistical methods relevant to the present work will be provided in Appendix E.

In the following, we present our analyses of the individual search channels and the corresponding results. Whenever explicit signal rates are needed, we adopt the benchmark point

$$\sqrt{2} \cdot |y_{bs}| = \sqrt{2} \cdot |y_{sb}| = 10^{-3} \quad \text{and} \quad |y_{bd}| = |y_{db}| = 0 \,, \tag{5.11}$$

giving a total QFV Higgs branching ratio of $\mathcal{B}(H \to bj) = 0.73\,\%$ as per equation (5.6).

5.3.2 Hadronic channel at 250 GeV

First, we investigate the case where the Higgs is produced in association with a Z boson, which decays hadronically to a pair of same-flavor quarks. The corresponding tree-level Feynman diagram is shown in Figure 5.3a. The sought-after signal process thus contains four final-state jets, namely

$$e^+e^- \to (Z \to q\bar{q}) + (H \to bj) \,. \tag{5.12}$$

Accordingly, the dominant SM background for this channel originates from inclusive four-jet production, i.e. $e^+e^- \to kkkk$, with k denoting gluons or any quark flavor barring the top quark. The aforementioned background process obtains contributions from two fundamentally different classes of Feynman diagrams, described in the following.

Non-resonant processes in the sense that the Higgs does not propagate in the corresponding Feynman diagrams. First and foremost, QCD four-jet production as displayed in Figures 5.3d and 5.3e belong to the present category. Further examples include double-W or double-Z

production with the weak bosons both decaying hadronically (cf. Figures 5.3g and 5.3h). In a slight abuse of notation, we will refer to the class of non-resonant processes as $4k$.

Resonant Higgs processes where an on-shell Higgs is produced in association with two quarks different from the top quark. If the Higgs then decays to a pair of jets – preferably to $b\bar{b}$, $c\bar{c}$ or gg – the four-jet background signature is reproduced. Note that this category itself consists of two sub-classes. First, there are Higgsstrahlung type processes where the Z decays hadronically (cf. Figure 5.3a). The second contribution comes from quark pair production with one of the quarks radiating off a Higgs (cf. Figure 5.3c).

As expected, the non-resonant modes will turn out to constitute by far the largest background in the hadronic channel due to their huge QCD cross sections, see Table 5.3.

In order to discriminate the signal process of equation (5.12) from the aforementioned backgrounds, we define a series of cuts and selection criteria, which are applied to the reconstructed Monte Carlo events. First, the final state of a signal event is required to consist of exactly four jets. Of those, at least one must be b-tagged and one must not obtain any flavor tag thereby being identified as a light jet. All jets are furthermore asked to have sufficiently large transverse momenta, $p_T > 10\,\mathrm{GeV}$, and are supposed to lie within $|\eta| < 1.8$, where η denotes pseudorapidity. Motivated by the signal topology, we then demand one b jet together with one light jet to reconstruct the Higgs mass within

$$\Delta_{mH} := |m_{bj} - m_H| < 5\,\mathrm{GeV}\ , \tag{5.13}$$

where m_{bj} is the appropriate two-jet invariant mass. Whenever more than one bj pair fulfills equation (5.13), we choose the one whose invariant mass is closest to the Higgs mass. Next, the two remaining jets are required to be of the same flavor k and must reconstruct the Z boson mass within

$$\Delta_{mZ} := |m_{kk} - m_Z| < 10\,\mathrm{GeV}\ . \tag{5.14}$$

The numerical values quoted in equations (5.13) and (5.14) were chosen as to maximize the signal significance according to equation (5.10) assuming a systematic background uncertainty of 1 %. Note, however, that because of the $4k$ mode's large inclusive cross section, applying only the two aforementioned invariant mass cuts still leaves an unacceptable amount of combinatorial four-jet background, see Table 5.3. For the sake of further improving the signal-to-background ratio, we define several additional selection criteria. For one, we demand the transverse momentum of the b-tagged jet associated with the Higgs boson decay (p_T^b) to exceed 50 GeV. Moreover, its angular distance from the light jet that also originates from the Higgs decay

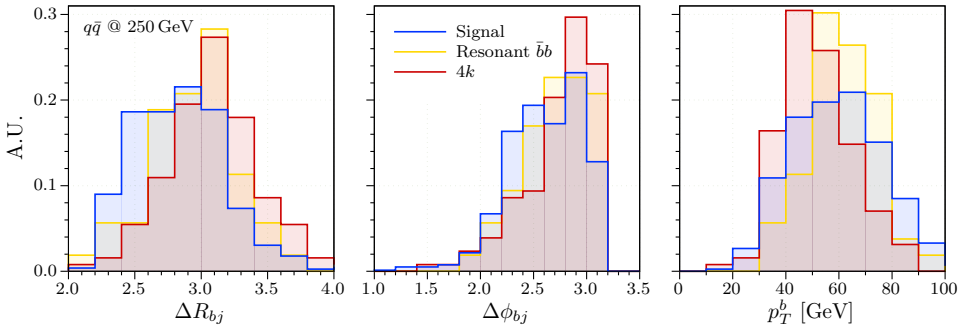

Figure 5.4: Different kinematic distributions of signal and dominant background events after the invariant mass cuts for the hadronic channel at 250 GeV with beam polarization $\mathcal{P}_{-+}$. Shown are the angular separation distributions (ΔR and $\Delta\phi$) between the bottom and the light jet attributed to be coming from the Higgs decay, as well as the transverse momentum spectrum of the aforementioned b jet. All histograms were normalized as to have a unit area.

must be sufficiently small, specifically $\Delta R_{bj} < 2.6$ and $\Delta\phi_{bj} < 2.5$, where ϕ is the azimuthal angle while the azimuthal-pseudorapidity separation ΔR is defined as

$$(\Delta R)^2 := (\Delta\eta)^2 + (\Delta\phi)^2 \,.$$

Our actual choices of the three last cuts' numerical values are guided by the features of the corresponding kinematic distributions of signal and background events, which are displayed in Figure 5.4.

The cutflow of event yields resulting from the selection procedure outlined above is given in Table 5.3 for an integrated luminosity of $2\,\text{fb}^{-1}$ with polarization sharing scenario 1 and assuming our benchmark point of equation (5.11). Crucially, it shows that the signal-to-background ratio is relatively small even after all cuts were applied. In particular, the residual combinatorial four-jet background is problematic, whereas the resonant modes are under control.

A more general assessment of the hadronic channel's performance can be based on Figure 5.5. Here, we show several contours of interest in the luminosity-branching ratio plane choosing different beam polarization configurations. First, in the left-hand plot, we contrast the two realistic polarization sharing scenarios from equation (5.9). For both cases, we calculated the $5\,\sigma$ as well as the 95 % CL contours. Whereas the former determines the *minimal* signal branching ratio necessary for a discovery, the latter gives the *maximal* value for $\mathcal{B}(H \to bj)$ that can still be excluded at the specified confidence level in the event of a null result. Second, the right-hand plot compares the 95 % CL contours of the four possible beam polarization combinations for the sake of finding the optimal one. Adopting a systematic background error of 1 %, the hadronic channel's performance can now

be summarized as follows. With the full amount of accumulated data and assuming that the experimental outcome is consistent with the SM predictions, the hadronic channel is anticipated to set a 95 % CL upper bound of around 4 % on the signal branching fraction. The same data set is expected to allow a $5\,\sigma$ discovery only for branching ratios larger than 10 %. Note that the two polarization sharing scenarios considered here yield very similar results for exclusion and discovery limits, respectively. Lastly, the optimal polarization combination is found to be $\mathcal{P}_{+-}$ in accordance with the fact that it is this configuration which suppresses the SM four-jet background the most. In summary, the hadronic channel's sensitivity is considerably limited and will not be able to compete with that of the indirect limits in equation (5.7).

	Signal	$4k$	$b\bar{b}$	$c\bar{c}$	jj
Reco.	2681	$2.8 \cdot 10^7$	$1.9 \cdot 10^5$	9490	$2.8 \cdot 10^4$
Jet tag	1080	$1.9 \cdot 10^6$	$6.9 \cdot 10^4$	1150	3470
Δ_{mH}	147	$1.4 \cdot 10^5$	6730	87	223
Δ_{mZ}	21	6946	98	5	2
p_T^b	14	3503	81	3	1
$\Delta\phi_{bj}$	5	419	15	1	1
ΔR_{bj}	4	165	12	1	0

Table 5.3: Cutflow of signal and background events in the hadronic channel at 250 GeV. An integrated luminosity of $2\,\text{ab}^{-1}$ with polarization sharing scenario 1 was assumed. The signal rate was set according to the benchmark point of equation (5.11), i.e. $\mathcal{B}(H \to bj) \simeq 0.73\,\%$. For details on the notation, see the main text.

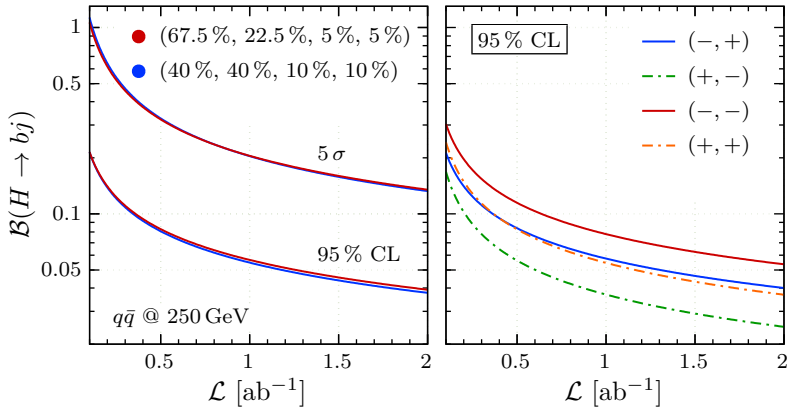

Figure 5.5: Expected performance of the hadronic channel at $\sqrt{s} = 250\,\text{GeV}$ as a function of the total integrated luminosity, assuming a systematic error of $\epsilon_{\text{syst}} = 1\,\%$. *Left*: Expected $5\,\sigma$ discovery and 95 % CL exclusion reaches on $\mathcal{B}(H \to bj)$ for the two polarization scenarios of equation (5.9). *Right*: Expected exclusion reaches for the four possible polarization configurations individually.

5.3.3 Leptonic channels

The analysis of the hadronic channel in the previous section showed that its sensitivity is inherently limited, mainly due to the large amount of combinatorial four-jet background. Thus, the hadronic channel alone cannot provide constraints that are comparable with the ones from indirect searches quoted earlier, in equation (5.7). Learning from these findings, we now go on to investigate different search modes, namely ones where the signal signatures contain only two rather than four jets. Considering the Higgs production channels relevant at the ILC as discussed in Section 5.1, such signatures necessarily involve either an additional pair of opposite-sign charged leptons, or missing energy originating from a pair of neutrinos. The corresponding two search modes will be referred to as *charged lepton channel* and *neutrino channel*, respectively. Obviously, both possibilities will come with their own advantages and drawbacks that are to be determined. We will present detailed analyses of the leptonic channels including a thorough background study in later parts of this section.

Here, let us briefly mention one important aspect of the background discussion which will apply to both of the leptonic channels. To this end, recall from Table 5.3 that the second largest SM background in the hadronic case is that from resonant processes where the Higgs decays to two bottom quarks. Likewise, we expect the dominant background for the leptonic channels to originate from on-shell Higgs production followed by its SM decay into a pair of same-flavor quarks. Importantly, the thus produced final states will exhibit the same kinematics as the sought-after signal and differ from the latter only in the realized flavor combination. Taking into account imperfections in the flavor tagging procedure, resonant processes can thus easily mimic the signal. Thereby, they become *irreducible* background which is only suppressed by flavor tagging requirements. At the same time, the resonant SM modes will typically occur at larger rates as compared to the signal. Based on these realizations, it is straightforward to give a rough estimate of the leptonic channels' reachable sensitivity, on the one hand, and of the relative importance of the individual resonant background modes, on the other hand. These estimates will be the subject of the next paragraph. Note that applying similar estimates to the hadronic search channel is less meaningful owing to the overwhelming combinatorial four-jet background.

A Estimated performance based on resonant background modes

In line with the reasoning above, the following discussion is dedicated to estimating the leptonic channels' performance taking into account only resonant background processes. All estimates will be based exclusively on flavor tagging specifications and Higgs branching ratios, rather than making use of simulations of any kind.

If S and B_X are numbers of signal and resonant background events, with X indicating the Higgs decay products, we can write

$$B_X = \mathcal{L} \cdot \sigma_{\text{prod}} \cdot \alpha \cdot \epsilon' \cdot \epsilon_{\text{tag},X} \cdot \mathcal{B}_X \ , \tag{5.15a}$$

$$S = \mathcal{L} \cdot \sigma_{\text{prod}} \cdot \alpha \cdot \epsilon' \cdot \epsilon_{\text{tag},bj} \cdot \mathcal{B}_{bj} \ , \tag{5.15b}$$

where we have abbreviated $\mathcal{B}_X \equiv \mathcal{B}(H \to X)$ for the sake of readability. Furthermore, we have introduced the flavor tagging efficiencies $\epsilon_{\text{tag},X}$ defined as the probability that a given jet pair X is identified as bj, i.e.

$$\epsilon_{\text{tag},X} := \mathcal{P}(bj\text{-tag} \,|\, X) \ .$$

Since signal and resonant background processes only differ by the respective Higgs decay products all other quantities in equation (5.15) – integrated luminosity $\mathcal{L}$, Higgs production cross section σ_{prod}, detector and analysis acceptance α and other detection and reconstruction efficiencies ϵ' – are the same in both relations. Dividing equation (5.15a) by (5.15b) therefore yields

$$r_X := \frac{B_X}{S} = \frac{\mathcal{B} \cdot \epsilon_{\text{tag}}|_X}{\mathcal{B} \cdot \epsilon_{\text{tag}}|_{bj}} \ . \tag{5.16}$$

The quantities r_X obviously still depend on new physics parameters via the QFV Higgs branching ratio. It is also convenient to define a measure for the relative importance of the individual resonant background modes that is independent of $\mathcal{B}_{bj}$. Such a measure is given by

$$\rho_X := \mathcal{B}_X \cdot \frac{\epsilon_{\text{tag},X}}{\epsilon_{\text{tag},bj}} \ . \tag{5.17}$$

Explicit values for ρ_X and r_X are listed in Table 5.4, demonstrating that the by far most severe background is expected to come from the $b\bar{b}$ process. Furthermore, the resonant $c\bar{c}$ contribution is anticipated to be of a similar size as the one due to gg. For our benchmark point of equation (5.11), Table 5.4 implies that each signal event comes with $r_{bb} = 5.4$ irreducible background events from the $b\bar{b}$ mode and so on.

As a next step, let us estimate the statistical significance z within reach of a search in one of the leptonic channels for a *given* signal branching fraction $\mathcal{B}_{bj}$. Again approximating the total background by the resonant processes only, and ignoring systematic uncertainties for the moment, we can write (cf. equation (5.10))

$$z \lesssim \frac{S}{\sqrt{S + B_{\text{res}}}} = \frac{S}{\sqrt{S + \sum_X B_X}} = \sqrt{\frac{S}{1 + r_B}} \ , \tag{5.18}$$

where we have used equation (5.16) in the last step and defined r_B as the sum of all relative background weights r_X. For instance, in the case of our benchmark point $\mathcal{B}_{bj} = 0.73\,\%$, the values from Table 5.4 yield $z \lesssim \sqrt{S}/2.6$.

Process X	$\mathcal{B}(H \to X)$ [%]	ϵ_{tag} [%]	relative weights	
			r	ρ [10^{-2}]
bj	0.73	71.2	1.0	–
bb	58.09	4.80	5.4	3.9
cc	2.884	3.52	0.20	0.14
gg	8.180	1.78	0.28	0.20

Table 5.4: Relative weights of the different irreducible background modes. Whereas ρ is independent of any BSM parameter, the given values for r were calculated using the benchmark point $\mathcal{B}_{bj} = 0.73\,\%$. Assuming that non-standard Higgs decays have a sufficiently small rate, SM Higgs branching fractions were adopted (see [162]). Tagging efficiencies ϵ_{tag} are computed on the basis of equation (5.8).

Note that the result thus obtained is merely a very rough approximation for z, which will typically overestimate its true value. Still, we can apply the logic from above in order to get a first quantitative indication of the importance of flavor identification for our analyses. Specifically, let us for now assume a degraded c tagging efficiency of only 60 % with the corresponding misidentification rates adjusted according to the `LCFIPlus` specifications [216]. Adopting the b tagging performance from equation (5.8) as before and re-calculating the relative weight factors, shows a significant enhancement in the $b\bar{b}$ mode, $r_{bb} = 13.5$. The charm weight also increases, but only slightly to $r_{cc} = 0.269$, while the gluon weight r_{gg} remains unchanged with respect to Table 5.4. According to equation (5.18) the estimated signal significance is now reduced to $z \lesssim \sqrt{S}/3.9$, which corresponds to a degradation by more than 30 %. This result clearly demonstrates the potentially strong dependence of the sensitivity of searches for QFV Higgs decays on the available flavor identification capabilities. At the same time, it motivates a more thorough study to find the optimal flavor tagging specifications given the existing software packages like `LCFIPlus`. Such a study, however, goes beyond the scope of the present thesis.

Finally, let us estimate the maximally achievable sensitivity of the leptonic channels. To put it differently, we are interested in the signal branching fraction needed to obtain a given statistical significance z. Starting again from the approximation in equation (5.18) and using the relation $\rho_B = r_B \mathcal{B}_{bj}$, we can write

$$z^2 \lesssim \frac{S}{1 + \rho_B/\mathcal{B}_{bj}} \,, \tag{5.19}$$

which we now want to solve for $\mathcal{B}_{bj}$. In doing so, we have to keep in mind that the number of observable signal events S is a function of $\mathcal{B}_{bj}$, as well, see equation (5.15b). However, their relation contains quantities which encode details about the experiment and the analysis, such that their values are in

general not known without having performed a dedicated simulation. (An exception is the case where one assumes an ideal detector and a trivial analysis, i.e. $\alpha = \epsilon' = 1$.) Alternatively, we may for the moment assume to know the number of observable events S_0 which are induced by some reference branching ratio $\mathcal{B}_0$. Equation (5.15b) then implies that $S/\mathcal{B}_{bj} = S_0/\mathcal{B}_0$. Inserting this into equation (5.19) yields

$$z^2 \lesssim \frac{\mathcal{B}_{bj} \cdot S_0/\mathcal{B}_0}{1 + \rho_B/\mathcal{B}_{bj}} ,$$

which can now readily be solved for the unknown signal branching fraction

$$\mathcal{B}_{bj}(z) \gtrsim \frac{z^2 \mathcal{B}_0}{2S_0} \left(1 + \sqrt{1 + \frac{4\rho_B S_0}{z^2 \mathcal{B}_0}} \right) . \tag{5.20}$$

Importantly, the quantities characterizing the reference point only enter as the ratio $S_0/\mathcal{B}_0$, so that $\mathcal{B}_{bj}(z)$ is independent of any BSM parameters as expected. Reading off the values of the weight factors ρ_X from Table 5.4, one finds $\rho_B = 4.24 \cdot 10^{-2}$. Equation (5.20) can now, for example, be used to estimate the minimally reachable 95 % upper bound on $\mathcal{B}_{bj}$. Plugging in $z = z_{95\%} \approx 1.64$ yields

$$\mathcal{B}_{95\%} \gtrsim 1.3 \cdot \mathcal{B}_0/S_0 \left(1 + \sqrt{1 + 0.063 \cdot S_0/\mathcal{B}_0} \right) , \tag{5.21}$$

A similar lower limit can be obtained for the branching fraction $\mathcal{B}_{5\sigma}$ necessary to get a $5\,\sigma$ discovery. Later, we will compare the estimates derived above with the outcome of our full analyses, in order to asses how dominant the resonant background processes truly are.

B Charged lepton channel at 250 GeV

Analogous to the hadronic case investigated in Section 5.3.2, let us assume that the Higgs is produced in association with a Z boson, which, however, is now supposed to decay leptonically into a pair of electrons or muons.[g] The corresponding tree-level Feynman diagram is again that of Figure 5.3a. The signature of the sought-after signal in the charged lepton channel is then

$$e^+e^- \to (Z \to \ell^+\ell^-) + (H \to bj) , \tag{5.22}$$

where $\ell \in \{e, \mu\}$. The process $e^+e^- \to \ell^+\ell^- bj$ itself does not exist in the minimal SM. However, flavor tagging imperfections imply that the SM final states $\ell^+\ell^- b\bar{b}$, $\ell^+\ell^- c\bar{c}$ or $\ell^+\ell^- jj$ may be erroneously identified as the one of the signal. The corresponding processes $e^+e^- \to \ell^+\ell^- b\bar{b}$, etc. therefore constitute the main SM background modes of the charged lepton channel. To be more precise, we distinguish the following two categories:

[g] We do not consider τ leptons here since they are not detector stable, such that their identification efficiency is significantly less than that of electrons and muons.

Resonant Higgs processes which have the exact same topology as the signal, namely a hadronically decaying on-shell Higgs is produced in association with a Z boson that decays into a pair of charged leptons. As opposed to the hadronic channel, topologies as in Figure 5.3c are irrelevant here since they are suppressed by tiny electron or muon Yukawa couplings.

Non-resonant processes in the sense that the Higgs does not propagate in the corresponding Feynman diagrams. Imposing appropriate invariant mass cuts will therefore help to reduce their contribution. Possible origins include ZZ, $\gamma\gamma$ or $Z\gamma$ production (cf. Figure 5.3h) as well as fermion pair production with one of the fermions radiating off an electroweak gauge boson (cf. Figure 5.3f). In the case of an electron-positron pair in the final state, also more complex topologies like that of Figure 5.3i become possible.

As already argued before, the resonant modes are expected to be the dominant ones since they share the signal process's kinematics. Additional background contributions may, in principle, arise from charged-current reactions such as $e^+e^- \to \nu_\ell \ell sc$ (cf. Figure 5.3g), provided the final-state jet pair is identified as bj and a second charged lepton is detected. Such an extra lepton will typically originate from hadronic activity within jets. Hence, requiring all charged leptons to be sufficiently isolated from such activity[h] as well as asking them to have sizable transverse momenta, will prove to be very efficient in rejecting this kind of background (cf. Table 5.5).

In more detail, our event selection consists of the following set of cuts. First, the final state is required to contain exactly one b jet as well as one light-flavor jet j, both of which are asked to have sufficiently large transverse momenta, $p_T^q > 10\,\text{GeV}$, and are supposed to lie within $|\eta| < 1.8$. Motivated by the signal topology, the jet pair is furthermore required to reconstruct the Higgs mass within $\Delta_{mH} < 30\,\text{GeV}$. Apart from the aforementioned jets we ask the final state to contain precisely one pair of same-flavor and opposite-sign isolated leptons. As argued above, we restrict ourselves here to the electron and muon flavors. Each lepton is supposed to satisfy $p_T^\ell > 10\,\text{GeV}$ and $|\eta| < 2.44$. The invariant mass of the lepton pair must be consistent with the Z boson mass, specifically $\Delta_{mZ} < 20\,\text{GeV}$. Lastly, in order to further reduce the signal contamination due to non-resonant background processes, the so-called recoil mass is required to reconstruct the Higgs mass within

$$\Delta_{\text{recoil}} := |m_{\text{recoil}} - m_H| < 20\,\text{GeV} \,,$$

where the recoil mass is exclusively defined through charged-lepton observ-

[h] The `DSiD` detector card already implements appropriate isolation criteria for electrons, muons and photons. For details, see [233].

	Signal	$\ell\ell b\bar{b}$	$\ell\ell c\bar{c}$	$\ell\ell jj$	$\nu_\ell \ell sc$	$\nu_\ell \ell du$
Reco.	225	$1.2 \cdot 10^5$	$1.4 \cdot 10^5$	$4.0 \cdot 10^5$	$5.2 \cdot 10^6$	$5.2 \cdot 10^5$
Jet tag	82	4320	1904	2960	305	152
p_T^ℓ	79	3616	1552	2419	0	0
Δ_{mZ}	77	2784	1051	1746	0	0
Δ_{recoil}	71	1272	325	553	0	0
Δ_{mH}	51	247	34	66	0	0

Table 5.5: Cutflow of signal and background events in the charged lepton channel at 250 GeV. An integrated luminosity of $2\,\text{ab}^{-1}$ with polarization sharing scenario 1 was assumed. The signal rate was set according to the benchmark point of equation (5.11), i.e. $\mathcal{B}(H \to bj) \simeq 0.73\,\%$. For details on the notation, see the main text.

ables, namely as

$$m_{\text{recoil}} := s - 2\sqrt{s}E_{\ell\ell} + m_{\ell\ell}^2 \quad \text{and} \quad E_{\ell\ell} := E_{\ell^+} + E_{\ell^-} \,.$$

For the above-quoted values of minimal transverse momenta and maximal pseudorapidity, the invariant mass and recoil mass cuts were chosen as to maximize the signal significance according to equation (5.10) assuming a systematic background uncertainty of 1 %.

Completely analogous to the hadronic channel analysis, our results are presented in two steps. First, Table 5.5 contains the cutflow of event yields resulting from the selection procedure described above. The displayed numbers were obtained assuming our benchmark point of equation (5.11) and $2\,\text{ab}^{-1}$ of accumulated data with a polarization splitting according to scenario 1. Most importantly, the final signal-to-background ratio can be seen to have improved by an order of magnitude with respect to that of the hadronic channel. Furthermore, note that the relative importance of the background modes is as anticipated from Table 5.4 – at least qualitatively. The exact values for the relative weights r introduced in equation (5.16) are, however, not reproduced. This is mainly due to additional non-resonant background contributions which are thus shown to be still relevant.

In a second step, we evaluate the charged lepton channel's performance based on Figure 5.6,[i] where we again adopt a systematic background error of 1 %. On the one hand, we find that the charged lepton channel is expected to put a 95 % CL upper limit of around 0.5 % on the quantity $\mathcal{B}(H \to bj)$ using $2\,\text{ab}^{-1}$ of data collected at a 250 GeV run. Interestingly, this upper bound turns out to be comparable to the ones from indirect measurements quoted in equation (5.7). On the other hand, a $5\,\sigma$ discovery would be possible only for branching ratios larger than roughly 2 %. In terms of sensitivity, the

[i] The plots displayed here are of the same type as the ones in Figure 5.5 which we discussed in the context of the hadronic channel in Section 5.3.2. Further details on what is shown and how to extract useful information can be found there.

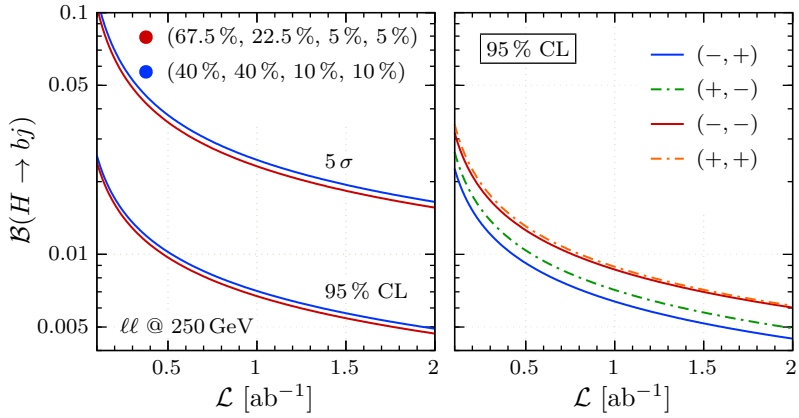

Figure 5.6: Expected performance of the charged lepton channel at $\sqrt{s} = 250\,\text{GeV}$ as a function of the total integrated luminosity, assuming a systematic error of $\epsilon_{\text{syst}} = 1\,\%$. *Left*: Expected $5\,\sigma$ discovery and 95 % CL exclusion reaches on $\mathcal{B}(H \to bj)$ for the two polarization scenarios of equation (5.9). *Right*: Expected exclusion reaches for the four possible polarization configurations individually.

charged lepton channel thus offers an improvement of an order of magnitude over the hadronic search mode. Lastly, we remark that results from the two considered polarization sharing scenarios again almost coincide. However, in contrast to the hadronic channel, the optimal combination is now found to be $\mathcal{P}_{-+}$.

C Neutrino channel at 250 GeV and 500 GeV

Lastly, let us consider the signal signature where the bj jet pair coming from the QFV Higgs decay is produced in association with missing energy originating from neutrinos. Importantly, this final state receives contributions from two Higgs production modes with sizable cross sections, namely Higgsstrahlung and W boson fusion. (For details see Section 5.1, in particular Figure 5.1, as well as the tree-level Feynman graphs in Figures 5.3a and 5.3b.) The corresponding reactions are

$$e^+e^- \to (Z \to \nu\bar{\nu}) + (H \to bj) \quad \text{and} \tag{5.23a}$$
$$e^+e^- \to \nu_e\bar{\nu}_e + (H \to bj)\,, \tag{5.23b}$$

respectively. Other than the hadronic or the charged lepton channel, searches in the neutrino mode are therefore potentially relevant at both the 250 GeV and the 500 GeV run. Since background discussion and signal selection criteria were found to be similar for both energies, the corresponding analyses as well as their outcome will be presented largely in parallel.

Starting with the relevant Standard Model background, first note that the process $e^+e^- \to \nu_e\bar{\nu}_e bj$ indeed exists in the minimal SM (cf. Figure 5.3i), but has a negligible rate due to GIM suppression. Furthermore, it exhibits

different kinematics than the signal processes in equation (5.23) since it does not involve a Higgs decay. Hence, it will not be taken into account during our present analysis. Instead, the dominant SM backgrounds again do not have the same final state as the signal, but may still be mistaken for it due to several reasons. Specifically, we consider the following background contributions.

Resonant Higgs processes ($e^+e^- \to \nu\bar{\nu}b\bar{b}$, etc.) which exist in the exact same topologies as the signal, but with final-state flavor combinations that are consistent with the SM. Apart from their suppression by flavor-tagging requirements, these processes are therefore irreducible and expected to constitute the dominant background (cf. the discussion in the first part of Section 5.3.3).

Non-resonant processes ($e^+e^- \to \nu\bar{\nu}b\bar{b}$, etc.) in the sense that the Higgs boson does not propagate in the corresponding Feynman diagrams, so that the final-state kinematics will be different from that of the signal. Double-Z production is one of their possible origins (cf. Figure 5.3h).

Quark pair productions ($e^+e^- \to b\bar{b}$, etc.) Since uncertainties in determining the jets' four momenta or other detector imperfections may result in the presence of artificial missing energy, also these processes are of relevance. However, the aforementioned effects are usually small and a cut on the minimal amount of missing energy is expected to be very efficient. Still, the large cross sections involved make this contribution non-negligible.

Charged-current processes ($e^+e^- \to \nu_\ell \ell sc$, etc.) originate, for instance, from WW production (cf. Figure 5.3g) and may contribute, provided the charged lepton remains undetected. Clearly, a veto on the presence of isolated leptons can be used to reduce the impact of this kind of background. Furthermore, the corresponding final states typically contain less missing energy as compared to the signal, since only one neutrino is present.

Apart from the resonant processes, none of the background modes listed above involves an actual Higgs decay. Therefore, a cut on the invariant mass of the final-state jet pair m_{bj} is expected to reject sizable parts of the total background. In order to asses the effect of such a cut on the different contributions, we plot the two-jet invariant mass spectra in Figure 5.7b. Similarly, for the purpose of reducing contamination from background modes with less than two neutrinos in the final state, we will require the presence of a minimal amount of missing transverse energy. The relevant distributions are shown in Figure 5.7a.

Our complete event selection procedure consists of the following series of cuts, which are applied to the reconstructed Monte Carlo events. First, we require the final state to contain precisely one b-tagged jet, as well as one jet

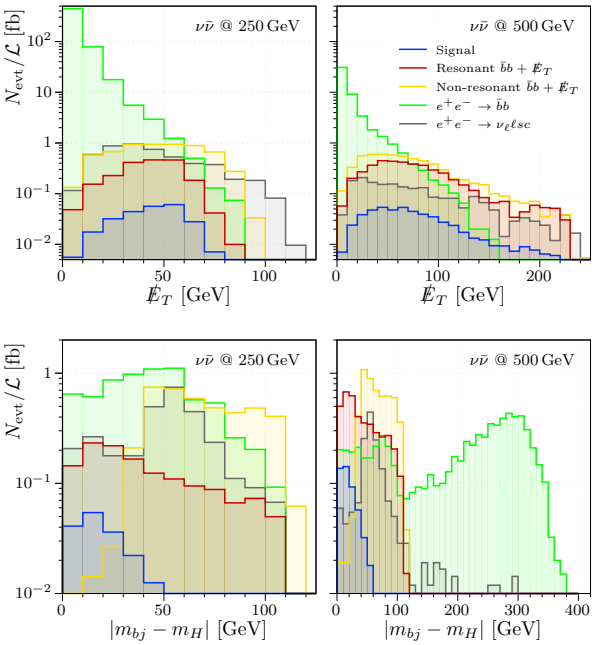

(a) Missing energy spectra after particle identification cuts.

(b) Two-jet invariant mass spectra after the missing energy cut.

Figure 5.7: Different kinematic distributions of signal and dominant background events in the neutrino channel at 250 GeV (*left*) and 500 GeV (*right*) with beam polarization $\mathcal{P}_{-+}$. All spectra are normalized to integrated luminosity.

which does not receive any flavor tag and is to be identified with a light-flavor jet. Both jets are asked to have sufficiently large transverse momenta, $p_T > 10\,\text{GeV}$, and are supposed to lie within $|\eta| < 1.8$. Next we reject all events with at least one reconstructed isolated charged lepton in the final state. As mentioned above, cuts on the two-jet invariant mass and the amount of missing transverse energy are crucial in discriminating the signal processes of equation (5.23) from several background sources. Specifically, we only select events which satisfy $\not{E}_T > 35\,\text{GeV}$ and $\Delta_{mH} < 30\,\text{GeV}$ for $\sqrt{s} = 250\,\text{GeV}$ or $\not{E}_T > 25\,\text{GeV}$ and $\Delta_{mH} < 25\,\text{GeV}$ for $\sqrt{s} = 500\,\text{GeV}$, respectively. The aforementioned values for $\not{E}_T^{\text{min}}$ and Δ_{mH}^{max} were determined to be the ones maximizing the signal significance in the presence of an assumed systematic background uncertainty of $\epsilon_{\text{syst}} = 1\,\%$ (cf. also Figure 5.7). Lastly, we ask the two final-state jets to be sufficiently close in the azimuthal plane, namely $\Delta\phi_{bj} < 3.0$. This cut was seen to further reduce the contamination from quark pair production events, for which the final-state jets are expected to be predominantly back-to-back due to momentum conservation.

Similar to the analysis channels discussed before, the presentation of our results will proceed in two steps. First, the cutflows of event yields resulting from the selection method detailed above are listed in Table 5.6 assuming the benchmark point of equation (5.11). The signal-to-background ratio for the 250 GeV case is found to be worse than that of the charged lepton

	Signal	$(\nu\bar{\nu})b\bar{b}$	$(\nu\bar{\nu})c\bar{c}$	$(\nu\bar{\nu})jj$	$\nu_\ell\ell sc$	$\nu_\ell\ell du$
Reco.	879	$2.4 \cdot 10^7$	$2.4 \cdot 10^7$	$7.2 \cdot 10^7$	$5.2 \cdot 10^6$	$5.2 \cdot 10^6$
Jet tag	435	$1.0 \cdot 10^6$	$5.2 \cdot 10^5$	$8.6 \cdot 10^5$	$2.4 \cdot 10^5$	$6.7 \cdot 10^4$
No ℓ	429	$9.7 \cdot 10^5$	$5.1 \cdot 10^5$	$8.5 \cdot 10^5$	7316	2430
$\not{E}_T$	301	$2.1 \cdot 10^4$	$1.2 \cdot 10^4$	$1.3 \cdot 10^4$	4400	1208
Δ_{mH}	222	4506	2420	2898	935	402
$\Delta\phi_{bj}$	201	1335	234	202	899	375

(a) Cutflow table for the neutrino channel at 250 GeV assuming an integrated luminosity of $2\,\mathrm{ab}^{-1}$ with polarization sharing scenario 1.

	Signal	$(\nu\bar{\nu})b\bar{b}$	$(\nu\bar{\nu})c\bar{c}$	$(\nu\bar{\nu})jj$	$\nu_\ell\ell sc$	$\nu_\ell\ell du$
Reco.	2490	$7.5 \cdot 10^6$	$8.2 \cdot 10^6$	$2.3 \cdot 10^7$	$3.6 \cdot 10^6$	$3.6 \cdot 10^6$
Jet tag	1147	$1.6 \cdot 10^5$	$9.8 \cdot 10^4$	$1.6 \cdot 10^5$	$1.3 \cdot 10^5$	$3.6 \cdot 10^4$
No ℓ	1137	$1.6 \cdot 10^5$	$9.8 \cdot 10^4$	$1.6 \cdot 10^5$	4092	1539
$\not{E}_T$	1040	$3.7 \cdot 10^4$	$2.0 \cdot 10^4$	$2.3 \cdot 10^4$	3450	1217
Δ_{mH}	695	4617	568	813	288	116
$\Delta\phi_{bj}$	655	3946	299	522	270	107

(b) Cutflow table for the neutrino channel at 500 GeV assuming an integrated luminosity of $4\,\mathrm{ab}^{-1}$ with polarization sharing scenario 2.

Table 5.6: Cutflows of signal and background events in the neutrino channels. The signal rate was chosen according to the benchmark point of equation (5.11), i.e. $\mathcal{B}(H \to bj) \simeq 0.73\,\%$. In the columns labeled $(\nu\bar{\nu})kk$, we summarize contributions from all background processes involving two final-state jets of flavor k. For further details on the notation, see the main text.

channel, being mainly limited by large background contributions of processes involving pairs of b quarks and the sc charged-current mode. In contrast, the value of S/B at 500 GeV is comparable to that in the charged lepton search. Interestingly, for the 500 GeV case the relative background weights r as defined in equation (5.16) turn out to be reasonably close to the idealized values from Table 5.4. This finding already indicates that the background in the 500 GeV analysis is dominated by resonant modes. In an analogous way, non-resonant contributions can be seen to be more relevant in the context of the search at 250 GeV.

In a second step, the neutrino channels' reachable sensitivity can be read off from Figure 5.8, where a systematic background error of 1 % was adopted (cf. also the footnote on page 121). The performance of the neutrino channel at 250 GeV is thereby found to be very similar to that of the charged lepton channel with slightly better expected upper bounds ($\mathcal{B}_{95\%} \simeq 0.4\,\%$) and discovery limits ($\mathcal{B}_{5\sigma} \simeq 1\,\%$). Therefore, we will largely concentrate on the

500 GeV variant in the following. Here, a 95 % CL upper bound of better than 0.2 % on the signal branching ratio is anticipated to be set in the event of a null result based on the full $4\,\mathrm{ab}^{-1}$ data set. A $5\,\sigma$ discovery could be expected if $\mathcal{B}(H \to bj)$ is larger than 0.5 %. Hence, given a signal branching fraction that is not yet entirely disfavored by the indirect constraints from equation (5.7), the neutrino channel at 500 GeV is the only search mode that may offer the possibility to actually discover the decay $H \to bj$ and thus measure the associated BSM Higgs couplings.

Finally, let us compare our actual findings for the performance of the neutrino channel at 500 GeV with our rough estimate in equation (5.21), which was obtained taking into account resonant background modes only. Adopting as a reference branching fraction that of our benchmark point, i.e. $\mathcal{B}_0 = 0.73\,\%$, we now have to anticipate the corresponding number of signal events S_0, which is schematically given by equation (5.15b), repeated here for convenience

$$S_0 = \mathcal{L} \cdot \sigma_{\mathrm{prod}} \cdot \alpha \cdot \epsilon' \cdot \epsilon_{\mathrm{tag},bj} \cdot \mathcal{B}_0 \; .$$

As a first simplification, we assume that the entire 500 GeV run with $\mathcal{L} = 4\,\mathrm{ab}^{-1}$ of accumulated data uses $\mathcal{P}_{-+}$-polarized beams. The production cross-section of interest can then be read off from Figure 5.1

$$\sigma_{\mathrm{prod}} \equiv \sigma(e^+e^- \to \nu\bar{\nu}H) = \sigma_{WBF} + \sigma_{ZH} \cdot \mathcal{B}(Z \to \nu\bar{\nu}) \approx 180\,\mathrm{fb} \; .$$

Additionally setting all acceptances and efficiencies to unity, we end up with a first approximation for the number of signal events to be produced, namely $S_0 \approx 5256$. At least factoring in the chosen tagging efficiency from Table 5.4 in a consistent way, we find the refined value of $S_0 \approx 3742$, which yields $\mathcal{B}_{95\%} \gtrsim 4.7 \cdot 10^{-4}$ as per equation (5.21). A more thorough estimate for S_0 and hence for $\mathcal{B}_{95\%}$ can be obtained by appropriate simulations thus additionally taking into account more realistic detector acceptances α, particle reconstruction efficiencies ϵ' and polarization splitting. Of course, this is what has been done in the course of our full analysis, so that S_0 can be read off from Table 5.6b. Not applying any kinematic cuts, we find $S_0 = 1137$ and therefore $\mathcal{B}_{95\%} \gtrsim 9 \cdot 10^{-4}$. In practice, imposing additional cuts like the ones listed in Table 5.6b is required for the sake of rejecting events from non-resonant background processes. Setting $S_0 = 655$ accordingly, gives $\mathcal{B}_{95\%} \gtrsim 1 \cdot 10^{-3}$. Note that the computation of the last two estimates involved simulations to reliably approximate the expected number of signal events, given some reference branching ratio $\mathcal{B}_0$. The results are otherwise still entirely based on our simple considerations from Section 5.3.3.A. Comparing these last estimates with the actual outcome of our full analysis, $\mathcal{B}_{95\%} \approx 2 \cdot 10^{-3}$, thus demonstrates that the neutrino channel at 500 GeV is indeed dominated by the resonant background modes. Its sensitivity is therefore mainly limited by flavor tagging capabilities.

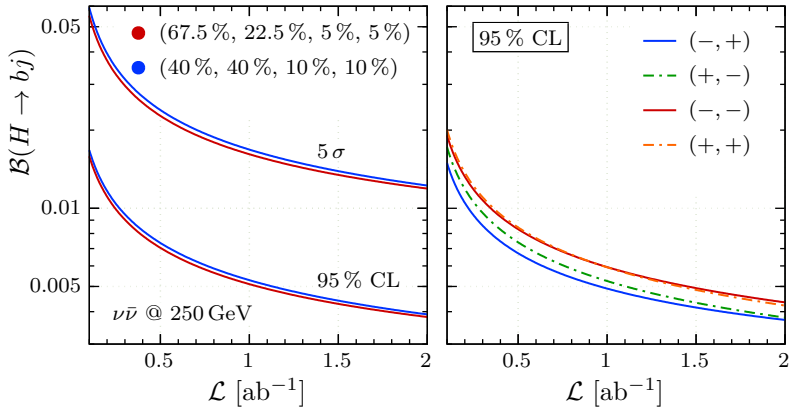

(a) Expected performance of the neutrino channel at $\sqrt{s} = 250\,\text{GeV}$.

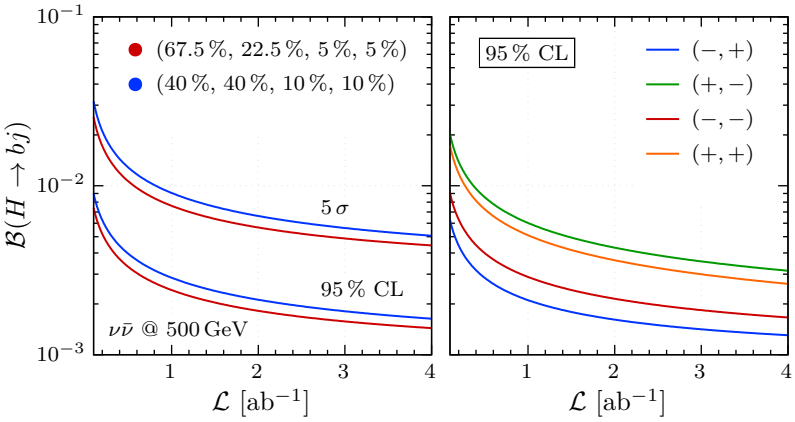

(b) Expected performance of the neutrino channel at $\sqrt{s} = 500\,\text{GeV}$.

Figure 5.8: Expected performance of the neutrino channels as a function of the total integrated luminosity, assuming a systematic error of $\epsilon_{\text{syst}} = 1\,\%$. *Left*: Expected $5\,\sigma$ discovery and 95 % CL exclusion reaches on $\mathcal{B}(H \to bj)$ for the two polarization scenarios of equation (5.9). *Right*: Expected exclusion reaches for the four possible polarization configurations individually.

5.4 Summary and conclusion

In the present chapter, following our original work in [50], we have performed the first thorough study of the prospects for the proposed International Linear Collider (ILC) to discover or constrain flavor-violating decays of the 125 GeV Higgs boson into a bottom and a light-flavor quark via direct searches. As a basis for our analyses, we adopted the original ILC baseline program, which includes physics runs at center-of-mass energies of 250 GeV and 500 GeV, and assumed appropriate luminosity and beam polarization sharing scenarios. Taking into account single-Higgs production both via Higgsstrahlung and via W boson fusion, we then investigated all final state signatures which potentially lend themselves to dedicated searches for the process $H \to bj$, and thus identified the most promising channels for each center-of-mass energy. Our main results are compiled in Figure 5.9.

The plot reveals that the 250 GeV ILC is expected to probe branching fractions down to roughly 0.5 % assuming the full targeted integrated luminosity of $2000\,\text{fb}^{-1}$. Similarly, a discovery at the $5\,\sigma$ level is anticipated to be feasible for decay rates of order 1 %. The above results were obtained employing search channels, in which the decay products of the Higgs boson are accompanied by a pair of electrons or muons, or by missing energy from two neutrinos. We also demonstrated that the sensitivity of the also possible purely hadronic final state is limited by the large combinatorial four-jet background.

For the 500 GeV run the only relevant search mode was argued to be that involving a pair of neutrinos. Provided that no deviations from the Standard Model predictions are observed, a corresponding analysis based on $4000\,\text{fb}^{-1}$ of accumulated data is expected to exclude branching ratios larger than approximately 0.2 % at 95 % CL. A $5\,\sigma$ discovery was shown to be realistic once $\mathcal{B}(H \to bj)$ exceeds roughly 0.5 %. Interestingly, even an initial run collecting only $500\,\text{fb}^{-1}$ of data is anticipated to probe branching ratios down to about 0.4 %.

Of course, more sophisticated analysis techniques or additional cuts may improve all or some of the aforementioned results. Recall furthermore that our findings were produced employing fast detector simulations. In order to provide more accurate predictions for the individual search modes' expected performances, full analyses involving dedicated simulations based on complete models of the proposed ILC detectors are clearly desirable. Still, the results presented here already offer a first assessment of the feasible sensitivity of direct searches for quark-flavor-violating (QFV) Higgs decays at future electron-positron colliders. They additionally reveal which of the considered final states have the most promising prospects for an actual analysis. In this context, let us also mention our estimate of the leptonic channels' performances, which was based on a simplified calculation taking into account only resonant background processes as well as projected flavor tagging

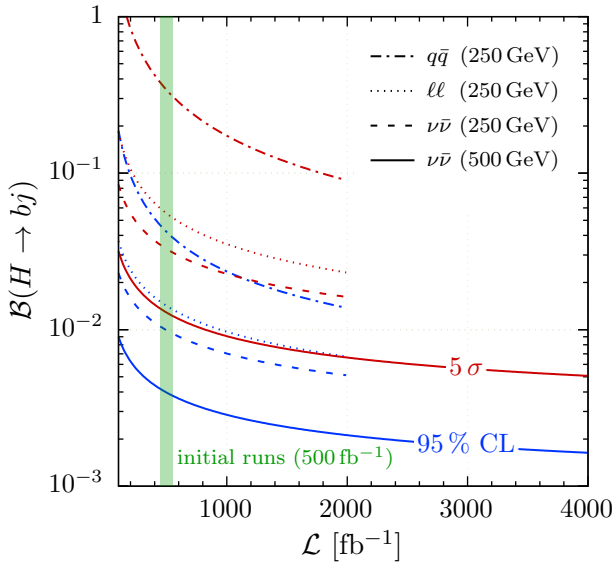

Figure 5.9: Comparison between the expected performances of all considered channels. We show $5\,\sigma$ discovery and 95 % CL exclusion reaches on $\mathcal{B}(H \to bj)$ as functions of total integrated luminosity, assuming a systematic error of $\epsilon_{\text{syst}} = 1\,\%$. Polarization sharing scenarios 1 and 2 were adopted for searches at 250 GeV and 500 GeV center-of-mass energy, respectively.

capabilities. Accordingly, said estimate was argued to yield an inherent upper bound on the achievable sensitivity, which was then demonstrated to be nearly saturated by our results obtained for the neutrino mode at 500 GeV.

With our projections for the ILC's sensitivity to $H \to bj$ decays at hand, it is finally interesting to compare these results with existing indirect constraints on the involved QFV Higgs couplings, as well as with theoretical predictions for the corresponding branching ratios as obtained in specific models of new physics. In this context, we have previously demonstrated that naively applying indirect limits coming from high-precision measurements of meson oscillations [41] restricts $\mathcal{B}(H \to bj)$ to be smaller than 10^{-3}–10^{-2}. Notably, values in said range could still be probed by both the 250 GeV and the 500 GeV ILC. Furthermore, it is interesting to observe that both the Minimal Supersymmetric Standard Model and two-Higgs-doublet models can produce values for $\mathcal{B}(H \to bj)$ larger than 10 %, if one accepts a certain degree of fine tuning of the models' couplings or masses [191, 197]. Barring any amount of such parameter tuning, those models may still lead to branching fractions of order 10^{-3}, which are also in reach of the ILC.

In conclusion, we have seen that *direct* searches for QFV Higgs couplings via exotic Higgs decays are crucial to fully explore models exhibiting quark-flavor violation. In particular, identifying the origin of potentially observed QFV effects and actually measuring the couplings that are used

to parameterize these effects necessarily require direct measurements. Also robustly excluding or confirming the aforementioned fine-tuned scenarios makes direct searches indispensable as an approach complementary to the well-studied class of indirect measurements, the limits from which are systematically avoided in these cases. In the present chapter, we have explicitly shown that future electron-positron colliders are the experiments of choice to perform such direct searches.

Chapter 6

Final conclusion and outlook

The persistent lack of clear signs of phenomena beyond the Standard Model (BSM) at the Large Hadron Collider (LHC) is one of the chief problems that particle physicists are facing today. Even though a major discovery within the lifespan of the LHC or its upgrades is still entirely conceivable, it is nevertheless instructive to explore potential underlying causes for a *systematic* absence of new physics from the available LHC results. In the present thesis, we did so by discussing three concrete examples of BSM scenarios, which current analyses may have failed to uncover for different reasons. In all three cases, we concentrated on extensions of the minimal Standard Model (SM) involving modified scalar sectors, meaning that the properties of the Higgs boson found by ATLAS and CMS in 2012 deviate from the corresponding SM predictions, or that there exist additional scalar states. Said modified scalar sectors were argued to be particularly well motivated since they are an integral part of many different models addressing one or more problems of contemporary particle physics.

Before we go on to recapitulate some of our principal findings, let us again draw the reader's attention to the more complete summaries of all results obtained in the course of this thesis and their physical impact, which were already given at the end of the respective chapters for the sake of coherence (cf. Sections 3.4, 4.4 and 5.4). Here, we instead focus on those findings which are directly correlated to our original question of how new physics may hide itself from being discovered. We will also try to give a somewhat broader outlook on particle physics in general.

Let us start by recalling the first potential reason for the absence of BSM phenomena from current LHC searches, which was previously phrased as:

We may be looking for the wrong models.

As an example for a category of possibly "right" models, we considered theories based on classical scale invariance. The latter constitute an alternative approach to solving the longstanding gauge hierarchy problem and

may thus explain the absence of any signs of supersymmetry or other traditional frameworks to remedy naturalness issues plaguing Higgs sectors of generic SM embeddings. In a systematic study of a broad class of classically conformal theories we identified the minimal model consistent with basic theoretical and experimental requirements to be the SM extension by two real scalar fields, one of which acquires a finite vacuum expectation value of order of the electroweak scale. The minimal model's particle spectrum was then demonstrated to contain a light scalar boson with a mass of order 10 GeV, which couples to SM fermions and gauge bosons via Higgs mixing, as well as a further scalar state heavier than 300 GeV and only interacting with the other scalars via appropriate portal couplings. More generally, it turned out that, just like conventional solutions to the gauge hierarchy problem, also the considered class of scale-invariant theories necessarily implies the existence of extra scalar particles at the TeV scale. Nevertheless, the coupling strengths of those new states to SM fields are considerably less restricted than, for example, in models based on supersymmetry. Also the simplest and most natural instances of classically conformal theories like the aforementioned minimal model can hence be consistent with the LHC's current null results.

On the other hand, theoretical consistency was demonstrated to prevent the light scalar from becoming arbitrarily weakly coupled to the SM sector. Correspondingly, upcoming runs of the LHC or future lepton machines (potentially supplemented by appropriate high-precision measurements at lower energies) are anticipated to nearly fully probe the simplest conformal models, which would thereby come under significant pressure, if no evidence for new physics was found. Importantly, though, one or more of our initial assumptions, which were used to define the investigated class of theories, can be relaxed (cf. the list on page 22). In particular, the possibly problematic necessity of additional particles in reach of the LHC or other near-future colliders can be traced back to the fact that our study was restricted to models where scale symmetry is spontaneously broken at around the electroweak scale. Theories in which radiative symmetry breaking takes place at much higher energies are therefore attractive alternatives. They are, however, much less explored in the literature since, if not implemented with great care, a fine-tuning problem is generally reintroduced. In this context, preliminary results from an ongoing study by the author and his collaborators indicate that large hierarchies between the scales of spontaneous conformal and electroweak symmetry breaking can indeed be realized in a classically scale-invariant model, where all small couplings are technically natural [121].

Let us now move on to the second aspect of how new physics may have escaped its detection so far, which was previously formulated as:

We may be looking in the wrong channels.

Observing that current LHC searches for light scalar particles h via decays

of the SM-like Higgs boson H exclusively rely on the two-body channel, $H \to 2h$, we took a closer look at the related, but yet still unexplored three-body mode $H \to 3h$. In particular, we discussed a simple model which predicts the latter decay process, namely the real scalar singlet extension of the SM. In doing so, we found that for light scalars heavier than roughly 5 GeV, there exist extensive regions of parameter space, where the two-body channel becomes anomalously rare and thus undetectable. Said behavior could be traced back to mild cancellations between the amplitudes of two Feynman diagrams contributing to the corresponding effective coupling κ_{H2h}. The three-body decay, on the other hand, was seen to be not affected by the aforementioned cancellations. Indeed, assuming sufficiently large but still perturbative self-interactions in the singlet sector, as well as not too small scalar mixing angles, we showed that Higgs cascade decays via three light scalars are abundant enough to be observable, even in situations where the two-body channel is virtually absent. It was therefore argued that many interesting six-body final states involving pairs of tau leptons and jets are expected to be in reach of the LHC or future electron-positron colliders. We thus demonstrated that exotic Higgs decays into three light scalars, which were previously thought of as phenomenologically irrelevant, can provide valuable and complementary information on the physics of light scalar sectors. Therefore, we strongly encourage the ATLAS and CMS experiments to consider including the three-body channel in their corresponding searches in the future.

We finally also considered the possibility that new physics at the TeV scale only manifests itself through rare processes with purely hadronic final states. The absence of BSM phenomena from current LHC searches could then be attributed to the fact that

we may be looking with the wrong experiment.

As an example for a well-motivated process which is anticipated to belong to the aforementioned class, we investigated the quark-flavor-violating Higgs decay into a bottom and a strange quark, as well as its prospects for being tested at the proposed International Linear Collider (ILC). In doing so, we found that the ILC is expected to be capable of probing the corresponding Higgs branching fraction down to the per mill level and would thereby be sensitive to scenarios which are clearly beyond the reach of the LHC or any of its upgrades. Specifically, our analyses based on fast detector simulations revealed that a potential 500 GeV run of the ILC collecting $4\,\text{ab}^{-1}$ of data is anticipated to facilitate a discovery at the $5\,\sigma$ level for branching ratios larger than roughly 0.5 %. Similarly, the same run is expected to lead to a 95 % CL upper bound of around 0.2 % in the event of a null result. Both of the above projections rely on studies of the final state signature, where the bottom and strange quarks are accompanied by missing energy coming from a pair of neutrinos. For the 250 GeV run, the expected sensitivity of

the ILC was shown to be somewhat reduced, but still of the same order of magnitude.

Although the presented findings are already promising and very well demonstrate the ILC's potential in complementing the LHC's quest to search for new physics, there is still a long way to go before actual results become available. Even if the Japanese government eventually decides to host the ILC project[a] and if the construction of the latter is started in a timely manner, its operation will not begin before 2028–2030 [215]. Accumulating the targeted amount of data will then take ten to 20 additional years of physics runs [214, 218]. But also without the ILC at hand in the immediate future, there are still ways to receive hints on potential quark-flavor violation in the Higgs sector. Apart from improved indirect constraints due to ongoing high-precision measurements of meson oscillations, said hints may even arise from direct searches at the LHC, namely by looking for the exotic top decays $t \to Hc$ or $t \to Hu$ [206, 207, 237].

Let us close with some more general and also more personal remarks on the current situation in particle physics. In my opinion, the absence of clear signs of new physics not only from the LHC, but also from other types of particle physics experiments like those directly searching for various kinds of dark matter, or those precisely measuring the properties of already known matter, entails a major difficulty, especially for model building: In many cases the principal problem is no longer how to accommodate a given aspect of BSM physics, such as the baryon asymmetry of the universe, the particle nature of dark matter or the smallness of neutrino masses, but how to distinguish between the large number of proposed solutions. This problem is related to the fact that physics in general and particle physics in particular crucially rely on the interplay between theory and experiment. The formulation and confirmation of the Standard Model over the last half century, which was partly sketched in the beginning of Chapter 2, is one of the prime examples for the success, but also for the necessity of said interplay.

Notably, uncovering the nature of elementary particles and their interactions at ever more fundamental levels was decisively driven by experiments at the high-energy frontier. With this in mind and guided by convincing arguments mainly based on naturalness, many physicists firmly believed that the LHC would not only detect the long-awaited Higgs boson, but would also find the first superpartners or other new particles in the TeV regime. In other words, apart from experimentally confirming the last missing piece of the SM, the LHC was also expected to determine the scale of new physics, thereby providing valuable orientation on how to include various BSM aspects in the particle physics picture. However, this is only partially what happened so far. Whereas the seminal discovery of the Higgs

[a] A decision on this matter is anticipated by the end of this year.

clearly demonstrated the truly remarkable capabilities of the experiments at the LHC, new particles at the TeV scale are still lacking. The scale of new physics therefore remains unknown. As a consequence, the TeV regime as the favored place to search for BSM phenomena is nowadays increasingly being called into question. This naturally elicits a renewed and enhanced interest in approaches towards experimental particle physics alternative to those exploring the high-energy frontier at colliders. Prime examples are high-precision measurements, like those pursued or planned at numerous existing and near-future neutrino and flavor physics experiments. Also direct searches for light and potentially long-lived hidden particles at proposed beam dump facilities such as SHiP [238, 239] fall into this category. These and other intensity-frontier experiments will certainly help to investigate otherwise inaccessible BSM scenarios.

In the case of the Higgs boson, however, precision measurements of its properties *do* require high-energy colliders. And it is especially these measurements, which in my opinion present a particularly good chance of discovering new physics. On the one hand, the Higgs is the most recent addition to the family of (presumably) elementary particles and thus the one whose properties are still the least known, so that enough room is left for all kinds of BSM phenomena to hide. On the other hand, the Higgs sector is virtually predestined to host such phenomena, since it offers one of the few possible portals to an otherwise secluded and perhaps diverse hidden sector of BSM particles. Searching for and exploring modified scalar sectors should therefore remain one of the priorities of particle physics in the future. Ideally, the results of the present thesis may provide some additional guidance to do so.

Appendix A

Calculating the Gildener-Weinberg scale

Based on the general discussion of the Gildener-Weinberg (GW) approach [120] given in Section 3.2, the present appendix will outline a method that we employed in our studies of classically scale-invariant models in Section 3.3. In particular, it was used to investigate the minimal conformal model in Section 3.3.3.B (for the notation, see there). Under some assumptions to be specified below, the described method allows to determine the *unique* scale of spontaneous symmetry breaking $\Lambda_{\rm GW}$ that is consistent with a given set of model parameters.

The basic idea relies on the observation that the full set of Lagrangian parameters can be divided into two classes: On the one hand, there are couplings which are empirically known at some particular scale (*class 1*). Typically, this will be the set of Standard Model (SM) Yukawa and gauge couplings whose numerical values are fixed at around the electroweak scale. On the other hand, there exist parameters whose values are set at $\Lambda_{\rm GW}$, independent of the GW scale itself (*class 2*). All couplings of the scalar potential as well as possible further new physics parameters belong to that second category.

In line with the above idea, we first rewrite the B function from equation (3.6b) separating the contributions due to SM fermions and gauge bosons ($B_{\rm SM}$) from those of the scalar sector and potential beyond-the-SM (BSM) fermions and gauge bosons ($B_{\rm add}$)

$$B = B_{\rm SM} + B_{\rm add} \,. \tag{A.1}$$

Next, we observe that in models where the electroweak symmetry is only broken by the usual Higgs doublet, we have $v = v_\phi = \sqrt{2} n_1 \langle\varphi\rangle$. Correspondingly, all SM particle masses apart from that of the Higgs can be brought into the form

$$m_i = \tilde{m}_i \, n_1 \langle\varphi\rangle \quad \text{for} \quad i \in \text{SM}^* \tag{A.2}$$

for appropriately defined dimensionless coefficients $\tilde{m}_i$, that will be functions of the class-1 parameters only, i.e. of the SM Yukawa and gauge couplings. The above identity (A.2) allows us to rewrite the loop function B yet again,

$$B(\Lambda_{\mathrm{GW}}) = n_1^4 \tilde{B}_{\mathrm{SM}}(\Lambda_{\mathrm{GW}}) + B_{\mathrm{add}} \,, \tag{A.3}$$

with the newly defined function

$$\tilde{B}_{\mathrm{SM}}(\Lambda_{\mathrm{GW}}) = \frac{1}{64\pi^2} \sum_{i \in \mathrm{SM}^*} (-1)^{2s_i} d_i \cdot \tilde{m}_i^4(\Lambda_{\mathrm{GW}}) \,.$$

The feature making equation (A.3) particularly useful is that all dependence on Λ_{GW} is now encoded in $\tilde{B}_{\mathrm{SM}}$ which, in turn, does not contain any scalar or BSM (i.e. class-2) parameters. Assuming that the system of beta functions describing the RG evolution of the couplings in $\tilde{B}_{\mathrm{SM}}$ is closed – as it is the case for the SM at one loop – the scale dependence of $\tilde{B}_{\mathrm{SM}}$ can be calculated *before* specifying any of the class-2 couplings.

Now, we are finally in the position to calculate the Gildener-Weinberg scale. Having our application in Chapter 3 in mind, we assume here that the 125 GeV Higgs boson is *not* identified with the pseudo-Goldstone boson of broken scale invariance. The alternative case, however, can be treated similarly. For a numerical implementation of the computation, it is convenient to define the following scale-dependent function

$$G(\Lambda) := n_1^4 \tilde{B}_{\mathrm{SM}}(\Lambda) + \underbrace{B'_{\mathrm{add}} + \frac{n_1^4}{16\pi^2} \frac{m_H^4}{v^4}}_{=B_{\mathrm{add}}} - \frac{n_1^2}{4} \frac{m_{\mathrm{PGB}}^2}{v^2} \,. \tag{A.4}$$

Inserting equation (A.3) into the expression for the scalon mass shown in equation (3.8) then implies that the *unique*[a] solution for Λ_{GW}, which is consistent with the given parameter point, is

$$G(\Lambda_{\mathrm{GW}}) \stackrel{!}{=} 0 \,. \tag{A.5}$$

In order to verify that the parameter point under consideration is indeed viable, the scale computed via equation (A.5) must pass two more sanity checks. First, it has to be reasonably close to the electroweak scale v in accordance with our initial assumption 2 on page 22 (cf. also the corresponding discussion on page 23). Second, we are to test whether the obtained Λ_{GW} actually reproduces the correct value for v, which we implicitly assumed up to now. If the result of equation (3.7),

$$v = \sqrt{2} n_1 \Lambda_{\mathrm{GW}} \cdot \exp\left(-\frac{1}{4} - \frac{A}{2B}\right) \,, \tag{A.6}$$

[a] The uniqueness property is guaranteed, as the function $\tilde{B}_{\mathrm{SM}}(\Lambda)$ was found to monotonically increase with the energy scale Λ.

does not coincide with the empirically known value, the parameter point has to be discarded as inconsistent.

In summary, the self-consistent solution of equations (A.5) and (A.6) for given v and m_{PGB} allows to fix two formerly free parameters at the GW scale, namely Λ_{GW} itself and B'_{add}. The latter will typically be a function of all BSM particle masses and thus depend on the model under investigation. For instance, for the minimal conformal model discussed in Section 3.3.3.B, one finds

$$B'_{\mathrm{add}} = \frac{m_R^4}{64\pi^2\langle\varphi\rangle^4} = \frac{\left(\kappa_{\phi R} n_1^2 + \kappa_{SR} n_2^2\right)^2}{16\pi^2} \,.$$

Appendix B

One-loop renormalization group equations

The aim of the present appendix is to collect the renormalization group equations (RGE) relevant to our studies of minimal conformal extensions of the Standard Model (SM) Higgs sector in Chapter 3. Correspondingly, we will exclusively be interested in the beta functions of dimensionless couplings and concentrate on scenarios where the SM is supplemented by either two real scalars (Section B.1) or one complex scalar (Section B.2). Furthermore, the extra scalars are assumed to be colorless $\mathrm{SU}(2)_L$ multiplets with hypercharge Y.[a] Some of the RGEs will therefore contain invariants of the appropriate SU(2) representations – namely the quadratic Casimir C and the Dynkin index D – which are given by

$$C = \tfrac{1}{4}(N^2-1)\,, \quad D = \tfrac{1}{3}NC = \tfrac{1}{12}N(N^2-1) \tag{B.1}$$

in case of an SU(2) N-plet. The beta functions themselves are presented employing the following notation which makes the underlying perturbative expansion manifest

$$\beta(g) \equiv \frac{\mathrm{d}g}{\mathrm{d}\log\mu} = \frac{\beta^{(1)}(g)}{16\pi^2} + \frac{\beta^{(2)}(g)}{(16\pi^2)^2} + \dots\,.$$

Finally, let us remark that all one-loop RGEs presented here are based on calculations by the author, which were cross-checked with the outcome of dedicated computer programs [240, 241] whenever possible. These programs, in turn, implement the general two-loop results from the original papers by Machacek and Vaughn [242–244].

[a] Note that real scalars necessarily have zero hypercharge.

B.1 SM + real scalar representation(s)

Let us start with the Higgs sector of the SM enlarged by up to two *real* scalar $\mathrm{SU}(2)_L$ multiplets, denoted as χ and ξ, respectively. In line with our discussion in Chapter 3, we will assume the underlying scalar potential to be of the form given in equation (3.34). Apart from classical scale invariance, the potential thus exhibits a global $\mathrm{O}(4) \times \mathrm{O}(N_\chi) \times \mathrm{O}(N_\xi)$ symmetry. The corresponding scalar-sector RGEs are then calculated to be

$$\begin{aligned}
\beta^{(1)}_{\lambda_\phi} &= 24\lambda_\phi^2 + 2N_\chi\kappa_{\phi\chi}^2 + 2N_\xi\kappa_{\phi\xi}^2 \,, \\
\beta^{(1)}_{\lambda_\chi} &= 8(N_\chi+8)\lambda_\chi^2 + 2\kappa_{\phi\chi}^2 + 2N_\xi\kappa_{\chi\xi}^2 \,, \\
\beta^{(1)}_{\kappa_{\phi\chi}} &= 8\kappa_{\phi\chi}\Big[\tfrac{3}{2}\lambda_\phi + (N_\chi+2)\lambda_\chi + \kappa_{\phi\chi}\Big] + 4N_\xi\kappa_{\phi\xi}\kappa_{\chi\xi} \,, \\
\beta^{(1)}_{\kappa_{\chi\xi}} &= 8\kappa_{\chi\xi}\Big[(N_\chi+2)\lambda_\chi + (N_\xi+2)\lambda_\xi + 2\kappa_{\chi\xi}\Big] + 4\kappa_{\phi\chi}\kappa_{\phi\xi} \,,
\end{aligned} \tag{B.2}$$

with Φ being the usual Higgs doublet. The beta functions of λ_ξ and $\kappa_{\phi\xi}$ emerge from those of λ_χ and $\kappa_{\phi\chi}$ upon exchanging $\chi \leftrightarrow \xi$ as well as identifying $\kappa_{\chi\xi} \equiv \kappa_{\xi\chi}$.

Of course, the scalars are not only mutually coupled, but generally also interact with the electroweak gauge bosons. Taking into account these effects, one finds additional contributions to the above RGEs, namely

$$\begin{aligned}
\Delta\beta^{(1)}_{\lambda_\phi} &= -3\lambda_\phi(g_1^2+3g_2^2) + \tfrac{3}{8}(g_1^4+3g_2^4+2g_1^2g_2^2) \,, \\
\Delta\beta^{(1)}_{\lambda_\chi} &= -12C_\chi\lambda_\chi g_2^2 + \tfrac{3}{32}\Big[\mathcal{T}(N_\chi,N_\chi) + 8\delta_{N_\chi,3}\Big]g_2^4 \,, \\
\Delta\beta^{(1)}_{\kappa_{\phi\chi}} &= -\tfrac{3}{2}\kappa_{\phi\chi}\Big[g_1^2 + (4C_\chi+3)g_2^2\Big] + \tfrac{3}{2}C_\chi g_2^4 \,, \\
\Delta\beta^{(1)}_{\kappa_{\chi\xi}} &= -6(C_\chi+C_\xi)\kappa_{\chi\xi}g_2^2 + \tfrac{3}{16}\mathcal{T}(N_\chi,N_\xi)g_2^4 \,,
\end{aligned} \tag{B.3}$$

where we introduced the abbreviation

$$\mathcal{T}(N_\chi,N_\xi) = (N_\chi-1)(N_\xi-1)\Big[N_\chi N_\xi - (N_\chi+N_\xi) + 3\Big] \,.$$

Furthermore, the Higgs doublet also interacts with SM fermions. However, only the Yukawa coupling y to the top quark is sizable modifying the scalar RGEs in the following way

$$\Delta\beta^{(1)}_{\lambda_\phi} = 6(2\lambda_\phi - y^2)y^2 \,, \quad \Delta\beta^{(1)}_{\kappa_{\phi\chi}} = 6\kappa_{\phi\chi}y^2 \,. \tag{B.4}$$

Finally, the presence of the extra $\mathrm{SU}(2)_L$ multiplets alters the beta function of the associated gauge coupling g_2, which now reads

$$\beta^{(1)}_{g_2} = \big[\tfrac{1}{6}(D_\chi+D_\xi) - \tfrac{19}{6}\big]\, g_2^3 \,. \tag{B.5}$$

All other SM beta functions are not modified at the one-loop level.

B.2 SM + one complex scalar representation

In this section, we consider an SM-like Higgs sector enlarged by one *complex* scalar $\mathrm{SU}(2)_L$ multiplet χ with hypercharge Y. The underlying scalar potential is assumed to be of the form displayed in equation (3.10) supplemented by the κ_3-term introduced in equation (3.28). The associated scalar RGEs then turn out to be

$$\begin{aligned}
\beta^{(1)}_{\lambda_1} &= 24\lambda_1^2 + N\kappa_1^2 + \tfrac{1}{4}D\kappa_2^2 + 2D\kappa_3^2 \,, \\
\beta^{(1)}_{\lambda_2} &= 4(N+4)\lambda_2^2 + \tfrac{1}{2}(N-1)^2\Big[N(10-N)-13\Big]\lambda_3^2 \\
&\quad + 8C\lambda_2\lambda_3 + 2\kappa_1^2 + \Big(\delta_{N,2} + \tfrac{9}{2}\delta_{N,4}\Big)\kappa_3^2 \,, \\
\beta^{(1)}_{\lambda_3} &= \tfrac{1}{3}(N-2)\Big[N(N+20)-33\Big]\lambda_3^2 \\
&\quad + 24\lambda_2\lambda_3 + \tfrac{1}{2}\kappa_2^2 - 2\delta_{N,4}\kappa_3^2 \,, \\
\beta^{(1)}_{\kappa_1} &= 4\kappa_1\Big[3\lambda_1 + (N+1)\lambda_2 + C\lambda_3 + \kappa_1\Big] + C\kappa_2^2 + 8C\kappa_3^2 \,, \\
\beta^{(1)}_{\kappa_2} &= 4\kappa_2\Big[\lambda_1 + \lambda_2 + (D+C-1)\lambda_3 + 2\kappa_1\Big] - 16\kappa_3^2 \,, \\
\beta^{(1)}_{\kappa_3} &= 4\kappa_3\Big[\lambda_1 + \lambda_2 - (C-1)\lambda_3 + 8\kappa_1 - 4\kappa_2\Big] \,,
\end{aligned}$$

with N, C and D denoting dimension and invariants of the SU(2) representation under which the extra scalar transforms. Again, incorporating SM Yukawa and electroweak gauge interactions yields additional contributions to the above scalar beta functions, which are found to be

$$\Delta\beta^{(1)}_{\lambda_1} = 6(2\lambda_1 - y^2)y^2 \,, \quad \Delta\beta^{(1)}_{\kappa_i} = 6\kappa_i y^2 \,,$$

and

$$\begin{aligned}
\Delta\beta^{(1)}_{\lambda_1} &= -3\lambda_1\big(g_1^2 + 3g_2^2\big) + \tfrac{3}{8}g_1^4 + \tfrac{9}{8}g_2^4 + \tfrac{3}{4}g_1^2g_2^2 \,, \\
\Delta\beta^{(1)}_{\lambda_2} &= -3\lambda_2\Big[4Y^2g_1^2 + (N^2-1)g_2^2\Big] + 6Y^4g_1^4 \\
&\quad + \tfrac{3}{8}(N-1)^2\Big[N(10-N)-13\Big]g_2^4 \,, \\
\Delta\beta^{(1)}_{\lambda_3} &= -3\lambda_3\Big[4Y^2g_1^2 + (N^2-1)g_2^2\Big] + 12Y^2g_1^2g_2^2 \\
&\quad + 3\Big[(N-3)^2 - 1\Big]g_2^4 \,, \\
\Delta\beta^{(1)}_{\kappa_1} &= -\tfrac{3}{2}\kappa_1\Big[(4Y^2+1)g_1^2 + (N^2+2)g_2^2\Big] + 12Y^4g_1^4 + 3Cg_2^4 \,, \\
\Delta\beta^{(1)}_{\kappa_2} &= -\tfrac{3}{2}\kappa_2\Big[(4Y^2+1)g_1^2 + (N^2+2)g_2^2\Big] + 24Y^2g_1^2g_2^2 \,, \\
\Delta\beta^{(1)}_{\kappa_3} &= -\tfrac{3}{2}\kappa_3\Big[(4Y^2+1)g_1^2 + (N^2+2)g_2^2\Big] \,.
\end{aligned}$$

Lastly, since χ is generally charged under the electroweak group, the RGEs of the associated gauge couplings g_1 and g_2 are modified with respect to the minimal SM, namely

$$\beta_{g_1}^{(1)} = \left(\tfrac{41}{6} + \tfrac{1}{3}NY^2\right)g_1^3 \,, \quad \beta_{g_2}^{(1)} = \left[\tfrac{1}{3}D - \tfrac{19}{6}\right]g_2^3 \,. \tag{B.6}$$

All other SM beta functions again remain unaltered.

Appendix C

Phase space threshold functions

The scalar-to-scalar multibody decay rates presented in equations (4.6) and (4.7) of Chapter 4 were formulated employing a certain set of auxiliary functions ℓ_i. These so-called threshold functions encode information about the processes' final-state kinematics and are obtained by performing the respective phase space integrals. A detailed discussion on the kinematics of particle decays can, for instance, be found in [83].

In this appendix, we will exclusively be interested in scenarios where the decaying particle is a scalar. Hence, the associated matrix elements do not depend on any angular variables, which greatly simplifies all calculations. In particular, the phase space integration for the two-body case is straightforward and yields

$$\ell_2(x) = \sqrt{1-4x^2}\,.$$

In contrast, an analytic expression is in general not available for a three-body final state and one has to resort to appropriate integral representations. For the relevant case of degenerate final-state masses, the corresponding function ℓ_3 can be brought into the following form (see e.g. [83]):

$$\ell_3^{(n,m)}(x) = 2\int_{\epsilon^-}^{\epsilon^+} \mathrm{d}\epsilon \int_{\eta^-}^{\eta^+} \mathrm{d}\eta \left(\epsilon - x^2\right)^{-n} \left(\eta - x^2\right)^{-m}\,,$$

where $n, m \in \mathbb{N}_0$. The integration boundaries are calculated to be

$$\begin{aligned}
\epsilon^- &= 4x^2\,, \quad \epsilon^+ = (1-x)^2\,,\\
\eta^\mp &= \frac{1}{4\epsilon}\left[(1-x^2)^2 - \left(\lambda^{1/2}(\epsilon, x^2, x^2) \pm \lambda^{1/2}(1, \epsilon, x^2)\right)^2\right],
\end{aligned}$$

with $\lambda(a,b,c) \equiv (a-b-c)^2 - 4bc$ being the Källén triangle function. In case of vanishing m (or n) the η-integration can be carried out such that

the three-body threshold function simplifies to

$$\ell_3^{(n)}(x) = \int_{\epsilon^-}^{\epsilon^+} \mathrm{d}\epsilon \, \frac{L_3(\epsilon, x^2)}{(\epsilon - x^2)^n} \, ,$$

where the integral kernel L_3 is given by

$$L_3(\epsilon, x^2) \equiv 2(\eta^+ - \eta^-) = \frac{2}{\epsilon} \lambda^{1/2}(\epsilon, x^2, x^2) \lambda^{1/2}(1, \epsilon, x^2) \, .$$

The threshold functions discussed in the present appendix exhibit two particular properties that are worth noting. For one, they are normalized such that they evaluate to unity in case of a massless final state:

$$\ell_2(0) = \ell_3^{(0)}(0) = 1 \, .$$

Furthermore, all ℓ_i vanish identically at the respective kinematic production threshold,

$$\ell_2\left(\tfrac{1}{2}\right) = \ell_3^{(n,m)}\left(\tfrac{1}{3}\right) = 0 \, ,$$

but are positive above it, i.e.

$$\ell_2(x) > 0 \quad \forall x > \tfrac{1}{2} \qquad \text{and} \qquad \ell_3^{(n,m)}(x) > 0 \quad \forall x > \tfrac{1}{3} \, .$$

The aforementioned feature also explains the nomenclature.

Appendix D

Tree-level perturbative unitarity

In Chapter 4, we employed arguments based on unitarity to set limits on the parameter space of a general model involving two scalar degrees of freedom. The present appendix is aimed at providing details on the corresponding calculations, thereby complementing our discussion in the main part of the text.

Starting from the unitarity of the scattering matrix (or S-matrix) of any well-behaved quantum field theory, one can derive a relation for its invariant matrix elements $\mathcal{M}$, the so-called optical theorem, which can schematically be written as (see e.g. [65])

$$-\mathrm{i}\big[\mathcal{M}(i \to f) - \mathcal{M}^*(f \to i)\big] = \sum_x \frac{1}{\eta_x} \int \mathrm{dLIPS}_x \, \mathcal{M}^*(f \to x)\mathcal{M}(i \to x) \; . \tag{D.1}$$

A few comments on the notation are in order. First, the labels i, f and x not only encode some initial or final state's particle content, but also said particles' kinematic variables such as four-momenta p, etc. In particular, equation (D.1) implicitly assumes overall four-momentum conservation, $p_i = p_f$. Second, the sum on the right-hand side runs over all viable combinations of final-state particles. For a given state x containing N particles, dLIPS_x is then the N-particle Lorentz-invariant phase space, which, among other things, parameterizes all possible momentum configurations of the particles in x. Lastly, the real number η_x is a symmetry factor introduced to avoid the double counting of equivalent momentum configurations in the presence of multiple identical particles in x.

In Chapter 4, we applied the generalized optical theorem of equation (D.1) to the case of two-to-two processes. Invariant matrix elements $\mathcal{M}$ can then be parameterized by only two kinematic variables, namely the squared center-of-mass energy s and one scattering angle ϑ. As a next step, it is

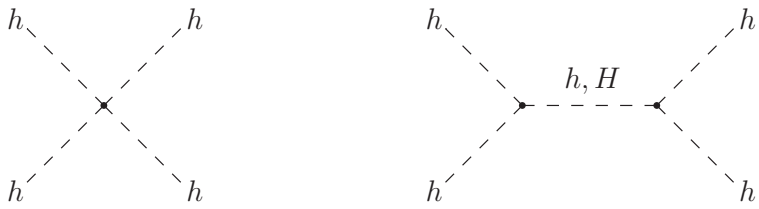

Figure D.1: Leading-order Feynman graphs contributing to light scalar elastic scattering $hh \to hh$: (a) contact interaction and (b) s-channel scalar exchange. Similar to (b), also the t- and u-channel diagrams exist, but are not shown.

convenient to expand the matrix elements in a complete set of Legendre polynomials $\mathcal{P}_j(\cos\vartheta)$, i.e.

$$\mathcal{M}(s,\vartheta) = 16\pi \sum_{j=0}^{\infty} (2j+1) a_j(s) \mathcal{P}_j(\cos\vartheta) \,. \tag{D.2}$$

The above re-writing is commonly referred to as partial-wave expansion, with the coefficients $a_j(s)$ being the partial-wave amplitudes. The latter can be obtained by inverting equation (D.2), which yields

$$a_j(s) = \frac{1}{32\pi} \int_{-1}^{1} \mathrm{d}\cos\vartheta \; P_j(\cos\vartheta) \mathcal{M}(s,\cos\vartheta) \tag{D.3}$$

for all $j \geqslant 0$.

In the context of our generic model introduced in Section 4.1, a review of all possible two-to-two processes involving the scalar degrees of freedom h and H demonstrated that the most interesting constraints on the parameter space arise from elastic scattering of low-mass scalars, $hh \to hh$, specifically from the associated s-wave amplitude $a_0(s)$. Namely, the aforementioned amplitude has to satisfy the unitarity bound

$$|\xi(s) \operatorname{Re} a_0(s)| \leqslant 1 \quad \text{with} \quad \xi(s) = \sqrt{1 - \frac{4m_h^2}{s}} \,, \tag{D.4}$$

which can be derived based on the optical theorem of equation (D.1) and the partial-wave expansion in equation (D.2) (see e.g. [163]). The leading-order Feynman diagrams that are needed to calculate $a_0(s)$ via equation (D.3) are displayed in Figure D.1. Importantly, the unitarity bound of equation (D.4) must be fulfilled for kinematically accessible center-of-mass energies $\sqrt{s} > 2m_h$. The constraints on λ_{4h}, κ_{H2h} and κ_{3h} presented in equations (4.17) to (4.19) will now be shown to derive from different energy ranges.

Let us first investigate energies close to the Higgs pole, i.e. $s \simeq m_H^2$. The s-channel Higgs exchange diagram of Figure D.1b is then resonantly

enhanced so that all other contributions are negligible. Consequently, the full matrix element of light scalar elastic scattering can be approximated as

$$\mathcal{M}(s \simeq m_H^2, \cos\vartheta) \simeq -\frac{4\kappa_{H2h}^2}{s - m_H^2 - \mathrm{i}m_H\Gamma_H} \ .$$

Using equation (D.3) together with $\mathcal{P}_0(\cos\vartheta) \equiv 1$, and defining $\delta s := s - m_H^2$, the associated s-wave amplitude is readily calculated as

$$|\mathrm{Re}\, a_0| = \frac{\kappa_{H2h}^2}{4\pi} \frac{|\delta s|}{\delta s^2 + m_H^2\Gamma_H^2} \ , \tag{D.5}$$

where we additionally employed $\xi(m_H^2) \simeq 1$, which holds for the considered mass hierarchy $m_h^2 \ll m_H^2$. The right-hand side of equation (D.5) attains a maximum at $\delta s_0 = m_H\Gamma_H$. Applying the unitarity bound of equation (D.4) to said maximum enables us to set an upper limit on the trilinear portal coupling κ_{H2h}, namely

$$\frac{|\kappa_{H2h}|}{m_H} \leqslant \sqrt{8\pi\frac{\Gamma_H}{m_H}} \ , \tag{D.6}$$

thus reproducing equation (4.18).

Next, we consider energies far away from the Higgs pole at $s = m_H^2$. All contributions involving the exchange of a virtual Higgs H are then suppressed by the large mass m_H and can therefore be neglected. Hence, the full matrix element of light scalar elastic scattering can now be approximated as

$$\mathcal{M}(s, \cos\vartheta) \simeq -24\lambda_{4h} - 36\kappa_{3h}^2 \Bigg[\frac{1}{s - m_h^2} \\ - \frac{1}{(1 - \cos\vartheta)s\xi(s)^2/2 + m_h^2} - \frac{1}{(1 + \cos\vartheta)s\xi(s)^2/2 + m_h^2} \Bigg] \ ,$$

where the first term arises from the contact interaction diagram of Figure D.1a, while the second, third and fourth terms correspond to s-, t- and u-channel h-exchange contributions, respectively. Additionally, we assumed that $\Gamma_h \ll m_h$. Using the above expression for the matrix element, the polar angle integral in equation (D.3) for $j = 0$ can be evaluated analytically. Defining the dimensionless quantity $y := 2m_h/\sqrt{s}$, the final result for the s-wave amplitude far away from the Higgs pole is conveniently written as

$$|\xi(y)\, \mathrm{Re}\, a_0(y)| = \frac{3\xi(y)}{2\pi} \left| \lambda_{4h} - \frac{3\kappa_{3h}^2}{2m_h^2} \cdot g(y) \right| \ , \tag{D.7}$$

with $\xi^2(y) = 1 - y^2$. Furthermore, the auxiliary function $g(y)$ is given by

$$g(y) := -\frac{y^2}{4 - y^2} + \frac{y^2}{2\xi^2(y)} \log\left(1 + \frac{4\xi^2(y)}{y^2}\right) \ .$$

Here, the first term originates from the s-channel h-exchange graph, while the second term combines t- and u-channel contributions. Note that the variable y ranges from zero at asymptotically high energies to one at the kinematic threshold $s = 4m_h^2$. In this domain, the function g has some interesting properties, all of which are straightforward to prove. First, $g(y)$ is non-negative thus demonstrating that t- and u-channel amplitudes always dominate over their s-channel counterpart. Second, $g(y)$ is strictly monotonously increasing and vanishes only in the high-energy limit $y \to 0$, where both terms independently tend to zero. From a physical point of view, this behavior reflects the fact that just the momentum-independent contact interaction from Figure D.1a stays finite at large $\sqrt{s}$. Imposing the general unitarity bound of equation (D.4) to equation (D.7) evaluated at $y \to 0$ therefore results in an upper limit on the quartic coupling λ_{4h}, namely

$$\lambda_{4h} \leqslant \frac{2\pi}{3} \,,$$

where we used $\xi(y) \to 1$ for $y \to 0$.

Finally, given the discussed properties of the functions $g(y)$ and $\xi(y)$, the right-hand side of equation (D.7) can be shown to attain a local maximum at some interior point $y_0 \in (0, 1)$, provided the dimensionless ratio κ_{3h}/m_h is large enough. Clearly, the precise location of y_0 depends on the value of λ_{4h}. Assuming for the moment that λ_{4h} is negligible, one numerically obtains the extremal point $y_0 = 0.85$. Evaluating equation (D.7) at y_0 and again imposing the general unitarity bound of equation (D.4) yields an upper limit on the trilinear light scalar self-coupling, specifically

$$\frac{|\kappa_{3h}|}{m_h} \lesssim 1.64 \,. \tag{D.8}$$

Finite quartic couplings $\lambda_{4h} > 0$ were found to relax the aforementioned limit. For instance, adopting $\lambda_{4h} = \frac{1}{2}$ implies a slightly less strict upper bound of $|\kappa_{3h}|/m_h \lesssim 1.73$.

Appendix E

Statistical methods

In the present appendix, we provide additional information on the statistical methods which we used in Chapter 5 to analyze the prospects for constraining or discovering quark-flavor-violating Higgs decays at the ILC. Specifically, we will discuss how to calculate expected upper limits and the expected statistical significance of a given signal in Sections E.1 and E.2, respectively.

E.1 Setting upper limits

Let us start by demonstrating how to obtain an *expected* upper limit S_{limit} on the number of signal events for a given number of background events B_0 and at a given confidence level (CL). Motivated by our application in Chapter 5, we consider a simple counting experiment. The corresponding statistical model is based on a Poisson distribution with random variable n, which represents the total number of events occurring in a given time interval. Assuming a known[a] number of background events B_0, the model is described by one parameter $S \geqslant 0$, specifying the number of events due to an unknown beyond-the-Standard Model (BSM) signal which is to be constrained. The statistical model can then be summarized as

$$\text{Poisson}(n; S) := \frac{(S + B_0)^n}{n!} \mathrm{e}^{-(S+B_0)} \,. \tag{E.1}$$

The computation of an upper limit S_{limit} is now based on a particular form of a statistical hypothesis test. The latter offers a procedure to decide whether or not to reject a given null hypothesis in favor of an alternative hypothesis on grounds of an actual observation. In the context of setting an upper limit within the framework of a counting experiment, we make the following identifications:

[a] In practice, the background B_0 is typically obtained by means of appropriate simulations. At the moment, we neglect effects due to systematic uncertainties in the background determination.

The null hypotheses (denoted as $H_0^{(i)}$) are the different signal hypotheses with an appropriate choice for the model parameter $S = S_i$.

The alternative hypotheses (denoted as $H_1^{(i)}$) state that the number of signal events is smaller than it is according to the null hypothesis $H_0^{(i)}$, i.e. $S < S_i$.

We also introduce the notion of a type-I error which corresponds to rejecting the null hypothesis when it is actually true. The probability to make such a type-I error is called the significance level and will be denoted as α. Its value characterizes the associated hypothesis test. A further crucial quantity is the so-called p-value. In the present context, it is defined as follows: Given a number of actually observed events n_{obs}, the p-value is the probability to obtain an experimental outcome containing an equal number of events or even less than found, assuming the null hypothesis $H_0^{(i)}$ is in fact true, i.e.

$$p(S_i) := \mathcal{P}(n \leqslant n_{\text{obs}} \,|\, H_0^{(i)} \text{ true}) \equiv \mathcal{P}(n \leqslant n_{\text{obs}} \,|\, S = S_i) \,. \tag{E.2}$$

The null hypothesis is now said to be rejected at significance level α (or confidence level $\text{CL} = 1 - \alpha$), if and only if the p-value $p(S_i)$ is not larger than the specified type-I error rate,

$$H_0^{(i)} \text{ is rejected} \quad \Leftrightarrow \quad p(S_i) \leqslant \alpha \,.$$

The upper limit S_{limit} on the number of signal events is then the smallest number, for which the corresponding null hypothesis can still be rejected in the above sense. All $S_i < S_{\text{limit}}$ will produce a p-value larger than α and can therefore not be rejected at the given significance level. Hence, the upper limit is implicitly defined via

$$p(S_{\text{limit}}) \stackrel{!}{=} \alpha \,. \tag{E.3}$$

The above procedure to compute an upper limit is referred to as the Neyman construction.

For a counting experiment based on the statistical model in equation (E.1), the p-value of equation (E.2) can be explicitly calculated as the sum

$$p(S_i) = \sum_{n=0}^{n_{\text{obs}}} \text{Poisson}(n; S_i) \,. \tag{E.4}$$

In Chapter 5, we only encountered cases with large numbers of (background) events. This allows us to employ the well-known Gaussian approximation of the Poisson distribution

$$\text{Poisson}(n; S) \simeq \text{Gauss}(n; S + B_0, \sqrt{S + B_0}) \,, \tag{E.5}$$

where the normal distribution is given by

$$\text{Gauss}(x;\mu,\sigma) = \frac{1}{\sqrt{2\pi}\sigma}\mathrm{e}^{-\frac{(x-\mu)^2}{2\sigma^2}} \ .$$

Equation (E.4) can now be approximately written as

$$\begin{aligned} p(S_i) &\simeq \int_0^{n_\text{obs}} \mathrm{d}n\ \text{Gauss}(n;\overbrace{S_i+B_0}^{=:\,\mu},\overbrace{\sqrt{S_i+B_0}}^{=:\,\sigma}) \\ &\simeq \int_{-\infty}^{n_\text{obs}} \mathrm{d}n\ \text{Gauss}(n;\mu,\sigma) \\ &= \int_{-\infty}^{(n_\text{obs}-\mu)/\sigma} \mathrm{d}x\ \text{Gauss}(x;0,1) \\ &= \Phi\left(\frac{n_\text{obs}-S_i-B_0}{\sqrt{S_i+B_0}}\right) \ . \end{aligned}$$

A few comments on the above calculation are in order. In going from the first to the second line, we used the fact that the integrand is peaked around a large, positive value μ and is thus negligible for negative numbers. In the next step, we performed a substitution of the integration variable, specifically $x = (n-\mu)/\sigma$. Afterwards, we simply insert the definition of the cumulative distribution function (CDF) Φ of the standard normal distribution. Using this final form of the p-value together with equation (E.3), we can isolate the upper limit

$$\frac{n_\text{obs}-S_\text{limit}-B_0}{\sqrt{S_\text{limit}+B_0}} = \Phi^{-1}(\alpha) \ . \tag{E.6}$$

Obviously, when it comes to future searches for new physics, the actual number of observations n_obs is not yet available. We must therefore make an assumption on the *expected* data sample. To this end, one introduces

the expected hypothesis (denoted as H_e). Assuming that the actual experiment yields a result that can be described without invoking new physics, H_e is the background-only hypothesis corresponding to the choice $S = 0$ for the model parameter.

Based on the expected hypothesis, one now defines the expected number of observations in an actual experiment to be

$$\langle n_\text{obs}\rangle := \text{median}\left(\text{Poisson}(n;0)\right) \simeq \text{median}\left(\text{Gauss}(n;B_0,\sqrt{B_0})\right) = B_0 \ ,$$

where the Gaussian approximation of equation (E.5) was used in the second step. Inserting the expected number of observations in equation (E.6), we obtain

$$\frac{-S_\text{limit}}{\sqrt{S_\text{limit}+B_0}} = \Phi^{-1}(\alpha) \quad\Leftrightarrow\quad \frac{S_\text{limit}}{\sqrt{S_\text{limit}+B_0}} = \Phi^{-1}(1-\alpha) \ , \tag{E.7}$$

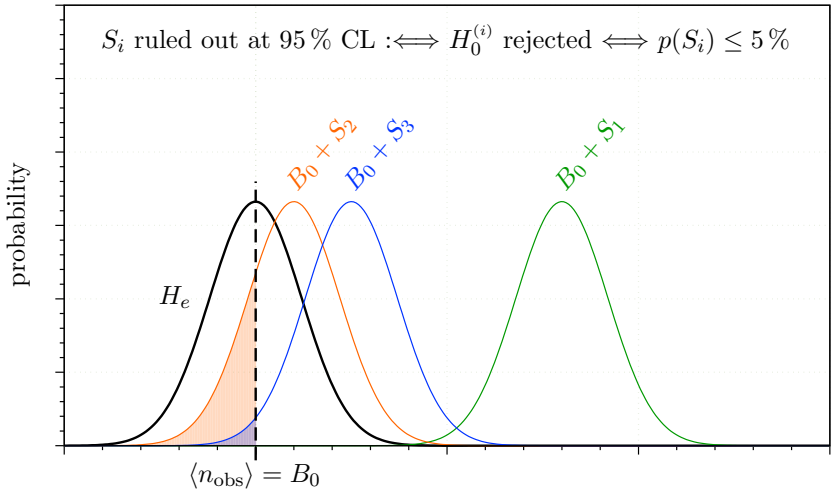

Figure E.1: Graphical illustration of the Neyman construction. The shaded areas correspond to the p-values associated with the null hypotheses $H_0^{(i)}$. In line with the expected hypothesis H_e, we assume that B_0 events are observed in an experiment.

Here, we used the identity for the quantile function $\Phi^{-1}(x) = -\Phi^{-1}(1-x)$ which derives from the following property of the CDF: $\Phi(-x) = 1 - \Phi(x)$. Calculating an upper limit at 95 % CL (equivalent to $\alpha = 0.05$), the right-hand side of the second relation in equation (E.7) gives $\Phi^{-1}(0.95) \approx 1.64$ thus reproducing the result that was quoted in Chapter 5 below equation (5.10).

In Figure E.1, we illustrate the concepts previously discussed. Specifically, we schematically display the probability distribution for the total number of events occurring in a given time interval under the expected hypothesis H_e, alongside with those distributions under three exemplary null hypotheses $H_0^{(i)}$, namely

- $\boldsymbol{H_0^{(1)}}$ for which the p-value is expected to be nearly zero so that the hypothesis can be rejected and the corresponding number of signal events S_1 can be excluded.
- $\boldsymbol{H_0^{(2)}}$ for which the p-value is expected to be larger than 5 % so that the hypothesis cannot be rejected at 95 % CL.
- $\boldsymbol{H_0^{(3)}}$ for which the p-value is expected to be equal to 5 % implying that S_3 is the *smallest* value that can still be ruled out at 95 % CL. In line with our definition in equation (E.3), we then set $S_{\mathrm{limit}} = S_3$.

E.2 Discovering signals

Let us also briefly recapitulate how to obtain the *expected* statistical significance of a given number of signal events S_0 in the context of a simple

counting experiment with a known number of Standard Model (SM) background events B_0. The relevant statistical model is again that based on the Poisson distribution, which was introduced in equation (E.1). The logic of the hypothesis test is, however, inverted with respect to before. Specifically, we now make the following identifications:

The null hypothesis (denoted as H_0) is the background-only hypothesis characterized by $S = 0$.

The alternative hypothesis (denoted as H_1) states that there exists a non-vanishing signal, i.e. $S > 0$.

The p-value is again defined as the probability to obtain an experimental outcome that is equally or more "extreme" as compared to an actual observation, assuming that the null hypothesis H_0 is in fact true. In the present context, this implies

$$p := \mathcal{P}(n \geqslant n_{\text{obs}} \,|\, H_0 \text{ true}) \equiv \mathcal{P}(n \geqslant n_{\text{obs}} \,|\, S = 0) \;, \tag{E.8}$$

with n_{obs} being the number of actually detected events. As before, we can explicitly calculate the p-value, namely

$$\begin{aligned} p &= \sum_{n=n_{\text{obs}}}^{\infty} \text{Poisson}(n; 0) \simeq \int_{n_{\text{obs}}}^{\infty} \mathrm{d}n \; \text{Gauss}(n; B_0, \sqrt{B_0}) \\ &= 1 - \int_{-\infty}^{n_{\text{obs}}} \mathrm{d}n \; \text{Gauss}(n; B_0, \sqrt{B_0}) \\ &= 1 - \int_{-\infty}^{(n_{\text{obs}} - B_0)/\sqrt{B_0}} \mathrm{d}x \; \text{Gauss}(x; 0, 1) \\ &= 1 - \Phi\left(\frac{n_{\text{obs}} - B_0}{\sqrt{B_0}}\right) \;, \end{aligned}$$

where we again employed the normal approximation from equation (E.5). The p-value decreases with growing argument of the CDF,

$$z := \frac{n_{\text{obs}} - B_0}{\sqrt{B_0}} \;, \tag{E.9}$$

which therefore lends itself as a measure of the observed signal's significance. Intuitively, the thus-defined Gaussian z-score counts the standard deviations $\sqrt{B_0}$ by which the observed event number n_{obs} differs from the mean of the background-only distribution B_0. The convention in particle physics is now to reject H_0, and thus to declare a discovery of a signal, if the observed significance is $z = 5$ or larger, corresponding to a p-value of maximally $2.87 \cdot 10^{-7}$.

Since real data are absent at this point, we again have to decide on

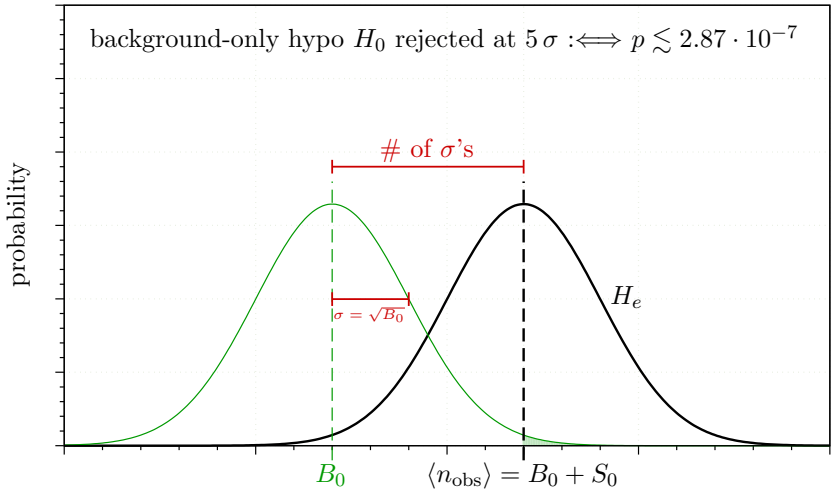

Figure E.2: Graphical illustration of how to determine a signal's statistical significance. The shaded area correspond to the p-values associated with the null hypothesis H_0. In line with the expected hypothesis H_e, we assume that $B_0 + S_0$ events are observed in an experiment.

the expected hypothesis (denoted as H_e). In the present case, we assume that the actual experiment yields a result that cannot be described by the minimal SM alone. Instead, BSM physics is supposed to induce $S = S_0$ signal events and we fix H_e accordingly.

The expected number of observations n_{obs} is then defined based on H_e as

$$\begin{aligned} \langle n_{\text{obs}} \rangle &:= \text{median}\left(\text{Poisson}(n; S_0)\right) \\ &\simeq \text{median}\left(\text{Gauss}(n; S_0 + B_0, \sqrt{S_0 + B_0})\right) \\ &= S_0 + B_0 \,, \end{aligned}$$

where the Gaussian approximation from equation (E.5) was employed in going from the first to the second line. Using the above result together with equation (E.9), we arrive at the formula for the expected signal significance

$$z = \frac{S_0}{\sqrt{B_0}} \,.$$

For $S_0 \ll B_0$ and negligible systematic errors on signal and background determination, this reproduces the expression quoted in Chapter 5, equation (5.10).

In complete analogy to Figure E.1, Figure E.2 illustrates the central concepts in determining the expected statistical significance of a given number of signal events S_0 over a known number of background events B_0.

List of Abbreviations

χPT	chiral perturbation theory
ALEPH	Apparatus for LEP Physics
ATLAS	A Toroidal LHC Apparatus
BaBar	B and B-bar
BSM	beyond the Standard Model
CDF	cumulative distribution function
CDR	conceptual design report
CEPC	Circular Electro Positron Collider
CFT	conformal field theory
CL	confidence level
CLIC	Compact Linear Collider
CMS	Compact Muon Solenoid
CKM	Cabibbo-Kobayashi-Maskawa
CP	combination of charge conjugation and parity
CSMTS	conformal SM extended by real triplet and singlet fields
EFT	effective field theory
EWSB	electroweak symmetry breaking
FCC	Future Circular Collider
FCNC	flavor-changing neutral currents
ggH	gluon fusion
GIM	Glashow-Iliopoulos-Maiani
GW	Gildener-Weinberg
HL-LHC	High Luminosity LHC
IDM	Inert Doublet Model

ILC . . . . . International Linear Collider

ILD . . . . . International Large Detector

IR . . . . . infrared (*in the sense of:* low energies)

irrep . . . . . irreducible representation

LEP . . . . . Large Electron-Positron Collider

LHC . . . . . Large Hadron Collider

LIPS . . . . . Lorentz-invariant phase space

MATHUSLA . . Massive Timing Hodoscope for Ultra Stable Neutral Particles

MCM . . . . . minimal conformal model

$\overline{\text{MS}}$ . . . . . modified minimal subtraction

OPAL . . . . . Omni Purpose Apparatus at LEP

PDG . . . . . particle data group

PGB . . . . . pseudo-Goldstone boson

QCD . . . . . quantum chromodynamics

QED . . . . . quantum electrodynamics

QFT . . . . . quantum field theory

QFV . . . . . quark-flavor violation

RG . . . . . renormalization group

RGE . . . . . renormalization group equation

SHiP . . . . . Search for Hidden Particles

SiD . . . . . Silicon Detector

SLAC . . . . . Stanford Linear Accelerator Center

SLC . . . . . SLAC Linear Collider

SM . . . . . Standard Model of particle physics

SSB . . . . . spontaneous symmetry breaking

SUSY . . . . . supersymmetry

TDR . . . . . technical design report

UV . . . . . ultraviolet (*in the sense of:* high energies)

VBF . . . . . vector boson fusion

vev . . . . . vacuum expectation value

YM . . . . . Yang-Mills

List of Figures

List of Tables

Bibliography

[1] **ATLAS** Collaboration, G. Aad *et al.*, "Observation of a new particle in the search for the Standard Model Higgs boson with the ATLAS detector at the LHC," *Phys. Lett.* **B716** (2012) 1–29, arXiv:1207.7214 [hep-ex].

[2] **CMS** Collaboration, S. Chatrchyan *et al.*, "Observation of a new boson at a mass of 125 GeV with the CMS experiment at the LHC," *Phys. Lett.* **B716** (2012) 30–61, arXiv:1207.7235 [hep-ex].

[3] S. L. Glashow, "Partial Symmetries of Weak Interactions," *Nucl. Phys.* **22** (1961) 579–588.

[4] S. Weinberg, "A Model of Leptons," *Phys. Rev. Lett.* **19** (1967) 1264–1266.

[5] A. Salam, "Weak and Electromagnetic Interactions," *Conf. Proc.* **C680519** (1968) 367–377.

[6] **Planck** Collaboration, R. Adam *et al.*, "Planck 2015 results. I. Overview of products and scientific results," *Astron. Astrophys.* **594** (2016) A1, arXiv:1502.01582 [astro-ph.CO].

[7] **Planck** Collaboration, P. A. R. Ade *et al.*, "Planck 2015 results. XIII. Cosmological parameters," *Astron. Astrophys.* **594** (2016) A13, arXiv:1502.01589 [astro-ph.CO].

[8] I. P. Ivanov, "Building and testing models with extended Higgs sectors," *Prog. Part. Nucl. Phys.* **95** (2017) 160–208, arXiv:1702.03776 [hep-ph].

[9] K. G. Wilson, "The Renormalization Group and Strong Interactions," *Phys. Rev.* **D3** (1971) 1818.

[10] E. Gildener, "Gauge Symmetry Hierarchies," *Phys. Rev.* **D14** (1976) 1667.

[11] S. Weinberg, "Implications of dynamical symmetry breaking," *Phys. Rev.* **D13** (1976) 974–996.

[12] S. Weinberg, "Implications of dynamical symmetry breaking: An addendum," *Phys. Rev.* **D19** (1979) 1277–1280.

[13] L. Susskind, "Dynamics of Spontaneous Symmetry Breaking in the Weinberg-Salam Theory," *Phys. Rev.* **D20** (1979) 2619–2625.

[14] G. 't Hooft, "Naturalness, chiral symmetry, and spontaneous chiral symmetry breaking," *NATO Sci. Ser. B* **59** (1980) 135.

[15] J. Wess and B. Zumino, "Supergauge Transformations in Four-Dimensions," *Nucl. Phys.* **B70** (1974) 39–50.

[16] P. Fayet and S. Ferrara, "Supersymmetry," *Phys. Rept.* **32** (1977) 249–334.

[17] H. P. Nilles, "Supersymmetry, Supergravity and Particle Physics," *Phys. Rept.* **110** (1984) 1–162.

[18] H. E. Haber and G. L. Kane, "The Search for Supersymmetry: Probing Physics Beyond the Standard Model," *Phys. Rept.* **117** (1985) 75–263.

[19] S. P. Martin, "A Supersymmetry primer," *Adv. Ser. Direct. High Energy Phys.* **21** (2010) 1–153, arXiv:hep-ph/9709356 [hep-ph]. [Adv. Ser. Direct. High Energy Phys.18,1(1998)].

[20] D. B. Kaplan and H. Georgi, "SU(2) x U(1) Breaking by Vacuum Misalignment," *Phys. Lett.* **136B** (1984) 183–186.

[21] D. B. Kaplan, H. Georgi, and S. Dimopoulos, "Composite Higgs Scalars," *Phys. Lett.* **136B** (1984) 187–190.

[22] M. J. Dugan, H. Georgi, and D. B. Kaplan, "Anatomy of a Composite Higgs Model," *Nucl. Phys.* **B254** (1985) 299–326.

[23] K. Agashe, R. Contino, and A. Pomarol, "The Minimal composite Higgs model," *Nucl. Phys.* **B719** (2005) 165–187, arXiv:hep-ph/0412089 [hep-ph].

[24] **ATLAS, CMS** Collaboration, G. Aad *et al.*, "Measurements of the Higgs boson production and decay rates and constraints on its couplings from a combined ATLAS and CMS analysis of the LHC pp collision data at $\sqrt{s} = 7$ and 8 TeV," *JHEP* **08** (2016) 045, arXiv:1606.02266 [hep-ex].

[25] O. Brüning and L. Rossi, "The High Luminosity Large Hadron Collider," *Adv. Ser. Direct. High Energy Phys.* **24** (2015) 1–393.

[26] G. Apollinari, I. Béjar Alonso, O. Brüning, P. Fessia, M. Lamont, L. Rossi, and L. Tavian, *High-Luminosity Large Hadron Collider (HL-LHC): Technical Design Report V. 0.1*. CERN Yellow Reports: Monographs. CERN, Geneva, 2017. http://cds.cern.ch/record/2284929.

[27] E. Todesco and F. Zimmermann, eds., *The High-Energy Large Hadron Collider*. CERN, Geneva, 2011. arXiv:1111.7188 [physics.acc-ph]. http://cds.cern.ch/record/1344820.

[28] P. W. Graham, D. E. Kaplan, and S. Rajendran, "Cosmological Relaxation of the Electroweak Scale," *Phys. Rev. Lett.* **115** no. 22, (2015) 221801, arXiv:1504.07551 [hep-ph].

[29] Z. Chacko, H.-S. Goh, and R. Harnik, "The Twin Higgs: Natural electroweak breaking from mirror symmetry," *Phys. Rev. Lett.* **96** (2006) 231802, arXiv:hep-ph/0506256 [hep-ph].

[30] N. Arkani-Hamed, T. Cohen, R. T. D'Agnolo, A. Hook, H. D. Kim, and D. Pinner, "Solving the Hierarchy Problem at Reheating with a Large Number of Degrees of Freedom," *Phys. Rev. Lett.* **117** no. 25, (2016) 251801, arXiv:1607.06821 [hep-ph].

[31] G. F. Giudice and M. McCullough, "A Clockwork Theory," *JHEP* **02** (2017) 036, arXiv:1610.07962 [hep-ph].

[32] W. A. Bardeen, "On naturalness in the standard model," in *Ontake Summer Institute on Particle Physics*. 1995. http://lss.fnal.gov/cgi-bin/find_paper.pl?conf-95-391.

[33] R. Hempfling, "The Next-to-minimal Coleman-Weinberg model," *Phys. Lett.* **B379** (1996) 153–158, arXiv:hep-ph/9604278 [hep-ph].

[34] K. A. Meissner and H. Nicolai, "Conformal Symmetry and the Standard Model," *Phys. Lett.* **B648** (2007) 312–317, arXiv:hep-th/0612165 [hep-th].

[35] K. A. Meissner and H. Nicolai, "Effective action, conformal anomaly and the issue of quadratic divergences," *Phys. Lett.* **B660** (2008) 260–266, arXiv:0710.2840 [hep-th].

[36] K. A. Meissner and H. Nicolai, "Conformal invariance from non-conformal gravity," *Phys. Rev.* **D80** (2009) 086005, arXiv:0907.3298 [hep-th].

[37] R. Foot, A. Kobakhidze, and R. R. Volkas, "Electroweak Higgs as a pseudo-Goldstone boson of broken scale invariance," *Phys. Lett.* **B655** (2007) 156–161, arXiv:0704.1165 [hep-ph].

[38] R. Foot, A. Kobakhidze, K. L. McDonald, and R. R. Volkas, "Neutrino mass in radiatively-broken scale-invariant models," *Phys. Rev.* **D76** (2007) 075014, arXiv:0706.1829 [hep-ph].

[39] D. Curtin *et al.*, "Exotic decays of the 125 GeV Higgs boson," *Phys. Rev.* **D90** no. 7, (2014) 075004, arXiv:1312.4992 [hep-ph].

[40] R. Aggleton, D. Barducci, N.-E. Bomark, S. Moretti, and C. Shepherd-Themistocleous, "Review of LHC experimental results on low mass bosons in multi Higgs models," *JHEP* **02** (2017) 035, arXiv:1609.06089 [hep-ph].

[41] R. Harnik, J. Kopp, and J. Zupan, "Flavor Violating Higgs Decays," *JHEP* **03** (2013) 026, arXiv:1209.1397 [hep-ph].

[42] T. Behnke, J. E. Brau, B. Foster, J. Fuster, M. Harrison, J. M. Paterson, M. Peskin, M. Stanitzki, N. Walker, and H. Yamamoto, "The International Linear Collider Technical Design Report - Volume 1: Executive Summary," arXiv:1306.6327 [physics.acc-ph].

[43] H. Baer, T. Barklow, K. Fujii, Y. Gao, A. Hoang, S. Kanemura, J. List, H. E. Logan, A. Nomerotski, M. Perelstein, *et al.*, "The International Linear Collider Technical Design Report - Volume 2: Physics," arXiv:1306.6352 [hep-ph].

[44] C. Adolphsen, M. Barone, B. Barish, K. Buesser, P. Burrows, J. Carwardine, J. Clark, H. Mainaud Durand, G. Dugan, E. Elsen, *et al.*, "The International Linear Collider Technical Design Report - Volume 3.I: Accelerator & in the Technical Design Phase," arXiv:1306.6353 [physics.acc-ph].

[45] C. Adolphsen, M. Barone, B. Barish, K. Buesser, P. Burrows, J. Carwardine, J. Clark, H. Mainaud Durand, G. Dugan, E. Elsen, *et al.*, "The International Linear Collider Technical Design Report - Volume 3.II: Accelerator Baseline Design," arXiv:1306.6328 [physics.acc-ph].

[46] H. Abramowicz *et al.*, "The International Linear Collider Technical Design Report - Volume 4: Detectors," arXiv:1306.6329 [physics.ins-det].

[47] **Linear Collider** Collaboration, L. Evans and S. Michizono, "The International Linear Collider Machine Staging Report 2017," arXiv:1711.00568 [physics.acc-ph].

[48] A. J. Helmboldt, P. Humbert, M. Lindner, and J. Smirnov, "Minimal conformal extensions of the Higgs sector," *JHEP* **07** (2017) 113, arXiv:1603.03603 [hep-ph].

[49] A. J. Helmboldt and M. Lindner, "Prospects for three-body Higgs boson decays into extra light scalars," *Phys. Rev.* **D95** no. 5, (2017) 055008, arXiv:1609.08127 [hep-ph].

[50] D. Barducci and A. J. Helmboldt, "Quark flavour-violating Higgs decays at the ILC," *JHEP* **12** (2017) 105, arXiv:1710.06657 [hep-ph].

[51] D. Hanneke, S. Fogwell, and G. Gabrielse, "New Measurement of the Electron Magnetic Moment and the Fine Structure Constant," *Phys. Rev. Lett.* **100** (2008) 120801, arXiv:0801.1134 [physics.atom-ph].

[52] T. Aoyama, M. Hayakawa, T. Kinoshita, and M. Nio, "Tenth-Order QED Contribution to the Electron g-2 and an Improved Value of the Fine Structure Constant," *Phys. Rev. Lett.* **109** (2012) 111807, arXiv:1205.5368 [hep-ph].

[53] **SLD Electroweak Group, DELPHI, ALEPH, SLD, SLD Heavy Flavour Group, OPAL, LEP Electroweak Working Group, L3** Collaboration, S. Schael *et al.*, "Precision electroweak measurements on the Z resonance," *Phys. Rept.* **427** (2006) 257–454, arXiv:hep-ex/0509008 [hep-ex].

[54] S. L. Glashow, J. Iliopoulos, and L. Maiani, "Weak Interactions with Lepton-Hadron Symmetry," *Phys. Rev.* **D2** (1970) 1285–1292.

[55] **E598** Collaboration, J. J. Aubert *et al.*, "Experimental Observation of a Heavy Particle J," *Phys. Rev. Lett.* **33** (1974) 1404–1406.

[56] **SLAC-SP-017** Collaboration, J. E. Augustin *et al.*, "Discovery of a Narrow Resonance in e^+e^- Annihilation," *Phys. Rev. Lett.* **33** (1974) 1406–1408. [Adv. Exp. Phys.5,141(1976)].

[57] M. Kobayashi and T. Maskawa, "CP Violation in the Renormalizable Theory of Weak Interaction," *Prog. Theor. Phys.* **49** (1973) 652–657.

[58] S. W. Herb *et al.*, "Observation of a Dimuon Resonance at 9.5-GeV in 400-GeV Proton-Nucleus Collisions," *Phys. Rev. Lett.* **39** (1977) 252–255.

[59] **CDF** Collaboration, F. Abe *et al.*, "Observation of top quark production in $\bar{p}p$ collisions," *Phys. Rev. Lett.* **74** (1995) 2626–2631, arXiv:hep-ex/9503002 [hep-ex].

[60] **D0** Collaboration, S. Abachi *et al.*, "Observation of the top quark," *Phys. Rev. Lett.* **74** (1995) 2632–2637, arXiv:hep-ex/9503003 [hep-ex].

[61] **UA1** Collaboration, G. Arnison *et al.*, "Experimental Observation of Isolated Large Transverse Energy Electrons with Associated Missing Energy at s**(1/2) = 540-GeV," *Phys. Lett.* **122B** (1983) 103–116. [,611(1983)].

[62] **UA1** Collaboration, G. Arnison *et al.*, "Experimental Observation of Lepton Pairs of Invariant Mass Around 95-GeV/c**2 at the CERN SPS Collider," *Phys. Lett.* **126B** (1983) 398–410.

[63] **UA2** Collaboration, M. Banner *et al.*, "Observation of Single Isolated Electrons of High Transverse Momentum in Events with Missing Transverse Energy at the CERN anti-p p Collider," *Phys. Lett.* **122B** (1983) 476–485.

[64] **UA2** Collaboration, P. Bagnaia *et al.*, "Evidence for Z0 → e+ e- at the CERN anti-p p Collider," *Phys. Lett.* **129B** (1983) 130–140.

[65] M. E. Peskin and D. V. Schroeder, *An Introduction to Quantum Field Theory*. Westview Press, 1st ed., 1995.

[66] D. H. Perkins, *Introduction to High Energy Physics*. Cambridge University Press, 4th ed., 2000.

[67] P. W. Higgs, "Broken symmetries, massless particles and gauge fields," *Phys. Lett.* **12** (1964) 132–133.

[68] P. W. Higgs, "Broken Symmetries and the Masses of Gauge Bosons," *Phys. Rev. Lett.* **13** (1964) 508–509.

[69] F. Englert and R. Brout, "Broken Symmetry and the Mass of Gauge Vector Mesons," *Phys. Rev. Lett.* **13** (1964) 321–323.

[70] G. S. Guralnik, C. R. Hagen, and T. W. B. Kibble, "Global Conservation Laws and Massless Particles," *Phys. Rev. Lett.* **13** (1964) 585–587.

[71] T. W. B. Kibble, "Symmetry breaking in non-Abelian gauge theories," *Phys. Rev.* **155** (1967) 1554–1561.

[72] T. Nakano and K. Nishijima, "Charge Independence for V-particles," *Prog. Theor. Phys.* **10** (1953) 581–582.

[73] M. Gell-Mann, "The interpretation of the new particles as displaced charge multiplets," *Nuovo Cim.* **4** no. S2, (1956) 848–866.

[74] J. Jaeckel and A. Ringwald, "The Low-Energy Frontier of Particle Physics," *Ann. Rev. Nucl. Part. Sci.* **60** (2010) 405–437, `arXiv:1002.0329 [hep-ph]`.

[75] N. Cabibbo, "Unitary Symmetry and Leptonic Decays," *Phys. Rev. Lett.* **10** (1963) 531–533. [,648(1963)].

[76] G. 't Hooft, "The Conceptual Basis of Quantum Field Theory," in *Philosophy of Physics*, J. Butterfield and J. Earman, eds., Handbook of the Philosophy of Science, pp. 661 – 729. North-Holland, Amsterdam, 2007. https://www.sciencedirect.com/science/article/pii/B9780444515605500105.

[77] C.-N. Yang and R. L. Mills, "Conservation of Isotopic Spin and Isotopic Gauge Invariance," *Phys. Rev.* **96** (1954) 191–195.

[78] G. 't Hooft, "Renormalization of Massless Yang-Mills Fields," *Nucl. Phys.* **B33** (1971) 173–199.

[79] G. 't Hooft, "Renormalizable Lagrangians for Massive Yang-Mills Fields," *Nucl. Phys.* **B35** (1971) 167–188.

[80] G. C. Branco, L. Lavoura, and J. P. Silva, "CP Violation," *Int. Ser. Monogr. Phys.* **103** (1999) 1–536.

[81] **ATLAS, CMS** Collaboration, G. Aad *et al.*, "Combined Measurement of the Higgs Boson Mass in pp Collisions at $\sqrt{s} = 7$ and 8 TeV with the ATLAS and CMS Experiments," *Phys. Rev. Lett.* **114** (2015) 191803, arXiv:1503.07589 [hep-ex].

[82] E. Fermi, "Versuch einer Theorie der beta-Strahlen. I," *Z. Phys.* **88** (1934) 161–177.

[83] **Particle Data Group** Collaboration, C. Patrignani *et al.*, "Review of Particle Physics," *Chin. Phys.* **C40** no. 10, (2016) 100001.

[84] P. A. M. Dirac, "The Cosmological constants," *Nature* **139** (1937) 323.

[85] P. A. M. Dirac, "New basis for cosmology," *Proc. Roy. Soc. Lond.* **A165** (1938) 199–208.

[86] **ATLAS, CMS** Collaboration, A. Ventura, "Searches for Supersymmetry," Tech. Rep. ATL-PHYS-PROC-2017-266, CERN, Geneva, Dec, 2017. http://cds.cern.ch/record/2296588.

[87] R. Barbieri and G. F. Giudice, "Upper Bounds on Supersymmetric Particle Masses," *Nucl. Phys.* **B306** (1988) 63–76.

[88] H. E. Haber, R. Hempfling, and A. H. Hoang, "Approximating the radiatively corrected Higgs mass in the minimal supersymmetric model," *Z. Phys.* **C75** (1997) 539–554, arXiv:hep-ph/9609331 [hep-ph].

[89] M. Papucci, J. T. Ruderman, and A. Weiler, "Natural SUSY Endures," *JHEP* **09** (2012) 035, arXiv:1110.6926 [hep-ph].

[90] N. Arkani-Hamed, S. Dimopoulos, and G. R. Dvali, "The Hierarchy problem and new dimensions at a millimeter," *Phys. Lett.* **B429** (1998) 263–272, arXiv:hep-ph/9803315 [hep-ph].

[91] N. Arkani-Hamed, S. Dimopoulos, and G. R. Dvali, "Phenomenology, astrophysics and cosmology of theories with submillimeter dimensions and TeV scale quantum gravity," *Phys. Rev.* **D59** (1999) 086004, arXiv:hep-ph/9807344 [hep-ph].

[92] L. Randall and R. Sundrum, "A Large mass hierarchy from a small extra dimension," *Phys. Rev. Lett.* **83** (1999) 3370–3373, arXiv:hep-ph/9905221 [hep-ph].

[93] S. Dimopoulos and L. Susskind, "Mass Without Scalars," *Nucl. Phys.* **B155** (1979) 237–252. [2,930(1979)].

[94] E. Eichten and K. D. Lane, "Dynamical Breaking of Weak Interaction Symmetries," *Phys. Lett.* **90B** (1980) 125–130.

[95] W. A. Bardeen, C. T. Hill, and M. Lindner, "Minimal Dynamical Symmetry Breaking of the Standard Model," *Phys. Rev.* **D41** (1990) 1647.

[96] N. Arkani-Hamed, A. G. Cohen, and H. Georgi, "Electroweak symmetry breaking from dimensional deconstruction," *Phys. Lett.* **B513** (2001) 232–240, arXiv:hep-ph/0105239 [hep-ph].

[97] N. Arkani-Hamed, A. G. Cohen, T. Gregoire, and J. G. Wacker, "Phenomenology of electroweak symmetry breaking from theory space," *JHEP* **08** (2002) 020, arXiv:hep-ph/0202089 [hep-ph].

[98] N. Arkani-Hamed, A. G. Cohen, E. Katz, and A. E. Nelson, "The Littlest Higgs," *JHEP* **07** (2002) 034, arXiv:hep-ph/0206021 [hep-ph].

[99] D. E. Kaplan and M. Schmaltz, "The Little Higgs from a simple group," *JHEP* **10** (2003) 039, arXiv:hep-ph/0302049 [hep-ph].

[100] D. J. Gross and J. Wess, "Scale invariance, conformal invariance, and the high-energy behavior of scattering amplitudes," *Phys. Rev.* **D2** (1970) 753–764.

[101] C. G. Callan, Jr., S. R. Coleman, and R. Jackiw, "A new improved energy-momentum tensor," *Annals Phys.* **59** (1970) 42–73.

[102] S. R. Coleman and R. Jackiw, "Why dilatation generators do not generate dilatations?," *Annals Phys.* **67** (1971) 552–598.

[103] T. Hambye and M. H. G. Tytgat, "Electroweak symmetry breaking induced by dark matter," *Phys. Lett.* **B659** (2008) 651–655, arXiv:0707.0633 [hep-ph].

[104] S. Iso, N. Okada, and Y. Orikasa, "Classically conformal $B - L$ extended Standard Model," *Phys. Lett.* **B676** (2009) 81–87, arXiv:0902.4050 [hep-ph].

[105] S. Iso, N. Okada, and Y. Orikasa, "The minimal $B - L$ model naturally realized at TeV scale," *Phys. Rev.* **D80** (2009) 115007, arXiv:0909.0128 [hep-ph].

[106] M. Holthausen, M. Lindner, and M. A. Schmidt, "Radiative Symmetry Breaking of the Minimal Left-Right Symmetric Model," *Phys. Rev.* **D82** (2010) 055002, arXiv:0911.0710 [hep-ph].

[107] L. Alexander-Nunneley and A. Pilaftsis, "The Minimal Scale Invariant Extension of the Standard Model," *JHEP* **09** (2010) 021, arXiv:1006.5916 [hep-ph].

[108] M. Holthausen, J. Kubo, K. S. Lim, and M. Lindner, "Electroweak and Conformal Symmetry Breaking by a Strongly Coupled Hidden Sector," *JHEP* **12** (2013) 076, arXiv:1310.4423 [hep-ph].

[109] A. Farzinnia, H.-J. He, and J. Ren, "Natural Electroweak Symmetry Breaking from Scale Invariant Higgs Mechanism," *Phys. Lett.* **B727** (2013) 141–150, arXiv:1308.0295 [hep-ph].

[110] A. Farzinnia and J. Ren, "Higgs Partner Searches and Dark Matter Phenomenology in a Classically Scale Invariant Higgs Boson Sector," *Phys. Rev.* **D90** no. 1, (2014) 015019, arXiv:1405.0498 [hep-ph].

[111] E. Gabrielli, M. Heikinheimo, K. Kannike, A. Racioppi, M. Raidal, and C. Spethmann, "Towards Completing the Standard Model: Vacuum Stability, EWSB and Dark Matter," *Phys. Rev.* **D89** no. 1, (2014) 015017, arXiv:1309.6632 [hep-ph].

[112] J. Kubo, K. S. Lim, and M. Lindner, "Electroweak Symmetry Breaking via QCD," *Phys. Rev. Lett.* **113** (2014) 091604, arXiv:1403.4262 [hep-ph].

[113] M. Lindner, S. Schmidt, and J. Smirnov, "Neutrino Masses and Conformal Electro-Weak Symmetry Breaking," *JHEP* **10** (2014) 177, arXiv:1405.6204 [hep-ph].

[114] W. Altmannshofer, W. A. Bardeen, M. Bauer, M. Carena, and J. D. Lykken, "Light Dark Matter, Naturalness, and the Radiative Origin of the Electroweak Scale," *JHEP* **01** (2015) 032, arXiv:1408.3429 [hep-ph].

[115] P. Humbert, M. Lindner, and J. Smirnov, "The Inverse Seesaw in Conformal Electro-Weak Symmetry Breaking and Phenomenological Consequences," *JHEP* **06** (2015) 035, arXiv:1503.03066 [hep-ph].

[116] P. Humbert, M. Lindner, S. Patra, and J. Smirnov, "Lepton Number Violation within the Conformal Inverse Seesaw," *JHEP* **09** (2015) 064, arXiv:1505.07453 [hep-ph].

[117] A. Ahriche, K. L. McDonald, and S. Nasri, "The Scale-Invariant Scotogenic Model," *JHEP* **06** (2016) 182, arXiv:1604.05569 [hep-ph].

[118] A. Ahriche, A. Manning, K. L. McDonald, and S. Nasri, "Scale-Invariant Models with One-Loop Neutrino Mass and Dark Matter Candidates," *Phys. Rev.* **D94** no. 5, (2016) 053005, arXiv:1604.05995 [hep-ph].

[119] S. R. Coleman and E. J. Weinberg, "Radiative Corrections as the Origin of Spontaneous Symmetry Breaking," *Phys. Rev.* **D7** (1973) 1888–1910.

[120] E. Gildener and S. Weinberg, "Symmetry Breaking and Scalar Bosons," *Phys. Rev.* **D13** (1976) 3333.

[121] V. Brdar, Y. Emonds, A. J. Helmboldt, and M. Lindner, "The conformal neutrino option." in preparation, 2018.

[122] S. Coleman, *Aspects of Symmetry: Selected Erice Lectures*. Cambridge University Press, 1st ed., 1988.

[123] K. G. Wilson, "Anomalous Dimensions and the Breakdown of Scale Invariance in Perturbation Theory," *Phys. Rev.* **D2** (1970) 1478.

[124] R. J. Crewther, "Nonperturbative evaluation of the anomalies in low-energy theorems," *Phys. Rev. Lett.* **28** (1972) 1421.

[125] M. S. Chanowitz and J. R. Ellis, "Canonical Anomalies and Broken Scale Invariance," *Phys. Lett.* **40B** (1972) 397–400.

[126] M. S. Chanowitz and J. R. Ellis, "Canonical Trace Anomalies," *Phys. Rev.* **D7** (1973) 2490–2506.

[127] P. Minkowski, "On the Anomalous Divergence of the Dilatation Current in Gauge Theories," *PRINT-76-0813 (BERN)* (1976) .

[128] N. Nielsen, "The Energy Momentum Tensor in a Nonabelian Quark Gluon Theory," *Nucl.Phys.* **B120** (1977) 212–220.

[129] S. L. Adler, J. C. Collins, and A. Duncan, "Energy-Momentum-Tensor Trace Anomaly in Spin 1/2 Quantum Electrodynamics," *Phys.Rev.* **D15** (1977) 1712.

[130] J. C. Collins, A. Duncan, and S. D. Joglekar, "Trace and Dilatation Anomalies in Gauge Theories," *Phys.Rev.* **D16** (1977) 438–449.

[131] H. Osborn, "Weyl consistency conditions and a local renormalization group equation for general renormalizable field theories," *Nucl. Phys.* **B363** (1991) 486–526.

[132] G. Mack and A. Salam, "Finite component field representations of the conformal group," *Annals Phys.* **53** (1969) 174–202.

[133] K. G. Wilson, "Renormalization group and critical phenomena. 1. Renormalization group and the Kadanoff scaling picture," *Phys. Rev.* **B4** (1971) 3174–3183.

[134] K. G. Wilson, "Renormalization group and critical phenomena. 2. Phase space cell analysis of critical behavior," *Phys. Rev.* **B4** (1971) 3184–3205.

[135] K. G. Wilson and J. B. Kogut, "The Renormalization group and the epsilon expansion," *Phys. Rept.* **12** (1974) 75–200.

[136] D. J. Gross and F. Wilczek, "Ultraviolet Behavior of Nonabelian Gauge Theories," *Phys. Rev. Lett.* **30** (1973) 1343–1346.

[137] H. D. Politzer, "Reliable Perturbative Results for Strong Interactions?," *Phys. Rev. Lett.* **30** (1973) 1346–1349.

[138] Y. Hamada, K. Kawana, and K. Tsumura, "Landau pole in the Standard Model with weakly interacting scalar fields," *Phys. Lett.* **B747** (2015) 238–244, arXiv:1505.01721 [hep-ph].

[139] J. F. Gunion, H. E. Haber, G. L. Kane, and S. Dawson, "The Higgs Hunter's Guide," *Front. Phys.* **80** (2000) 1–404.

[140] T. Hambye, F. S. Ling, L. Lopez Honorez, and J. Rocher, "Scalar Multiplet Dark Matter," *JHEP* **07** (2009) 090, arXiv:0903.4010 [hep-ph]. [Erratum: JHEP05,066(2010)].

[141] N. G. Deshpande and E. Ma, "Pattern of Symmetry Breaking with Two Higgs Doublets," *Phys. Rev.* **D18** (1978) 2574.

[142] R. Barbieri, L. J. Hall, and V. S. Rychkov, "Improved naturalness with a heavy Higgs: An Alternative road to LHC physics," *Phys. Rev.* **D74** (2006) 015007, arXiv:hep-ph/0603188 [hep-ph].

[143] L. Lopez Honorez, E. Nezri, J. F. Oliver, and M. H. G. Tytgat, "The Inert Doublet Model: An Archetype for Dark Matter," *JCAP* **0702** (2007) 028, arXiv:hep-ph/0612275 [hep-ph].

[144] G. C. Branco, P. M. Ferreira, L. Lavoura, M. N. Rebelo, M. Sher, and J. P. Silva, "Theory and phenomenology of two-Higgs-doublet models," *Phys. Rept.* **516** (2012) 1–102, arXiv:1106.0034 [hep-ph].

[145] S. L. Glashow and S. Weinberg, "Natural Conservation Laws for Neutral Currents," *Phys.Rev.* **D15** (1977) 1958.

[146] K. Kannike, "Vacuum Stability Conditions From Copositivity Criteria," *Eur. Phys. J.* **C72** (2012) 2093, arXiv:1205.3781 [hep-ph].

[147] M. Sher, "Electroweak Higgs Potentials and Vacuum Stability," *Phys. Rept.* **179** (1989) 273–418.

[148] M. Cirelli, N. Fornengo, and A. Strumia, "Minimal dark matter," *Nucl. Phys.* **B753** (2006) 178–194, arXiv:hep-ph/0512090 [hep-ph].

[149] M. Cirelli and A. Strumia, "Minimal Dark Matter: Model and results," *New J. Phys.* **11** (2009) 105005, arXiv:0903.3381 [hep-ph].

[150] P. Minkowski, "$\mu \to e\gamma$ at a Rate of One Out of 10^9 Muon Decays?," *Phys. Lett.* **67B** (1977) 421–428.

[151] T. Yanagida, "Horizontal Symmetry and Masses of Neutrinos," *Conf. Proc.* **C7902131** (1979) 95–99.

[152] M. Gell-Mann, P. Ramond, and R. Slansky, "Complex Spinors and Unified Theories," *Conf. Proc.* **C790927** (1979) 315–321, arXiv:1306.4669 [hep-th].

[153] R. N. Mohapatra and G. Senjanovic, "Neutrino Mass and Spontaneous Parity Violation," *Phys. Rev. Lett.* **44** (1980) 912.

[154] M. Maniatis, "The Next-to-Minimal Supersymmetric extension of the Standard Model reviewed," *Int. J. Mod. Phys.* **A25** (2010) 3505–3602, arXiv:0906.0777 [hep-ph].

[155] U. Ellwanger, C. Hugonie, and A. M. Teixeira, "The Next-to-Minimal Supersymmetric Standard Model," *Phys. Rept.* **496** (2010) 1–77, arXiv:0910.1785 [hep-ph].

[156] **ATLAS** Collaboration, G. Aad *et al.*, "Constraints on new phenomena via Higgs boson couplings and invisible decays with the ATLAS detector," *JHEP* **11** (2015) 206, arXiv:1509.00672 [hep-ex].

[157] **CMS** Collaboration, V. Khachatryan *et al.*, "Searches for invisible decays of the Higgs boson in pp collisions at $\sqrt{s} = 7$, 8, and 13 TeV," *JHEP* **02** (2017) 135, arXiv:1610.09218 [hep-ex].

[158] S. Dawson *et al.*, "Working Group Report: Higgs Boson," in *Proceedings, 2013 Community Summer Study on the Future of U.S. Particle Physics: Snowmass on the Mississippi (CSS2013): Minneapolis, MN, USA, July 29-August 6, 2013*. 2013. arXiv:1310.8361 [hep-ex].

[159] J. D. Clarke, R. Foot, and R. R. Volkas, "Phenomenology of a very light scalar ($100\,\text{MeV} < m_h < 10\,\text{GeV}$) mixing with the SM Higgs," *JHEP* **02** (2014) 123, arXiv:1310.8042 [hep-ph].

[160] B. Batell, N. Lange, D. McKeen, M. Pospelov, and A. Ritz, "Muon anomalous magnetic moment through the leptonic Higgs portal," *Phys. Rev.* **D95** no. 7, (2017) 075003, arXiv:1606.04943 [hep-ph].

[161] **LHC Higgs Cross Section Working Group** Collaboration, A. David, A. Denner, M. Duehrssen, M. Grazzini, C. Grojean, G. Passarino, M. Schumacher, M. Spira, G. Weiglein, and M. Zanetti, "LHC HXSWG interim recommendations to explore the coupling structure of a Higgs-like particle," arXiv:1209.0040 [hep-ph].

[162] **LHC Higgs Cross Section Working Group** Collaboration, D. de Florian *et al.*, "Handbook of LHC Higgs Cross Sections: 4. Deciphering the Nature of the Higgs Sector," arXiv:1610.07922 [hep-ph].

[163] D. A. Dicus and H.-J. He, "Scales of fermion mass generation and electroweak symmetry breaking," *Phys. Rev.* **D71** (2005) 093009, arXiv:hep-ph/0409131 [hep-ph].

[164] A. Schuessler and D. Zeppenfeld, "Unitarity constraints on MSSM trilinear couplings," in *SUSY 2007 Proceedings*, pp. 236–239. 2007. arXiv:0710.5175 [hep-ph]. http://www.susy07.uni-karlsruhe.de/Proceedings/proceedings/susy07.pdf.

[165] V. Silveira and A. Zee, "Scalar Phantoms," *Phys. Lett.* **B161** (1985) 136–140.

[166] N. V. Krasnikov, "Invisible scalars visible in Higgs decay," *Phys. Lett.* **B291** (1992) 89–91.

[167] R. Schabinger and J. D. Wells, "A Minimal spontaneously broken hidden sector and its impact on Higgs boson physics at the large hadron collider," *Phys. Rev.* **D72** (2005) 093007, arXiv:hep-ph/0509209 [hep-ph].

[168] B. Patt and F. Wilczek, "Higgs-field portal into hidden sectors," arXiv:hep-ph/0605188 [hep-ph].

[169] D. O'Connell, M. J. Ramsey-Musolf, and M. B. Wise, "Minimal Extension of the Standard Model Scalar Sector," *Phys. Rev.* **D75** (2007) 037701, arXiv:hep-ph/0611014 [hep-ph].

[170] R. S. Chivukula and A. V. Manohar, "Limits On A Light Higgs Boson," *Phys. Lett.* **B207** (1988) 86. [Erratum: Phys. Lett.B217,568(1989)].

[171] F. Wilczek, "Decays of Heavy Vector Mesons Into Higgs Particles," *Phys. Rev. Lett.* **39** (1977) 1304.

[172] **ALEPH** Collaboration, D. Buskulic *et al.*, "Search for a nonminimal Higgs boson produced in the reaction $e^+e^- \to$ h Z^*," *Phys. Lett.* **B313** (1993) 312–325.

[173] **L3** Collaboration, M. Acciarri *et al.*, "Search for neutral Higgs boson production through the process e+ e- → Z* H0," *Phys. Lett.* **B385** (1996) 454–470.

[174] **OPAL** Collaboration, G. Abbiendi *et al.*, "Decay mode independent searches for new scalar bosons with the OPAL detector at LEP," *Eur. Phys. J.* **C27** (2003) 311–329, arXiv:hep-ex/0206022 [hep-ex].

[175] C.-Y. Chen, S. Dawson, and I. M. Lewis, "Exploring resonant di-Higgs boson production in the Higgs singlet model," *Phys. Rev.* **D91** no. 3, (2015) 035015, arXiv:1410.5488 [hep-ph].

[176] J. F. Donoghue, J. Gasser, and H. Leutwyler, "The Decay of a Light Higgs Boson," *Nucl. Phys.* **B343** (1990) 341–368.

[177] A. Djouadi, J. Kalinowski, and M. Spira, "HDECAY: A Program for Higgs boson decays in the standard model and its supersymmetric extension," *Comput. Phys. Commun.* **108** (1998) 56–74, arXiv:hep-ph/9704448 [hep-ph].

[178] M. B. Voloshin and V. I. Zakharov, "Measuring QCD Anomalies in Hadronic Transitions Between Onium States," *Phys. Rev. Lett.* **45** (1980) 688.

[179] M. B. Voloshin, "Once Again About the Role of Gluonic Mechanism in Interaction of Light Higgs Boson with Hadrons," *Sov. J. Nucl. Phys.* **44** (1986) 478. [Yad. Fiz.44,738(1986)].

[180] R. S. Chivukula, A. G. Cohen, H. Georgi, B. Grinstein, and A. V. Manohar, "Higgs decay into Goldstone bosons," *Annals Phys.* **192** (1989) 93–103.

[181] S. Raby and G. B. West, "The Branching Ratio for a Light Higgs to Decay Into $\mu^+\mu^-$ Pairs," *Phys. Rev.* **D38** (1988) 3488.

[182] J. P. Chou, D. Curtin, and H. J. Lubatti, "New Detectors to Explore the Lifetime Frontier," *Phys. Lett.* **B767** (2017) 29–36, arXiv:1606.06298 [hep-ph].

[183] A. Belyaev, N. D. Christensen, and A. Pukhov, "CalcHEP 3.4 for collider physics within and beyond the Standard Model," *Comput. Phys. Commun.* **184** (2013) 1729–1769, arXiv:1207.6082 [hep-ph].

[184] **ATLAS** Collaboration, "Expected performance for displaced Lepton Jets: ATLAS trigger and reconstruction efficiency in LHC 2015 run.," *ATL-PHYS-PUB-2016-010* (2016) . https://cds.cern.ch/record/2153376.

[185] **ATLAS** Collaboration, "Search for long-lived neutral particles decaying into displaced lepton jets in proton–proton collisions at $\sqrt{s}$ = 13 TeV with the ATLAS detector," *ATLAS-CONF-2016-042* (2016) . https://cds.cern.ch/record/2206083.

[186] S. Frixione, V. Hirschi, D. Pagani, H. S. Shao, and M. Zaro, "Electroweak and QCD corrections to top-pair hadroproduction in association with heavy bosons," *JHEP* **06** (2015) 184, arXiv:1504.03446 [hep-ph].

[187] A. Bredenstein, A. Denner, S. Dittmaier, and S. Pozzorini, "NLO QCD corrections to pp —> t anti-t b anti-b + X at the LHC," *Phys. Rev. Lett.* **103** (2009) 012002, arXiv:0905.0110 [hep-ph].

[188] **CMS** Collaboration, V. Khachatryan *et al.*, "A search for pair production of new light bosons decaying into muons," *Phys. Lett.* **B752** (2016) 146–168, arXiv:1506.00424 [hep-ex].

[189] T. Barklow, J. Brau, K. Fujii, J. Gao, J. List, N. Walker, and K. Yokoya, "ILC Operating Scenarios," arXiv:1506.07830 [hep-ex].

[190] Z. Liu, L.-T. Wang, and H. Zhang, "Exotic decays of the 125 GeV Higgs boson at future e^+e^- lepton colliders," *Chin. Phys.* **C41** no. 6, (2017) 063102, arXiv:1612.09284 [hep-ph].

[191] S. Bejar, F. Dilme, J. Guasch, and J. Sola, "Higgs boson flavor changing neutral decays into bottom quarks in supersymmetry," *JHEP* **08** (2004) 018, arXiv:hep-ph/0402188 [hep-ph].

[192] G. Barenboim, C. Bosch, J. S. Lee, M. L. López-Ibáñez, and O. Vives, "Flavor-changing Higgs boson decays into bottom and strange quarks in supersymmetric models," *Phys. Rev.* **D92** no. 9, (2015) 095017, arXiv:1507.08304 [hep-ph].

[193] M. E. Gómez, S. Heinemeyer, and M. Rehman, "Quark flavor violating Higgs boson decay h$\to \bar{b}$s+b$\bar{s}$ in the MSSM," *Phys. Rev.* **D93** no. 9, (2016) 095021, arXiv:1511.04342 [hep-ph].

[194] A. Arhrib, Y. Cheng, and O. C. W. Kong, "Comprehensive analysis on lepton flavor violating Higgs boson to $\mu^{\mp}\tau^{\pm}$ decay in supersymmetry without R parity," *Phys. Rev.* **D87** no. 1, (2013) 015025, arXiv:1210.8241 [hep-ph].

[195] A. Crivellin, A. Kokulu, and C. Greub, "Flavor-phenomenology of two-Higgs-doublet models with generic Yukawa structure," *Phys. Rev.* **D87** no. 9, (2013) 094031, arXiv:1303.5877 [hep-ph].

[196] F. J. Botella, G. C. Branco, M. Nebot, and M. N. Rebelo, "Flavour Changing Higgs Couplings in a Class of Two Higgs Doublet Models," *Eur. Phys. J.* **C76** no. 3, (2016) 161, arXiv:1508.05101 [hep-ph].

[197] A. Crivellin, J. Heeck, and D. Müller, "Large $h \to bs$ in generic two-Higgs-doublet models," *Phys. Rev.* **D97** no. 3, (2018) 035008, arXiv:1710.04663 [hep-ph].

[198] K. Agashe and R. Contino, "Composite Higgs-Mediated FCNC," *Phys. Rev.* **D80** (2009) 075016, arXiv:0906.1542 [hep-ph].

[199] S. Casagrande, F. Goertz, U. Haisch, M. Neubert, and T. Pfoh, "Flavor Physics in the Randall-Sundrum Model: I. Theoretical Setup and Electroweak Precision Tests," *JHEP* **10** (2008) 094, arXiv:0807.4937 [hep-ph].

[200] A. Azatov, M. Toharia, and L. Zhu, "Higgs Mediated FCNC's in Warped Extra Dimensions," *Phys. Rev.* **D80** (2009) 035016, arXiv:0906.1990 [hep-ph].

[201] **CMS** Collaboration, V. Khachatryan *et al.*, "Search for Lepton-Flavour-Violating Decays of the Higgs Boson," *Phys. Lett.* **B749** (2015) 337–362, arXiv:1502.07400 [hep-ex].

[202] **ATLAS** Collaboration, G. Aad *et al.*, "Search for lepton-flavour-violating $H \to \mu\tau$ decays of the Higgs boson with the ATLAS detector," *JHEP* **11** (2015) 211, arXiv:1508.03372 [hep-ex].

[203] **CMS** Collaboration, "Search for lepton flavour violating decays of the Higgs boson to $\mu\tau$ and eτ in proton-proton collisions at $\sqrt{s} = 13$ TeV," *CMS-PAS-HIG-17-001* (2017) . https://cds.cern.ch/record/2264540.

[204] **CMS** Collaboration, V. Khachatryan *et al.*, "Search for lepton flavour violating decays of the Higgs boson to $e\tau$ and $e\mu$ in proton-proton collisions at $\sqrt{s} = 8$ TeV," *Phys. Lett.* **B763** (2016) 472–500, arXiv:1607.03561 [hep-ex].

[205] **ATLAS** Collaboration, G. Aad *et al.*, "Search for lepton-flavour-violating decays of the Higgs and Z bosons with the ATLAS detector," *Eur. Phys. J.* **C77** no. 2, (2017) 70, arXiv:1604.07730 [hep-ex].

[206] **ATLAS** Collaboration, G. Aad *et al.*, "Search for flavour-changing neutral current top quark decays $t \to Hq$ in pp collisions at $\sqrt{s} = 8$ TeV with the ATLAS detector," *JHEP* **12** (2015) 061, arXiv:1509.06047 [hep-ex].

[207] **CMS** Collaboration, V. Khachatryan *et al.*, "Search for top quark decays via Higgs-boson-mediated flavor-changing neutral currents in pp collisions at $\sqrt{s} = 8$ TeV," *JHEP* **02** (2017) 079, arXiv:1610.04857 [hep-ex].

[208] M. Aicheler, P. Burrows, M. Draper, T. Garvey, P. Lebrun, K. Peach, N. Phinney, H. Schmickler, D. Schulte, and N. Toge, "A Multi-TeV Linear Collider Based on CLIC Technology: CLIC Conceptual Design Report," *CERN-2012-007* (2012) .

[209] L. Linssen, A. Miyamoto, M. Stanitzki, and H. Weerts, "Physics and Detectors at CLIC: CLIC Conceptual Design Report," *CERN-2012-003* (2012) , arXiv:1202.5940 [physics.ins-det].

[210] P. Lebrun, L. Linssen, A. Lucaci-Timoce, D. Schulte, F. Simon, S. Stapnes, N. Toge, H. Weerts, and J. Wells, "The CLIC Programme: Towards a Staged e+e- Linear Collider Exploring the Terascale: CLIC Conceptual Design Report," *CERN-2012-005* (2012) , arXiv:1209.2543 [physics.ins-det].

[211] **CLICdp, CLIC** Collaboration, M. J. Boland *et al.*, "Updated baseline for a staged Compact Linear Collider," arXiv:1608.07537 [physics.acc-ph].

[212] **CEPC-SPPC Study Group** Collaboration, M. Ahmad *et al.*, "CEPC-SPPC Preliminary Conceptual Design Report. Volume I: Physics and Detector,".

[213] **CEPC-SPPC Study Group** Collaboration, A. Apyan *et al.*, "CEPC-SPPC Preliminary Conceptual Design Report. Volume II: Accelerator,".

[214] K. Fujii *et al.*, "Physics Case for the 250 GeV Stage of the International Linear Collider," arXiv:1710.07621 [hep-ex].

[215] S. Asai, J. Tanaka, Y. Ushiroda, M. Nakao, J. Tian, S. Kanemura, S. Matsumoto, S. Shirai, M. Endo, and M. Kakizaki, "Report by the Committee on the Scientific Case of the ILC Operating at 250 GeV as a Higgs Factory," arXiv:1710.08639 [hep-ex].

[216] T. Suehara and T. Tanabe, "LCFIPlus: A Framework for Jet Analysis in Linear Collider Studies," *Nucl. Instrum. Meth.* **A808** (2016) 109–116, arXiv:1506.08371 [physics.ins-det].

[217] A. Arbey *et al.*, "Physics at the e+ e- Linear Collider," *Eur. Phys. J.* **C75** no. 8, (2015) 371, arXiv:1504.01726 [hep-ph].

[218] K. Fujii *et al.*, "Physics Case for the International Linear Collider," arXiv:1506.05992 [hep-ex].

[219] D. M. Asner *et al.*, "ILC Higgs White Paper," in *Proceedings, Community Summer Study 2013: Snowmass on the Mississippi (CSS2013): Minneapolis, MN, USA, July 29-August 6, 2013*. 2013. arXiv:1310.0763 [hep-ph].

[220] T. Barklow, K. Fujii, S. Jung, M. E. Peskin, and J. Tian, "Model-Independent Determination of the Triple Higgs Coupling at e+e- Colliders," arXiv:1708.09079 [hep-ph].

[221] M. Thomson, "Model-independent measurement of the $e^+ e^- \to HZ$ cross section at a future $e^+ e^-$ linear collider using hadronic Z decays," *Eur. Phys. J.* **C76** no. 2, (2016) 72, arXiv:1509.02853 [hep-ex].

[222] T. Appelquist and J. Carazzone, "Infrared Singularities and Massive Fields," *Phys. Rev.* **D11** (1975) 2856.

[223] H. Georgi, "Effective field theory," *Ann. Rev. Nucl. Part. Sci.* **43** (1993) 209–252.

[224] B. Grzadkowski, M. Iskrzynski, M. Misiak, and J. Rosiek, "Dimension-Six Terms in the Standard Model Lagrangian," *JHEP* **10** (2010) 085, arXiv:1008.4884 [hep-ph].

[225] A. Djouadi, "The Anatomy of electro-weak symmetry breaking. I: The Higgs boson in the standard model," *Phys. Rept.* **457** (2008) 1–216, arXiv:hep-ph/0503172 [hep-ph].

[226] C. Degrande, C. Duhr, B. Fuks, D. Grellscheid, O. Mattelaer, and T. Reiter, "UFO - The Universal FeynRules Output," *Comput. Phys. Commun.* **183** (2012) 1201–1214, arXiv:1108.2040 [hep-ph].

[227] A. Alloul, N. D. Christensen, C. Degrande, C. Duhr, and B. Fuks, "FeynRules 2.0 - A complete toolbox for tree-level phenomenology," *Comput. Phys. Commun.* **185** (2014) 2250–2300, arXiv:1310.1921 [hep-ph].

[228] W. Kilian, T. Ohl, and J. Reuter, "WHIZARD: Simulating Multi-Particle Processes at LHC and ILC," *Eur. Phys. J.* **C71** (2011) 1742, arXiv:0708.4233 [hep-ph].

[229] M. Moretti, T. Ohl, and J. Reuter, "O'Mega: An Optimizing matrix element generator," arXiv:hep-ph/0102195 [hep-ph].

[230] T. Ohl, "CIRCE version 1.0: Beam spectra for simulating linear collider physics," *Comput. Phys. Commun.* **101** (1997) 269–288, arXiv:hep-ph/9607454 [hep-ph].

[231] T. Sjöstrand, S. Ask, J. R. Christiansen, R. Corke, N. Desai, P. Ilten, S. Mrenna, S. Prestel, C. O. Rasmussen, and P. Z. Skands, "An Introduction to PYTHIA 8.2," *Comput. Phys. Commun.* **191** (2015) 159–177, arXiv:1410.3012 [hep-ph].

[232] **DELPHES 3** Collaboration, J. de Favereau, C. Delaere, P. Demin, A. Giammanco, V. Lemaître, A. Mertens, and M. Selvaggi, "DELPHES 3, A modular framework for fast simulation of a generic collider experiment," *JHEP* **02** (2014) 057, arXiv:1307.6346 [hep-ex].

[233] C. T. Potter, "DSiD: a Delphes Detector for ILC Physics Studies," in *Proceedings, International Workshop on Future Linear Colliders (LCWS15): Whistler, B.C., Canada, November 02-06, 2015*. 2016. arXiv:1602.07748 [hep-ph].

[234] M. Cacciari, G. P. Salam, and G. Soyez, "FastJet User Manual," *Eur. Phys. J.* **C72** (2012) 1896, arXiv:1111.6097 [hep-ph].

[235] M. Cacciari, G. P. Salam, and G. Soyez, "The Anti-k(t) jet clustering algorithm," *JHEP* **04** (2008) 063, arXiv:0802.1189 [hep-ph].

[236] E. Conte, B. Fuks, and G. Serret, "MadAnalysis 5, A User-Friendly Framework for Collider Phenomenology," *Comput. Phys. Commun.* **184** (2013) 222–256, arXiv:1206.1599 [hep-ph].

[237] **ATLAS** Collaboration, "Expected sensitivity of ATLAS to FCNC top quark decays $t \to Zu$ and $t \to Hq$ at the High Luminosity LHC," *ATL-PHYS-PUB-2016-019* (2016) . https://cds.cern.ch/record/2209126.

[238] **SHiP** Collaboration, M. Anelli *et al.*, "A facility to Search for Hidden Particles (SHiP) at the CERN SPS," arXiv:1504.04956 [physics.ins-det].

[239] S. Alekhin *et al.*, "A facility to Search for Hidden Particles at the CERN SPS: the SHiP physics case," *Rept. Prog. Phys.* **79** no. 12, (2016) 124201, arXiv:1504.04855 [hep-ph].

[240] F. Lyonnet and I. Schienbein, "PyR@TE 2: A Python tool for computing RGEs at two-loop," *Comput. Phys. Commun.* **213** (2017) 181–196, arXiv:1608.07274 [hep-ph].

[241] F. Staub, "SARAH 4 : A tool for (not only SUSY) model builders," *Comput. Phys. Commun.* **185** (2014) 1773–1790, arXiv:1309.7223 [hep-ph].

[242] M. E. Machacek and M. T. Vaughn, "Two Loop Renormalization Group Equations in a General Quantum Field Theory. 1. Wave Function Renormalization," *Nucl. Phys.* **B222** (1983) 83–103.

[243] M. E. Machacek and M. T. Vaughn, "Two Loop Renormalization Group Equations in a General Quantum Field Theory. 2. Yukawa Couplings," *Nucl. Phys.* **B236** (1984) 221–232.

[244] M. E. Machacek and M. T. Vaughn, "Two Loop Renormalization Group Equations in a General Quantum Field Theory. 3. Scalar Quartic Couplings," *Nucl. Phys.* **B249** (1985) 70–92.

Acknowledgements

The completion of the present thesis would have been impossible, if it were not for the help and support of many people. First and foremost, I am very grateful to my advisor Prof. Manfred Lindner for his guidance and continuous support throughout my PhD studies, for triggering many interesting discussions and for providing a truly stimulating work environment. I would also like to thank Prof. Tilman Plehn not only for kindly accepting to be the second referee, but also for encouraging me to pursue the idea of three-body Higgs decays. Likewise, I thank Prof. Hans-Christian Schultz-Coulon and Prof. Björn Malte Schäfer for agreeing to be members of my examination committee. I also thank Werner Rodejohann for giving me the possibility to participate in the IMPRS-PTFS program and for the ensuing support.

I would like to express my gratitude to Daniele Barducci, Juri Smirnov and Pascal Humbert for fruitful collaborations, the results of which form this work's basis. Much of the physics I learned during the last years came from insightful discussions with them. I would also like to thank Kevin Max, Moritz Platscher, Vedran Brdar and Yannick Emonds for working with me on projects that unfortunately did not make it into this thesis.

I am furthermore deeply indebted to Julia Haser, Meike Danisch, Thomas Hugle, Vedran Brdar and Yannick Emonds for carefully proof-reading different parts of this thesis and for providing numerous helpful comments as well as suggestions for improvement.

Let me also thank all of the group members for creating a particularly nice atmosphere in our division. I am especially grateful to Anja Berneiser and Britta Schwarz for their constant help and assistance in dealing with all kinds of administrative tasks, as well as for always providing cookies and other sweets. Furthermore, I have to mention Julia Haser and Natascha Rupp at this point, with whom sharing an office was a real pleasure. A special thanks also goes to Miguel Campos for officiating the most memorable bird funeral I ever attended, and for being my Valentine's date in 2016. (I hope we get to see Deadpool 2 soon!)

My physics studies in Heidelberg would have been considerably less fun, if I hadn't had the pleasure of meeting Diddi, Hannes, Joscha, Mario, Martin, Meike, Natascha, Paul and Tanja. Thank you for all the good times we had and hopefully will be having in the future. I am equally thankful to my friends from Ludwigshafen and Mannheim for making sure that I don't take myself too seriously. Special thanks go to Max for motivating conversations and for his advice that writing may become easier through the occasional

gin and tonic, as well as to Julia for her many good tips and her constant encouragement.

I am deeply grateful to my parents for everything they taught me, for their continuous support and for always reminding me of the truly important things in life. Last but not least I thank Meike for her multifaceted,[b] invaluable help and support during all stages of my PhD studies, for accompanying me through all the ups and downs and for always finding the right means to cheer me up.

Heidelberg, May 2018 Alexander Helmboldt

[b] I know you are particularly fond of this word.